Università Politecnica delle Marche
Scuola di Dottorato di Ricerca in Scienze dell'Ingegneria
Curriculum in Ingegneria Civile, Edile e Architettura

Application of adhesive joints on a tensegrity floor: verification of technology and mechanical performance

Ph.D. Dissertation of:

Francesco Marchione

Advisor:

Prof. Placido Munafò

Curriculum supervisor:

Prof. Francesco Fatone

XXXIV edition - new series

Università Politecnica delle Marche
Scuola di Dottorato di Ricerca in Scienze dell'Ingegneria
Curriculum in Ingegneria Civile, Edile e Architettura

Application of adhesive joints on a tensegrity floor: verification of technology and mechanical performance

Ph.D. Dissertation of:

Francesco Marchione

Advisor:

Prof. Placido Munafò

Curriculum supervisor:

Prof. Francesco Fatone

XXXIV edition - new series

Università Politecnica delle Marche
Dipartimento di Ingegneria Civile, Edile ed Architettura (DICEA)
Via Brecce Bianche — 60131 - Ancona, Italy

A mia madre

Acknowledgements

First of all, I would like to thank Prof. P. Munafò for the precious opportunity he has given me and for introducing me to the wonderful world of research, as well as for his helpfulness and competence.
I would also like to thank the laboratory staff for their great helpfulness and for providing the necessary technical support during the extensive experimental phases.
I would like to thank my friends and fellow students for sharing these intense years of work and training with me.
Finally, I would like to thank my mother Bernardetta, my father Buono, and my brother Luca, for never letting me lack their presence, supporting and comforting me every moment of this new experience.

Abstract

Il presente lavoro verifica l'applicabilità della tecnologia adesiva su componenti edilizi innovativi. L'impiego degli adesivi strutturali rappresenta la traduzione costruttiva del principio della "semplificazione tecnologica", ovvero della possibilità di realizzare prodotti industrializzabili caratterizzati da elevate prestazioni e da un numero limitato di componenti, riducendo le emissioni ambientali nelle fasi di produzione, assemblaggio, manutenzione e smaltimento del prodotto.

Nel seguito viene verificata la fattibilità tecnico-costruttiva della realizzazione di un solaio tensegrale in acciaio e vetro, sviluppando l'idea brevettuale espressa nel brevetto n. 00014426973, inventore Prof. P. Munafò. L'attività di ricerca si è sviluppata attraverso la sperimentazione di diverse tipologie di giunti adesivi con diversi aderendi (acciaio, alluminio, vetro) e adesivi sia dopo maturazione in condizioni di laboratorio che dopo invecchiamento artificiale accelerato (durabilità). A tale fase è seguita l'ingegnerizzazione e la definizione strutturale dell'elemento costruttivo brevettato (solaio tensegrale), in cui la collaborazione strutturale tra impalcato e sottostruttura, ottenuto mediante l'impiego di adesivi strutturali, ne rappresenta l'innovazione principale. Infine, è stato costruito un prototipo in scala 1:2 per verificare sperimentalmente le prestazioni meccaniche in condizioni d'esercizio.

Il risultato principale è rappresentato dalla verifica delle prestazioni meccaniche del solaio "Tensegrity Floor", attraverso prove di carico su prototipo in scala, quantificando l'incremento di rigidezza ottenuto variando la condizione di vincolo dell'impalcato rispetto alla tradizionale configurazione di semplice appoggio.
Dal punto di vista delle prestazioni meccaniche, l'impiego della giunzione adesiva ha consentito di incrementare la rigidezza della struttura risultante fino ad un massimo del +75%. Considerando l'aspetto costruttivo, l'uso degli adesivi ha permesso di ridurre la sezione resistente degli elementi strutturali impiegati, soddisfacendo i limiti imposti dalla normativa.

Le risultanze sperimentali hanno dimostrato la possibilità di ottenere – mediante i vantaggi offerti dagli adesivi strutturali – un elemento costruttivo versatile, modulare, leggero e trasparente, costituito da un impalcato in vetro collaborante con la sottostruttura metallica tensegrale in grado di esaltarne sia le proprietà fisiche che estetiche.

Contents

1. Introduction **1**
1.1 Objectives…….…… 1
1.2 Work phases…… 2
1.3 Methodology……... 2
1.4 References…….…… 3

2. "Tensegrity Smart", a tensegrity floor patent **4**
2.1. Tensegrity principle: definitions and hystorical background…..…….. 4
2.2. Patents and developments.……..…….. 9
2.3. Main projects……...……..13
2.3.1 Archaeological Museum of R. Calabria, ABDR Studio, 2007…..13
2.3.2 De La Plata Stadium, Buenos Aires, 2003…..……..…….... 15
2.3.3 Olympiastadion, Munich, O. Frei, 1972……..…….…..... 15
2.3.4 Cloister of Neunmunster, RFR, Luxembourg, 2001-03..…..….... 16
2.3.5 Inner courtyard of the Maximilian Museum, Augsburg, 1999..... 17
2.4. Patent No. 00014426973……..……..……..19
2.4.1 Description of the structural element.……..…..... 19
2.5. Product information..…..……..……..…….. 21
2.6. References……...……..21
2.7. List of figures……...…… 23

3. "Tensegrity Floor" prototype **24**
3.1. Introduction……..…….…….. 24
3.1.1 Methodology……..…..... 24
3.2. Identification of the basic module……..…….. 25
3.3. Construction hypothesis……..……..…….. 26
3.4. Form-finding……...……..…….. 26
3.4.1 3D modelling with SAP2000…….…….…..... 28
3.5. Materials…….……...……..……..30
3.6. Prototype……...……..…….. 31
3.7. Numerical analysis of the adhesive joint…….……32
3.7.1 FE modelling……..…….…..... 32
3.7.2 FE results…….…….…...34
3.8. References……...……..…….. 42
3.9. List of figures and tables……...…… 43

4. Experimental strength evaluation of glass-aluminium double-lap adhesive joints 44
4.1. Abstract……..…….…….. 44
4.2. Introduction……..…….…….. 46
4.3. Materials and methods……..…….…….. 47
4.3.1 Materials properties……..……..…….. 48

4.3.1.1 Adherends…….…….. 48
4.3.1.2 Adhesives…….…….. 48
4.4. Specimens dimensions…….…….…….. 49
4.5. Artificial ageing……..…….…….…….. 51
4.6. Test setup……..…….…….…….. 52
4.7. Results and discussion……..…….…….…….. 53
4.7.1 Mechanical performances……...…….…….. 53
4.8. Failure modes……..…….…….…….. 63
4.9. Conclusions..……..…….…….…….. 67
4.10. References..……..…….…….…….. 69
4.11. List of figures and tables.……...…… 71

5. Effect of temperature and relative humidity on the shear performance of double-lap adhesive joints between steel and glass adherends 72
5.1. Abstract……..…….…….. 72
5.2. Introduction…..……..…….…….. 74
5.3. Materials and methods……..…….…….. 77
5.3.1 Materials properties…….…..…... 77
5.3.1.1 Adherends……..…….. 77
5.3.1.2 Adhesives……..…….. 77
5.3.2 Specimens geometry……..…….…..…... 78
5.3.3 Artificial ageing……..…….…..…... 79
5.3.4 Test setup…….…….…….…..…... 80
5.4. Results and discussion……..…….…….. 81
5.4.1 Mechanical performances……..…….…..…... 81
5.4.2 Failure modes……..…….…..…... 85
5.5. Conclusions……..…….…….. 88
5.6. References……..…….…….. 89
5.7. List of figures and tables.……...……..… 92

6. Influence of high temperature exposure on the mechanical performance of double-lap adhesive joints between glass and aluminium adherends 93
6.1. Abstract……..…….…….. 93
6.2. Introduction…..……..…….…….. 95
6.3. Materials and methods……..…….…….. 97
6.3.1 Materials properties…….…..…... 97
6.3.1.1 Adherends……..…….. 97
6.3.1.2 Adhesives……..…….. 97
6.4. Experimental tests……..…….…….. 98
6.4.1 Dogbones specimens geometry……..…...99
6.4.2 Double-lap specimens geometry……...99
6.4.3 Test setup…….…….…..…... 101
6.5. Results and discussion…..……..…….…….. 102
6.5.1 Dogbones tensile tests…….……..…... 102

6.5.2 Mechanical performance of double-lap specimens……..…... 103
6.5.2.1 Shear test on dljs at laboratory conditions……..….. 103
6.5.2.2 Shear test on dljs after one heating cycle (T_{1-85})…….. 105
6.5.2.3 Shear test on dljs after ten heating cycle (T_{10-85})……..106
6.5.3 Failure modes……..…... 114
6.6. Conclusions……..……..…….…….. 118
6.7. References……..……..……..…….. 119
6.8. List of figures and tables.……...……..… 121

7. Preliminary experimental verification of glass deck applied on metal beams 122
7.1. Abstract……..…….…….. 122
7.2. Introduction…..……..…….…….. 124
7.3. Materials and methods……..…….…….. 125
7.3.1 Materials properties……..…... 125
7.3.1.1 Adherends……..…….. 125
7.3.1.2 Adhesives……..…….. 125
7.4. Experiments…….……..…….…….. 130
7.5. Results and discussion…..……..…….…….. 134
7.6. Numerical analysis…..……..…….…….. 137
7.7. Conclusions……..……..…….…….. 139
7.8. References……..……..…….…….. 140
7.9. List of figures and tables.……...……..… 142

8. Experimental assessment of the mechanical behaviour of the steel-glass adhesive joint on a 1:2 scale Tensegrity Floor prototype 143
8.1. Abstract……..…….…….. 143
8.2. Introduction…..……..…….…….. 145
8.3. Tensegrity Floor…….……..…….…….. 147
8.3.1 Prototype…….……..…... 148
8.4. Materials and methods.……..…….…….. 150
8.4.1 Materials properties……..…... 150
8.4.1.1 Adherends……..…….. 150
8.4.1.2 Adhesives……..…….. 153
8.5. Experiments…….……..…….…….. 154
8.6. Results and discussion…..……..…….…….. 157
8.6.1 Simply supported glass deck configuration – S. SUPP…...…... 158
8.6.2 Adhesively bonded glass deck - EPX1 adhesive.……..…... 163
8.6.3 Adhesively bonded glass deck – EPX2 adhesive.……..…... 169
8.6.4 Adhesively bonded glass deck - SIL adhesive.……..……..…... 174
8.7. Conclusions……..……..…….…….. 181
8.8. References.……..……..…….…….. 182
8.9. List of figures and tables.……...……..… 183

9. Conclusions and future developments **185**
9.1. Objectives reached..…….. 185
9.2. Application values and limits..…….. 186
9.3. Installation and maintenance procedures…...…….. 188
9.4. Optimisation of the construction system..…….. 190
9.4.1 FE modelling……..……...191
9.4.2 FE results……..…..……..…... 193
9.5. Future developments…..…..…….. 200
9.6. References…..…..…….. 201
9.7. List of figures and tables..……...…… 202

Appendices **203**
Appendix 1. Adhesives **203**
1.1. Adhesives…..…..…… 203
1.2. Benefits of adhesives…..…..…… 203
1.3. Classification of adhesives…..…..…… 204
1.3.1 Load carrying capacity…..……...204
1.3.1.1 Structural…..……..204
1.3.1.2 Semi-structural and non-structural...…….. 205
1.3.1.3 Pressure sensitive……..……..205
1.3.2 Cure mechanisms……..……... 205
1.3.2.1 Phisically hardening……..……..205
1.3.2.2 Chemically curing……...……..206
1.3.2.3 Pressure sensitive……..……..207
1.3.3. Forms……..……..……... 207
1.4. Epoxy adhesives……..……..…… 208
1.5. Glass transition temperature..…..…… 209
1.6. References…..…..…… 210
1.7. List of figures..…..…..…… 210

Appendix 2. Experimental data **211**
2.1. Simply supported glass deck……..…..…… 211
2.2. Glass deck adhesively bonded with EPX1 adhesive……..… 218
2.3. Glass deck adhesively bonded with EPX2 adhesive……..… 224
2.4. Glass deck adhesively bonded with SIL adhesive……..…..… 230
2.5. List of figures..…..…..…..…… 236

Annexes

Chapter 1.

Introduction

1.1. Objectives

The present work deals with the construction of light and transparent floors, characterised by a dynamic operation and able to adapt to the environment. In particular, it addresses the problem of realisation of self-supporting structural elements made of steel and glass with advanced technology, able to provide high performances and to adapt to the stresses generated by endogenous and exogenous factors. Fast assembly, low cost – due to both the reduced number and mass-producibility of the parts – and versatility are the basic characteristics of these structural elements.
The need to achieve these objectives led to the choice of a tensegrity construction technology applied to steel and glass floor elements. The reduction in the number of components and the consequent reduction in environmental emissions, as well as the optimisation of the overall performance of the structure were achieved through the study and application of adhesive bonding in the tensegrity technology.
The main objective of the present research is to verify the applicability of the adhesive joint in civil engineering, especially in building components designed for the realisation of horizontal tensegrity floors.
The patent "Tensegrity Floor", No. 00014426973 (inventor Prof. Placido Munafò) [1] consists of a modular, lightweight and transparent glass deck structurally cooperating with a tensegrity substructure which improves both its aesthetic and physical properties. In this type of structure, the main problem is the connection between the glass deck and the metal substructure through adhesive joints, which is the main design principle of the described system. The structural cooperation between the tensegrity structure and the glass panels allows to significantly reduce the deformations of the floor compared to the classic supported configuration. This aspect also allows to assemble a lightweight metal substructure.
Another objective of the research is to verify the functionality of this construction element, which is characterised by a reduced number of components (technological simplification) [2] and which can offer several advantages: easy and fast assembly, reduction of production times and processes while reducing environmental emissions.
Other aspects addressed in this work concern the possibility of assembling ductile structures thanks to the structural cooperation between glass and substrate (e.g. steel, aluminium) [3–7] achieved by the adhesive bonding; these aspects are discussed and experimentally analysed.

1.2. Work phases

In order to achieve the set objectives, the research work was carried out in the following phases:

i. experimental verification of bonded joints through extensive experimental campaigns, which allowed the evaluation of the mechanical compatibility between adherends and adhesives under different curing conditions and environmental exposure. This initial experimental phase allowed the behaviour of various commercially available structural adhesives to be evaluated in order to select the most suitable ones for the performance of the component under study;

ii. the verification of the technical-constructive feasibility of the tensegrity floor and the assembly of the 1:2 scale prototype. This research phase allowed the verification of the studied structural component in view of mass production;

iii. the verification of the mechanical performance of the prototype under service conditions through static load tests with different load distributions.

1.3. Methodology

In order to achieve the set objectives, the research was carried out in different phases:

- Research results: “Tensegrity Floor”, tensegrity floor patent. In this section, in addition to describing the tensegrity principle and the state of the art in the construction of horizontal steel and glass structures, the main features of the patent “Tensegrity Smart” are described;
- Floor prototype: “Tensegrity Smart”. The patent idea for the Tensegrity floor was developed by assembling a 1:2 scale prototype. Considerations for exploring the research of the form-finding and construction hypothesis are reported. Numerical analyses to investigate the mechanical behaviour of the adhesive joint follow;
- Experimental studies on adhesive joints between glass and metal adherends. In this section the results of extensive experimental campaigns are reported, aimed at verifying the compatibility between adherends and adhesives in different types of joints, loads and environmental conditions;
- Experimental evaluation of the adhesive joint mechanical behaviour on a “Tensegrity Floor” prototype. The results of the load tests carried out on the 1:2 scale prototype are presented;
- Expected results;
- Future developments.

1.4. References

[1] P. Munafò, Solaio Tensegrale, 00014426973, 2014.

[2] P. Munafò, Considerazioni sulle tematiche di ricerca del Settore Scientifico Disciplinare di Architettura Tecnica, in: Colloqui.AT.E, Artec, Bologna, 2015: pp. 21–24.

[3] S. De La Pierre, T. Scalici, P. Tatarko, A. Valenza, L. Goglio, D.S. Paolino, M. Ferraris, Torsional shear strength and elastic properties of adhesively bonded glass-to-steel components, Mater. Des. 192 (2020) 108739. https://doi.org/10.1016/j.matdes.2020.108739.

[4] K. V Machalická, M. Vokáč, P. Pokorný, M. Pavlíková, Effect of various artificial ageing procedures on adhesive joints for civil engineering applications, Int. J. Adhes. Adhes. 97 (2020) 102476. https://doi.org/https://doi.org/10.1016/j.ijadhadh.2019.102476.

[5] C. Wu, Y.-Z. Yu, L. Tam, J. Orr, L. He, Effect of glass fiber sheet in adhesive on the bond and galvanic corrosion behaviours of CFRP-Steel bonded system, Compos. Struct. 259 (2021) 113218. https://doi.org/10.1016/j.compstruct.2020.113218.

[6] I. Katsivalis, O. Thybo, S. Feih, M. Achintha, International Journal of Adhesion and Adhesives Development of cohesive zone models for the prediction of damage and failure of glass / steel adhesive joints, Int. J. Adhes. Adhes. (2019) 102479. https://doi.org/10.1016/j.ijadhadh.2019.102479.

[7] M. Overend, Q. Jin, J. Watson, The selection and performance of adhesives for a steelglass connection, Int. J. Adhes. Adhes. 31 (2011) 587–597. https://doi.org/10.1016/j.ijadhadh.2011.06.001.

Chapter 2.

"Tensegrity Smart", a tensegrity floor patent

2.1 Tensegrity principle: definitions and historical background

The definition of "*tensegrity*" is still debated today, as in Ref. [1]. On the one hand, there is the mathematical definition, according to which a tensegrity structure consists of cables (elements stressed only in tension), and "struts", stressed only in compression. On the other hand, there is the widespread idea that a tensegrity structure is such if it has its compressed elements not in contact with each other, as reported by Connelley and Withley [2].
The term "*tensegrity*" was coined by Richard Buckminister Fuller[1] and represents the crasis of the words "*tensional*" and "*integrity*", as reported by Fuller himself in his work "*Synergetics: Explorations in the geometry of thinking*" [3]. In this sense, the term "*tensegrity*" implies the integrity of a structure, achieved by continuous elements (cables) under tensile stress and discontinuous compressed elements (struts). Thus, it is possible to distinguish between continuous and flexible elements and discrete and stiff elements [4], depending on a structural configuration that optimises the use of materials intrinsically.
Another qualitative definition is given by Fuller himself [5]: "*islands of compression in an ocean of tension*". This expression encompasses different types of structural configurations; tires are an example: the compressed air is enclosed in a continuous stretched membrane.
The most recent definition comes from Motro [6]: "*a tensegrity system is defined as a system in a state of stable self-equilibrium comprising a discontinuous series of compressed components within a continuum of stretched components*". Self-equilibrium means the existence of a stable equilibrium configuration of the structure, achieved by pre-stressing before it is subjected to both exogenous (external loads) and endogenous (self-weight) actions.
The concept of "*tensegrity*" dates back to 1948, after Kenneth Snelson – then a student of Fuller – proposed a first spatial geometric configuration based on the concept of "*floating compression*" [7] (Fig. 2.1).

[1] Richard Buckminister Fuller (1895-1983) was an American inventor, architect, designer, philosopher, writer and television host. He was also a professor at Southern Illinois University.

Figure 2.1. Snelson's "X" column.

The "X" column sculpture consists of a reduced number of compressed elements (struts) surrounded by continuous tensioned cables. This work expresses the idea of "*continuous tension and discontinuous compression*" and – as Snelson himself stated – represents a first tensegrity plane module consisting of two struts and four continuous wires, with the compressed elements not in contact with each other.
In his work as a sculptor, Snelson later assembled structures with "*floating*" compressed elements that further developed the "X" module. One example is the Needle Tower in Washington, DC (Fig. 2.2), a structure characterised by the superimposition of modular tensegrity substructures.

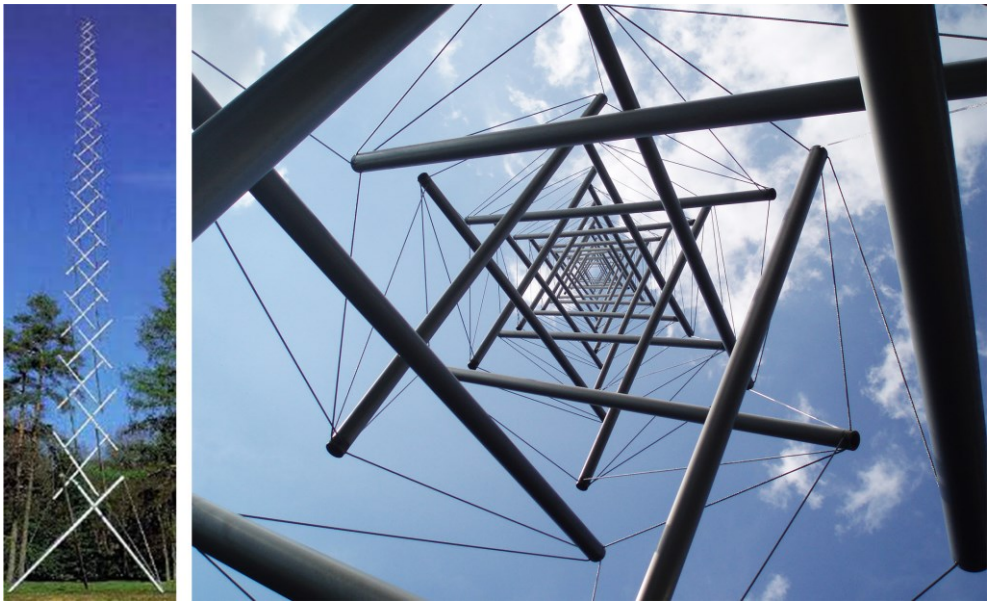

Figure 2.2. Needle Tower, global and detail view.

The Hungarian David Georges Emmerich studied – independently of Snelson and Fuller – on some three-dimensional structures defined as "*tensile and self-tensioning*", inspired by Ioganson's prototensegral models known as "*Gleichgewichtkonstruktion*", exhibited in Moscow in 1921 (Figs. 2.3-2.4).

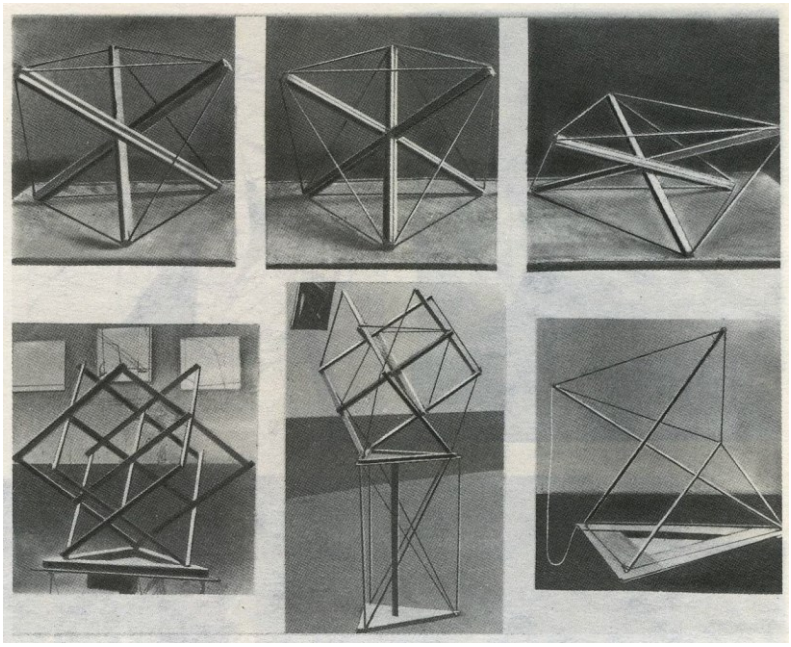

Figure 2.3. Iogansen, Spatial Constructions, 1921.

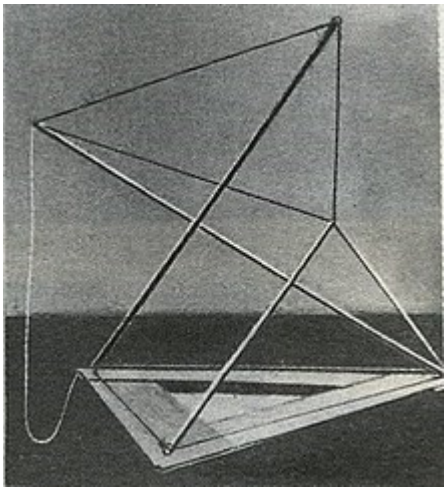

Figure 2.4. Ioganson, prototensegrity structure.

The Ioganson's structure, the "*prototensegral structure*", also known as "*Elemental Equilibrium*", consists of four struts and seven cables. The function of the eighth unstressed cable is to change the geometric configuration of the structural system.
Emmerich's work focused on the study of tension prisms and assembled tensegrity systems (Fig. 2.5). These studies formed the basis for the subsequent industrial patents described below.

Figure 2.5. Emmerich in front of his tensegrity structure, Warsaw, 1981.

2.2 Patents and developments

The first patent applications date from the early 1960s and were signed by Fuller and D. G. Emmerich, in the USA and France respectively. However, the first publications on tensegrity inventions were those by Fuller in 1962.
The patents of Fuller and Emmerich [8–11] were filed between 1959 and 1964. In particular, Snelson's patent application [8] is from 1965. Emmerich's first patent concerns a first system called "*Pearl Frameworks*" at INPI (National Institute of Industrial Property) [8–13]. His second patent (1964) is entitled "*Construction de reseaux autotendant*" - No. 1377290 (Fig. 2.6).

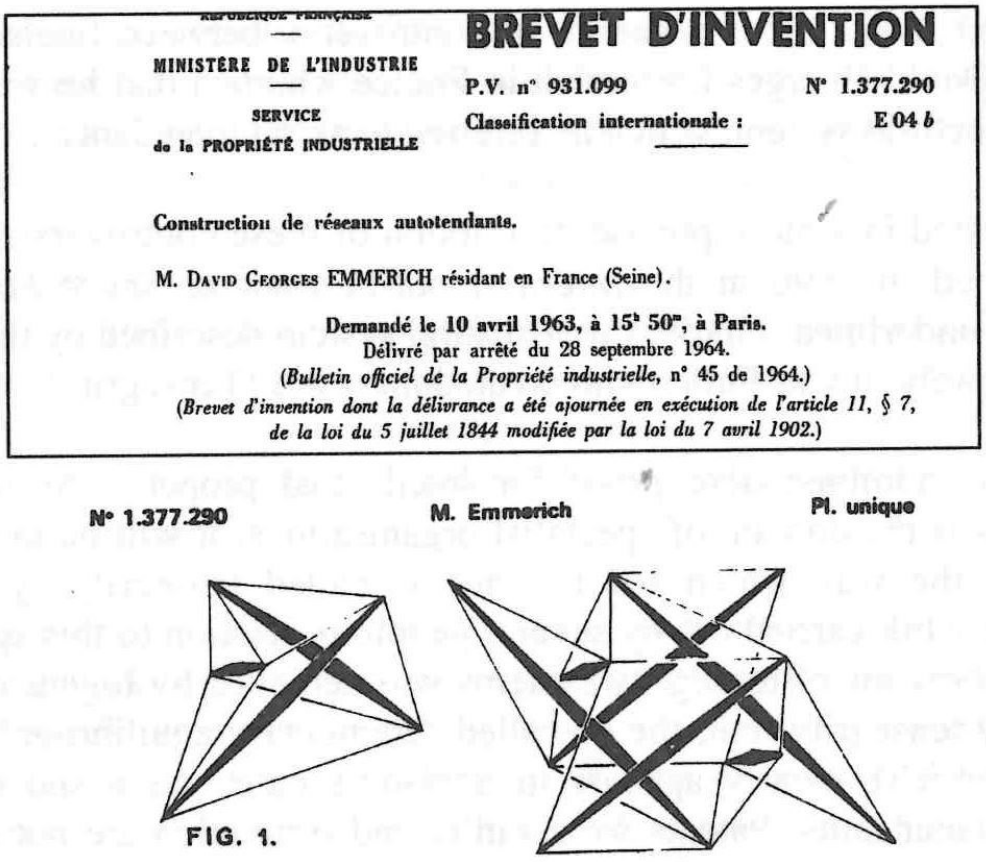

RÉPUBLIQUE FRANÇAISE

MINISTÈRE DE L'INDUSTRIE

SERVICE
de la PROPRIÉTÉ INDUSTRIELLE

BREVET D'INVENTION

P.V. n° 931.099 — N° 1.377.290

Classification internationale : — E 04 *b*

Construction de réseaux autotendants.

M. DAVID GEORGES EMMERICH résidant en France (Seine).

Demandé le 10 avril 1963, à 15h 50m, à Paris.
Délivré par arrêté du 28 septembre 1964.
(*Bulletin officiel de la Propriété industrielle*, n° 45 de 1964.)
(*Brevet d'invention dont la délivrance a été ajournée en exécution de l'article 11, § 7, de la loi du 5 juillet 1844 modifiée par la loi du 7 avril 1902.*)

N° 1.377.290 — M. Emmerich — Pl. unique

FIG. 1.

Figure 2.6. Emmerich's Patent.

Fig. 2.7 shows the patent by Fuller (1962).

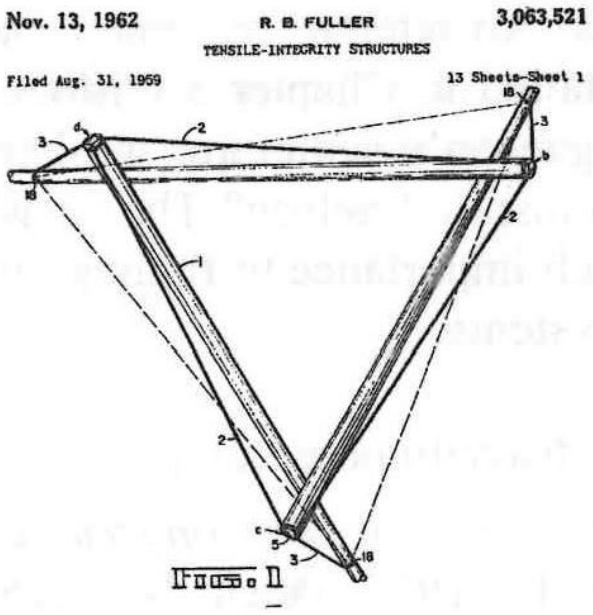

Figure 2.7. Fuller's Patent.

Snelson's patent "*Continuous tension, discontinuous compression structures*" is dated February 1965 (No. 3169611) and is shown in Fig. 2.8.

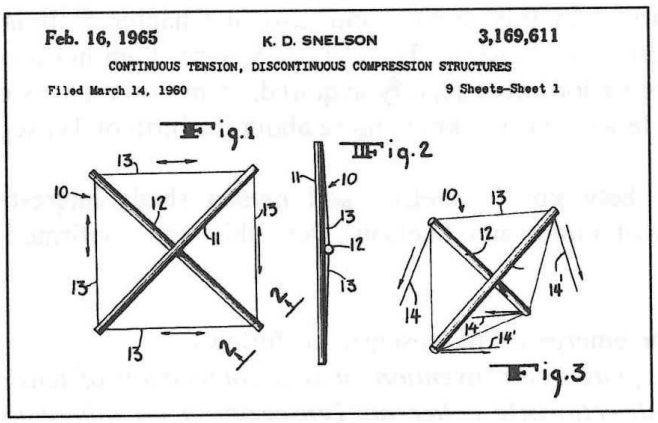

Figure 2.8. Snelson's Patent.

With this invention, Snelson explored the basic principles of tensegrity theory and deepened its artistic aspect. Fuller and Emmerich – on the other hand – elaborated applications using geometric and mathematical models, even if their studies were limited to this theoretical modelling.
To them, however, belongs the great credit of having made the first classification of the principal families and types of tensegrity structures:

- tensegral towers and domes;
- tensegral icosahedron with six isolated rods;
- tensegral tetrahedron with six isolated rods.

Studies on tensegrity systems subsequently followed different developments: Snelson continued to study the tensegrity principle in his work as a sculptor and applied it to his artistic and compositional work, assembling complex forms characterised by various assembly techniques and the use of different materials.
After filing a patent in 1962, Fuller deepened his study of tensegrity domes with large dimensions. However, the domes lacked the necessary stiffness to be used in the architectural field, so in 1967 he resorted to a geodesic structure for the American pavilion at Montreal[2] Expo (Fig. 2.9).

[2] The 1967 Montreal Expo took place from 28 April to 27 October 1967. The event, whose theme was 'Terre des Hommes', was attended by 62 countries. Among the pavilions, the most famous was that of the USA, designed by Fuller. The famous geodesic dome will be known as the Biosphere.

Figure 2.9. American pavillon at Montreal Expo, 1967.

Fuller continued his research, which led to numerous studies and texts on the tensegrity construction system [3,14].

Tensegrity technology always attracted great interest from artists, especially in the field of sculpture. The studies on the different geometrical configurations of tensegrity structures have been carried out for several decades; the works of Emmerich [15] and Fuller [3], have been joined by the more recent ones of Pugh [16]. The polyhedron represents the basic geometry from which these studies have been developed.

The first approaches to the study of the mechanical behaviour of tensegrity structures can be found in the work of Calladine [17], Pellegrino [18], Roth and Whiteley [19].

The study carried out by Calladine [17] illustrates the possibility of using linear algebraic operations to determine the number of "incipient" modes of frame stiffness as a function of the number of components (struts and cables) and independent self-stress states. Pellegrino et al. [18] developed an algorithm capable of determining the details of the self-stress states and inextensive deformation modes that a structural assembly may exhibit. Further experimental insights are provided by the work of Motro [20,21] and more recently by Hagiwara et al. [22], Bossens et al. [23], Kuhl et al. [24].

In particular, the studies of Motro investigated the relationship between shapes and forces in building systems. This relationship is studied in terms of "self-confined" spatial grid systems as equilibrium figures. The results are represented by non-linear dynamic mathematical models and qualitative models based on both graph theory and on the form-finding using dynamic relaxation theory.

2.3 Main projects

The following is a summary of the projects that are closest to the research area being addressed and that were most useful in the cognitive phase of research development.

2.3.1 Archaeological Museum of R. Calabria, ABDR Studio, 2007

The renovation of the Archaeological Museum in Reggio Calabria – which houses the famous Riace Bronzes – led to the roofing of the central courtyard, made with a light metal structure in tensegrity technology. The upper deck of semi-transparent glass panels allows the courtyard to be used as an entrance hall and exhibition space for large exhibits (Fig. 2.10).

Figure 2.10. Roof of the Archeological Museum of R. Calabria.

The roof consists of welded metal support structures with a trapezoidal cross-section, equipped with a tensioning system of steel bars and special devices for anchoring the perimeter structures in reinforced concrete. The glass floor consists of large, double-glazed panels, 42 mm thick, supported by a steel grid of T-section, formed by the combination of two hollow rectangles of 150×15 mm^2, supported by a lightweight and dynamic metal structure. However, the resulting structural configuration leads to a combination of a tensegrity substructure and a metal grid that provides stiffness to the roof (Fig. 2.11).

Figure 2.11. Tensegrity floor, detail.

The new roof of the archaeological museum in Reggio Calabria is the only example in Italy of a steel-glass floor made with tensegrity technology and, in general, a non-permanent application of this technology in the civil engineering field.

2.3.2 De La Plata Stadium, Buenos Aires, 2003

The De La Plata Stadium in Buenos Aires (Fig. 2.12) is one of the largest examples of a tensegrity roof structure to date. The geometrically complex roof has a free span of 219 m in the longitudinal direction and 171 m in the transverse direction. It consists of a circumferential steel beam that support the gravity and horizontal loads transmitted by the dome.

Figure 2.12. Stadium De La Plata, Buenos Aires, interior, and detail.

The use of tensegrity technology improves the load-bearing capacity and allows the assembly of an unconventional geometry. The final layer of the roof consists of Teflon-coated fibreglass fabric panels attached to the cables. The considerable overall stiffness achieved by the tensegrity substructure allows for versatile roof configurations (i.e., partial or full), as required.

2.3.3 Olympiastadion, Munich, Otto Frei, 1972

A significant example of membrane systems supported by a substructure of cables is the construction of the Olympic Stadium in Munich (Fig. 2.13), built in 1972 to a design by Otto Frei, who was associated with Fuller's experiments.

Figure 2.13. Olympiastadion, Munich, 1972.

The architectural concept is the cable network, inspired by the spider's web, and the way in which weight is transmitted in and around the web. Technically, the structure consists of a web of pre-tensioned cables suspended between steel pylons and grid bridges. During construction, the cables were first mounted at the base of the pylons, and then raised to the required height. The resulting net supports acrylic glass panels that are connected to each other and anchored to the substructure with supports.

2.3.4 Cloister of Neunmunster, RFR, Luxembourg, 2001-03

The project presented concerns the roofing of the cloister of the Neunmunster Abbey, carried out simultaneously with the transformation of the monastery into a multicultural centre. The structural solution chosen is that of a hybrid and reticular envelope, characterised by a combination of a lightweight metal substructure of tubular section arches and movable point supports (rotules) supported by a double chain of tensioned cables, as in the case of Reggio Calabria, for the covering of tempered glass panels (Fig. 2.14).

Figure 2.14. Neunmunster Abbey: the courtyard and detail.

To ensure the correct membrane behaviour of the shell structure, the network of pre-stressed cables transmits the loads between the arches and gives continuity to the in-plane stresses.
The contribution of the pre-stressed cables is fundamental, as they can replace the bars, that would be otherwise necessary but would weigh down the resulting system. The rotules used to support the glass guarantee the isostatic of the glazed part with respect to the differential displacements of the metal substructure.

2.3.5 Inner courtyard of the Maximilian Museum, L. Augsburg, 1999

The roof of the inner courtyard of Maximilian Museum consists of a barrel vault with a plan dimension of 37×14 m^2. It is a highly transparent construction system in which the opaque steel parts are reduced to a minimum. The panels – 527 in total – are made of 12+12 mm thick tempered glass laminated with a layer of PVB in between. To ensure the stability of the structure, membranes made of cables are arranged to enable the membrane behaviour of the roof. Compressive stresses are transferred to the underlying structure via nodes. Each glazed panel is supported on the node plate by means of stainless-steel dowels in the corners. A pin set screws in the middle of the node is used to position the plate and make a connection with steel caps (Fig. 2.15).

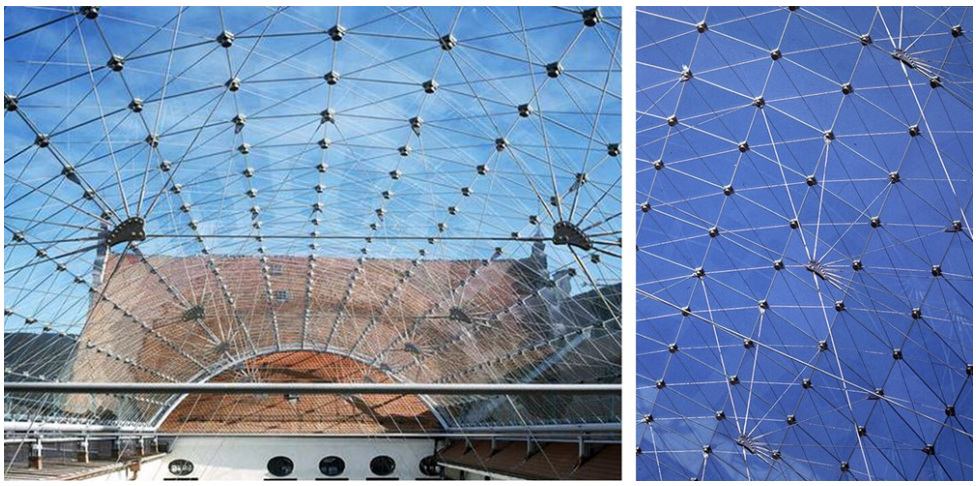

Figure 2.15. Maximilian Museum, courtyard and detail.

These construction results allow to understand the construction possibilities of glass, which can also be considered as a material with high structural capacities as well as a load-bearing element. The use of tempered and laminated glass plates and the study of special joints with the substructure (i.e., structural adhesives) allow the creation of a ductile structure with high load-bearing capacity, obtained by joining materials (i.e., steel and glass) with different mechanical properties.

2.4 Patent No. 00014426973

2.4.1 Description of the structural element

The patent “Tensegrity Floor” by Prof. Placido Munafò (Patent No. 00014426973) [25] illustrates the application of the tensegrity concept for the construction of a new type of floor, where the glass deck (Fig. 2.16) cooperates with the underlying metal structure (Fig. 2.17) with reduced dimensions, and where the modular elements can be repeated planimetrically (Fig. 2.18-2.19). The innovatione consists in the use of structural adhesives in the joints between the deck and the metal substructure. The result is a spatial building element characterised by a high load-bearing capacity, small resistant cross-sections, a reduced number of components and versatility. It can be used in various construction fields, both for new and existing buildings.

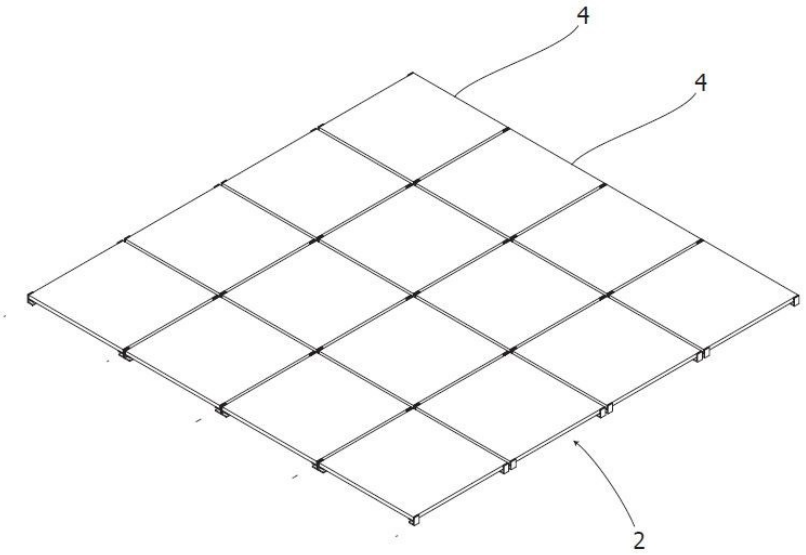

Figure 2.16. Glass deck.

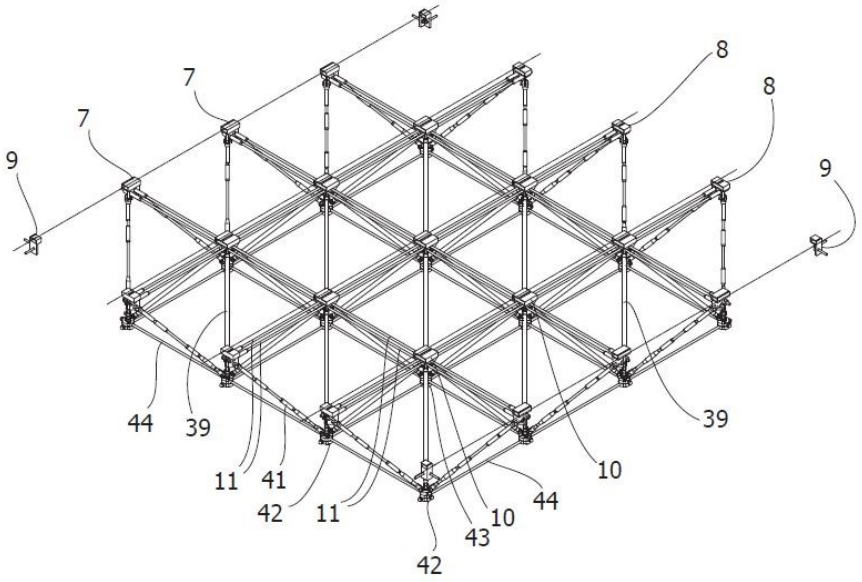

Figure 2.17. Lightweight metallic substructrure.

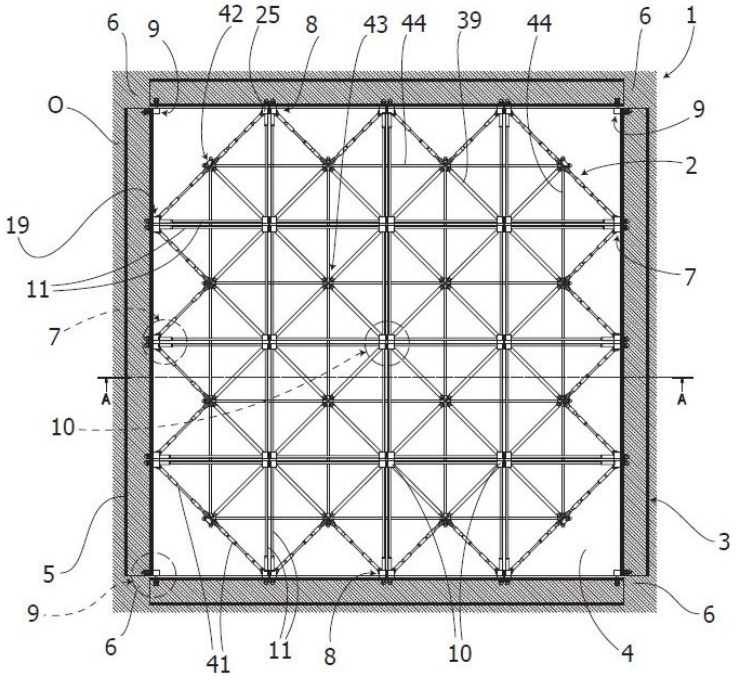

Figure 2.18. Plan view.

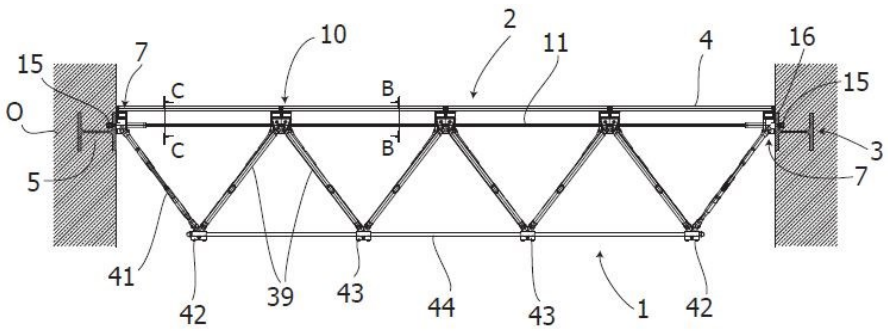

Figure 2.19. Cross-section view.

2.5 Product information

The "Tensegrity Floor" consists of:

- deck made of tempered laminated safety glass;
- a double row of metal nodes placed at the corners of the modular pyramid elements;
- a double order of pre-stressed cables, perpendicular to each other, forming two parallel grids, at the intersections of which the structural metal nodes are located;
- metal struts, connecting the upper and lower levels of the nodes;
- adhesive joints between the glass panel and the metal substructure using commercial structural adhesives.

2.6 References

[1] R. Motro, Tensegrity, Elsevier, 2003. https://doi.org/10.1016/B978-1-903996-37-9.X5028-8.

[2] R. Connelly, W. Whiteley, Second-Order Rigidity and Prestress Stability for Tensegrity Frameworks, SIAM J. Discret. Math. 9 (1996) 453–491. https://doi.org/10.1137/S0895480192229236.

[3] R.B. Fuller, Synergetics: Explorations in the geometry of thinking, Estate of R. Buckminster Fuller, 1982.

[4] J.Y. Zhang, M. Ohsaki, Tensegrity Structures, Springer Japan, Tokyo, 2015. https://doi.org/10.1007/978-4-431-54813-3.

[5] G.G. Estrada, H. Bungartz, C. Mohrdieck, On cylindrical tensegrity structures Form-finding, Sci. York. (2005) 4–7.

[6] R. Motro, B. Maurin, C. Silvestri, Tensegrity rings and the hollow rope, in: IASS Symposium 2006 (Ed.), New Olympics, New Shells and Spatial Structures, Beijing,

China, 2006: pp. 470–471.
[7] W. Bin Bing, Free-standing Tension Structures, CRC Press, 2004. https://doi.org/10.1201/9781482288308.
[8] K.D. Snelson, Continuous Tension, Discontinuous Compression Structures, (1965) United States Patent.
[9] D.G. Emmerich, I. Riseauxp, Conf. on Space Structures, (1966).
[10] D.G. Emmerich, Cours de géométrie constructive: morphologie, Unité pégagogique d'architecture no 6, 1981. https://books.google.it/books?id=5fuHmwEACAAJ.
[11] F.A. Graybill, Introduction to Matrices with Applications in Statistics, Wadsworth Publishing Company, 1969. https://books.google.it/books?id=X9E-AAAAIAAJ.
[12] D.G. Emmerich, Exercices de géométrie constructive: Travaux d'etudiants. École Nationale Supérieure des Beaux-Arts. Paris. Architecture, 1970. https://books.google.it/books?id=t3wGOwAACAAJ.
[13] K. Linkwitz, H.-J. Schek, Einige Bemerkungen zur Berechnung von vorgespannten Seilnetzkonstruktionen, Ingenieur-Archiv. 40 (1971) 145–158. https://doi.org/10.1007/BF00532146.
[14] R.B. Fuller, E.J. Applewhite, Synergetics : explorations in the geometry of thinking, Macmillan, New York, 1975.
[15] D.G. Emmerich, D.G. Emmerich, D.G. Emmerich, H. Architect, D.G. Emmerich, H. Architecte, Structures tendues et autotendantes, Ecole d'Architecture La Villette, 1988.
[16] A. Pugh, An Introduction to Tensegrity, University of California Press, 1976. https://books.google.it/books?id=McEOfJu3NQAC.
[17] C.R. Calladine, Buckminster Fuller's "Tensegrity" structures and Clerk Maxwell's rules for the construction of stiff frames, Int. J. Solids Struct. 14 (1978) 161–172. https://doi.org/10.1016/0020-7683(78)90052-5.
[18] S. Pellegrino, C.R. Calladine, Matrix analysis of statically and kinematically indeterminate frameworks, Int. J. Solids Struct. 22 (1986) 409–428. https://doi.org/10.1016/0020-7683(86)90014-4.
[19] W. Whiteley, Tensegrity Frameworks, 265 (1981) 419–446.
[20] R. Motro, Formes et forces dans les systèmes constructifs, cas des systèmes réticulés spatiaux autocontraints, Université Montpellier II, 1983.
[21] R. Motro, E.. Brochiero, P.. Jouanna, Etude quantitative de systemes autotendants, in: IASS (Ed.), World Congr. Non Typ. Struct., Mar del Plata, Argentine, 1982.
[22] Y. Hagiwara, M. Oda, Transformation experiment of a tensegrity structure using wires as actuators, in: 2010 IEEE Int. Conf. Mechatronics Autom., IEEE, 2010: pp. 985–990. https://doi.org/10.1109/ICMA.2010.5589344.
[23] F. Bossens, R. a De Callafon, R.E. Skelton, D. Systems, C. Group, S. Diego, L. Jolla, Modal Analysis of a Tensegrity Structure – an experimental study, (2005) 1–20.
[24] D. Kuhl, Y.C. Lim, D.S. Long, Tensegrity structures - Computational and experimental tensegrity mechanics, in: 2017: p. 410005. https://doi.org/10.1063/1.4992585.
[25] P. Munafò, Solaio Tensegrale, 00014426973, 2014.

2.7 List of figures

Figure 2.1. Snelson's "X" column. 5
Figure 2.2. Needle Tower, global and detail view. 6
Figure 2.3. Iogansen, Spatial Constructions, 1921. 7
Figure 2.4. Ioganson, prototensegrity structure. 7
Figure 2.5. Emmerich in front of his tensegrity structure, Warsaw, 1981. 8
Figure 2.6. Emmerich's Patent. 9
Figure 2.7. Fuller's Patent. 10
Figure 2.8. Snelson's Patent. 11
Figure 2.9. American pavillon at Montreal Expo, 1967. 12
Figure 2.10. Roof of the Archeological Museum of R. Calabria. 13
Figure 2.11. Tensegrity floor, detail. 14
Figure 2.12. Stadium De La Plata, Buenos Aires, interior, and detail. 15
Figure 2.13. Olympiastadion, Munich, 1972. 16
Figure 2.14. Neunmunster Abbey: the courtyard and detail. 17
Figure 2.15. Maximilian Museum, courtyard and detail. 18
Figure 2.16. Glass deck. 19
Figure 2.17. Lightweight metallic substructrure. 20
Figure 2.18. Plan view. 21
Figure 2.19. Cross-section view. 21

Chapter 3.

“Tensegrity Floor” prototype

3.1 Introduction

This section illustrates the construction hypothesis and the subsequent assembly of a scale prototype of a tensegrity floor, based on the idea presented in the patent “Tensegrity Floor” by P. Munafò (Patent No. 000144269 73) [1].
The definition of the 1:2 scale prototype is the result of an in-depth study of the state of the art regarding existing tensegrity floor constructions [2–5] and the applications of adhesive technology in construction [6–9]. The assembly of the prototype is an effective research method to evaluate the various advantages and disadvantages of considered construction system. The model also allows to identify critical points from a technical-constructive point of view, thus optimising the resulting system both structurally and economically.
The technological verification during the assembly phase and the subsequent results of the experimental campaigns to study the mechanical performance of the prototype allow the project to be further detailed both from the point of view of functionality and technical feasibility).

3.1.1 Methodology

The development of the prototype is the result of several phases of investigation of the tensegrity and adhesive technologies described in the patent “Tensegrity Floor” [1]. A first phase – described in detail in the following sections – concerned the verification of the mechanical compatibility of the adhesive joint between different adherends (i.e., aluminium, steel, glass) and allowed the selection of the most suitable structural adhesives based on their mechanical performance also in terms of the durability, through shear tests carried out in different environmental conditions.
The second phase – here described – included the analytical verification of the resulting structure and the FE modelling of the adhesive joints applied to the studied prototype. The assembly of the prototype was aimed at verifying its technical-constructive feasibility with a view to industrial production.
Once the geometric configuration of the construction module had been determined on a real scale, it was possible to determine the constructive measures as well as the geometric and physical-mechanical properties of the structural elements used.

3.2 Identification of the basic module

Tensegrity structures differ from conventional grid structures by the presence of elements without bending stiffness (cables), which can only support tensile loads. This aspect inevitably leads to the identification of a structural module determined by the distribution of the different structural elements (tensed or compressed). Moreover, the modularity of the system allows the standardisation of the construction process, by assembling and repeating the whole based on elementary units to assemble the intended geometry.
The proposed basic module allows each planar surface to be subdivided into *n* glass sub-surfaces, which form the basis of the module itself (Fig. 3.1).

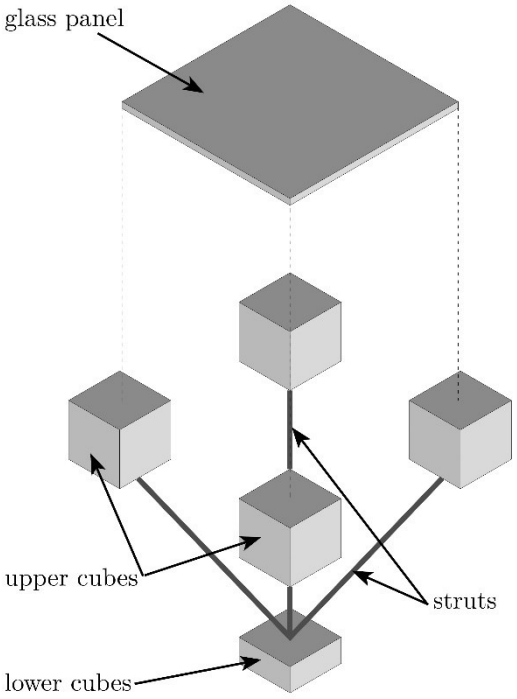

Figure 3.1. Construction module.

The proposed module has a pyramidal shape; the internal elements (struts and cables) were constrained using hinges to avoid the transmission of bending moments. The proposed configuration, characterised by the serial repetition of pyramidal modules, can be classified in the category of "class 4" tensegrity structure, since 4 struts converge in a single vertex – as in Ref. [4] – whose elements are spatially distributed according to a "double layer" grid, i.e., with a double order of perpendicular cables.

3.3 Construction hypothesis

The construction hypothesis investigated and developed in the following analyses is that of a double grid of tensioned cables with compressed elements (struts) connecting the structural nodes, distributed on two levels. The order of the upper nodes (cubes) supports the glass deck and structurally cooperates with the substructure through adhesive joints (Fig. 3.2).

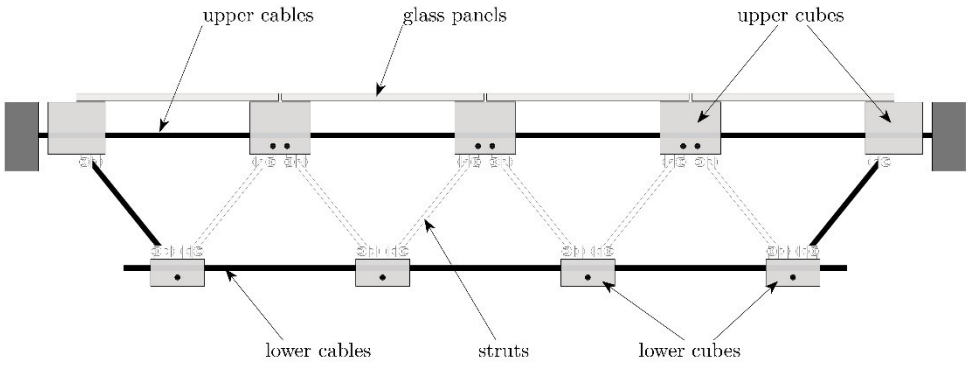

Figure 3.2. Section view.

The validation of the proposed structural configuration using 3D structural modelling is the initial phase for the definition of the scaled prototype. The results of the preliminary analysis allow to evaluate the stresses in the structural elements and to optimise the choice of cross-sections and materials used.

3.4 Form-finding

The form-finding question is fundamental to the definition of a tensegrity structure.
The study carried out by Calladine [10] illustrates the possibility of using linear algebra to determine the number of "incipient" stiffness modes of the frame in terms of the number of components and independent self-stress states. Pellegrino et al. [11] developed an algorithm able to provide the details of the self-stress states and inextensive deformation modes that a structural assembly may possess. However, to date, there is no unique method to determine a closed-form solution to the problem. Indeed, a tensegrity structure can be in equilibrium - without external action - in a state of internal prestress (cable prestress). From a structural point of view, tensegrity structures can be identified as statically indeterminate spatial grid structures.
Many of the basic properties of a tensegrity system are identical to those of a simple system in two dimensions. Tensegrity systems belong to the most general class of first-order infinitesimal mechanisms [12]. Fig. 3.3 shows the internal actions and displacements of the first-order mechanism (when the deflection D is approximated to zero) compared to those of "normal" geometry (i.e., when D is not very small).

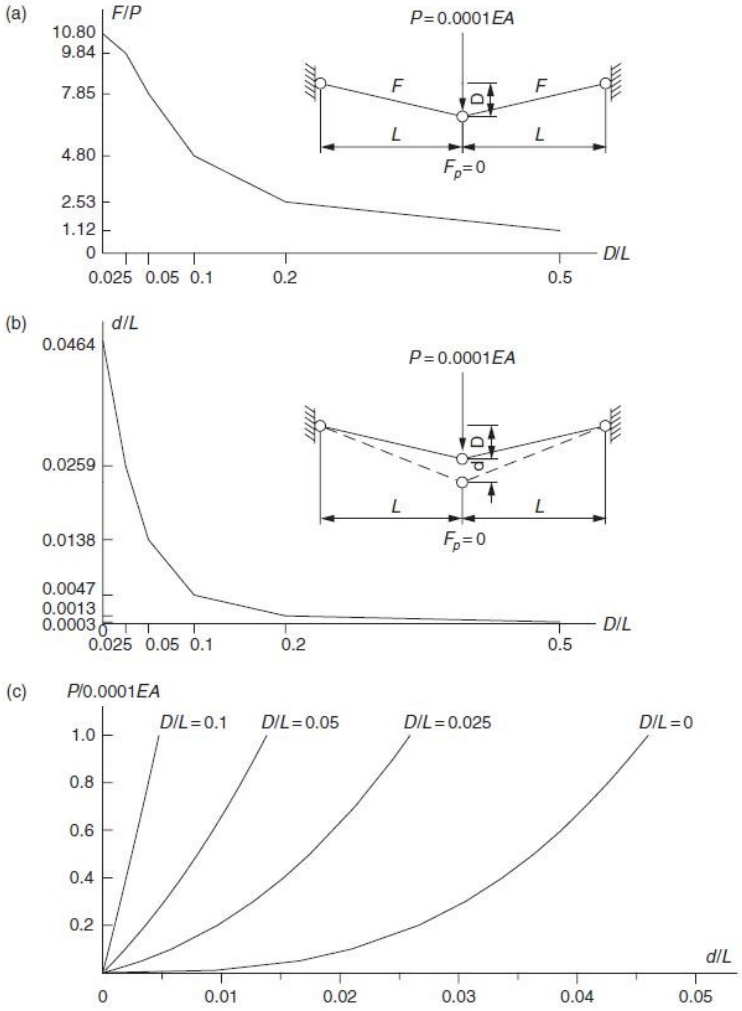

Figure 3.3. Mechanical properties of two-cable model with different sags: (a) internal force; (b) deflection; (c) load-displacement curve.

The first-order mechanism is also characteristic of large internal forces and particularly large displacements relative to the "normal" geometry, indicating insufficient use of the strength of the material. The case of first-order mechanism often occurs in cable networks, whose lightness is mainly due to the high strength of the cables and the anchoring system at the boundary [12].

Tensegrity systems therefore require a form-finding process to reach a state of self-tensioning equilibrium, which can be achieved by prestressing the cables. In such a case, the finite

mechanisms are eliminated; however, infinitesimal mechanisms such as those described above persist, which can be stabilised by pre-tensioning the tensegrity elements.
In some simple cases, the "form" can be determined by seeking the maximum length of the compressed elements compatible with that of the stretched elements; this method is called "kinematic". It is also possible to combine a geometric condition with an equilibrium condition for certain tensegrity systems such as elementary equilibrium.
Two main methods for determining "form" can be distinguished: one method is governed by form; the other by force, as presented by Motrò [4].
The first method is derived from artistic applications (e.g., sculptures) of tensegrity technology. In this method, tensegrity systems are developed lack both the regularity of their structural elements and any claim to a specific mechanical performance. The result (i.e., the "form") is obtained by an experimental method of trial and error.
The second method searches for form through theoretical modelling and has been developed to assemble resulting structures that are characterised by specific mechanical performances. Theoretical modelling, like kinematic modelling, must take into account both the geometric configuration and the stress state of the components. The result is characterised by a regularity in the distribution of the elements, which, however, involves onerous computational analyses [4].
Other methods of shape calculation are represented by the following:

- non-linear programming;
- dynamic relaxation;
- static methods – analytical solution;
- force density method (Vassart [13]);
- energy method;
- reduced coordinates method (Sultan [14]).

3.4.1 3D modelling with SAP2000

This section presents the numerical analysis carried out to analyse the mechanical behaviour of the prototype tensegrity floor at scale. The analyses performed are static non-linear and were carried out using the commercial software SAP2000© (Fig. 3.4).

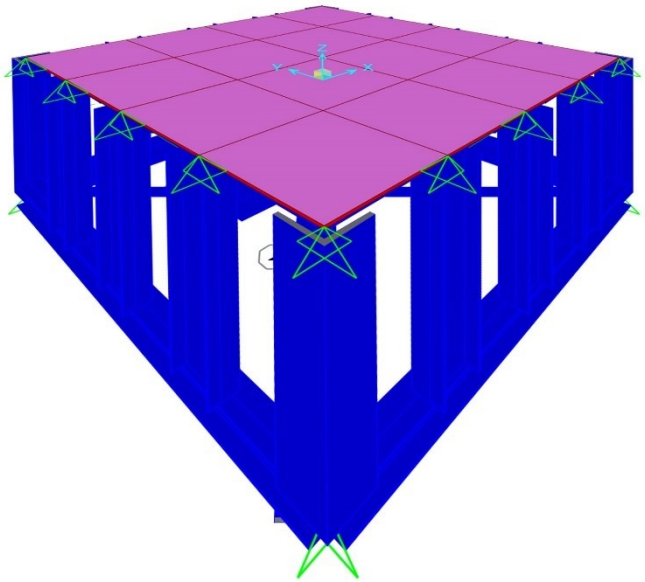

Figure 3.4. 3D SAP model of "Tensegrity Floor".

The adopted model consists of the planimetric repetition of 16 modules, with a total size of 1.20 × 1.20 m^2. The cables were modelled in such a way that the length between the supports remains unchanged, regardless of the applied load, while the support is free to translate according to the applied load. The results were evaluated according to the envelope combination of different load cases (i.e., uniformly distributed, symmetrically distributed on the central span, asymmetrically distributed on the lateral span). The value of distributed load used for the analyses corresponds to the pedestrian live load of 4.00 kN/m^2, as specified by the Italian building code (NTC2018 [15]). The results obtained using the "*combinazione fondamentale*" at SLU have allowed, in this first phase of analysis, to validate the proposed form and to determine the stresses in the structural elements and, consequently, the value of the pretension (6 Nm) to be applied to the cables in order to keep the deformations within the limits imposed by the standards.

3.5 Materials

The materials used for the construction of the scale prototype are: S355JR steel and tempered glass panels laminated with PVB film, according to CNR-DT 210/2013 [16]. The mechanical properties of the materials are summarised in Table 3.1. For the threaded rods, diameters M8, CL 8.8 according to NTC 2018 [15].

Table 3.1. Mechanical characteristics of steel and glass, as reported by manufacturers.

GLASS*			**STEEL (S355JR) ****			
α ($°C^{-1}$)	E_t (GPa)	σ_t (MPa)	α ($°C^{-1}$)	E_t (GPa)	σ_{yk} (MPa)	σ_t (MPa)
9×10^{-6}	70	120	2.30×10^{-5}	210	355	510

*according to CNR-DT 210/2013 standard, tempered glass [16]
**according to EN 10025-2:2004 standard [17]

In the study of the adhesive joint applied to the Tensegrity Floor, two commercially available structural epoxy adhesives and one silicone adhesive were selected, namely: 3M™ Scotch-Weld™ 7260 B/A (**EPX1**), 3M™ Scotch-Weld™ 7240 B/A (**EPX2**), Dow Corning™ 895 Structural Glazing Sealant (**SIL**). The choice of these adhesives is due to their different elastic modulus values. A thickness of 1.10 mm was used for all adhesives.
Table 3.2 shows the mechanical properties provided by the manufacturer in the data sheets.

Table 3.2. Mechanical characteristics of the adhesives reported by manufacturers.

Adhesive	**EPX 1**	**EPX 2**	**SIL**
Chemical base	Two-part epoxy	Two-part epoxy	One- parti silicone
Viscosity	Thixotropic	Thixotropic	Pasty
W_t (min)	90÷300	16	15
A_t (°C)	15÷25	15÷25	15÷30
T_g (°C)	61.07	66.87	-
S_t (°C)	-50÷120	-40÷80	-50÷150
τ*(MPa)	33.50	29.40*	-
E_t (MPa)	3000	1500	1
ε_t **(%)	3	-	600
Use	Structural	Semi-Structural	Structural

* On aluminium-steel adherends
**At failure.

3.6 Prototype

The patent idea “Tensegrity Floor” [1] was developed with the construction of the prototype in 1:2 scale, as shown in Fig. 3.5(a-b).

(a)

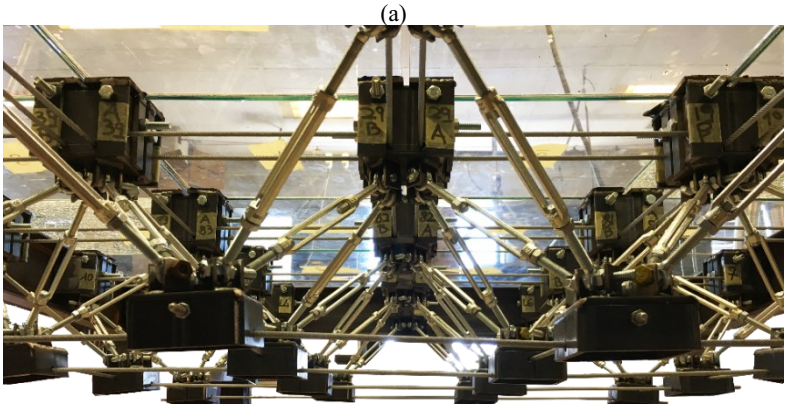

(b)

Figure 3.5. Prototype "Tensegrity Floor": (a) overall view, (b) detail.

The prototype was built by assembling 16 modules, according to the geometrical characteristics presented for the numerical model. The construction of the prototype highlighted the problems associated with the installation of the cables, which lack bending stiffness and are therefore difficult to install, especially for large spans. This aspect led to the replacement of the cables with threaded rods; in fact, the stiffness of the rods facilitates both the installation of the tensioned elements and the arrangement of the upper nodes. Another problem in the assembling of the proposed form is the simultaneous application of tension to

the tensioned elements. To stiffen the two levels and to limit the differential displacements of the nodes caused by the manual application of the prestressing, steel connecting profiles (UPN50) were introduces between the lower structural nodes.

3.7 Numerical analysis of the adhesive joint

3.7.1 FE modelling

This section presents the FE simulations to determine the stress distribution in the bonded joint. In particular, two different configurations were investigated for the central node (most heavily loaded) and the edge node, respectively (Fig. 3.6(a-b)). All numerical simulations were performed using the commercial software ANSYS 19.

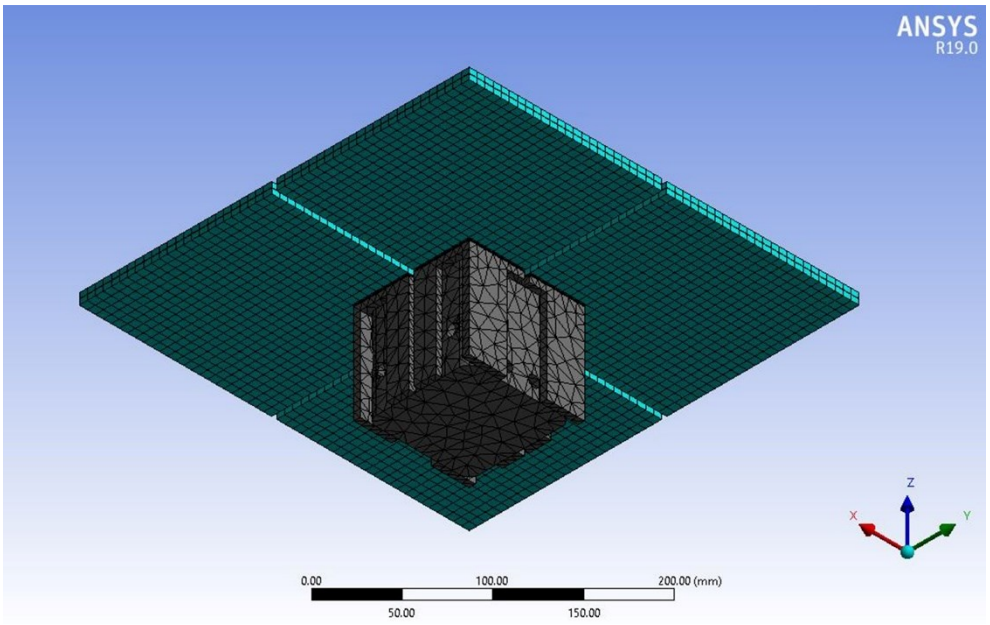

(a)

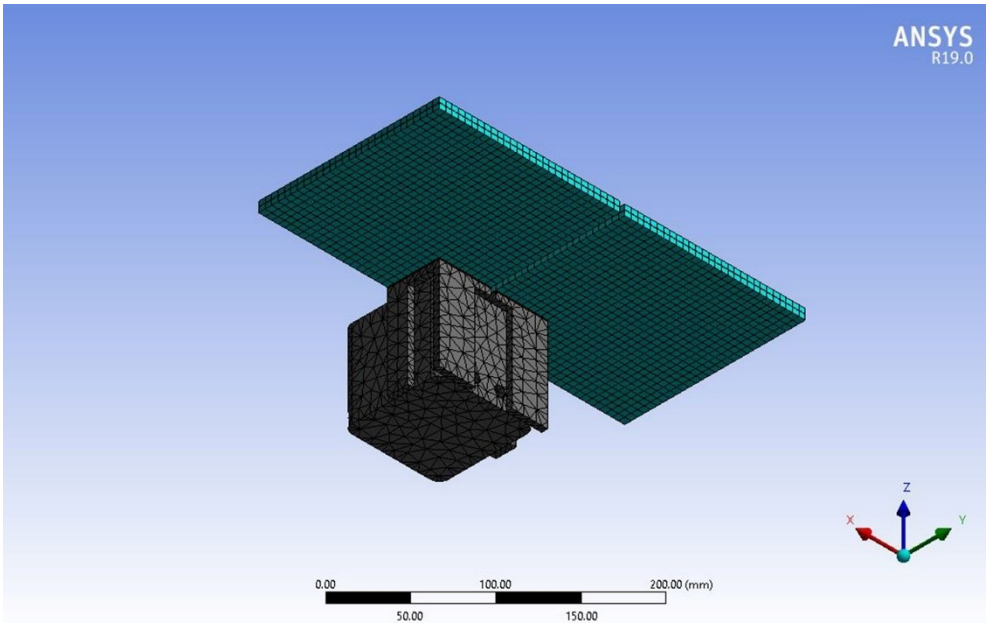

(b)

Figure 3.6. Axonometric view of the nodes: (a) middle joint; (b) lateral joint.

Since the single glass panel has double symmetry, only a quarter of the glass area was modelled to reduce the computational model complexity.
The connection between the steel headers and the substructure (upper cubes), which is made by bolting, was modelled by a bonded contact, so that a linear analysis could be performed (as opposed to the nonlinear analysis required for frictional contacts).
The upper order cubes are supported by rods passing through holes in the cube. To simulate this condition, the constraint Cylindrical Support (Radial=Axial=FIXED; Tangential=FREE) was set on the surface of each hole.
An Eight noded three-dimensional structural volume element (SOLID185 element) mesh and a maximum mesh size of 0.50 mm was used to model the adhesive layer.
Each modelled glass surface was loaded with its share of the service load, specified in the Italian regulations (NTC 2018 [15]). In the present case, the distributed load was considered to be 4.00 kN/m^2. This load value is assigned as a load acting on the whole surface of the glass panel. In this case, the load supported by each modelled panel part was estimated to be 67.5 N.
Finally, all modelled elements were loaded with to the inertia load “Standard Earth Gravity”.

3.7.2 FE results

The results of the FE simulations for the distribution of normal and shear stresses evaluated in the mid-plane of the adhesive layer, are shown below.
Fig. 3.7a, 3.7b and 3.7c show the normal stresses for the central joint, in the middle plane of the adhesive EPX1, EPX2 and SIL respectively.

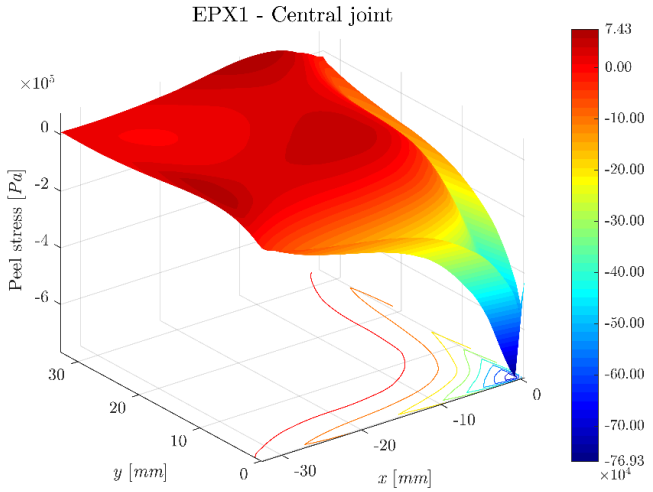

(a)

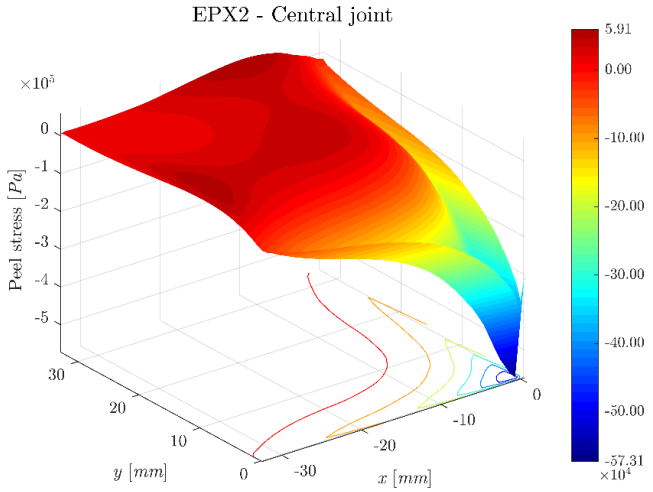

(b)

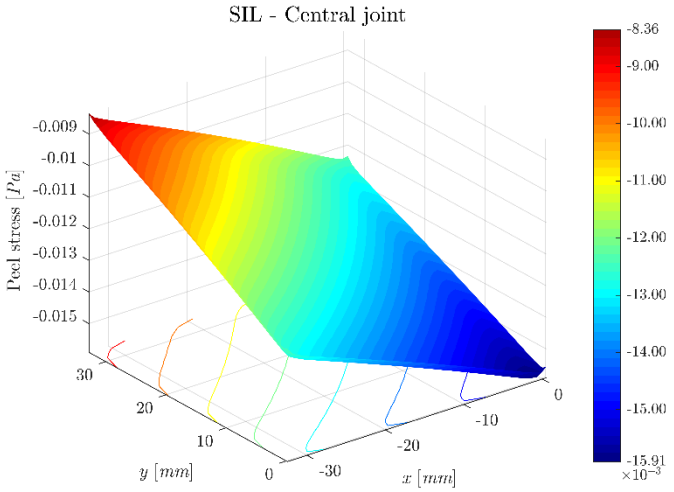

(c)

Figure 3.7. Peel stress for central joint: (a) EPX1 adhesive, (b) EPX2 adhesive, (c) SIL adhesive.

Fig. 3.8a, 3.8b and 3.8c show the shear stresses for the central joint, in the mid-plane of adhesives EPX1, EPX2 and SIL, respectively.

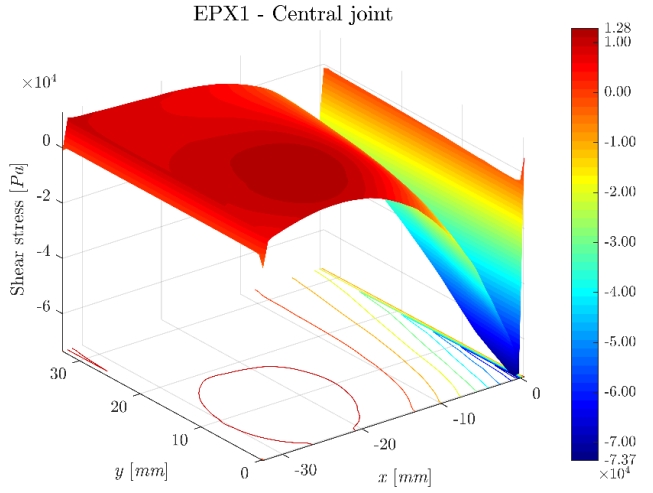

(a)

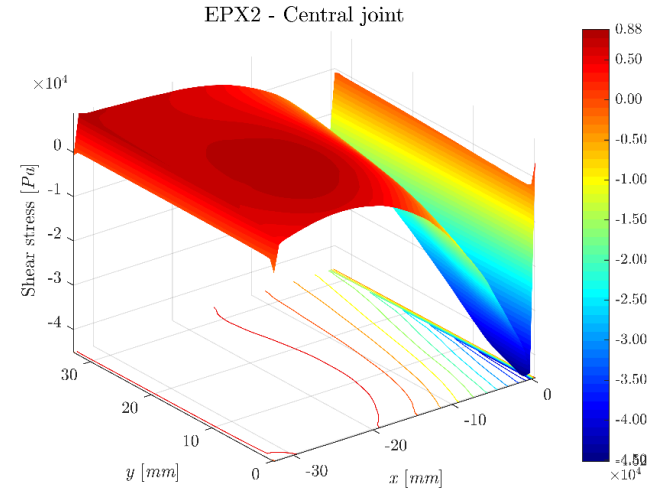

(b)

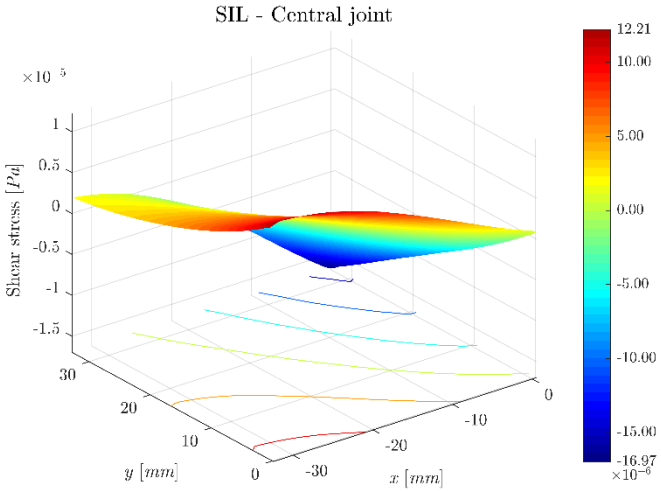

(c)

Figure 3.8. Shear stress for central joint: (a) EPX1 adhesive, (b) EPX2 adhesive, (c) SIL adhesive.

Fig. 3.9a, 3.9b and 3.9c show the normal stresses for the lateral joint, in the mid-plane of the adhesives EPX1, EPX2 and SIL respectively.

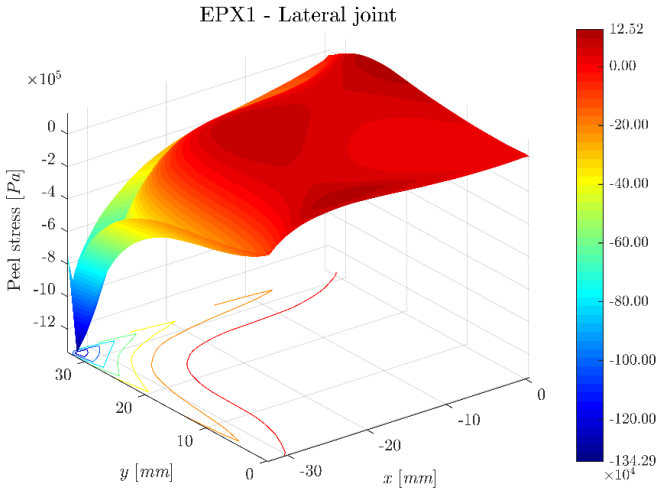
EPX1 - Lateral joint
×10^5
0
-2
-4
-6
-8
-10
-12
Peel stress [Pa]
30
20
10
0
y [mm]
0
-10
-20
-30
x [mm]
12.52
0.00
-20.00
-40.00
-60.00
-80.00
-100.00
-120.00
-134.29
×10^4

(a)

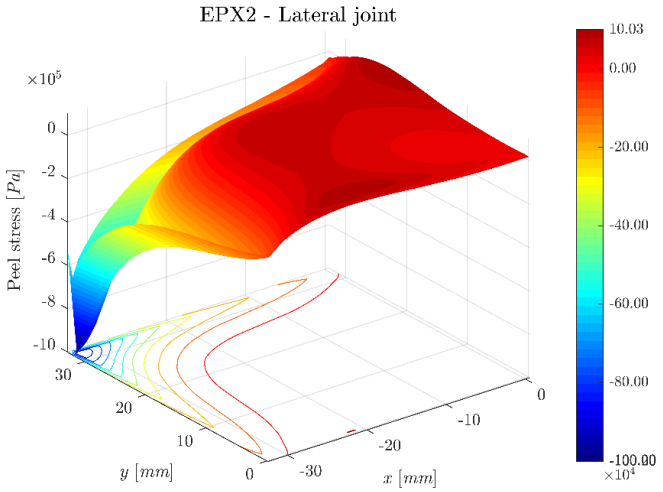
EPX2 - Lateral joint
×10^5
0
-2
-4
-6
-8
-10
Peel stress [Pa]
30
20
10
0
y [mm]
0
-10
-20
-30
x [mm]
10.03
0.00
-20.00
-40.00
-60.00
-80.00
-100.00
×10^4

(b)

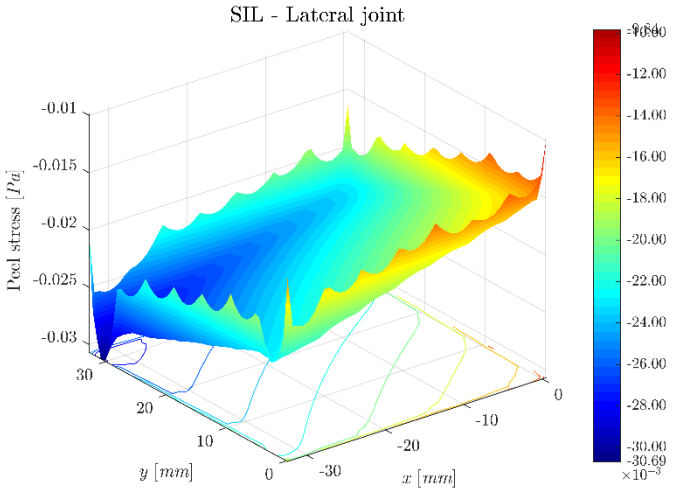

(c)

Figure 3.9. Peel stress for lateral joint: (a) EPX1 adhesive, (b) EPX2 adhesive, (c) SIL adhesive.

Fig. 3.10a, 3.10b and 3.10c show the shear stresses for the lateral joint, in the middle plane of the adhesives EPX1, EPX2 and SIL respectively.

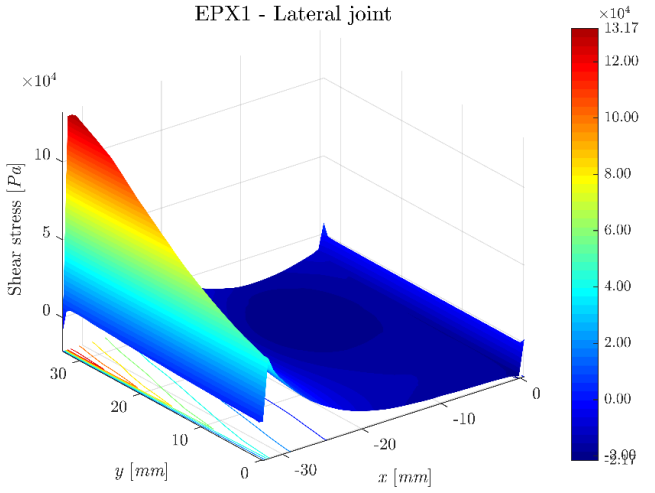

(a)

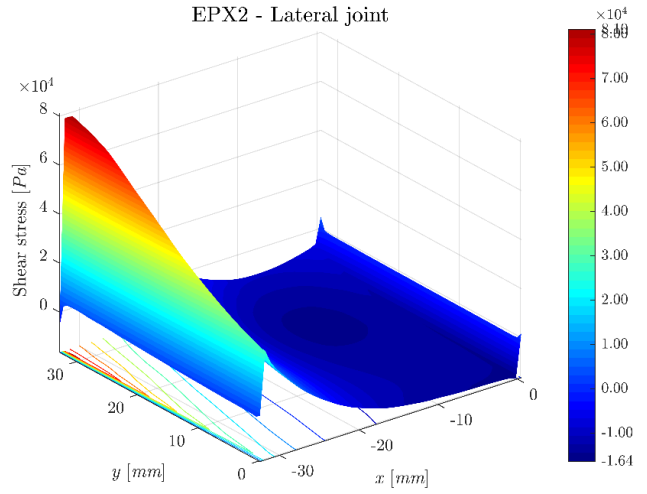

(b)

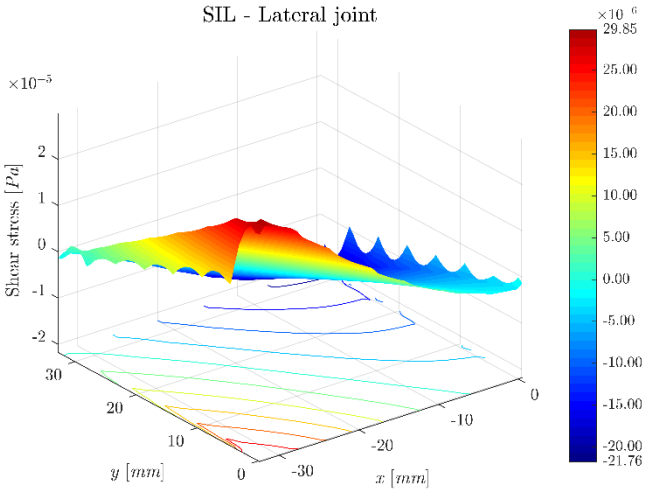

(c)

Figure 3.10. Shear stress for lateral joint: (a) EPX1 adhesive, (b) EPX2 adhesive, (c) SIL adhesive.

In both the investigated joints, a non-uniform distribution is observed for both normal and shear stresses, characterised by the presence of stress peaks at the edge of the adhesive region near the load application. The magnitude of the stress peaks observed are shown graphically in Fig. 3.11 for the EPX1 and EPX2 adhesives, in Fig. 3.12 for SIL adhesive, and in tabulated form in Tab. 3.3.

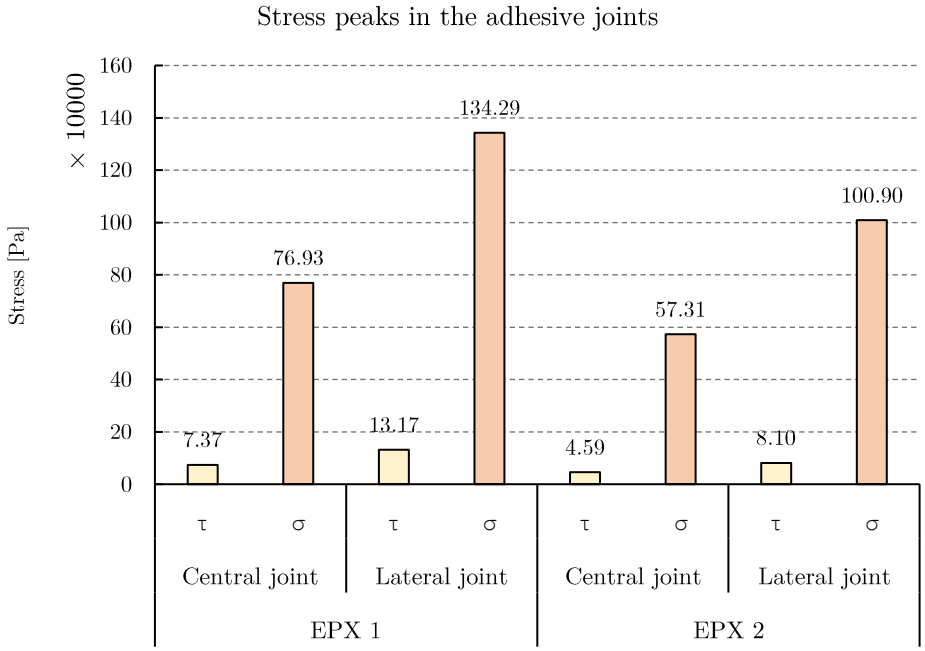

Figure 3.11. Stress peaks in the adhesive layer.

Table 3.3. Stress peaks for the joints assembled with EPX1 and EPX2 adhesives.

Adhesive	Central joint		Lateral joint	
	Shear [Pa]	Peel [Pa]	Shear [Pa]	Peel [Pa]
EPX 1	$7.37 \cdot 10^{4}$	$76.93 \cdot 10^{4}$	$13.17 \cdot 10^{4}$	$134.29 \cdot 10^{4}$
EPX 2	$4.59 \cdot 10^{4}$	$57.31 \cdot 10^{4}$	$8.10 \cdot 10^{4}$	$100.90 \cdot 10^{4}$
SIL	$1.70 \cdot 10^{-5}$	$1.60 \cdot 10^{-2}$	$2.99 \cdot 10^{-5}$	$3.07 \cdot 10^{-2}$

The results presented show that the adhesive joint - for each combination considered – is more stressed in bending, as evidenced by the high values of normal stress observed. The peak values of normal stress are recorded for the lateral joints, where the bending phenomenon is higher than in the central joints due to the lack of equilibrium of the external loads (unbalanced joint).
The EPX1 adhesive exhibits the highest stresses in each configuration due to its higher stiffness.
Fig. 3.12 shows graphically the peak stresses for the SIL adhesive. The results show that silicone, which has a lower modulus of elasticity than epoxy adhesives, develops lower stress values (up to nine orders of magnitude), corresponding to higher strain values.

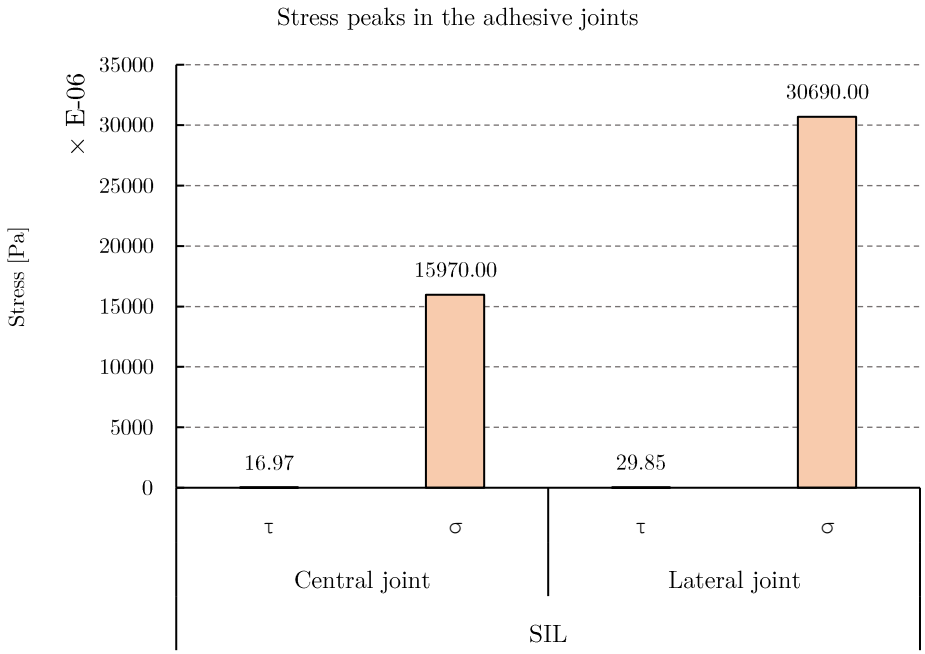

Figure 3.12. Stress peaks in the SIL adhesive middle plane.

The greater deformability of the silicone adhesive results in relatively high shear stresses. In this case, the adhesive is mainly subjected to compressive stress and exhibits high strain values in the direction normal to the plane of the adhesive. This aspect underlines the lower mechanical performance of silicone compared to the epoxies in relation to the intended applications.

3.8 References

[1] P. Munafò, Solaio Tensegrale, 00014426973, 2014.

[2] R. Motrò, B. Maurin, C. Silvestri, Tensegrity rings and the hollow rope, in: IASS Symposium 2006 (Ed.), New Olympics, New Shells and Spatial Structures, Beijing, China, 2006: pp. 470–471.

[3] M.C. Oliveira, R.E. Skelton, Tensegrity Systems, Springer US, Boston, MA, 2009. https://doi.org/10.1007/978-0-387-74242-7.

[4] R. Motrò, Tensegrity, Elsevier, 2003. https://doi.org/10.1016/B978-1-903996-37-9.X5028-8.

[5] K.D. Snelson, Continuous Tension, Discontinuous Compression Structures, (1965) United States Patent.

[6] L.F.M. da Silva, A. Öchsner, R.D. Adams, Introduction to Adhesive Bonding Technology, in: Handb. Adhes. Technol., Springer Berlin Heidelberg, Berlin, Heidelberg, 2011: pp. 1–7. https://doi.org/10.1007/978-3-642-01169-6_1.

[7] R.D. Adams, J. Comyn, W.C. Wake, Structural adhesive joints in engineering, Chapman and Hall, 1997.

[8] F. Marchione, Stress distribution in double-lap adhesive joints: Effect of adherend reinforcement layer, Int. J. Adhes. Adhes. 105 (2021). https://doi.org/10.1016/j.ijadhadh.2020.102780.

[9] L.J. Tabor, Adhesives in construction. A contractor's viewpoint, Int. J. Adhes. Adhes. 2 (1982) 73–76. https://doi.org/10.1016/0143-7496(82)90118-X.

[10] C.R. Calladine, Buckminster Fuller's "Tensegrity" structures and Clerk Maxwell's rules for the construction of stiff frames, Int. J. Solids Struct. 14 (1978) 161–172. https://doi.org/10.1016/0020-7683(78)90052-5.

[11] S. Pellegrino, C.R. Calladine, Matrix analysis of statically and kinematically indeterminate frameworks, Int. J. Solids Struct. 22 (1986) 409–428. https://doi.org/10.1016/0020-7683(86)90014-4.

[12] W. Bin Bing, Free-standing Tension Structures, CRC Press, 2004. https://doi.org/10.1201/9781482288308.

[13] R. Motrò, B. Maurin, N. Vassart, Density Methods Applied to Form Finding of Initially Stressed Systems, in: 2004: pp. 341–350. https://doi.org/10.1007/978-3-540-45287-4_30.

[14] C. Sultan, M. Corless, R. Skelton, Reduced prestressability conditions for tensegrity structures, in: 40th Struct. Struct. Dyn. Mater. Conf. Exhib., American Institute of Aeronautics and Astronautics, Reston, Virigina, 1999. https://doi.org/10.2514/6.1999-1478.

[15] NTC. Norme Tecniche Per Le Costruzioni. Rome, Italy; 2018, (n.d.).

[16] CNR DT 210/2013, Istruzioni per la progettazione, l'Esecuzione ed il Controllo di Costruzioni con Elementi Strutturali di Vetro, (n.d.).

[17] EN 10025-2:2004, "Hot rolled products of structural steels - Part 2: Technical delivery conditions for non-alloy structural steels," (2004).

3.9 List of figures and tables

Figure 3.1. Construction module. 25
Figure 3.2. Section view. 26
Figure 3.3. Mechanical properties of two-cable model with different sags: (a) internal force; (b) deflection; (c) load-displacement curve. 27
Figure 3.4. 3D SAP model of "Tensegrity Floor". 29
Figure 3.5. Prototype "Tensegrity Floor": (a) overall view, (b) detail. 31
Figure 3.6. Axonometric view of the nodes: (a) middle joint; (b) lateral joint. 33
Figure 3.7. Peel stress for central joint: (a) EPX1 adhesive, (b) EPX2 adhesive, (c) SIL adhesive. 35
Figure 3.8. Shear stress for central joint: (a) EPX1 adhesive, (b) EPX2 adhesive, (c) SIL adhesive. 36
Figure 3.9. Peel stress for lateral joint: (a) EPX1 adhesive, (b) EPX2 adhesive, (c) SIL adhesive. 38
Figure 3.10. Shear stress for lateral joint: (a) EPX1 adhesive, (b) EPX2 adhesive, (c) SIL adhesive. 39
Figure 3.11. Stress peaks in the adhesive layer..... 40
Figure 3.12. Stress peaks in the SIL adhesive middle plane. 41

Table 3.1. Mechanical characteristics of steel and glass, as reported by manufacturers. 30
Table 3.2. Mechanical characteristics of the adhesives reported by manufacturers. 30
Table 3.3. Stress peaks for the joints assembled with EPX1 and EPX2 adhesives. 40

Chapter 4.

Experimental strength evaluation of glass-aluminium double-lap adhesive joints

The aim of the reported experimental campaign is to evaluate the mechanical compatibility of adhesive joints between aluminium and glass adherends with different finishes, for their application on innovative building components. The content of this chapter has been published in a previous work, reported in Ref. [1].

4.1 Abstract

The use of structural adhesives in the field of civil engineering has increased substantially over the last decades. Although adhesive joints offer significant advantages if compared with conventional connections, the prediction of their behaviour must consider several aspects such as environmental exposure both during application and service life, the type of adherends, etc.
This section reports on an experimental campaign on glass-aluminium adhesive joints, with different finishes for adherend materials (float glass, float cold-painted glass, raw aluminium, anodized aluminum) and on the adhesion of selected epoxy adhesives.
The effects of artificial aging on the mechanical performance of adhesive joints, compared to unaged condition, are also investigated.
Four series of double-lap specimens made with different materials and exposed to different aging conditions were tested. The experiments showed that EPX2 adhesive provided the best mechanical performance to artificial aging; the best adherends configuration was the aluminum and cold-painted glass adhesive joint. The artificial aging had different effects depending on the adhesive, causing a decay of the joint performance in each combination.

Nomenclature

AF	Adhesive failure	T_0	Un-aged temperatures
A_t	Application temperature	T_{CC} - ***48 h***	Artificial aging in climatic chamber (48 hours)
CF	Cohesive failure	T_{CC}	Artificial aging in climatic chamber (6 months)
EPX1	First Epoxy Adhesive	***TLC***	Thin layer cohesive failure
EPX2	Second Epoxy Adhesive	***Wt***	Working temperature
EPX3	Third Epoxy Adhesive	***24 h***	24 h curing phase
E_t	Young Modulus in tension	α	Thermal coefficient of expansion
F	Applied load	ε_t	Tensile strain
k	Stiffness	σ_t	Tensile strength
MF	Mixed failure	τ	Shear strength
SB	Stock break failure	γ	Shear strain at failure
S_t	Service temperature		

4.2 Introduction

The use of glass is a distinctive element of modern architecture. Glass is an increasingly used material for various applications: curtain walls, structural elements [2–4], glass floors [5]. However, in common application cases (e.g. windows or curtain wall), glazed panels are usually treated as an infill element inserted into a frame, without any structural value [6].
This study contributes to the experimental research about structural cooperation between the elements that make up a window or a curtain wall. A further purpose is the technical development of the European patents (Patent No. EP.3071775B1[1] [7]) for a new type of window with the mobile frame inside the glazing unit (Fig. 4.1) and (Patent No. EP 00014426973 [8]) for a new tensegrity floor characterised by a glass deck that cooperates with the metal substructure through the use of structural adhesives.

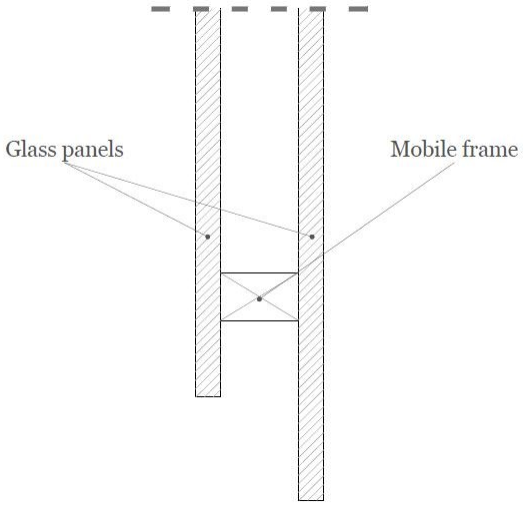

Figure 4.1. Scheme of the mobile frame referring to EP 3071775B1.

The main problem for the mechanical performance of the junction between metal and glass is the glass brittleness which makes the design of structural elements with cooperating glass difficult. This characteristic of glass does not make traditional junctions (e.g., bolted joints) suitable. Adhesive joints represent a viable alternative since they allow uniform stress distribution, avoiding stress concentration and reducing the junction weight if compared with traditional ones. However, their non–linear mechanical behaviour and mechanical performance under different environmental exposure conditions are difficult to determine.
Recent developments in the study of structural adhesives involved experiments on hybrid adhesive joints with wood [9–11] and other materials such as pultruded GFRP [12].

[1] CIC Properties – Componenti Innovativi per Costruire srl., innovative startup.

Other studies [13] showed that by joining together a brittle and a ductile materials (e.g. glass and steel, respectively), an improvement of the mechanical behaviour of the glass structure could be obtained. This combination allows to realize a highly ductile structure characterized by gloss and transparency.
Overend et al. [14] studied the performance of five adhesives for load-bearing steel-glass connections by means of mechanical and numerical modelling tests. Mechanical tests on steel-glass connections provided useful data for the selection of a suitable adhesive (silicone). The systematic characterization of time-dependent constitutive models adhesives for bulk materials provided essential data for analytical and numerical models.
Richter et al. [15] illustrated the possibilities offered by existing hyper elastic material models for specific steel-glass components. Small-scale tests were performed to characterize the adhesives and determine the material model for the next FEA.
Other studies [5,13,16] verified the effect of different artificial aging modes on mechanical performance of adhesive joints, by observing the effect of moisture on the ultimate shear strength.
Zhang et al. [17,18] studied the temperature and relative humidity influence on adhesive joints made with composite adherends. After hot-wet exposure, double-lap joints showed a mechanical performance decay because of moisture.
Lancker et al. [19] verified the effect of moisture, temperature and UV radiation on glass-metal adhesive joints. Epoxy adhesives showed limited strength to moisture.
During their service life, the elements constituting building components are exposed to various factors (e.g., UV, temperature, moisture) that may affect their mechanical performance. This study aims to verify the mechanical compatibility of the adhesive joint between glass and aluminum and to evaluate the effects of artificial aging on this type of connection.
In order to verify the compatibility of the adhesive joints between glass and aluminum, three different epoxy adhesives (EPX1, EPX2, EPX3) are analysed and compared. The environmental aging effects are studied by performing shear tests on double-lap adhesive joints both in unaged and aged condition. In detail, a first artificial aging mode simulates environmental exposure to high temperature and moisture for six months. A second mode consists in verifying the effect of temperature and moisture during the curing phase, to reduce the timing of curing and handling of the joint.

4.3 Materials and methods

The experimental campaign consists in shear tests on double-lap adhesive joints made of aluminum adhesively bonded on transparent or cold-painted float glass. The joints strength depends both on their geometric design and on the properties of the materials used.
Experimental tests investigate the compatibility of the bonding system between aluminum and glass, under unaged conditions (T_0), aged conditions (T_{CC}), 24 hours artificial aging conditions (24h) and under accelerated 48 hours aging conditions (T_{CC} – 48h).
Double-lap adhesive joints are manufactured with raw or anodized aluminum profiles, adhesively bonded on transparent or water-based cold-painted float glass, according to ASTM D3528 [20]. For accelerated aging test (T_{CC} – 48h) raw aluminum (hereinafter

aluminium) adherends and transparent float glass (hereinafter float glass) are used since this configuration exhibited lower mechanical performance in unaged conditions (T_0).
The effectiveness of the adhesion between adherends is studied by analysing the ultimate shear strength, maximum tension, displacement, and stiffness of the adhesive joints.

4.3.1 Materials properties

4.3.1.1 Adherends

In this experimental campaign three different materials have been used: float glass both transparent and with surface finish made with water-based paint, provided by Vetromarche (Italy) and aluminum profiles provided by Frame (Italy); the materials properties, provided by the manufacturers, are shown in Tab. 4.1.

Table 4.1. Glass and aluminum mechanical properties according to manufacturer's data sheet.

GLASS			**ALUMINUM PROFILES (Alloy EN AW-6060) ***			
α ($°C^{-1}$)	E_t (GPa)	σ_t (MPa)	α ($°C^{-1}$)	E_t (GPa)	σ_t (MPa)	ε_t (%)
9×10^{-6}	75	40	2.30×10^{-5}	69,00	160	8

* According to EN 755-2

4.3.1.2 Adhesives

Three commercial two-part epoxy structural adhesives (EPX1, EPX2, EPX3) were used. Relevant technical and mechanical characteristics, reported by manufacturers data sheet, are summarized in Tab. 4.2.

Table 4.2. Technical and mechanical characteristics of the adhesives reported by manufacturers.

Adhesive	**EPX 1**	**EPX 2**	**EPX 3**
Chemical base	Two-part epoxy	Two-part epoxy	Two-part epoxy
Viscosity	thixotropic	thixotropic	Controlled flow
Wt (min)	90-300	16	60-90
At (° C)	15-25	15-25	-
St (° C)	-50 + 120	-40 + 80	-
τ (MPa)	33.50 *	29.40 *	18.90-23.60 *
σt (MPa)	-	17	-
Et (MPa)	3000	1500	-
εt ** (%)	3	-	-
Use	Structural	Semi-structural	Structural

* On aluminum-steel Adherends ** At failure

4.4 Specimens dimensions

The geometry of the specimens was manufactured according to ASTM D638: 2014 [21]; for each configuration five specimens were realized and tested.
The size of the glass panels was 200 mm × 100 mm and thickness 5 mm; the width of the aluminum profiles was 25.40 mm and length 140 mm. The thickness of the aluminum adherends was 5 mm, with 25.40 mm × 12.70 mm bonding area - as stated by ASTM D 3528-16 [20].
The bonding thickness employed was the same for all specimens, as recommended by the manufacturer, i.e., 0.30 mm. The specimen geometry is depicted in Fig. 4.2.

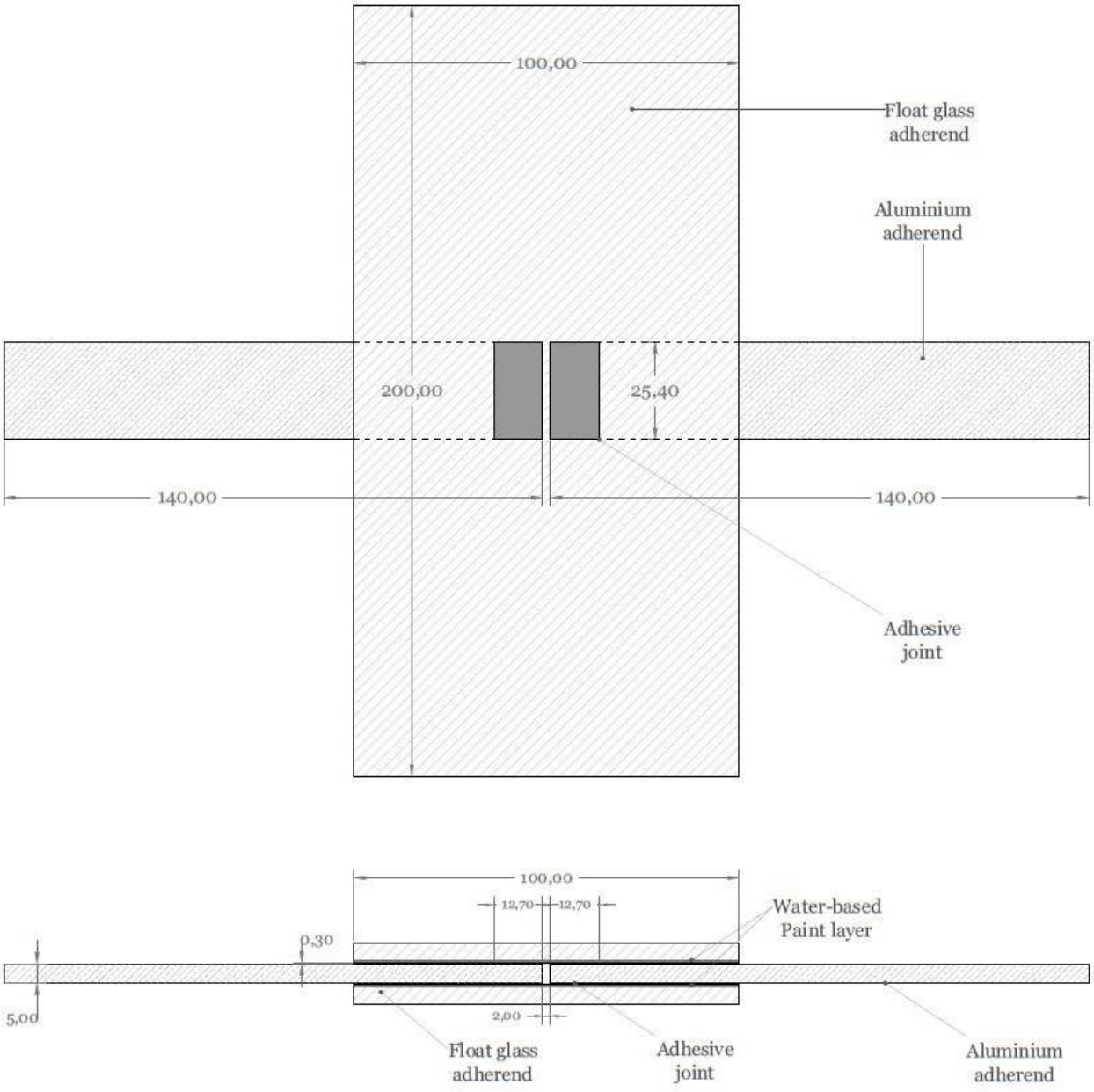

Figure 4.2. Double lap specimens' geometry (mm), section and plan view.

Before the assembly phase, the surfaces of the aluminum adherends were subjected to manual abrasive treatment with sandpaper, as reported by the manufacturers in technical sheets. The bonding areas were then cleaned using isopropyl alcohol.
Fig. 4.3 illustrates the assembly phase, which took place under laboratory conditions. The bonding activity was carried out at a temperature of 20 ± 1 °C and relative humidity of 60 ± 5%. All samples were labelled according to the adhesive used and cured in laboratory for 28 days (24 hours for those tested to 24h and T_{CC} - 48h), as recommended by manufacturers.

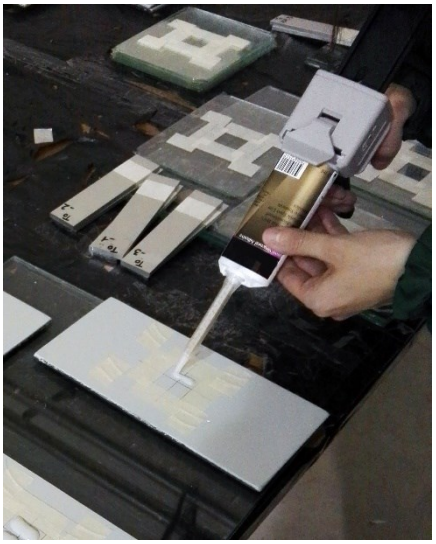

Figure 4.3. Assembly phase.

4.5 Artificial aging

Two different artificial aging conditions were conducted.
The first aging condition (TCC) was performed in accordance with the ISO 6270-2 standard [22]. The specimens were subjected to a temperature of 40 ± 2 °C and a relative humidity of 100 ± 5% for six months without interruption.
The second aging condition (T_{CC} – 48h) consisted of exposure of the specimens to an artificial aging of 48 hours before the shear test, at the temperature of 50 ± 2 °C and relative humidity of 30 ± 6%. The purpose of this aging condition was to speed up the curing process of the adhesive and compare its performance with that of the adhesives subjected to normal curing process. These aging conditions were simulated using a climatic chamber “Angelantoni” CST-130S model (Fig. 4.4).

Figure 4.4. Angelantoni "CST-130S model Climatic chamber.

4.6 Test setup

Tools and methods of tests setup were the same for all types of specimens. Shear tests allowed to evaluate the compatibility between the adherends and to compare the mechanical behaviour of three epoxy adhesives, namely their load carrying capacity, displacement and stiffness.

All tests were carried out on an electromechanical machine Zwick/Roell Z050 of 50 kN capacity. All tests took place under laboratory conditions; a datalogger registered a temperature of 20 °C and a relative humidity of 50%. All tests were performed under displacement control at the slow rate of 1.25 mm/min.

In order to arrange an optical extensometer, two synchronized CMOS cameras with 1280×1024 resolution (Pixelink®B371F), with different angle (Fig. 4.5), were used.

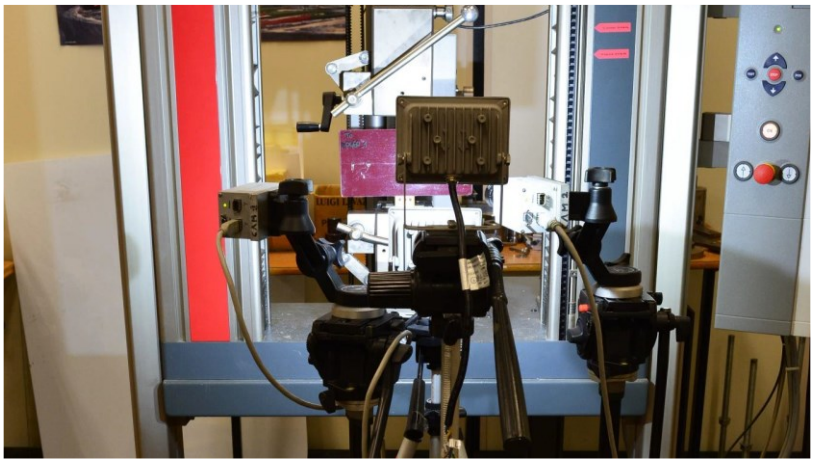

Figure 4.5. Shear test setup.

4.7 Results and discussion

In this section, the load-displacement curves and failure modes of double-lap specimens are presented and discussed. For each combination of adherends and aging modes, five repetitions were carried out. All results discussed in the following are given in terms of mean value of five tests.

4.7.1 Mechanical performances

Figs. 4.6-4.9 show the load-displacement curves of double-lap specimens made with the three epoxy adhesives, under unaged and different aged conditions for the adherends and adhesives.

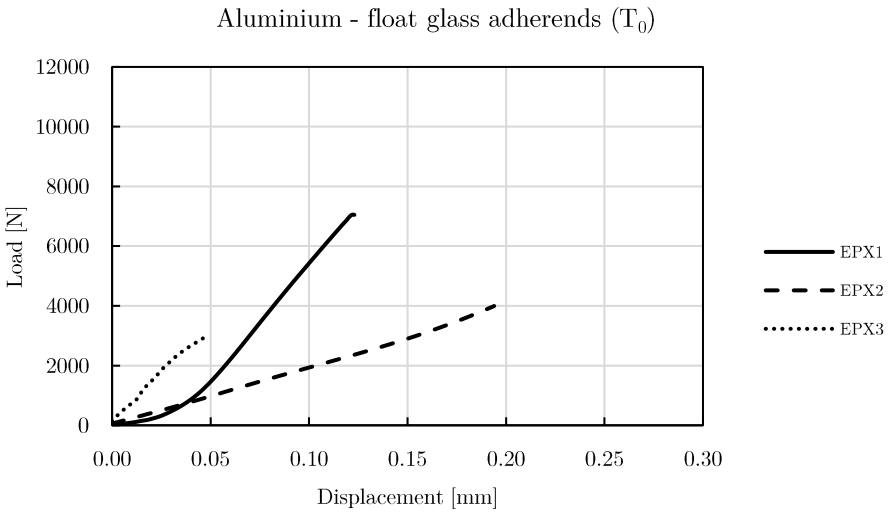
Aluminium - float glass adherends (T_0)
Load [N]
Displacement [mm]
EPX1
EPX2
EPX3

(a)

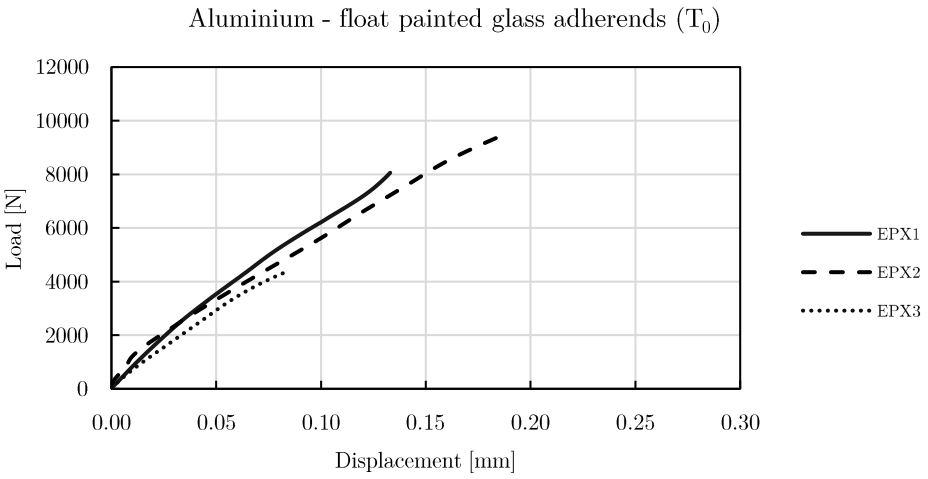
Aluminium - float painted glass adherends (T_0)
Load [N]
Displacement [mm]
EPX1
EPX2
EPX3

(b)

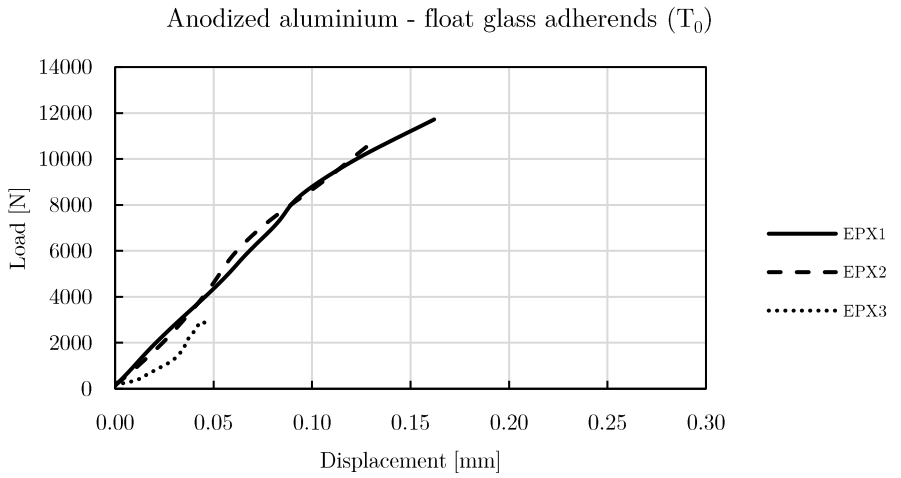

(c)

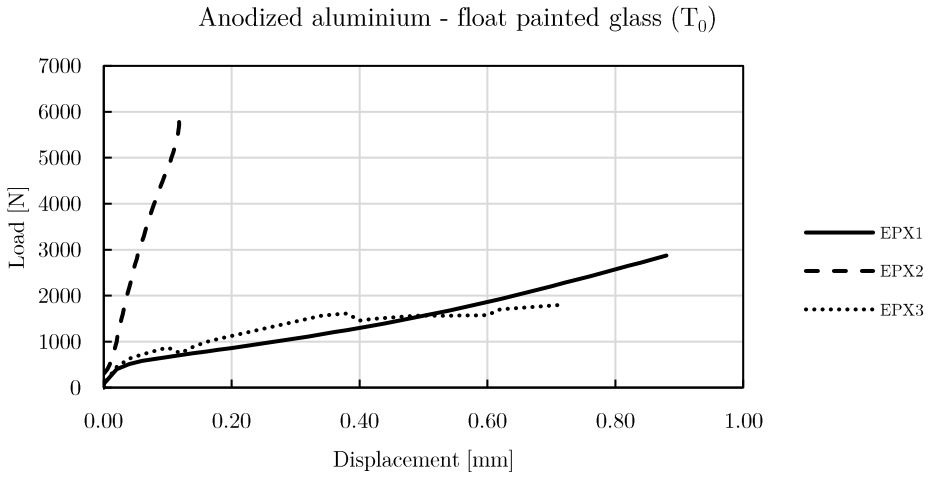

(d)

Figure 4.6. Load displacement curves for: (a) aluminium-float glass, unaged; (b) aluminium-float glass, unaged; (c) anodized aluminium-float glass, unaged; (d) anodized aluminium-painted glass, unaged.

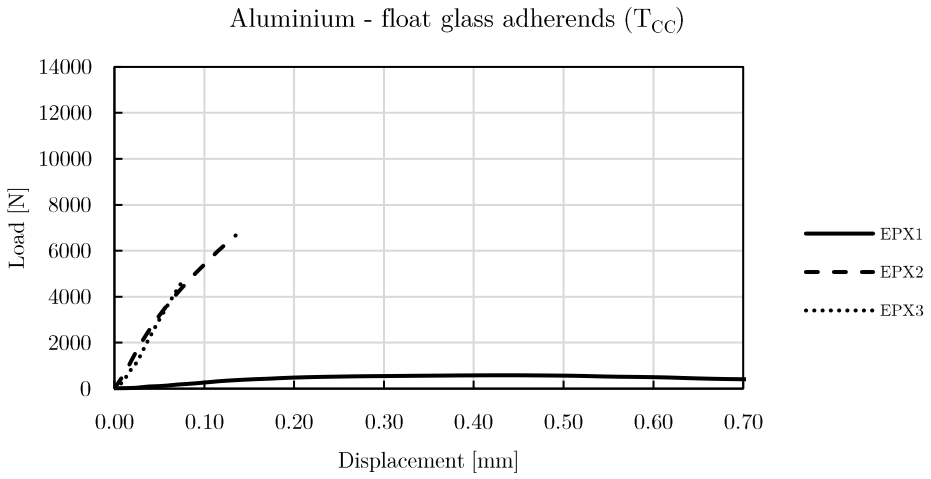
Aluminium - float glass adherends (T_{CC})
Load [N]
14000
12000
10000
8000
6000
4000
2000
0
0.00
0.10
0.20
0.30
0.40
0.50
0.60
0.70
Displacement [mm]
EPX1
EPX2
EPX3

(a)

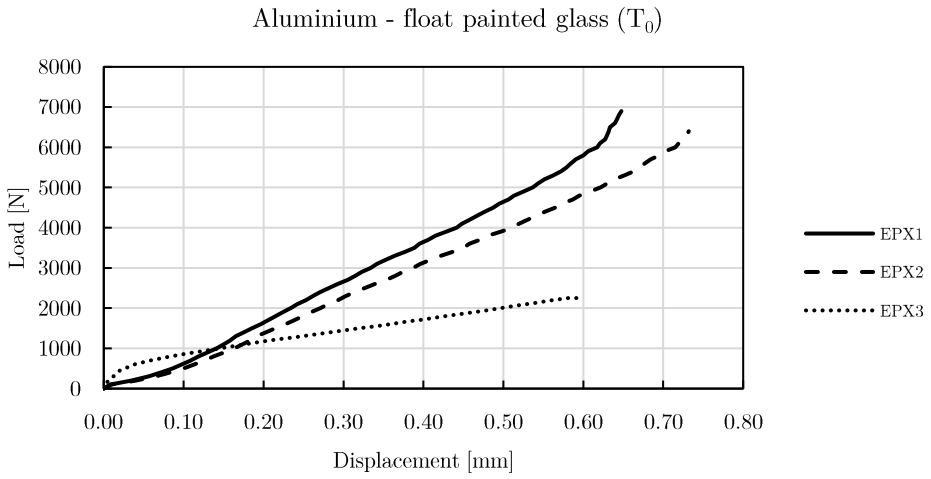
Aluminium - float painted glass (T_0)
Load [N]
8000
7000
6000
5000
4000
3000
2000
1000
0
0.00
0.10
0.20
0.30
0.40
0.50
0.60
0.70
0.80
Displacement [mm]
EPX1
EPX2
EPX3

(b)

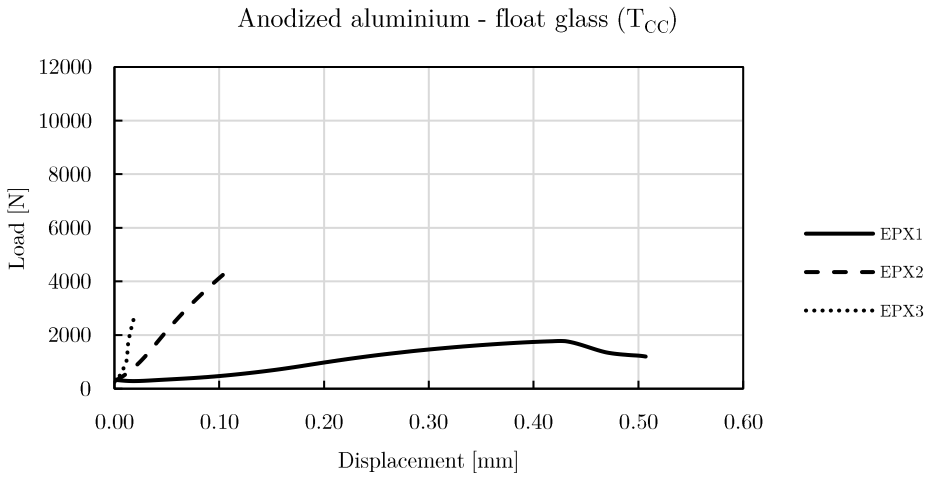

(c)

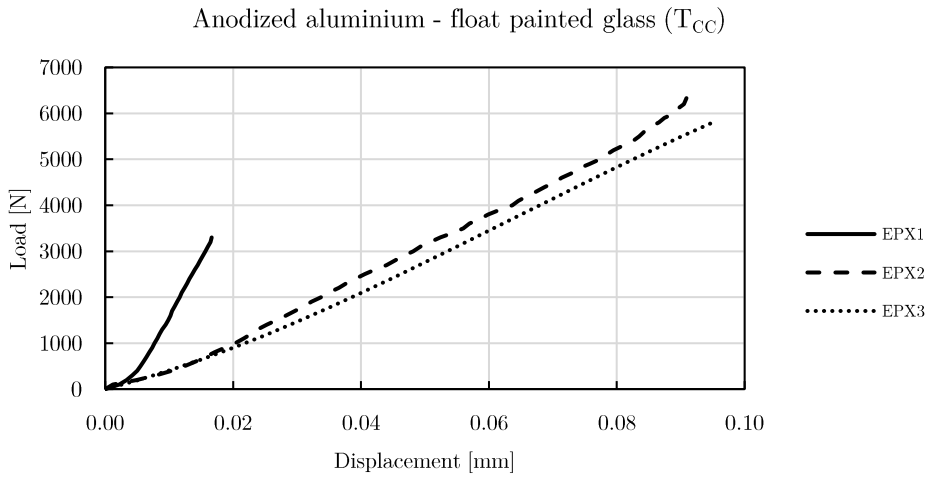

(d)

Figure 4.7. Load displacement curves for: (a) aluminium-float glass, T_{CC}; (b) aluminium-float glass, T_{CC}; (c) anodized aluminium-float glass, T_{CC}; (d) anodized aluminium-painted glass, T_{CC}.

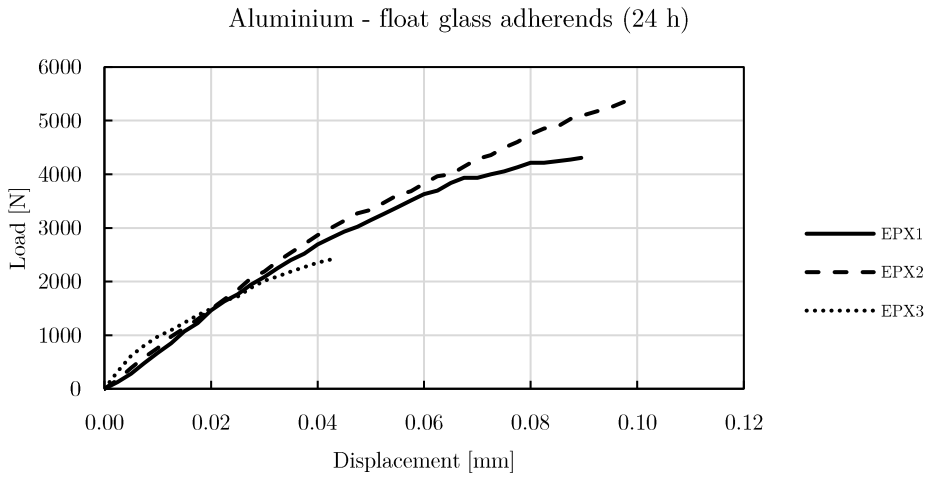

Figure 4.8. Load displacement curves for aluminium-float glass specimen after 24h maturation.

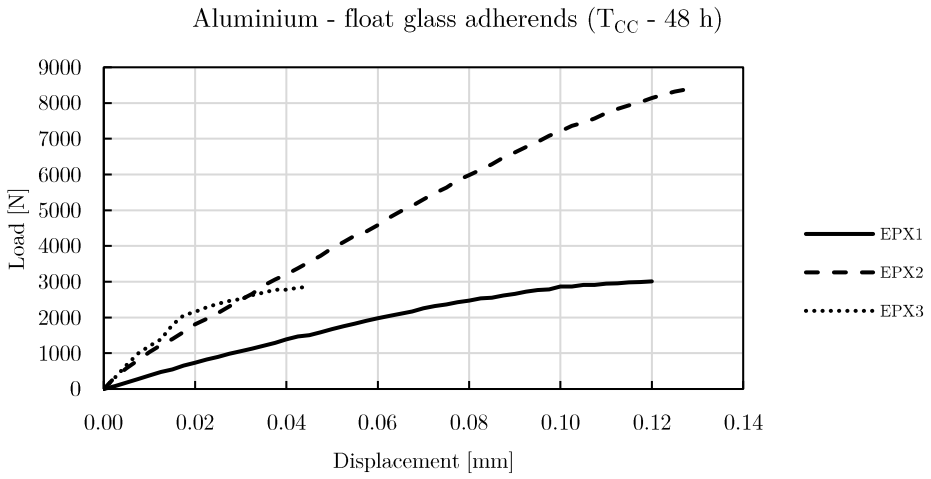

Figure 4.9. Load displacement curves for aluminum - float glass $T_{CC\text{-}48h}$ aged joints.

The results obtained for the combination of adherends under unaged conditions (T_0) are shown in Figs. 4.6 (a-b-c-d). Fig. 4.5a shows the load-displacement curve for aluminum-float glass joints. EPX1 adhesive shows the best results in terms of stiffness and strength. In the

aluminum and cold-painted glass configuration an almost homogeneous trend for all adhesives is observed, with comparable stiffness. In terms of ultimate strength, EPX2 adhesive proves to be the most performing one. Fig. 4.6c shows the results for the float glass and anodized aluminum configuration. Joints made with EPX1 and EPX2 adhesives allow to obtain a stiffness and ultimate strength greater than those offered by EPX3. In the anodized aluminum and cold-painted glass adherends configuration (Fig. 4.6d), a different behaviour of the adhesives is observed. EPX2 adhesive shows a significantly greater stiffness than EPX1 and EPX3 adhesives, which exhibit a greater ductility with an ultimate strength equal to about half of that obtained by EPX2.

The results for the combination of adherends and adhesive subjected to artificial aging (TCC) are illustrated in Figs. 4.7 (a-b-c-d). Fig. 4.7a shows the load-displacement curve for the aluminum-float glass specimens. EPX1 adhesive shows stiffness values lower than other adhesives, with low strength values and great displacement. EPX2 and EPX3 adhesives exhibit stiffness values greater if compared with the unaged condition. In the aluminum and cold-painted glass configuration (Fig. 4.7b) a similar trend for EPX1 adhesives and EPX2 is observed. Both stiffness, ultimate strength and displacement are comparable. EPX2 adhesive shows a totally different behaviour, exhibiting a stiffness equal to about half of the other adhesives, with a lower displacement at failure. The anodized aluminum and float glass configuration (Fig. 4.7c) shows how EPX1 adhesive suffers the artificial aging effects exhibiting great displacements for low load values. In the case of anodized aluminum and cold-painted glass adherends (Fig. 4.7d), a different behaviour from unaged configuration can be observed. EPX1 adhesive proves to offer the greatest stiffness. EPX2 and EPX3 adhesives show a similar trend both for stiffness and for ultimate strength.

The mechanical performance of the aluminum-float glass joints, subjected to shear tests after 24 hours curing phase, are shown in Fig. 4.8. Similar stiffness for all adhesives could be observed. Both EPX1 adhesive and EPX2 exhibit ultimate strain values greater if compared to unaged specimens, with a greater ultimate strength for the EPX2. EPX3 adhesive does not show significant changes in its behaviour.

The load-displacement curve for aluminum-float glass joints, tested after 24 hours curing and accelerated 48 hours aging (T = 50 °C, RH=100%), is illustrated in Fig. 4.9. EPX1 adhesive shows a performance decay. EPX2 adhesive presents an improvement in stiffness, but worse results if compared to aging in unaged conditions. EPX3 adhesive does not report performance variations but exhibits stiffness values lower than those in unaged condition.

Tabs. 4.3-4.4-4.5-4.6 summarize data obtained from the experiments.

Table 4.3. Mechanical properties of aluminum-float glass double-lap joints bonded with three different epoxy adhesives: results before (T_0) and after (T_{CC}, $T_{CC\text{-}24h}$) the aging treatments.

Adhesive	*Aging condition*	F_{max} *(N)*	τ_{max} *(N / mm²)*	γ_{max} *(%)*	*Displacement * (mm)*	*k (KN / mm)*
EPX 1	T_0	8089 ± 2217	6.27 ± 1.72	0.43 ± 0.06	0.14 ± 0.02	74816 ± 7244
	T_{CC}	724 ± 230	0.56 ± 0.18	1.40 ± 0.07	1.89 ± 0.63	2886 ± 1154
	24 h	4771 ± 2114	3.70 ± 1.64	0.30 ± 0.08	0.08 ± 0.03	80864 ± 29437
	T_{CC} - 48 h	3235 ± 908	2.53 ± 0.68	0.38 ± 0.11	0.12 ± 0.04	34302 ± 2614
EPX 2	T_0	11070 ± 1379	8.58 ± 1.07	0.82 ± 0.26	0.37 ± 0.19	24390 ± 4818
	T_{CC}	7654 ± 1627	5.93 ± 1.26	0.53 ± 0.08	0.18 ± 0.04	53545 ± 16866
	24 h	6062 ± 1435	4.70 ± 1.11	0.48 ± 0.48	0.10 ± 0.04	69509 ± 21750
	T_{CC} - 48 h	9106 ± 1810	7.06 ± 1.40	0.41 ± 0.09	0.13 ± 0:04	76919 ± 19390
EPX 3	T_0	5295 ± 1009	4.10 ± 0.78	0.40 ± 0.20	0.13 ± 0.07	67753 ± 57029
	T_{CC}	5932 ± 2008	4.60 ± 1.56	0.33 ± 0.05	0.10 ± 0.02	76460 ± 25920
	24 h	2765 ± 792	2.14 ± 0.60	0.14 ± 0.10	0.04 ± 0.03	118889 ± 119148
	T_{CC} - 48 h	3105 ± 794	2.41 ± 0.62	0.15 ± 0.12	0.05 ± 0.04	179160 ± 132856

* At failure

Table 4.4. Mechanical properties of anodized aluminum-float glass double-lap joints bonded with three different epoxy adhesives: results before (T_0) and after (T_{CC}) the aging treatment.

Adhesive	*Aging condition*	F_{max} *(N)*	τ_{max} *(N / mm²)*	γ_{max} *(%)*	*Displacement * (mm)*	*k (kN / mm)*
EPX 1	T_0	13106 ± 1647	10.16 ± 1.28	0.68 ± 0.26	0.28 ± 0.20	79807 ± 6287
	T_{CC}	1666 ± 381	1.29 ± 0.30	1.14 ± 0.08	0.67 ± 0.13	4887 ± 1026
	24 h	-	-	-	-	-
	T_{CC} - 48 h	-	-	-	-	-
EPX 2	T_0	11905 ± 2972	9.23 ± 2.30	0.46 ± 0.15	0.15 ± 0.06	118363 ± 25194
	T_{CC}	5936 ± 1179	4.60 ± 0.91	0.41 ± 0.04	0.13 ± 0.02	52550 ± 19388
	24 h	-	-	-	-	-
	T_{CC} - 48 h	-	-	-	-	-
EPX 3	T_0	5855 ± 2291	4.54 ± 1.78	0.43 ± 0.19	0.15 ± 0.07	174000 ± 104794
	T_{CC}	5947 ± 2433	4.61 ± 1.89	0.27 ± 0.21	0.09 ± 0.07	173 487 ± 173 237
	24 h	-	-	-	-	-
	T_{CC} - 48 h	-	-	-	-	-

* At failure

Table 4.5. Mechanical properties of aluminum-cold-painted float glass double-lap joints bonded with three different epoxy adhesives: results before (T_0) and after (T_{CC}) the aging treatment.

Adhesive	*Aging condition*	F_{max} *(N)*	τ_{max} *(N / mm²)*	γ_{max} *(%)*	*Displacement * (mm)*	*k (kN / mm)*
EPX 1	T_0	91377 ± 984	7.08 ± 0.76	0.53 ± 0.12	0.18 ± 0.05	54007 ± 7040
	T_{CC}	6709 ± 1293	10.51 ± 2.03	1.15 ± 0.07	0.70 ± 0.06	9716 ± 1255
	24 h	-	-	-	-	-
	T_{CC} - 48 h	-	-	-	-	-
EPX 2	T_0	9377 ± 938	7.27 ± 0.73	0.53 ± 0.10	0.18 ± 0.04	55831 ± 13989
	T_{CC}	6400 ± 1124	10.51 ± 2.03	1.21 ± 0.06	0.81 ± 0.18	6216 ± 2148
	24 h	-	-	-	-	-
	T_{CC} - 48 h	-	-	-	-	-
EPX 3	T_0	6154 ± 1296	4.77 ± 1.00	0.38 ± 0.10	0.12 ± 0.04	60112 ± 14848
	T_{CC}	2473 ± 1519	1.92 ± 1.18	1.02 ± 0.03	0.61 ± 0.36	4025 ± 979
	24 h	-	-	-	-	-
	T_{CC} - 48 h	-	-	-	-	-

* At failure

Table 4.6. Mechanical properties of anodized aluminum-cold-painted float glass double-lap joints bonded with three different epoxy adhesives: results before (T_0) and after (T_{CC}) the aging treatment.

Adhesive	*Aging condition*	F_{max} *(N)*	τ_{max} *(N / mm²)*	γ_{max} *(%)*	*Displacement * (mm)*	*k (kN / mm)*
EPX 1	T_0	2873 ± 946	2.22 ± 0.73	1.24 ± 0.12	0.88 ± 0.25	3264 ± 305
	T_{CC}	3302 ± 364	2.56 ± 0.56	0.05 ± 0.03	0.02 ± 0.04	198201 ± 989
	24 h	-	-	-	-	-
	T_{CC} - 48 h	-	-	-	-	-
EPX 2	T_0	5942 ± 2972	4.57 ± 1.82	0.37 ± 0.04	0.12 ± 0.02	49502 ± 19388
	T_{CC}	6420 ± 1179	4.96 ± 0.01	0.29 ± 0.10	0.09 ± 0.01	70242 ± 25190
	24 h	-	-	-	-	-
	T_{CC} - 48 h	-	-	-	-	-
EPX 3	T_0	1793 ± 540	1.39 ± 0.42	1.17 ± 0.12	0.71 ± 0.18	2526 ± 1568
	T_{CC}	5801 ± 2008	4.49 ± 3.11	0.30 ± 0.11	0.09 ± 0.02	61067 ± 25920
	24 h	-	-	-	-	-
	T_{CC} - 48 h	-	-	-	-	-

* At failure

4.8 Failure modes

In this section the failure modes of the tested specimens are described and analyzed. Reference is made to the standard ASTM D 5573-99 [23]. Fig. 4.10e illustrates the various failure modes occurred:

- ***Adhesive Failure*** (AF - Fig. 4.10a). Adhesive failure occurs in the interface between adhesive and adherends. The adhesive remains on the glass surface or on the aluminium adherend and no adhesion is observed on the opposite side;
- ***Cohesive Failure*** (CF). This failure takes place within the adhesive layer, which remains on both surfaces of the adherends;
- ***Thin-Layer Cohesive Failure*** (TLC - Fig. 4.10b). Failure similar to CF, characterized by a thin adhesive layer on an adherend surface and a thicker one on the another. The separation occurs inside the adhesive layer, which remains on both surfaces but with different thickness;
- ***Stock-Break Failure*** (SB - Fig. 4.10c). Failure of the material outside the adhesive area;

- ***Mixed Failure*** (MF - Fig. 4.10d). Combination of one or more mentioned failure modes (AF and CF for example).
- ***Delamination of Glass*** (GD - Fig. 4.10e). Glass plates appear adhering to the adhesive interface.

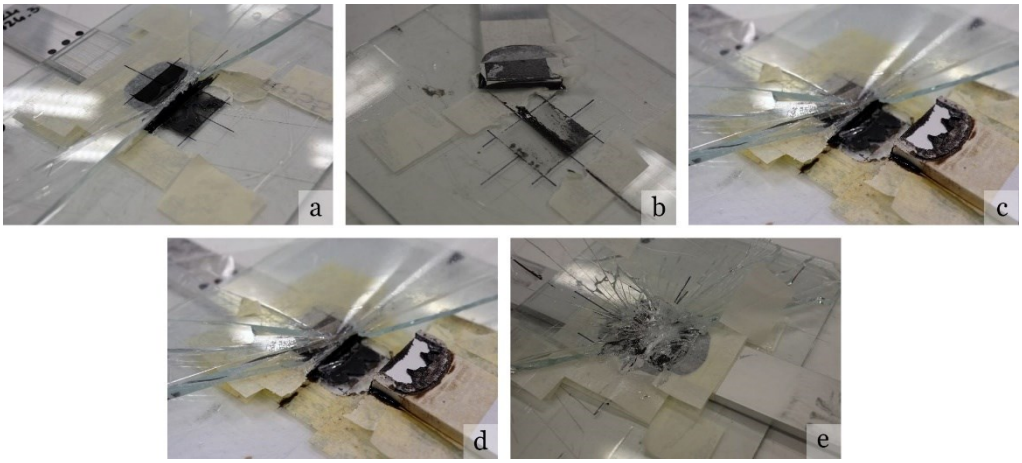

Figure 4.10. Failure modes of single lap adhesive joints: a) AF failure; b) CF failure; c) SB failure; d) MF failure; e) GD failure.

Tab. 4.7 summarizes the failure modes of the specimens.
Shear tests on unaged specimens (T_0), showed that for EPX1 and EPX3 adhesives the failure is adhesive (AF) for the aluminum-float glass specimens, without adhesion to the glass surface. In the case of the EPX2 adhesive, the failure was mixed (MF): a slight TLC cohesive failure accompanied by delamination of the glass could be observed. The aluminum adherend with anodized surface treatment showed a MF failure for all adhesives, with TLC failure accompanied by delamination of the glass. For the cold-painted glass - aluminum configuration, the failure for all specimens was adhesive (AF).
Shear tests on aged (T_{CC}) specimens, showed adhesive (AF) failure type. In some specimens this failure was accompanied by CF or TLC failure modes. In the case of anodized aluminum and float glass, the specimens with EPX1 and EPX2 adhesives presented mixed failures with AF and CF failure combined modes. In the case of EPX3 adhesive, there were different failures with a prevalence of MF consisting of CF or TLC failures with failure of the glass support (SB).

Table 4.7. Summary of failure modes observed in unaged and aged conditions.

Adhesive	*Adherends*	*T_0*	*T_{CC}*	*24 h*	*T_{CC} - 48 h*
EPX 1	Aluminum Float glass	5 AF	5 AF	2 MF: (50% CF + 50% AF) 1 CF 2 MF: (TLC 90% + 10% SB)	2 TLC 1 MF: (30% AF + 70% TLC) 1 MF: (50% AF + 50% CF) 1 MF: (TLC 90% + 10% SB)
	Andodized aluminum Float glass	3 GD 1 MF: (TLC 30% + 70% GD) 1 MF: (TLC 80% + 20% GD)	1 MF: (80% CF+ 20% AF) 2 AF 1 MF: (80% CF + 20% AF) 1 MF: (TLC 90% + 10% GD)	-	-
	Aluminum Float cold-painted glass	5 AF	3 CF 1 MF: (80% CF + 20% AF) 1 MF: (40% AF + 60% CF)	-	-
	Andodized aluminum Float cold-painted glass	2 MF: (60% AF + 40% TLC) 3 MF: (70% + 30% AF TLC)	1 MF: (40% AF + 60% CF) 4 AF	-	-
EPX 2	Aluminum Float glass	1 MF: (TLC 80% + 20% GD) 1 TLC 3 MF: (TLC 80% + 20% GD)	2 MF: (80% AF + 20% TLC) 2 MF: (60% AF + 40% TLC) 1 MF: (60% AF + 40% TLC)	2 MF: (50% + 50% CF AF) 1 CF 2 MF: (TLC 90% + 10% SB)	1 TLC 1 MF: (20% AF + 80% TLC) 3 MF: (80% CF + 20% SB)
	Andodized aluminum Float glass	2 GD 3 MF: (TLC 80% + 20% GD)	2 MF: (80% AF + 20% TLC) 2 MF: (60% AF + 40% TLC) 1 MF: (60% AF + 40% TLC)	-	-
	Aluminum Float cold-painted glass	5 AF	2 AF 2 MF: (85% + 15% CF AF) 1 MF: (95% + 5% CF AF)	-	-
	Andodized aluminum Float glass painted	3 MF: (80% AF + 20% TLC) 2 MF: (60% AF + 40% TLC)	5 CF	-	-
EPX 3	Aluminum Float glass	5 AF	2 MF: (90% CF + 10% CF) 1 AF 1 MF: (60% AF + 40% GD)	2 MF: (50% CF+ 50% AF) 2 CF 1 MF: (TLC 90% + 10% SB)	3 AF 2 MF: (80%CF + 20% AF)

			1 MF: (50% AF + 50% CF)		
	Andodized aluminum Float glass	1 SB 1 AF 3 MF: (TLC 60% + 40% GD)	1 TLC 2 MF: (80% AF + 20% SB) 2 MF: (60% AF + 40% SB) 1 AF	-	-
	Aluminum Float cold-painted glass	5 AF	1 MF: (95%CF + 5% AF) 1 AF 1 MF: (80% CF+ 20% AF) 1 MF: (70% CF+ 30% AF) 1 MF: (70% CF+ 30% AF)	-	-
	Andodized aluminum Float cold-painted glass	3 AF 2 MF: (45% + 55% AF TLC)	2 MF: (20% CF+ 80% AF) 3 AF	-	-

4.9 Conclusions

In the present study, an experimental campaign to study the bonding connection of glass (float glass and cold-painted glass) and two different adherends (raw aluminum and anodized aluminum profiles) through three different epoxy adhesives is proposed. The main purpose is to study the applicability of the adhesive joints to building components (e.g., windows).
The experimental tests included:

- 60 double-lap joints made with aluminum or anodized aluminum profiles and float glass or cold-painted float glass, using three epoxy adhesives tested in shear after 28 days curing phase in laboratory conditions;
- 60 double-lap joints made with aluminum or anodized aluminum profiles and float glass or cold-painted float glass, using three epoxy adhesives tested in shear after 28 days curing phase and subsequent aging in climatic chamber for 6 months;
- 15 double-lap joints made with aluminum and float glass adherends, and with three epoxy adhesives tested in shear after 24 hours curing phase;
- 15 double-lap specimens made with aluminum profiles and float glass, using three adhesives. Shear tests took place after 24 hours curing phase and subsequent 48 hours aging in a climatic chamber.

The main outcomes are:

- EPX1 adhesive exhibited great stiffness values (k_{max} = 79807 kN/mm) to 28 days after maturation (T_0). It is the most affected adhesive from the effects of aging (T_{CC} – kmax = 9716 kN/mm);
- EPX2 adhesive, to the different aging conditions, for all tested configurations and maturation, shows great stiffness values (k_{max} = 118363 kN/mm);
- EPX3 adhesive, despite it was able to achieve great stiffness values (k_{max} = 179160 kN/mm), showed an irregular mechanical behavior.
- Joints made with anodized aluminum and float glass were the best in terms of stiffness, for all adhesives in unaged conditions (T0);
- Artificial aging T_{CC} (exposure to aggressive environment with a constant temperature of 40 °C and 100% RH) leads to a reduction of the loading carrying capacities for all adhesives. In fact, ultimate strength decreases up to 90% in the case of EPX1 A decay in adhesion between the materials could be observed;
- Artificial aging T_{CC} – 48h with 48-hour exposure to 50 °C and 100% relative humidity, allows to speed up the curing phase of the adhesive, worsening the other hand, in the case of the EPX1 adhesive the mechanical performance of the joint (up to 41% of the ultimate strength);
- Comparing the failure modes, it could be observed that in the case of raw aluminium adherends the failure modes are different depending on the adhesive. EPX2 adhesive showed better adhesion to different materials. The configuration with anodized aluminum adherends, for all adhesives, showed greater adhesion. In the case of cold-painted glass adherends, AF (adhesive failure) modes were observed.

The configurations which showed the best mechanical performance are those with anodized aluminum profiles. Tests at high temperature (T_{CC} – 48h), performed in order to accelerate the adhesive maturation process, showed relevant results for EPX2 adhesive. This aging

mode improved its stiffness (+75%) and ultimate strength (+33%) if compared with the shear test results after 24 hours curing phase.
In summary, for the purposes of the applicability of adhesive joints for the construction of building components, the EPX2 adhesive proved to be the most suitable adhesive in terms of load-bearing capacity and maintenance of the mechanical performance under artificial aging.

4.10 References

[1] F. Marchione, P. Munafò, Experimental strength evaluation of glass/aluminum double-lap adhesive joints, J. Build. Eng. 30 (2020). https://doi.org/10.1016/j.jobe.2020.101284.

[2] F. Oikonomopoulou, T. Bristogianni, L. Barou, F.A. Veer, R. Nijsse, The potential of cast glass in structural applications . Lessons learned from large-scale castings and state-of-the art load-bearing cast glass in architecture, J. Build. Eng. 20 (2018) 213–234. https://doi.org/10.1016/j.jobe.2018.07.014.

[3] F. Oikonomopoulou, T. Bristogianni, F.A. Veer, R. Nijsse, The construction of the Crystal Houses façade: challenges and innovations, Glas. Struct. Eng. 3 (2018) 87–108. https://doi.org/10.1007/s40940-017-0039-4.

[4] H. Schober, J. Schneider, S. Justiz, J. Gugeler, C. Paech, M. Balz Innovations with Glass, Steel and Cables Glass Performance Days, Tampere, Finland (2007), pp. 198-201, (n.d.).

[5] T. Alderucci, V. Terlizzi, S. Urso, C. Borsellino, P. Munafò, International Journal of Adhesion and Adhesives Experimental study of the adhesive glass-steel joint behavior in a tensegrity fl oor, Int. J. Adhes. Adhes. 85 (2018) 293–302. https://doi.org/10.1016/j.ijadhadh.2018.04.017.

[6] V. Alexandru, G. Kolany, B. Freytag, J. Schneider, O. Englhardt, Adhesively bonded glass-metal façade elements with composite structural behaviour under in-plane and out-of-plane loading, Eng. Struct. 200 (2019) 109692. https://doi.org/10.1016/j.engstruct.2019.109692.

[7] P. Munafò, F. Stazi, INVISIBLE WINDOW FRAME, European Patent 3071775, 2013.

[8] P. Munafò, Solaio Tensegrale, 00014426973, 2014.

[9] E. Eriksson, J & Ludvigsson, M & Dorn, Michael & Enquist, Bertil & Serrano, Load bearing timber glass composites – A WoodWisdom-Net project for innovative building system, in: COST Action TU0905 Mid-Term Conf. Struct. Glas., 2013: p. 269. https://doi.org/http://dx.doi.org/10.1201/b14563-38.

[10] Ž. Unuk, A. Ivanič, V.Ž. Leskovar, M. Premrov, S. Lubej, International Journal of Adhesion and Adhesives Evaluation of a structural epoxy adhesive for timber-glass bonds under shear loading and different environmental conditions, Int. J. Adhes. Adhes. 95 (2019) 102425. https://doi.org/10.1016/j.ijadhadh.2019.102425.

[11] K. Rodacki, M. Tekieli, K. Furtak, Contactless optical measurement methods for glass beams and composite timber-glass I-beams, Measurement. 134 (2019) 662–672. https://doi.org/10.1016/j.measurement.2018.09.061.

[12] M. Giampaoli, V. Terlizzi, M. Rossi, G. Chiappini, P. Munafò, Mechanical performances of GFRP-steel specimens bonded with different epoxy adhesives, before and after the aging treatments, Compos. Struct. 171 (2017) 145–157. https://doi.org/10.1016/j.compstruct.2017.03.020.

[13] K. Machalická, M. Eliášová, Adhesive joints in glass structures: effects of various materials in the connection, thickness of the adhesive layer, and ageing, Int. J. Adhes. Adhes. 72 (2017) 10–22. https://doi.org/10.1016/j.ijadhadh.2016.09.007.

[14] M. Overend, Q. Jin, J. Watson, International Journal of Adhesion & Adhesives The

selection and performance of adhesives for a steel – glass connection, Int. J. Adhes. Adhes. 31 (2011) 587–597. https://doi.org/10.1016/j.ijadhadh.2011.06.001.
[15] C. Richter, B. Abeln, A. Geßler, M. Feldmann, International Journal of Adhesion & Adhesives Structural steel – glass facade panels with multi-side bonding – Nonlinear stress – strain behaviour under complex loading situations, Int. J. Adhes. Adhes. 55 (2014) 18–28. https://doi.org/10.1016/j.ijadhadh.2014.07.004.
[16] T. Alderucci, M. Rossi, G. Chiappini, P. Munafò, Effect of different aging conditions on the shear performance of joints made between GFRP and glass with a UV absorbance coating, Int. J. Adhes. Adhes. 94 (2019) 76–83. https://doi.org/10.1016/j.ijadhadh.2019.05.009.
[17] Y. Zhang, A.P. Vassilopoulos, T. Keller, Environmental effects on fatigue behavior of adhesively-bonded pultruded structural joints, Compos. Sci. Technol. 69 (2009) 1022–1028. https://doi.org/10.1016/j.compscitech.2009.01.024.
[18] Y. Zhang, A.P. Vassilopoulos, T. Keller, Effects of low and high temperatures on tensile behavior of adhesively-bonded GFRP joints, Compos. Struct. 92 (2010) 1631–1639. https://doi.org/10.1016/j.compstruct.2009.11.028.
[19] B. Van Lancker, J. Dispersyn, W. De Corte, J. Belis, Durability of adhesive glass-metal connections for structural applications, Eng. Struct. 126 (2016) 237–251. https://doi.org/10.1016/j.engstruct.2016.07.024.
[20] ASTM D3528-96(2016), Standard Test Method for Strength Properties of Double Lap Shear Adhesive Joints by Tension Loading, ASTM International, West Conshohocken, PA, 2016, www.astm.org, (2016).
[21] ASTM D638-14, Standard Test Method for Tensile Properties of Plastics, ASTM International, West Conshohocken, PA, 2014, www.astm.org, (2014).
[22] ISO 6270-2. Paints and varnishes — determination of resistance to humidity — Part 2: procedure for exposing test specimens in condensation water atmospheres, (2005).
[23] ASTM D5573-99(2019), Standard Practice for Classifying Failure Modes in Fiber-Reinforced-Plastic (FRP) Joints, ASTM International, West Conshohocken, PA, 2019, www.astm.org, (n.d.). http://www.astm.org/cgi-bin/resolver.cgi?D5573.

4.11 List of figures and tables

Figure 4.1. Scheme of the mobile frame referring to EP 3071775B1..... 46
Figure 4.2. Double lap specimens' geometry (mm), section and plan view. 50
Figure 4.3. Assembly phase. 51
Figure 4.4. Angelantoni "CST-130S model Climatic chamber..... 52
Figure 4.5. Shear test setup. 53
Figure 4.6. Load displacement curves for: (a) aluminium-float glass, unaged; (b) aluminium-float glass, unaged; (c) anodized aluminium-float glass, unaged; (d) anodized aluminium-painted glass, unaged. 55
Figure 4.7. Load displacement curves for: (a) aluminium-float glass, T_{CC}; (b) aluminium-float glass, T_{CC}; (c) anodized aluminium-float glass, T_{CC}; (d) anodized aluminium-painted glass, T_{CC}. 57
Figure 4.8. Load displacement curves for aluminium-float glass specimen after 24h maturation..... 58
Figure 4.9. Load displacement curves for aluminum - float glass $T_{CC\text{-}48h}$ aged joints. 58
Figure 4.10. Failure modes of single lap adhesive joints: a) AF failure; b) CF failure; c) SB failure; d) MF failure; e) GD failure. 64

Table 4.1. Glass and aluminum mechanical properties according to manufacturer's data sheet. 48
Table 4.2. Technical and mechanical characteristics of the adhesives reported by manufacturers. 49
Table 4.3. Mechanical properties of aluminum-float glass double-lap joints bonded with three different epoxy adhesives: results before (T_0) and after (T_{CC}, $T_{CC\text{-}24h}$) the aging treatments. 60
Table 4.4. Mechanical properties of anodized aluminum-float glass double-lap joints bonded with three different epoxy adhesives: results before (T_0) and after (T_{CC}) the aging treatment. 61
Table 4.5. Mechanical properties of aluminum-cold-painted float glass double-lap joints bonded with three different epoxy adhesives: results before (T_0) and after (T_{CC}) the aging treatment. 62
Table 4.6. Mechanical properties of anodized aluminum-cold-painted float glass double-lap joints bonded with three different epoxy adhesives: results before (T_0) and after (T_{CC}) the aging treatment. 63
Table 4.7. Summary of failure modes observed in unaged and aged conditions. 65

Chapter 5.

Effect of temperature and relative humidity on the shear performance of double-lap adhesive joints between steel and glass adherends

The aim of the reported experimental campaign is to evaluate the mechanical performance of adhesive joints between steel and glass adherends, both after curing under laboratory conditions and artificial ageing, for applications in the field of civil engineering (Tensegrity Floor). The content of this chapter has been published in a previous work, reported in Ref. [1].

5.1 Abstract

The use of large glass areas is a hallmark of modern architecture, and glass is also used as a structural element in many applications. Recent developments in the field of structural adhesives have led to the development of bonding solutions between steel and glass adherends that meet the structural and aesthetic requirements for high performance buildings. Indeed, the use of adhesive bonding technology allows for uniform stress distribution, enabling ductile hybrid joints to be achieved by combining materials with different mechanical properties. However, the main weakness of this assembly system is the influence of high values of temperature and humidity values on the mechanical behaviour of bonded joints. This paper reports the experimental results obtained on double-lap adhesive joints between steel and float glass adherends. In particular, the results obtained after curing under laboratory conditions are compared with those obtained after exposure to high temperature (40 °C) and relative humidity (100% RH). The performances obtained with two two-component epoxy adhesives (EPX1, EPX2), one polyurethane adhesive (PU) and one silicone adhesive (SIL) are compared and discussed. The results of the experimental campaigns show that the epoxy adhesives achieve the best mechanical performance in relation to the studied application, while the SIL adhesive exhibits the worst mechanical performance in each case.

Nomenclature

A_t	Application temperature	T_{CC}	Artificial aging in climatic chamber
AF	Adhesive failure	T_g	Glass transition temperature
CF	Cohesive failure	W_t	Working time
GF	Glass failure	α	Thermal coefficient of expansion
MF	Mixed failure	ε_t	Tensile strain
EPX1	First Epoxy Adhesive	σ_t	Tensile strength
EPX2	Second Epoxy Adhesive	σ_c	Compressive strength
PU	Polyurethane Adhesive	σ_{yk}	Yield stress
SIL	Silicone	τ	Shear strenght
E_t	Young Modulus in tension	k	Stiffness
F_{max}	Ultimate load	γ	Shear strain at failure
S_t	Service temperature	s	Ultimate displacement
T_0	Un-aged condition		

5.2 Introduction

The use of adhesive joints is an increasingly popular alternative to traditional mechanical joining methods, due to the many advantages they offer, such as low cost, reduced machining effort, high strength-to-weight ratio, lower and more uniform stress distribution [2,3]. Thanks to these aspects, adhesive bonding technology has been widely used in various industrial fields, such as naval [4], automotive [5] and civil engineering [6]. The use of large glass surfaces and transparent spaces is now a defining feature of modern architecture. This trend makes glass a widely used material, both for curtain walls and for the construction of new buildings [7], floors and elements with a purely structural function [8].

There are numerous examples of the use of sealants in curtain wall construction. However, silicone adhesives only allow to create simple supports, since they do not allow to obtain structurally cooperating ductile hybrid structures. In fact, structures using such sealants exhibit high displacements and very low failure loads [9]. The development of research in the field of structural adhesives - e.g. acrylic, polyurethane and epoxy adhesives - has made it possible to combine materials with different mechanical properties and to create ductile and cooperating structures [10,11].

Silvestru et al. [12] investigated linear adhesive joints between steel and glass adherends using acrylic adhesives. In addition, the influence of different joint sizes on the stress-strain properties of the adhesive in glass-to-metal joints under shear and tensile loads is investigated. The best results in terms of adhesion are obtained on stainless steel surfaces.

Machalická and Eliasova [13] carried out an experimental analysis of adhesive joints in glass structures with regard to the influence of various adherends (glass, stainless steel, aluminium) and their surface treatment (sandblasting for the glass surface) on the adhesion of selected adhesives. The results show that sandblasting of the glass surface can improve the adhesion and thus the strength values of an adhesive joint where cohesive failure is not achieved with a smooth glass surface.

Overend et al. [14] investigated the application of adhesive bonding to curtain walls consisting of glass panels applied on a metal substructure. Five adhesives for steel-glass joints were tested using experimental testing and numerical modelling.

Despite the many advantages of adhesive technology, exposure to severe environmental conditions (e.g., high temperatures, relative humidity, UV light) is a major weakness of this joining system. Maintaining mechanical performance over time, in relation to various environmental conditions is a fundamental element of proper adhesive joint design.

The study of the mechanical behaviour of adhesive joints exposed to severe environmental conditions is particularly complicated when the degradation phenomena such as temperature and relative humidity occur simultaneously [10,15,16]. As stated in previous studies by Ashcroft et al. [17], Bowditch [18], the mechanical performance of structural adhesives can be severely affected by exposure to moisture due to the possible permeation of water molecules into the adhesive layer. In fact, high values of relative humidity determine the absorption of water by the adhesive layer, which is the main cause of the reduction of the internal cohesive forces of the polymer and, consequently, of the characteristic Tg value of the adhesive [19,20]. Another effect of moisture is the possible premature failure of the adhesive joint due to the migration of water towards the interface between the adhesive and the glass substrate, as in Ref. [10].

Studies by Davis et al. [21] investigated the residual strengths and failure times of adhesive joints between steels with different surfaces finishes and epoxy adhesives that were both loaded and unloaded and exposed to elevated temperatures for 2.5 years. The results showed that all unloaded joints survived ageing, while loaded joints exhibited a significant decrease in failure time and residual strength as a function of loading level. A further result is the increased durability of joints with low Tg adhesives, which provide greater protection of the adhesive interface from corrosion.

Bowditch [18] conducted studies on butt joints between mild steel adhesives bonded with epoxy-amine adhesive. The results showed a cohesive failure mode and a significant effect of environmental conditions on adhesive creep under load.

The effects of surface treatment of steel joints were tested by Fay e Maddison [22], on joints exposed to severe environmental conditions (100% RH and temperatures between 42-48 °C every 30 minutes). The results showed that the surface treatment affects the mechanical behaviour of the joint also in terms of failure time.

Exposure to high/low temperature cycling and UV radiation was investigated by Van Lancker et al. [23] on glass–steel adhesive joints.

Calvez et al. [24] studied the durability of galvanised steel joints bonded with hardened epoxy adhesives under the influence of temperature and humidity. The effect of hydrothermal ageing on the adherend and adhesive properties was first determined and then correlated to the durability of the bonded joints. The mechanical properties of the adhesive joints were evaluated by a shear stress–strain analysis on single–lap joints. The experimental results showed a loss of adhesion during ageing.

Despite numerous studies on the subject, relatively few data are available to date on the mechanical behaviour of adhesive joints between glass and steel adhesives, particularly with respect to durability. This is due to the highly nonlinear properties of polymers (adhesives) in relation to mechanical and environmental stresses [25,26].

The presented work consists of an experimental campaign aimed at investigating the effects of exposure to high values of temperature and relative humidity (40 °C and 100% RH) on the mechanical performance of adhesive joints between steel and float glass adherends. In particular, the present study contributes to the research on the applicability of adhesive bonding for innovative building elements. The experimental campaign presented here evaluates the compatibility of the tested adherends and adhesives for the construction of a novel tensegrity floor – Patent No. 00014426973 [27] – characterised by a glass floor that cooperates with the metal substructure through the use of structural adhesives (Fig. 5.1).

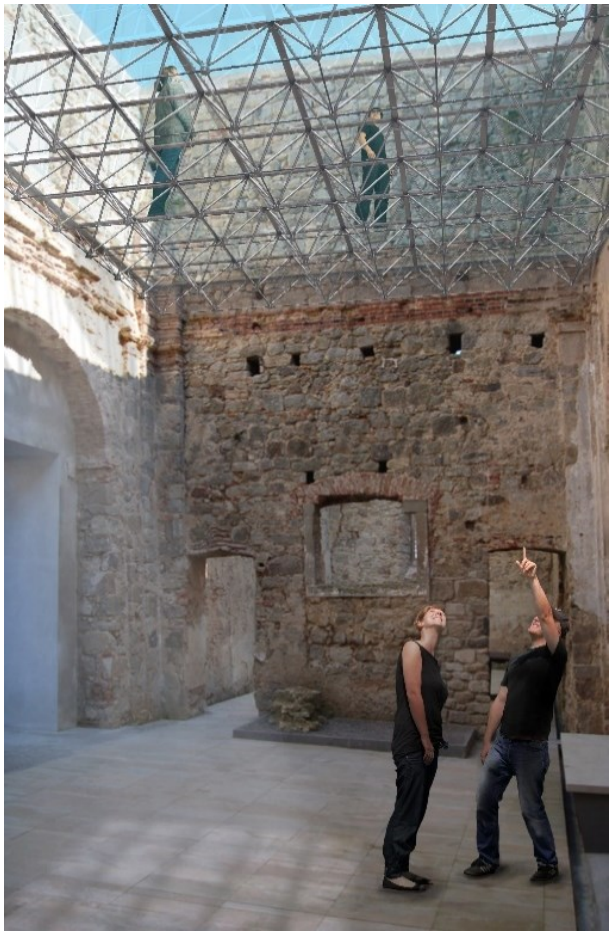

Figure 5.1. Tensegrity floor, rendering

5.3 Materials and methods

The experimental campaign described in the following is composed of two series of shear tests on double-lap specimens with steel and glass adherends, after curing under laboratory conditions and after exposure to severe environmental conditions, respectively. The mechanical compatibility between the joined materials and the global performance of the joints are investigated by analysing the ultimate strength, ultimate displacements and, consequently, the ductility.

5.3.1 Materials properties

This section describes the mechanical properties of the materials used in the experimental campaign described below.

5.3.1.1 Adherends

Two different substrates were used in the present work, namely: transparent float glass panels supplied by Vetreria Incicco (Italy) and steel profiles, supplied by METAG (Italy). The mechanical properties of the materials are listed in the data sheets provided by the manufacturers in Tab. 5.1.

Table 5.1. Mechanical characteristics of the adherends reported by manufacturers.

GLASS*			**STEEL PROFILES (S360JR) ****			
α ($°C^{-1}$)	E_t (GPa)	σ_t (MPa)	α ($°C^{-1}$)	E_t (GPa)	σ_{yk} (MPa)	σ_t (MPa)
9×10^{-6}	75	40	2.30×10^{-5}	210	355	510

*according to CNR-DT 210/2013 standard [28]
** according to EN 10025-2:2004 standard [29]

5.3.1.2 Adhesives

Four commercial structural adhesives were selected for the experimental campaign described below, namely: 3M™ Scotch-Weld™ 7260 B/A (**EPX1**), 3M™ Scotch-Weld™ 7240 B/A (**EPX2**), 3M™ Scotch-Weld™ DP6310NS (**PU**), Dow Corning TM 895 Structural Glazing Sealant (**SIL**). This selection was made considering their different mechanical and chemical properties in terms of elastic modulus, ultimate strength, and glass transition temperature. Table 5.2 shows the mechanical properties given by the manufacturers in the technical data sheets.

Table 5.2. Mechanical characteristics of the adhesives reported by manufacturers.

Adhesive	EPX 1	EPX 2	PU	SIL
Chemical base	Two-part epoxy	Two-part epoxy	Two-part polyurethane	One-part silicone sealant
Viscosity	Thixotropic	Thixotropic	Non-sag paste	Pasty
W_t (min)	90÷300	16	10	15
A_t (°C)	15÷25	15÷25	-	15÷30
T_g (°C)	61.07	66.87	60	-
S_t (°C)	-50÷120	-40÷80	-40÷180	-50÷150
τ*(MPa)	33.50	29.40*	24.82*	-
E_t (MPa)	3000	1500	600	1
ε_t **(%)	3	-	12	600
Use	Structural	Semi-Structural	Semi-Structural	Structural

* On aluminium-steel adherends
**At failure.

5.3.2 Specimens' geometry

In the present study, double-lap adhesive joints are considered. The choice of specimen geometry was derived from the possibility that this configuration minimises bending stresses due to its geometric symmetry. The test specimens were assembled in accordance with the ASTM D3528-16 [30]. Five specimens were prepared for each combination of adhesives, adherends and ageing methods.
The dimensions of the glass panels are 200 mm × 100 mm; the width of the steel profiles is 25.40 mm, with a length of 140 mm. All the adherends have a thickness of 5 mm. The single bonding region has a dimension of 25.40 mm × 12.70 mm, as specified in ASTM D3528-16 [30].
The thickness of the adhesives used was set at 0.30 mm for the epoxy adhesives and 2 mm for the silicone adhesive, as recommended by the manufacturers. The geometry of the test specimens is shown in Fig. 5.2. No chemical treatments were applied to the adherends surfaces. Before the bonding phase, the steel adherends were treated by manual sandblasting with sandpaper with a grain size of 120 (P120) in the bonding region, and all surfaces of both steel and glass adherends were cleaned with denatured isopropyl alcohol.

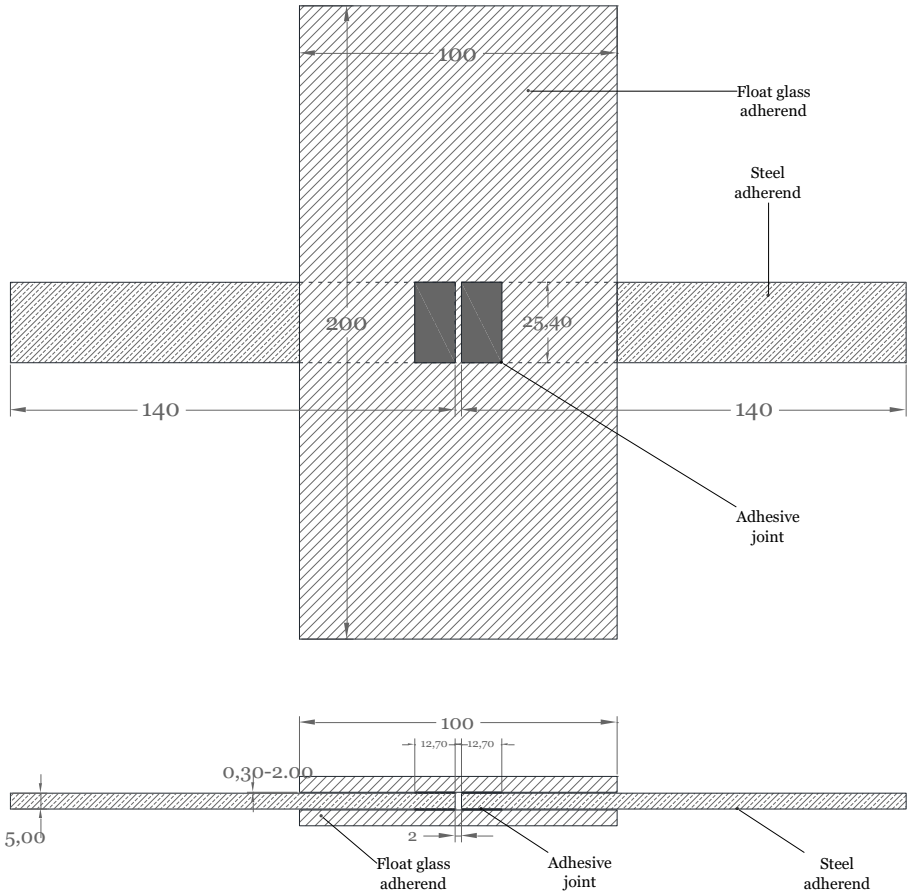

Figure 5.2. Double-lap specimen geometry (mm) ; section and plan view.

5.3.3 Artificial ageing

The artificial ageing was carried out following the specifications of ISO 6270-2 [31]. After the first ageing phase of 28 days under laboratory conditions (20 ± 1 °C, 50 % RH), the specimens were subjected to an exposure period of 3 months under severe environmental conditions (40 ± 2 °C, 98 ± 3 % RH). This experimental phase was carried out in a climatic chamber of the "Angelantoni" CST-130S type.

5.3.4 Test setup

The tests carried out in this experimental campaign aim to determine the mechanical properties of the joints tested through shear tests. The tests are carried out in accordance with ISO 4587 [32]. All tests were carried out using a Zwick/Roell Z050 tensile machine, with a capacity of 50 kN. All tests were carried out under ambient conditions of 20°C and 50% RH. The load speed rate, as specified by the standard, is 1.27 mm/min. An optical measurement method based on stereoscopic calculation with a geometric grid was used to acquire the displacement values. Two CMOS cameras with a resolution of 1280 × 1024 pixels (Pixelink®B371F) with different angles were installed to capture stereoscopic images at a rate of 2 frames/second. The experimental setup is shown in Fig. 5.3.

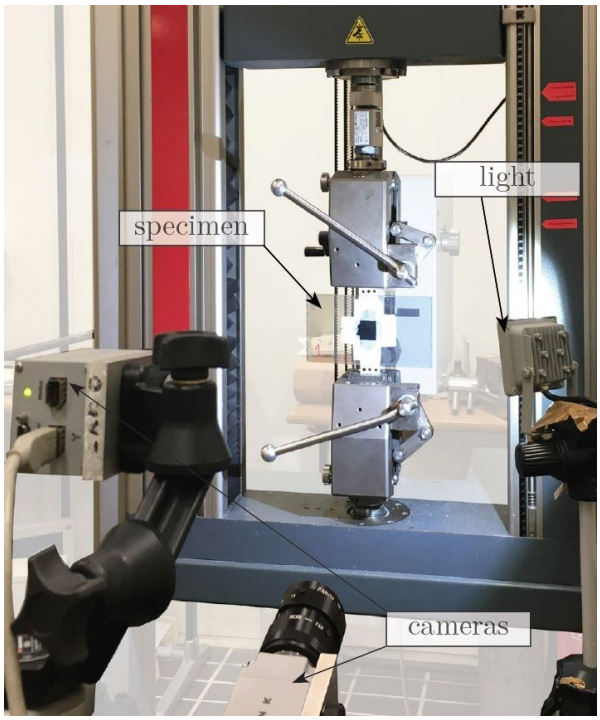

Figure 5.3. Shear test setup.

5.4 Results and discussion

In this section, load-displacement graphs and failure modes are reported and discussed. Results are analysed in terms of mean values for ultimate strengths, ultimate displacements, and global stiffnesses. The average results are obtained by averaging all obtained experimental values. No experimental values were excluded as the observed data scatter was very low.

5.4.1 Mechanical performances

Fig. 5.4 shows the average load-displacement graphs for double-lap joints between steel and float glass adherends after curing under laboratory conditions (T_0).

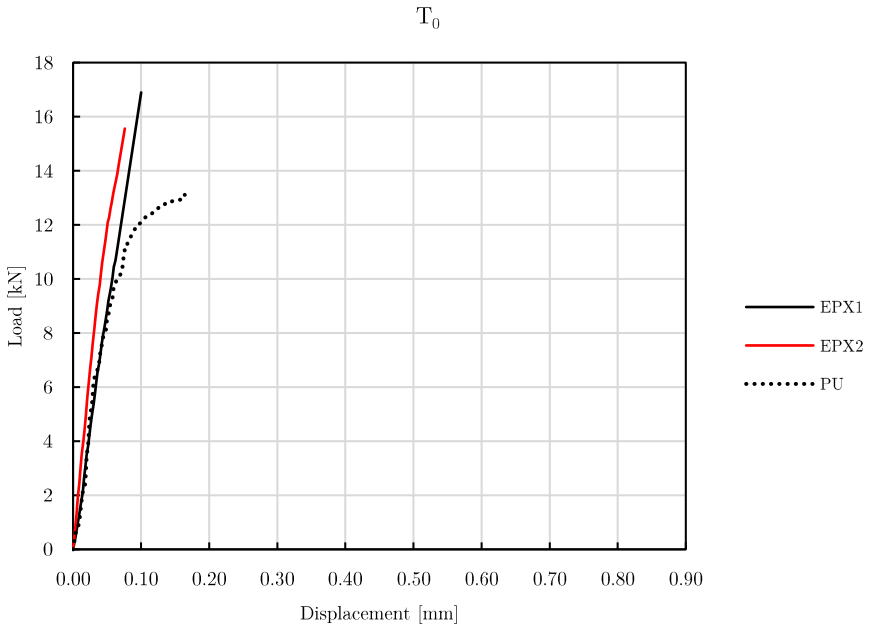

Figure 5.4. Average load-displacement curves of double-lap joints after maturation under laboratory conditions (EPX1, EPX2, PU adhesives).

Fig. 5.5 shows the average graphs obtained from the test specimens after exposure to different temperature and relative humidity values (T_{CC}).

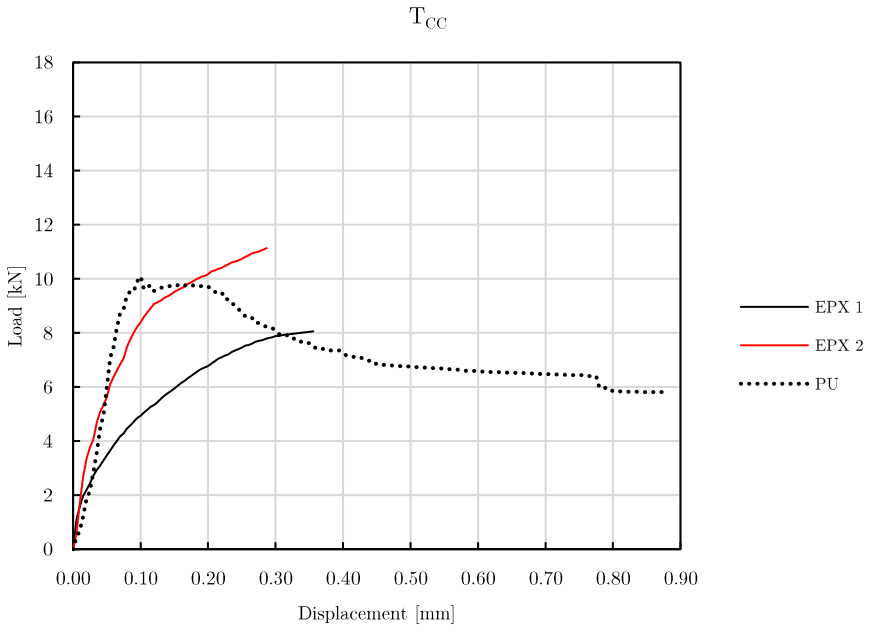

Figure 5.5. Average load-displacement curves of double-lap joints after maturation and artificial ageing in climatic chamber (EPX1, EPX2, PU adhesives).

Fig. 5.6 shows the load-displacement diagrams for the SIL adhesive under the different curing conditions.

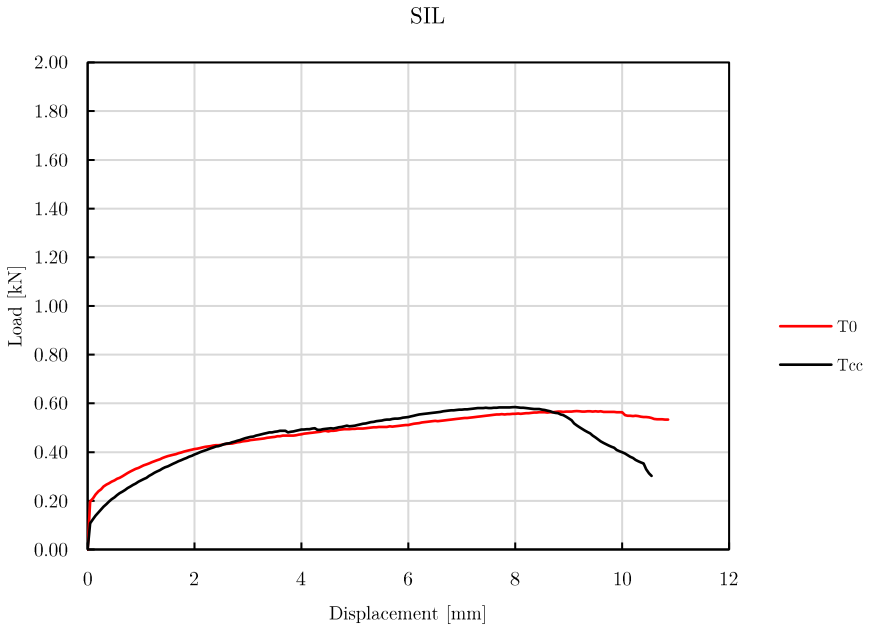

Figure 5.6. Load-displacement curves for SIL adhesive after different aging conditions.

Table 5.3 summarises the mechanical parameters measured. The obtained results are compared in terms of strength and ultimate displacements, as well as global stiffness of the joint. In particular, the stiffness - equal to the ratio between force and displacement - is calculated in the first linear section of each curve, before the nonlinearity due to the initiation of the damage in the adhesive joint occurs.

Table 5.3. Mechanical properties of steel-float glass double-lap adhesive joints.

Adhesive	*Aging condition*	F_{max} *(kN)*	*s* (mm)*	*τ* (MPa)*	*g* (-)*	*k (kN/mm)*
EPX1	T_0	16.89 ± 2.34	0.10 ± 0.03	21.33 ± 8.12	0.10 ± 0.04	191.17 ± 48.07
	T_{CC}	8.06 ± 1.56	0.36 ± 0.05	12.48 ± 2.42	0.59 ± 0.08	84.97 ± 33.25
EPX2	T_0	15.56 ± 2.06	0.07 ± 0.01	24.12 ± 3.19	0.13 ± 0.03	255.50 ± 54.67
	T_{CC}	10.17 ± 2.18	0.28 ± 0.19	15.76 ± 3.38	0.48 ± 0.33	136.01 ± 13.54
PU	T_0	13.11 ± 0.64	0.16 ± 0.03	20.15 ± 0.88	0.27 ± 0.06	186.88 ± 42.64
	T_{CC}	11.30 ± 1.29	0.88 ± 0.49	17.52 ± 2.00	1.47 ± 0.82	161.00 ± 7.80
SIL	T_0	0.58 ± 0.09	10.86 ± 2.44	0.89 ± 0.14	18.10 ± 4.06	0.26 ± 0.11
	T_{CC}	0.62 ± 0.88	10.54 ± 0.70	0.90 ± 0.12	17.56 ± 3.19	0.24 ± 0.04

*at failure

The joints tested after curing under laboratory conditions achieved very high failure loads in the case of EPX and PU joints. In particular, EPX1 adhesive shows the highest ultimate load (16.89 kN), while all EPX adhesives and PU adhesive show comparable failure loads, much higher than SIL adhesive (up to +3148% in the case of EPX1 adhesive). The EPX and PU adhesives showed high average stiffness values. The EPX2 adhesive exhibited the highest average stiffness of 255.50 kN/mm and the lowest displacement. The EPX1 and EPX2 adhesives exhibited near linear behaviour, while the PU adhesive exhibited initial linear trend, followed by a non-linear stretch at damage initiation. The SIL silicone adhesive showed very high displacements (10.86 mm) and a very low ultimate load (0.58 kN). The results obtained in this phase show that structures with high load bearing capacities could be obtained with the tested adherends and adhesives combinations. Moreover, depending on the properties of the adhesive, it is possible to obtain joints with more or less ductile overall behaviour, depending on the intended applications.

Prolonged exposure (3 months) to severe environmental conditions (40 ± 2 °C, 98 ± 3 % RH) negatively affected the mechanical performance of the joints considered (Fig. 5.5). Three out of four of the tested adhesives showed a significant reduction of the ultimate load (-52%, -35% and -14% for EPX1, EPX2 and PU, respectively) and a significant increase of the ultimate displacements, resulting in a decrease in stiffness. Artificial ageing resulted in a decrease in stiffness for the three adhesives EPX1, EPX2, PU (-56%, -53% and -23% respectively). In particular, the PU adhesive showed the highest average failure load (11.30 kN), and the lowest reduction in the ultimate load (-14%) and stiffness (-23%) compared to the laboratory conditions. The trend of the curves showed an initial linear behaviour for EPX2 and PU, while EPX1 showed a nonlinear behaviour on average. The PU adhesive showed – after the initial elastic strain – a plastic behaviour with a decreasing trend of the load-

displacement curve, characterised by high plastic deformations, with the largest ultimate displacements (0.88 mm) recorded while the smallest displacement is registered by the EPX2 adhesive. The SIL adhesive showed the worst mechanical performance, with high displacements even after artificial ageing (10.54 mm), in correlation with reduced maximum load values. In general, with the exception of the SIL adhesive, ageing leads to an increase in the global ductility of the bonded joint, as the observed fracture loads decrease, and the fracture displacements increase.
High relative humidity has a negative effect on the mechanical performance of the joints due to the polarity of the water that can penetrate the polymeric materials, as in Ref. [17,33,34]. This can lead to a decrease in the mechanical properties of the adhesive and make it more deformable, as the glass transition temperature decreases due to the reduction of cohesive forces in the polymer chains of the adhesive. Another effect of temperature and relative humidity is hydrolysis within the adhesive layer, which is reflected in the more cohesive failure modes highlighted in the following section.

5.4.2 Failure modes

After the shear tests, all tested specimens were analysed to describe their particular failure modes. To highlight the different types of failure, reference is made to standard ASTM D 5573-99 [35]. Fig. 5.7(a-e) shows the different failure modes observed:

- **Adhesive Failure** (AF). Failure of the adhesive joint, with the adhesive remaining adherent to the surface of the glass or substrate; no adhesion on the opposite side;
- **Cohesive Failure** (CF). The separation takes place within the adhesive layer, which remains on both surfaces of the adherends;
- **Mixed Failure** (MF). Combination of one or more of the above mentioned failure modes (e.g., AF and LFTF).
- **Glass Failure** (GF), failure of the glass adherends.

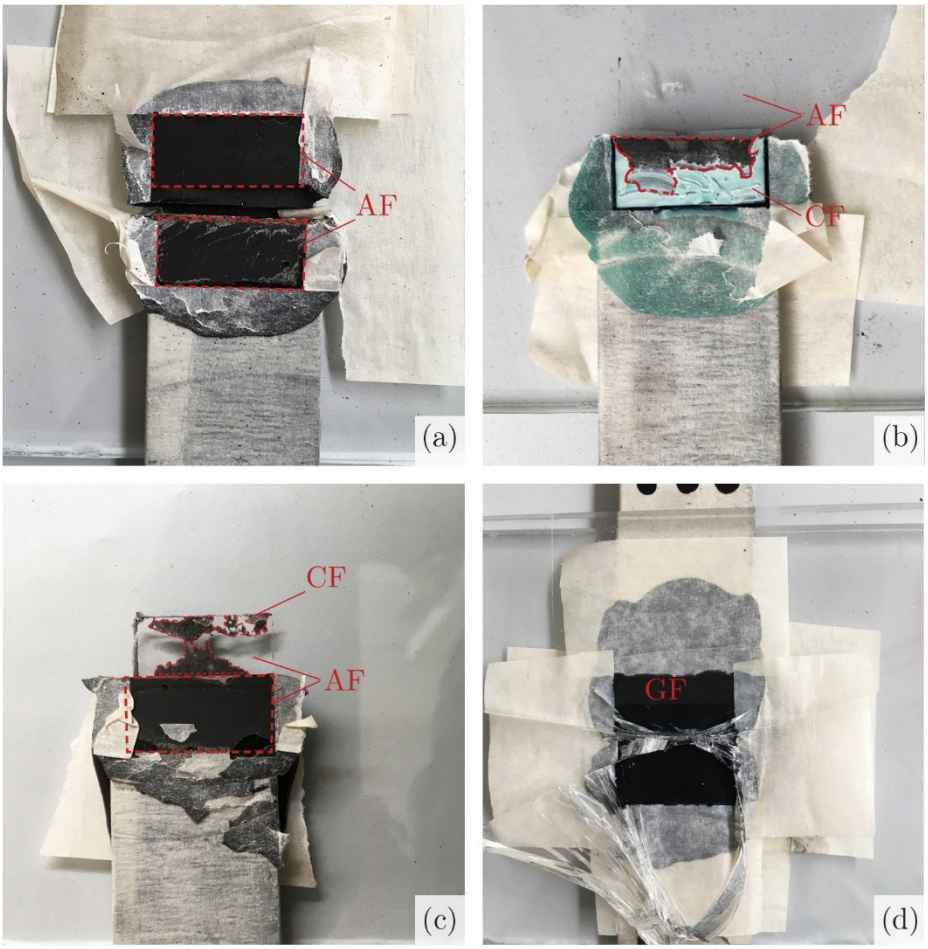

Figure 5.7. Failure modes: a) Adhesive failure (AF); b) and c) Mixed Failure (MF); d) Glass Failure (GF).

Table 5.4 summarises the failure modes of the tested specimens. A mixed failure (MF) mode was observed in most of the tested specimens.

The specimens assembled with the stiffest EPX1 adhesive are the only ones exhibiting 40% of GF failure in both curing conditions. The combinations obtained with the other adhesive types showed a predominant MF failure mode, with high percentages of AF adhesive failure. In particular, it is found that artificial ageing has no significant effect on the failure mode for the EPX1 and SIL adhesives compared to the joints cured under laboratory conditions. In contrast, EPX2 and PU adhesives show an improvement in failure modes, with increasing CF failure modes values. This can be attributed to hydrolysis-induced changes in the polymer microstructure of the adhesive when exposed to high temperatures and relative humidity for a prolonged period. This aspect leads to a reduction in mechanical properties and a cohesive

failure mode (CF). As shown by further studies - also for different substrates [36,37], [38,39] – the adhesion forces between adhesive and substrate may be severely affected by the action of moisture. Indeed, migration of water from the polymer into the adhesive-substrate interface is observed, promoting premature failure of the joint.
The mechanical performance of adhesive joints subjected to severe conditions can be greatly improved using primers or chemical treatments of the adhesive surfaces.

Table 5.4. Failure modes.

Adhesive	*Ageing condition*	*Failure modes*
EPX 1	T_0	2 GF 3 AF
	T_{CC}	3 AF 2 GF
EPX 2	T_0	3 AF 1 MF:(97% AF + 3% CF) 1 MF:(75% AF + 25% CF)
	T_{CC}	2 MF:(80% AF + 20% CF) 1 MF:(75% AF + 15% CF) 1 MF:(60% AF + 40% CF) 1 MF:(70% AF + 30% CF)
PU	T_0	4 AF 1 MF:(70% AF + 30% CF)
	T_{CC}	2 AF 1 MF:(75% AF + 15% CF) 1 MF:(90% AF + 10% CF) 1 MF:(82% AF + 12% CF)
SIL	T_0	5 AF
	T_{CC}	5 AF

5.5 Conclusions

In the present work, the mechanical properties of adhesive joints between float glass and steel adherends are investigated using different structural adhesives. The aim is to verify the compatibility of the structural system and the applicability of adhesive bonding in new building components. Four different adhesives, two epoxy, one polyurethane and one silicone, were tested in shear in double-lap adhesive joints. The mechanical parameters investigated are failure loads, ultimate displacements and global joint stiffnesses. In order to investigate the effects of exposure to high temperature and relative humidity, the joints were subjected to accelerated ageing according to ISO 6270-2 [19].
The main results are:

- The best mechanical performance in terms of ultimate load and strength is achieved with EPX1 and EPX2 epoxy adhesives, under laboratory conditions;
- The best performance in terms of loads in TCC condition is achieved by PU adhesive;
- Silicone adhesive (SIL) has not proven to be suitable for structural applications, due to high deformation (more than 10 mm) at low load compared to the other adhesives;
- Artificial ageing leads to a reduction in ultimate strengths and stiffnesses for all adhesives tested, except for SIL which has a slight improvement in mechanical performance. However, EPX1, EPX2, PU adhesives retain a mechanical behaviour suitable to ensure functionality for the intended applications.

The results obtained underline the applicability of the combination of the adherends and adhesives for the purposes considered. In particular, by using PU adhesives it is possible to realise joints characterised by a lower load-bearing capacity and a higher ductility, especially in aged conditions. By using EPX adhesives, it is possible to assemble rigid joints, characterised by high ultimate strength and stiffness.

5.6 References

[1] F. Marchione, G. Chiappini, P. Munafò, Effect of temperature and relative humidity on the shear performance of double-lap adhesive joints between steel and glass adherends, J. Build. Eng. 45 (2022) 103546. https://doi.org/10.1016/j.jobe.2021.103546.

[2] R.D. Adams, J. Comyn, W.C. Wake, Structural adhesive joints in engineering, Chapman and Hall, 1997.

[3] F. Marchione, Stress distribution in double-lap adhesive joints: Effect of adherend reinforcement layer, Int. J. Adhes. Adhes. 105 (2021). https://doi.org/10.1016/j.ijadhadh.2020.102780.

[4] M. Ortega-Iguña, M. Chludzinski, C. Churiaque, R.E. Dos Santos, M. Porrúa-Lara, F. Abad-Fraga, J.M. Sánchez-Amaya, Mechanical behaviour of double side high performance PSA adhesive applied to painted naval structures, Polym. Test. 93 (2021) 106894. https://doi.org/10.1016/j.polymertesting.2020.106894.

[5] J.J.M. Machado, E.A.S. Marques, L.F.M. da Silva, Influence of low and high temperature on mixed adhesive joints under quasi-static and impact conditions, Compos. Struct. 194 (2018) 68–79. https://doi.org/10.1016/j.compstruct.2018.03.093.

[6] Y. Ciupack, H. Pasternak, C. Mette, E. Stammen, K. Dilger, Adhesive Bonding in Steel Construction-Challenge and Innovation, Procedia Eng. 172 (2017) 186–193. https://doi.org/10.1016/j.proeng.2017.02.048.

[7] V.A. Silvestru, G. Kolany, B. Freytag, J. Schneider, O. Englhardt, Adhesively bonded glass-metal façade elements with composite structural behaviour under in-plane and out-of-plane loading, Eng. Struct. 200 (2019) 109692. https://doi.org/10.1016/j.engstruct.2019.109692.

[8] C. Richter, B. Abeln, A. Geßler, M. Feldmann, International Journal of Adhesion & Adhesives Structural steel – glass facade panels with multi-side bonding – Nonlinear stress – strain behaviour under complex loading situations, Int. J. Adhes. Adhes. 55 (2014) 18–28. https://doi.org/10.1016/j.ijadhadh.2014.07.004.

[9] K. Machalická, M. Vokáč, M. Kostelecká, M. Eliášová, Structural behavior of double-lap shear adhesive joints with metal substrates under humid conditions, Int. J. Mech. Mater. Des. 15 (2019) 61–76. https://doi.org/10.1007/s10999-018-9404-y.

[10] F. Marchione, P. Munafò, Experimental investigation on timber-glass double-lap adhesive joints, Int. J. Adhes. Adhes. 106 (2021) 102818. https://doi.org/10.1016/j.ijadhadh.2021.102818.

[11] M. Giampaoli, V. Terlizzi, M. Rossi, G. Chiappini, P. Munafò, Mechanical performances of GFRP-steel specimens bonded with different epoxy adhesives, before and after the aging treatments, Compos. Struct. 171 (2017) 145–157. https://doi.org/https://doi.org/10.1016/j.compstruct.2017.03.020.

[12] V.A. Silvestru, M. Drass, O. Englhardt, J. Schneider, Performance of a structural acrylic adhesive for linear glass-metal connections under shear and tensile loading, Int. J. Adhes. Adhes. 85 (2018) 322–336. https://doi.org/10.1016/j.ijadhadh.2018.07.006.

[13] K. Machalická, M. Eliášová, Adhesive joints in glass structures: effects of various

materials in the connection, thickness of the adhesive layer, and ageing, Int. J. Adhes. Adhes. 72 (2017) 10–22. https://doi.org/10.1016/j.ijadhadh.2016.09.007.
[14] M. Overend, Q. Jin, J. Watson, The selection and performance of adhesives for a steelglass connection, Int. J. Adhes. Adhes. 31 (2011) 587–597. https://doi.org/10.1016/j.ijadhadh.2011.06.001.
[15] F. Marchione, P. Munafò, Experimental strength evaluation of glass/aluminum double-lap adhesive joints, J. Build. Eng. 30 (2020). https://doi.org/10.1016/j.jobe.2020.101284.
[16] F. Marchione, P. Munafò, Influence of high temperature exposure on the mechanical performance of double-lap adhesive joints between glass and aluminium adherends, Constr. Build. Mater. 299 (2021) 124268. https://doi.org/10.1016/j.conbuildmat.2021.124268.
[17] I.A. Ashcroft, J. Comyn, A. Mubashar, Effect of Water and Mechanical Stress on Durability, in: Handb. Adhes. Technol., Springer International Publishing, Cham, 2018: pp. 879–914. https://doi.org/10.1007/978-3-319-55411-2_31.
[18] M.R. Bowditch, The durability of adhesive joints in the presence of water, Int. J. Adhes. Adhes. 16 (1996) 73–79. https://doi.org/10.1016/0143-7496(96)00001-2.
[19] E.M. Petrie, Handbook of Adhesives and Sealants, Second Edition, 2nd ed., McGraw-Hill Education, New York, 2007. https://www.accessengineeringlibrary.com/content/book/9780071479165.
[20] G. Viana, M. Costa, M.D. Banea, L.F.M. da Silva, A review on the temperature and moisture degradation of adhesive joints, Proc. Inst. Mech. Eng. Part L J. Mater. Des. Appl. 231 (2016) 488–501. https://doi.org/10.1177/1464420716671503.
[21] R.E. Davis, P.A. Fay, The durability of bonded coated steel joints, Int. J. Adhes. Adhes. 13 (1993) 97–104. https://doi.org/10.1016/0143-7496(93)90020-A.
[22] P.A. Fay, A. Maddison, Durability of adhesively bonded steel under salt spray and hydrothermal stress conditions, Int. J. Adhes. Adhes. 10 (1990) 179–186. https://doi.org/10.1016/0143-7496(90)90101-3.
[23] B. Van Lancker, J. Dispersyn, W. De Corte, J. Belis, Durability of adhesive glass-metal connections for structural applications, Eng. Struct. 126 (2016) 237–251. https://doi.org/10.1016/j.engstruct.2016.07.024.
[24] P. Calvez, S. Bistac, M. Brogly, J. Richard, D. Verchère, Mechanisms of Interfacial Degradation of Epoxy Adhesive/Galvanized Steel Assemblies: Relevance to Durability, J. Adhes. 88 (2012) 145–170. https://doi.org/10.1080/00218464.2012.648067.
[25] F. Stazi, M. Giampaoli, F. Tittarelli, C. Di Perna, P. Munaf, Durability of different glass coatings in humid and saline environments , ageing impact on heat-light transmission and thermal comfort, Build. Environ. 105 (2016) 210–224. https://doi.org/10.1016/j.buildenv.2016.05.029.
[26] T. Alderucci, M. Rossi, G. Chiappini, P. Munafò, Effect of different aging conditions on the shear performance of joints made between GFRP and glass with a UV absorbance coating, Int. J. Adhes. Adhes. 94 (2019) 76–83. https://doi.org/10.1016/j.ijadhadh.2019.05.009.
[27] P. Munafò, Solaio Tensegrale, 00014426973, 2014.
[28] CNR DT 210/2013, Istruzioni per la progettazione, l'Esecuzione ed il Controllo di Costruzioni con Elementi Strutturali di Vetro, (n.d.).

[29] EN 10025-2:2004, “Hot rolled products of structural steels - Part 2: Technical delivery conditions for non-alloy structural steels,” (2004).
[30] ASTM D3528-16, Standard Test Method for Strength Properties of Double Lap Shear Adhesive Joints by Tension Loading, (n.d.).
[31] ISO 6270-2. Paints and varnishes — determination of resistance to humidity — Part 2: procedure for exposing test specimens in condensation water atmospheres, (2005).
[32] ISO 4587:2003 - Adhesives — Determination of tensile lap-shear strength of rigid-to-rigid bonded assemblies, (2003).
[33] I. Katsivalis, O.T. Thomsen, S. Feih, M. Achintha, Effect of elevated temperatures and humidity on glass/steel adhesive joints, Int. J. Adhes. Adhes. 102 (2020) 102691. https://doi.org/10.1016/j.ijadhadh.2020.102691.
[34] I. Katsivalis, O.T. Thomsen, S. Feih, M. Achintha, Failure prediction and optimal selection of adhesives for glass/steel adhesive joints, Eng. Struct. 201 (2019) 109646. https://doi.org/10.1016/j.engstruct.2019.109646.
[35] ASTM 5573-99. Standard practice for classifying failure modes in fiber-reinforced-plastic (FRP) joints, Annu. B. ASTM Stand. 15 (2002).
[36] F. Marchione, P. Munafò, Experimental investigation on timber-glass double-lap adhesive joints, Int. J. Adhes. Adhes. 106 (2021). https://doi.org/10.1016/j.ijadhadh.2021.102818.
[37] G. Viana, M. Costa, M. Banea, L. da Silva, A review on the temperature and moisture degradation of adhesive joints, Proc. Inst. Mech. Eng. Part L J. Mater. Des. Appl. 231 (2017) 488–501. https://doi.org/10.1177/1464420716671503.
[38] K. Machalická, M. Vokáč, M. Eliášová, Influence of artificial aging on structural adhesive connections for façade applications, Int. J. Adhes. Adhes. 83 (2018) 168–177. https://doi.org/10.1016/j.ijadhadh.2018.02.022.
[39] F. Marchione, P. Munafò, Experimental strength evaluation of glass/aluminum double-lap adhesive joints, J. Build. Eng. 30 (2020) 101284. https://doi.org/10.1016/j.jobe.2020.101284.

5.7 List of figures and tables

Figure 5.1. Tensegrity floor, rendering 76
Figure 5.2. Double-lap specimen geometry (mm) ; section and plan view..... 79
Figure 5.3. Shear test setup. 80
Figure 5.4. Average load-displacement curves of double-lap joints after maturation under laboratory conditions (EPX1, EPX2, PU adhesives). 81
Figure 5.5. Average load-displacement curves of double-lap joints after maturation and artificial ageing in climatic chamber (EPX1, EPX2, PU adhesives). 82
Figure 5.6. Load-displacement curves for SIL adhesive after different aging conditions. . 83
Figure 5.7. Failure modes: a) Adhesive failure (AF); b) and c) Mixed Failure (MF); d) Glass Failure (GF). 86

Table 5.1. Mechanical characteristics of the adherends reported by manufacturers. 77
Table 5.2. Mechanical characteristics of the adhesives reported by manufacturers. 78
Table 5.3. Mechanical properties of steel-float glass double-lap adhesive joints. 84
Table 5.4. Failure modes. 87

Chapter 6.

Influence of high temperature exposure on the mechanical performance of double-lap adhesive joints between glass and aluminium adherends

The reported experimental campaign aims to study the mechanical performance of adhesive joints between aluminium and glass adherends, subjected to exposures of different duration to high temperatures and to heating-cooling cycles. The content of this chapter has been published in a previous work, reported in Ref. [1].

6.1 Abstract

The present section illustrates an experimental investigation on double-lap adhesive joints between glass and aluminium adherends. Four different commercial structural adhesives (three epoxies and one urethane) are selected for tensile tests on adhesive joints subjected to different loading conditions (i.e., quasi-static and cyclic) and high temperature exposures (85 °C). The main objective is to verify the mechanical performance and the applicability of the joint in the field of civil engineering.
The results show - after curing under laboratory conditions (20 ± 1 °C/50 ± 5% RH) - a good adhesion between the tested materials. A suitable mechanical behaviour for the assembly of building components with adhesive technology is observed. The first epoxy adhesive shows the best performance both in terms of stiffness and ultimate load, which is due to a better and complete catalysis of the two components of the epoxy adhesive. Exposure to a heating (85 °C) and cooling (20 °C) cycle shows a positive effect on the mechanical performance of the joints. An increase in stiffness and ultimate loads is observed for the first and second epoxy and urethane adhesives. Cyclic loading/unloading tests performed after each heating (85 °C) and cooling (20 °C) process - up to ten repetitions - show a nonlinear trend of displacements and stiffnesses. However, at the end of each loading/unloading cycle, an increase in the ductility of the joint is observed. Moreover, a short exposure of the joints to high temperatures (85 °C) leads to an improvement in the failure modes: mixed failure modes are observed, with CF and GF failure rates coexisting with adhesive failures. Prolonged exposure to high temperatures has a negative effect on the failure modes of the joints and leads to an increase in the percentage of adhesive failures.

Nomenclature

A_t	Application temperature	T_g	Glass transition temperature
EPX1	First Epoxy Adhesive	S_t	Service temperature
EPX2	Second Epoxy Adhesive	W_t	Working temperature
EPX3	Third Epoxy Adhesive	ε_t	Tensile strain
UR	Urethane Adhesive	σ_t	Tensile strength
AF	Adhesive Failure	k_i	Stiffness at i-th load cycle
CF	Cohesive Failure	τ	Shear strength
GF	Glass Failure	α	Thermal coefficient of expansion
MF	Mixed Failure	$T_{1\text{-}85}$	i-th thermal cycle from 20 °C to 85 °C
E_t	Young Modulus in tension	T_0	Unaged temperature
s_i	Displacement at i-th load cycle		

6.2 Introduction

The growing interest in the use of structural adhesives is due to the specific properties of this technology, which allows a more uniform distribution of interfacial stress between the adherends, avoiding the need to drill holes in the material. The better stress distribution allows the load to be supported by reducing the local stress peaks characteristic of mechanical joints [2,3]; this aspect is particularly advantageous for hybrid joints with fragile materials such as glass. Other advantages include low weight, the ability to join dissimilar components, good sealing and low production costs [4–9].

The joints between glass and aluminium adherends allow to overcome – even if only partially – the problem of brittleness of glass obtaining a hybrid joint whose overall behaviour could no longer be called brittle, so that they could be used in the building components studied here. Machalickà and Eliàšovà [10] demonstrated the effectiveness of adhesive joints for different materials, such as glass and steel. Adhesive joints between glass and aluminium were investigated in studies by Overend et al. [11] and da Silvestru et al. [12], who tested the effectiveness of different types of adhesives and their application to curtain wall components, respectively.

Considering the possibility of hybrid joints between dissimilar materials, it is important to take into account the different coefficients of thermal expansion for such adhesive joints [13]. This aspect must be considered in the design phase of the joint: the stresses to be considered result from the combination of mechanical stresses and those generated by the effects of temperature differences and relative humidity. In particular, it is important to consider thermal effects, as they generally lead to a reduction in joint strength, as shown by Apalak et al. [14], although in certain cases - especially for epoxy adhesives - an increase in ultimate strength has been observed, as in the work of Da Silva et al. [15].

Previous studies by Banea et al. [16] and by Machalickà et al. [17], have experimentally shown that thermal cycles develop internal stresses in the adhesive joint. Indeed, tensile stresses are observed with increasing temperature and compressive stresses with decreasing temperature. Thermal cycles, as shown, could lead to embrittlement, shrinkage and failure of the adhesive layer.

Kothe et al. [18] studied the mechanical and thermomechanical performance of different combinations of typical 3D printed polymers and transparent adhesives. In addition, the influences of temperature and UV ageing occurring in the area of facades are investigated. Katsivalis et al. [19] investigated experimentally and numerically the effects of high temperatures and humidity on adhesive joints between glass and steel adherends. Two numerical simulations were compared on the basis of their failure prediction accuracy following environmental exposure, namely a continuous mechanical approach based on the properties of the adhesive and a cohesive zone modelling approach that assesses damage and failure based on the properties of the glass/steel interface.

Fiore et al. [20] studied the durability of glass/steel adhesive joints exposed to salt spray environmental conditions. Mechanical pull-off tests were performed to evaluate the evolution of the performance and damage phenomena of the joints during exposure to ageing, comparing epoxy and polyurethane adhesives. Epoxy resin-based joints showed greater strength and durability than polyurethane ones.

Overend et al. [11] demonstrated that temperature cycles lead to the reduction of the ultimate strength of the joint and its stiffness; the failure mode of the joint is also affected by the thermal cycle.
Nevertheless, research on adhesive joints between glass and aluminium adhesives is still scarce, especially regarding their mechanical behaviour at different temperatures.
The aim of the present study is to experimentally investigate the performance of the adhesive joint between glass and aluminium adherends, used for the fabrication of a window, shown in Fig. 6.1(a-b), (Patent No. EP.14015036) which includes joints bonded with structural adhesives. Another aim is to verify the joint performance for a tensegrity floor (Patent No. 00014426973 [21]), characterised by a glass deck that cooperates with the metal substructure through the use of structural adhesives.

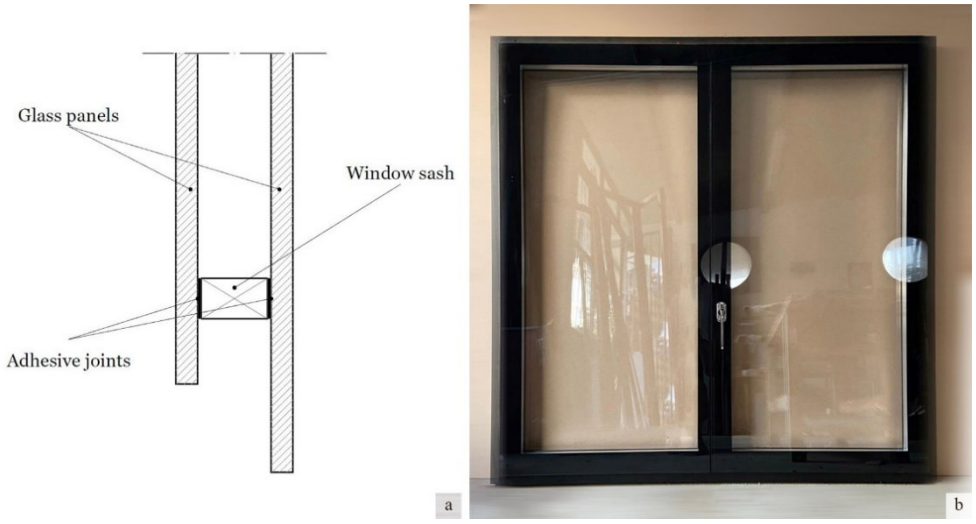

Figure 6.1. Scheme of the mobile frame (a) and window prototype (b).

The mechanical properties of joints bonded with three epoxy and one urethane adhesives are presented. First, the compatibility of the bonding system is verified at room temperature, using quasi-static tensile tests on double-lap specimens. Then, considering hybrid joints with materials characterised by thermal expansion coefficients, the decay of mechanical performance at different temperatures is investigated. The results of tensile tests on double-lap joints subjected to various heating cycles up to a temperature value close to the glass transition temperature of the adhesives (i.e., 85°C) are reported, with both fracture tests and load-unload cycles performed for load values compatible with the service conditions.
Specifically, the following tests were performed: tensile tests at failure on specimens after curing under laboratory conditions; tensile tests at failure on specimens after curing and exposure (for 30 min) at high temperatures; 10 cyclic tensile tests under service life conditions interspersed with exposure at high temperatures and followed by a final test at break to compare the final mechanical performance with the previously presented combinations.

An analysis of the effect of temperature on the failure modes was also performed. Several modes, classified as “Adhesive failure” (AF), “Cohesive failure” (CF), “Glass failure” (GF) and “Mixed failure” (MF), were observed under different test conditions. The present section shows that high temperatures affect both the mechanical properties of the hybrid adhesive joints and the failure modes.

6.3 Materials and methods

The experimental campaign carried out consists of several tensile tests on double-lap joints, made with aluminium profiles bonded to transparent float glass, and assembled according to ASTM D3528-16 [22]. These tests investigate the effectiveness of the bonding system between the adhesives and the adherends, both under laboratory conditions and at elevated temperature, examining the following mechanical parameters: failure load, ultimate displacement, and global stiffness of the bonded joint.

6.3.1 Materials properties

6.3.1.1 Adherends

Two different materials were used in this work: transparent float glass supplied by VetroMarche (Italy) and aluminium profiles, supplied by METAG (Osimo, Italy). The material properties, provided by the manufacturers, are shown in Tab. 6.1.

Table 6.1. Technical and mechanical characteristics of the adhesives reported by manufacturers.

GLASS*			**ALUMINIUM PROFILES (Alloy EN AW-6060) ****			
α ($°C^{-1}$)	E_t (GPa)	σ_t (MPa)	α ($°C^{-1}$)	E_t (GPa)	σ_t (MPa)	ε_t (%)
9×10^{-6}	75	40	2.30×10^{-5}	69,00	160	8

*according to CNR-DT 210/2013 [19]
**according to EN 755-2:2016 [20]

6.3.1.2 Adhesives

Three types of commercial two-component structural adhesives were used to assemble the joints between glass and aluminium, namely: 3M™ Scotch-Weld™ 7260 B/A (***EPX1***), 3M™ Scotch-Weld™ 7240 B/A (***EPX2***), 3M™ Scotch-Weld™ DP760 (***EPX3***), and 3M™ Scotch-Weld™ DP620NS (***UR***), which are commonly used in the automotive and marine industries. The choice of these adhesives is due to their different properties in terms of glass transition temperature (T_g) and their different ultimate strengths, which are known from previous studies. Tab. 6.2 summarises the mechanical parameters of the adhesives used, according to the manufacturer’s data sheets.

Table 6.2. Technical and mechanical characteristics of the adhesives reported by manufacturer.

Adhesive	EPX 1	EPX 2	EPX 3	UR
Chemical base	Two-component epoxy	Two-component epoxy	Two-component epoxy	Two-component urethane
Viscosity	Thixotropic	Thixotropic	Non-sagging paste	Non-sagging paste
W_t (min)	90÷300	16	40÷60	20
A_t (°C)	15÷25	15÷25	15÷25	15÷25
T_g (°C)	61.07	66.87	145÷150	-
S_t (°C)	-50÷120	-40÷80	-55÷230	51÷121
τ*(MPa)	33.50	29.40*	20÷29	-
E_t (MPa)	3000	1500	-	-
ε_t **(%)	3	-	-	110
Use	Structural	Semi-Structural	Semi-Structural	Structural

* On aluminium-steel adherends
**At failure.

6.4 Experimental tests

The experiments presented are tensile tests on double-lap adhesive joints between aluminium and glass adherends and on dogbones of the adhesives considered. The choice of the double-lap adhesive joint allows to avoid bending phenomena due to eccentric loads. In the experimental campaign described below, the following tests were carried out for each type of adhesive:

- tensile test at failure on dogbones of the adhesives after curing under laboratory conditions (T_0);
- tensile test at failure on dogbones of the adhesives after curing under laboratory conditions and subsequent exposure for 30 minutes at a temperature of (85±2) °C ($T_{1\text{-}85}$);
- tensile test at failure on double-lap joints after curing under laboratory conditions (T_0);
- tensile test at failure on double-lap joints after curing under laboratory conditions and subsequent exposure for 30 minutes at a temperature of (85±2) °C ($T_{1\text{-}85}$);
- ten cyclic tensile tests (i.e., loading and unloading) on double-lap joints up to a load value determined after the fracture tests, after curing under laboratory conditions and subsequent exposure for 30 minutes at a temperature of (85±2) °C ($T_{10\text{-}85}$). At the end of the last loading cycle, the specimens were subjected to failure with increasing monotonic quasi-static loading.

The tensile tests at failure allowed to determine the mechanical performance of the joint and to identify loading values consistent with a tensile condition in the elastic range of the joint itself. Specifically, these load values were determined to be 2.00 kN for the EPX 1 and EPX 2 adhesives and 1.30 kN for the EPX3 and UR adhesives. The temperature value of 85°C is considered here as it represents the typical glass transition value (Tg) for structural adhesives. Since the adhesives used in this study have different Tg values, the same temperature exposure value (85°C) is used for each adhesive tested.

6.4.1 Dogbones specimens geometry

For the mechanical characterization of the adhesives, dogbones were prepared for each adhesive considered in the test program according to UNI EN ISO 527-2 [23]. Five test specimens were assembled for each type of adhesive and each test. Fig. 6.2 shows the geometry of the tested specimens. The characterisation of the adhesives was performed by comparing the properties of the adhesives after curing under laboratory conditions (T0) and the properties of the adhesives after ten cycles of heating (85 ± 2 °C per 30 min) and cooling to room temperature (20 ± 2 °C).

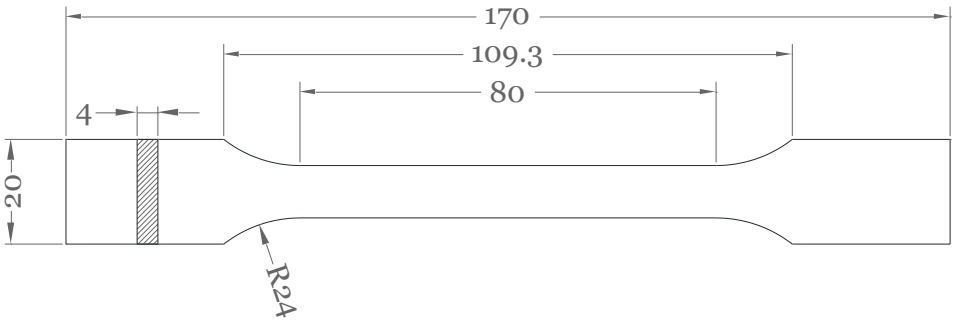

Figure 6.2. Test specimen, according to UNI EN ISO 527-2 [21] (measures in mm).

6.4.2 Double-lap specimens geometry

Double-lap joints were assembled in accordance with the requirements of ASTM D3528:16 [22]. Five test specimens were made for each adhesive type and test. Fig. 6.3 shows the geometry of the test specimens with adhesives EPX1, EPX2, EPX3, UR.
The width of the aluminium adherends is 25.4 mm and the length is 140 mm. The aluminium adherends are 5 mm thick, with a bonding area of 25.4 mm × 12.7 mm, as recommended by the manufacturer for all adhesives used. A gap of 2 mm is left between the two aluminium bonding surfaces without adhesive.

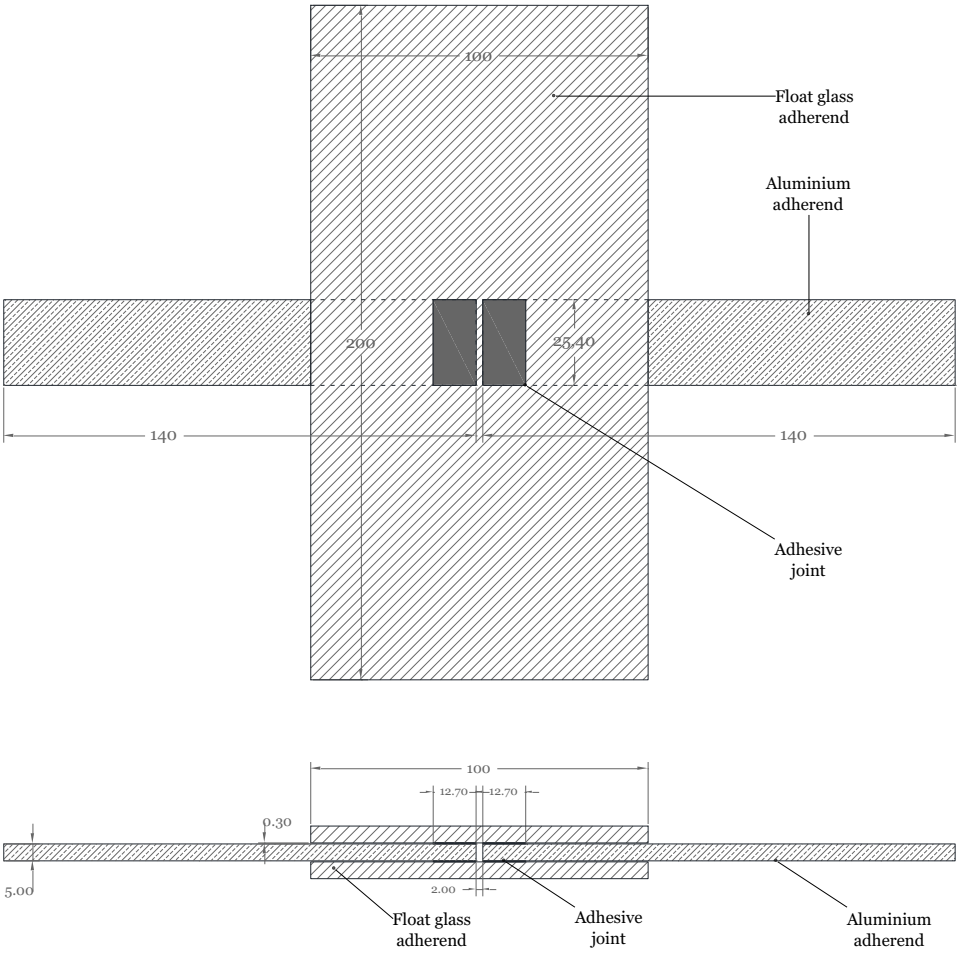

Figure 6.3. Double-lap specimens geometry (mm), section view and plan view.

The specimens were assembled under laboratory conditions (20 ± 1 °C/50 ± 5% RH). As recommended by the manufacturer, the surfaces of the aluminium adherends near the bonding region were treated by manual abrasion with sandblasting paper and degreased with acetone and isopropyl alcohol. All specimens were labelled according to the adhesive used and cured in the laboratory for 28 days, as recommended by the manufacturers. (Fig. 6.4).

Figure 6.4. Manufactured specimen, curing phase at laboratory condition.

6.4.3 Test setup

All tests listed were performed using a Zwick/Roell Z050 tensile machine with a capacity of 50 kN and displacement control set to 1.26 mm/min. An optical measurement method based on a stereoscopic calculation using a geometric grid was used to record the displacement values. Two CMOS cameras with a resolution of 1280×1024 pixels (Pixelink®B371F) with different angles were installed to capture stereoscopic images at regular intervals of 2 frames/second. The synchronized cameras were used to measure displacement, with a measurement length of 110 mm.
All specimens subjected to the heating cycles were exposed to temperatures of (85 ± 2) °C and relative humidity of (50 ± 4) % for 30 min. The heating process of the samples was carried out in a climatic chamber "Angelantoni" CST-130S. At the end of the heating process the samples are brought to room temperature (20 ± 1) °C and relative humidity of (50 ± 2) % for 60 min before the tensile tests are performed.

6.5 Results and discussion

In this section the load–displacement curves and failure modes of the tested specimens are presented and investigated. The analysed mechanical parameters in terms of failure load, ultimate displacement and stiffness are given. The results are reported in terms of mean value and standard deviation with respect to the five repetitions performed for each combination, for tests on both dogbones and double-lap specimens.

6.5.1 Dogbones tensile tests

The stress-strain graphs are shown in Fig. 6.5.
The experimental mechanical parameters for the tested adhesives are summarised in Tab. 6.3.

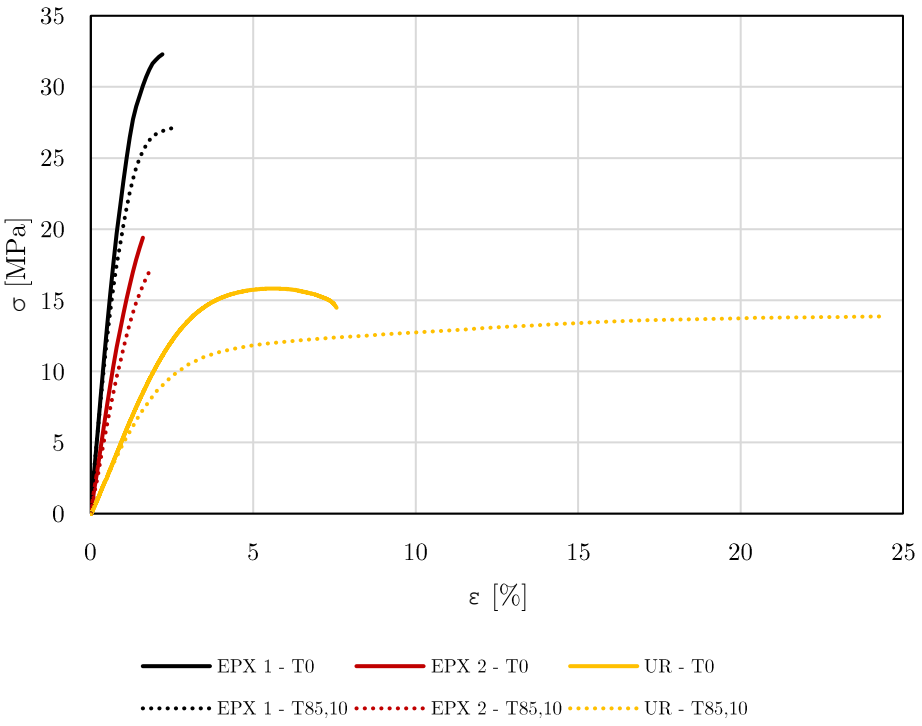

Figure 6.5. Comparison on stress-strain average curves.

Table 6.3. Dogbones mechanical parameters.

Adhesive	Test condition	σ_y (MPa)	ε_y (%)	σ_{max} (MPa)	ε_{max} (%)	E_t (MPa)
EPX 1	T_0	32.55 ±5.64	2.01 ±0.52	32.10 ±5.66	3.01 ±2.24	2981 ±560
	$T_{10\text{-}85}$	29.46 ±7.64	2.30 ±0.53	25.52 ±9.36	3.68 ±2.68	2440 ±736
EPX 2	T_0	-	-	21.88 ±2.87	2.11 ±0.42	1373 ±289
	$T_{10\text{-}85}$	-	-	21.63 ±1.58	2.46 ±0.37	1187 ±168
UR	T_0	15.82 ±4.12	5.57 ±1.10	14.47 ±2.87	7.57 ±2.06	690 ±105
	$T_{10\text{-}85}$	11.96 ±3.33	4.84 ±0.71	14.17 ±3.15	24.43 ±9.99	531 ±118

The results obtained after room temperature curing show better performance in terms of ultimate strength and stiffness for the EPX1 adhesive due to better and complete catalysis of the epoxy adhesive components. The urethane adhesive exhibits the lowest modulus of elasticity with the highest elongation at failure (+150% and +258% compared to the EPX1 and EPX2 adhesives, respectively). After exposure to high temperatures, a general decrease in elastic modulus was observed for each tested adhesive, i.e., -22% for EPX1, -15% for EPX2, -29% for UR. UR adhesive shows a significant increase in elongation at failure (+222%) after heating.
Overall, an increase in nonlinear behaviour is observed in the representative curves of each adhesive even after exposure to high temperatures, which could be attributed to the exceeding of the glass transition temperature (Tg) of the studied adhesives. This leads to a more viscous mechanical behaviour of the material, which is partially restored after cooling to room temperature before testing.

6.5.2 Mechanical performance of double-lap specimens

6.5.2.1 Shear test on double-lap specimens at laboratory conditions (T_0)

The tensile tests were carried out on double-lap adhesive joints cured under laboratory conditions (20 ± 1 °C) and a relative humidity of (50 ± 2 %). The mean force-displacement curves are shown in Fig. 6.6. Table 6.4 summarises the measured mechanical parameters in terms of mean and standard deviation for ultimate load, ultimate displacement and stiffness. The global stiffness of the joint (measured in kN/mm) was calculated in the linear section of the mean load-displacement curve of each test.

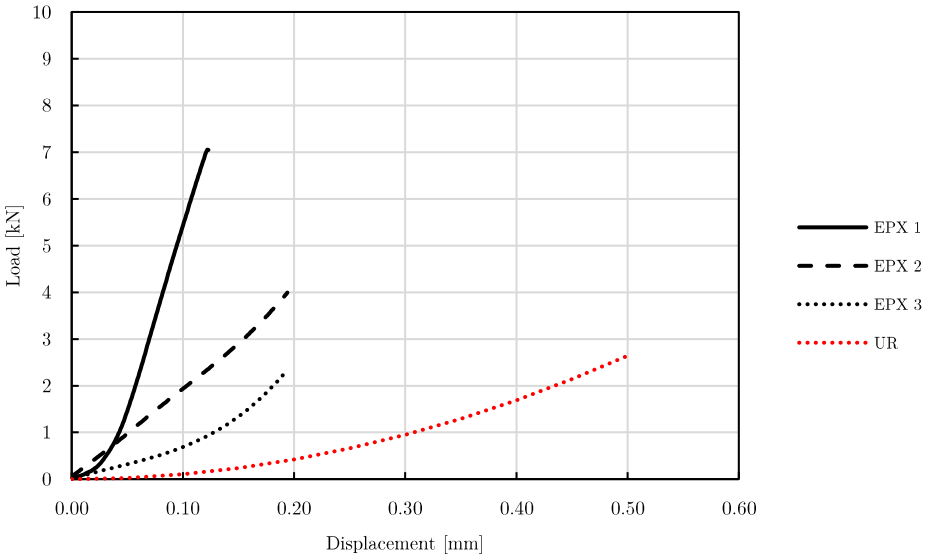

Figure 6.6. Load-displacement curves of glass-aluminium double-lap specimens after maturation under laboratory conditions (T_0).

Table 6.4. Mechanical properties of the glass-aluminium double-lap specimens after maturation under laboratory conditions.

Adhesives	F_{max} *(kN)*	*Displacement* (mm)*	τ_{max} ** (MPa)*	γ_{max} ** (%)*	*k* (kN/mm)*
EPX 1	7.04 ± 1.82	0.13 ± 0.03	5.45 ± 1.42	0.41 ± 0.14	54.15 ± 6.30
EPX 2	3.99 ± 1.77	0.19 ± 0.10	3.09 ± 1.38	0.56 ± 0.13	21.31 ± 10.09
EPX 3	2.04 ± 0.60	0.19 ± 0.13	1.60 ± 0.47	0.56 ± 0.15	10.73 ± 4.03
UR	2.64 ± 0.84	0.50 ± 0.10	2.07 ± 0.66	1.03 ± 0.10	5.29 ± 1.07

*at failure

The mechanical behaviour of epoxy and urethane adhesives is different. Joints made with epoxy adhesives (EPX1 and EPX2) show higher average ultimate loads, with mechanical behaviour characterised by higher stiffness on average. Joints assembled with urethane adhesive (UR) show the largest displacements, with a lower average failure load. EPX3 adhesive shows an intermediate behaviour, characterised by twice the stiffness of the UR adhesive and the lowest average ultimate load (2.04 kN). EPX1 showed the best performance in terms of ultimate load (7.04 kN) and stiffness (54.15 kN/mm). UR adhesive showed the

highest value for ultimate displacements (0.50 mm) and consequently the lowest values for stiffness (5.29 kN/mm).
The difference between the adhesives is reflected in the different overall stiffness values of the joints. This aspect is fundamental in the design phase. In particular, with the EPX1 adhesive, high load-bearing capacity and stiffness values could be obtained, while with the UR adhesive larger displacements could be obtained, with a lower ultimate strength.

6.5.2.2 Shear test on double-lap specimens after one heating cycle ($T_{1\text{-}85}$)

Tensile tests were performed on double-lap adhesive joints cured under laboratory conditions (20 ± 1 °C) and relative humidity of (50 ± 2 %) followed by exposure to a temperature of (85 ± 2 °C) for 30 minutes and then brought to room temperature (20 ± 1 °C). The average load-displacement diagrams are shown in Fig. 6.7. Table 6.5 summarises the mechanical parameters measured.

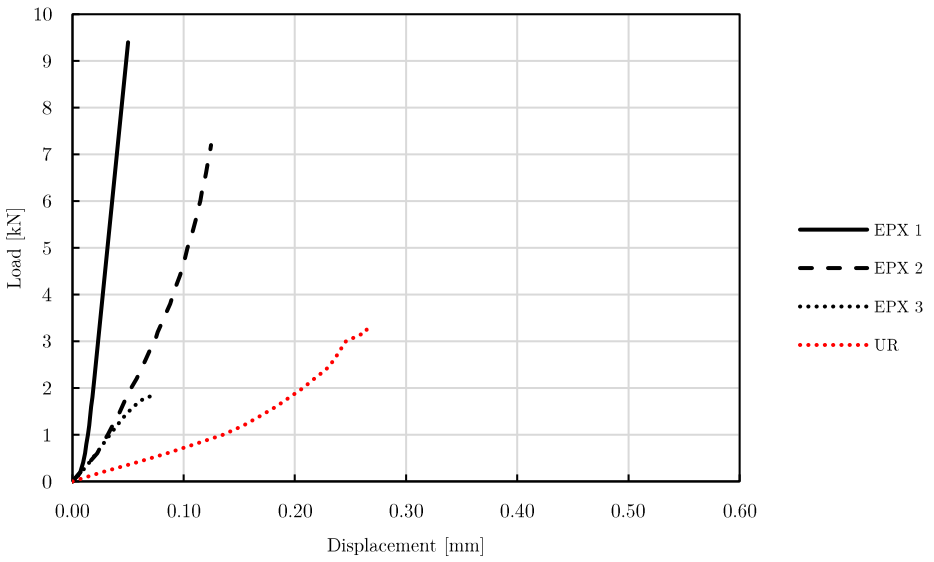

Figure 6.7. Load-displacement curves of glass-aluminium double-lap specimens after one high temperature cycle esposition ($T_{1\text{-}85}$).

Table 6.5. Mechanical properties of the glass-aluminium double-lap specimens after one high temperature cycle esposition ($T_{1\text{-}85}$).

Adhesives	F_{max} *(kN)*	*Displacement* (mm)*	τ_{max}* *(MPa)*	γ_{max}* *(-)*	*k* (kN/mm)*
EPX 1	9.40 ± 1.71	0.05 ± 0.03	7.28 ± 1.33	0.15 ± 0.09	263.13 ± 164.50

EPX 2	7.20 ± 2.03	0.13 ± 0.10	5.58 ± 1.10	0.39 ± 0.29	170.92 ± 100.92
EPX 3	1.82 ± 0.66	0.07 ± 0.04	1.41 ± 0.51	0.24 ± 0.11	28.13 ± 16.94
UR	3.36 ± 0.62	0.31 ± 0.20	2.60 ± 0.48	0.72 ± 0.32	17.34 ± 15.51

*at failure

The mechanical performance of adhesive joints after one cycle of exposure to high temperatures reflects the general trend of joints cured under laboratory conditions. An increase in performance in terms of stiffness is observed for all adhesives. In addition, with the exception of the joints made with the EPX3 adhesive, a general increase in ultimate load was observed. In particular, there was a +33%, +80% and +27% increase in ultimate strength for the EPX1, EPX2 and UR adhesives respectively. The exposure to high temperatures had a negative effect on the joints made with the EPX3 adhesive, which reached failure at low load values, which were even lower (-12%) than for the joints cured under laboratory conditions. Thus, an overall improvement in the mechanical behaviour of the tested joints can be observed, both in terms of stiffness and ultimate strength, which could be attributed to the acceleration of the polymerisation process of the adhesives due to the exposure to high temperatures.

6.5.2.3 Shear test on double-lap specimens after ten heating cycles ($T_{10\text{-}85}$)

After the quasi-static tensile tests with monotonic loading until failure, a relative loading value could be determined for each adhesive, which could be assigned to the elastic phase behaviour of the bonded joint. These values were determined to be 2.00 kN for the EPX1 and EPX2 adhesives and 1.30 kN for UR adhesive. Due to the reduced mechanical performance obtained during the shear tests on the specimens bonded using EPX3 adhesive, it was decided to exclude this adhesive from the following tests.
The experimental phase described here consists of exposing the adhesive joints to a temperature of (85 ± 2 °C) for 30 minutes, followed by cooling to room temperature (20 ± 1 °C). After thermal exposure, each specimen was tested with 5 load/unload cycles up to the above load values, which varied depending on the adhesive used. Ten repetitions of this test were performed for each specimen. At the end of the tenth heat exposure and loading/unloading cycle, the test specimens were loaded to failure. The test setup and loading speed rate remained unchanged from the previously described tests. The parameters studied at this stage of the experiment are the recorded changes in global stiffness of the joint, and the ultimate load at the end of the heat exposure and cyclic loads. The obtained results are presented in the form of load envelope curves for each thermal loading cycle. Fig. 6.8(a-c) shows the load-displacement envelopes of the obtained average curves. Tab. 6.6 shows the values of the investigated mechanical parameters. In particular, the studied quantities after each high temperature loading cycle are the displacements relative to the first load path and to the fifth (and last) load path (s_1 and s_5, respectively) and the corresponding stiffnesses (k_1 and k_5, respectively).

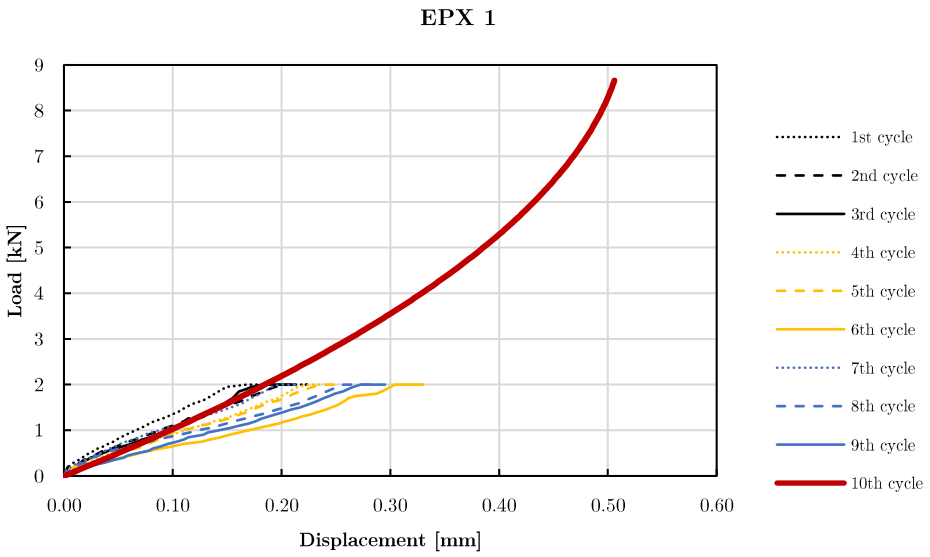
EPX 1
Load [kN]
Displacement [mm]
0
1
2
3
4
5
6
7
8
9
0.00
0.10
0.20
0.30
0.40
0.50
0.60
1st cycle
2nd cycle
3rd cycle
4th cycle
5th cycle
6th cycle
7th cycle
8th cycle
9th cycle
10th cycle

(a)

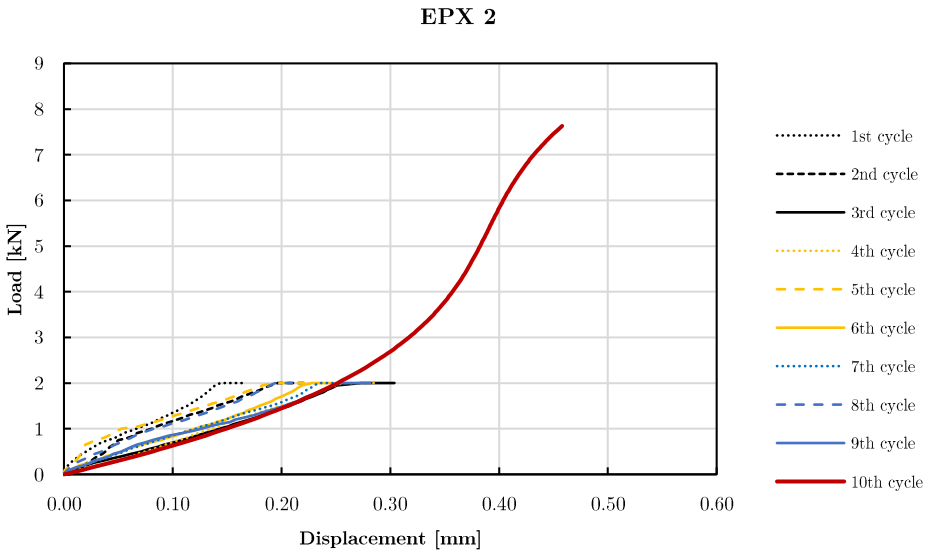
EPX 2
Load [kN]
Displacement [mm]
0
1
2
3
4
5
6
7
8
9
0.00
0.10
0.20
0.30
0.40
0.50
0.60
1st cycle
2nd cycle
3rd cycle
4th cycle
5th cycle
6th cycle
7th cycle
8th cycle
9th cycle
10th cycle

(b)

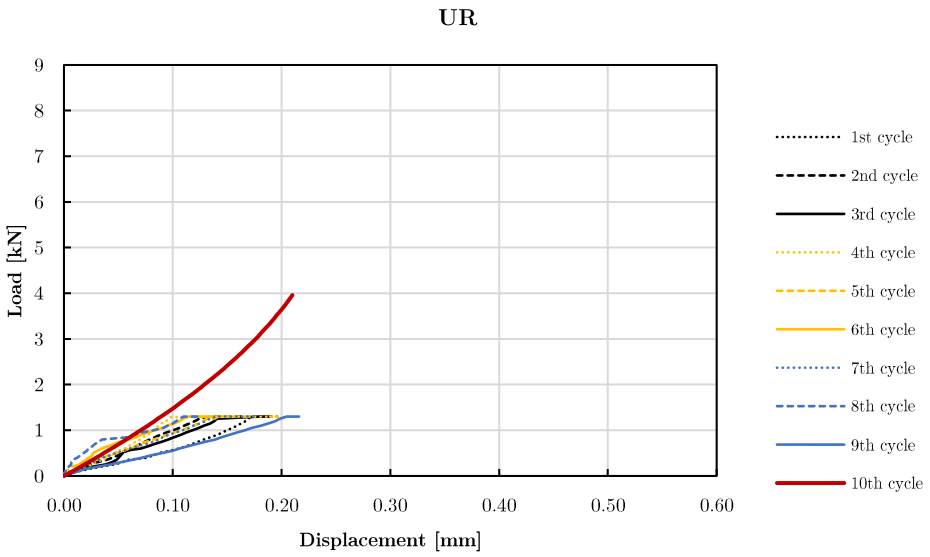

(c)

Figure 6.8. Load-displacement curves of specimens after high-temperature exposure cycles ($T_{10\text{-}85}$).

Table 6.6. Mechanical properties of double-lap joints after each exposure cycle at a temperature of 85°C.

Cycle	*Adhesive*	F_{max} *(kN)*	s_1 *(mm)*	s_5 *(mm)*	Δs_{avg} *(mm)*	k_1 *(kN/mm)*	k_5 *(kN/mm)*	Δk_{avg} *(kN/mm)*
1	EPX 1	2.00	0.16 ± 0.07	0.23 ± 0.12	0.07	11.92 ± 5.88	8.81 ± 5.54	- 3.11
	EPX 2		0.14 ± 0.13	0.16 ± 0.15	0.02	13.89 ± 6.40	12.28 ± 6.28	- 1.61
	UR	1.30	0.23 ± 0.17	0.26 ± 0.16	0.03	9.85 ± 9.21	7.46 ± 6.11	- 2.39
2	EPX 1	2.00	0.20 ± 0.16	0.22 ± 0.17	0.02	9.87 ± 4.32	8.98 ± 6.44	- 0.89
	EPX 2		0.19 ± 0.11	0.22 ± 0.10	0.03	10.12 ± 4.50	9.08 ± 2.10	- 1.04
	UR	1.30	0.14 ± 0.09	0.16 ± 0.09	0.02	9.60 ± 5.13	8.12 ± 4.86	- 1.48
3	EPX 1	2.00	0.18 ± 0.10	0.20 ± 0.09	0.02	10.96 ± 1.60	9.66 ± 7.21	- 1.30

	EPX 2		0.27 ± 0.17	0.30 ± 0.16	0.03	7.33 ± 9.51	6.58 ± 5.66	- 0.75
	UR	1.30	0.18 ± 0.09	0.19 ± 0.08	0.01	7.24 ± 8.61	6.85 ± 7.32	- 0.39
4	EPX 1	2.00	0.23 ± 0.08	0.24 ± 0.08	0.01	8.86 ± 5.00	8.40 ± 3.81	- 0.46
	EPX 2		0.25 ± 0.14	0.28 ± 0.15	0.03	7.80 ± 4.70	6.98 ± 3.20	- 0.82
	UR	1.30	0.19 ± 0.15	0.18 ± 0.12	-0.01	6.56 ± 9.74	6.91 ± 6.55	0.35
5	EPX 1	2.00	0.23 ± 0.08	0.25 ± 0.07	0.02	8.48 ± 3.80	8.02 ± 2.65	- 0.46
	EPX 2		0.19 ± 0.10	0.22 ± 0.09	0.03	10.34 ± 4.88	9.06 ± 3.55	- 1.28
	UR	1.30	0.14 ± 0.07	0.17 ± 0.07	0.03	8.97 ± 6.80	7.68 ± 5.98	- 1.29
6	EPX 1	2.00	0.30 ± 0.17	0.33 ± 0.18	0.03	6.28 ± 3.59	6.05 ± 3.02	- 0.23
	EPX 2		0.23 ± 0.08	0.24 ± 0.08	0.01	8.78 ± 5.01	8.18 ± 5.02	- 0.60
	UR	1.30	0.11 ± 0.03	0.15 ± 0.05	0.04	11.37 ± 3.64	8.47 ± 3.77	- 2.90
7	EPX 1	2.00	0.19 ± 0.11	0.21 ± 0.11	0.02	10.04 ± 7.92	9.38 ± 7.49	- 0.66
	EPX 2		0.23 ± 0.16	0.26 ± 0.18	0.03	8.53 ± 6.69	7.76 ± 5.95	- 0.77
	UR	1.30	0.14 ± 0.09	0.18 ± 0.09	0.04	9.30 ± 3.46	7.31 ± 1.85	- 1.99
8	EPX 1	2.00	0.26 ± 0.15	0.28 ± 0.16	0.02	7.77 ± 2.93	7.04 ± 2.32	- 0.73
	EPX 2		0.19 ± 0.09	0.21 ± 0.09	0.02	10.30 ± 7.50	9.54 ± 6.96	- 0.76
	UR	1.30	0.11 ± 0.07	0.12 ± 0.07	0.01	11.84 ± 1.44	10.61 ± 8.93	- 1.23
9	EPX 1	2.00	0.27 ± 0.07	0.29 ± 0.07	0.02	7.33 ± 2.98	6.77 ± 2.25	- 0.56
	EPX 2		0.25 ± 0.16	0.28 ± 0.15	0.03	7.85 ± 5.25	7.10 ± 3.85	- 0.75
	UR	1.30	0.20 ± 0.09	0.22 ± 0.09	0.02	6.35 ± 5.30	6.01 ± 4.67	- 0.34
10	EPX 1	2.00	0.16 ± 0.06	0.22 ± 0.12	0.06	11.92 ± 4.78	8.81 ± 4.58	- 3.11
	EPX 2		0.17 ± 0.06	0.23 ± 0.12	0.06	11.91 ± 4.79	8.81 ± 4.58	-3.10
	UR	1.30	0.17 ± 0.07	0.23 ± 0.12	0.40	11.92 ± 4.79	8.81 ± 4.58	- 3.11
Failure	EPX 1	8.66 ± 2.99	-	0.61 ± 0.25	-	-	11.42 ± 5.67	-

EPX 2	7.63 ± 1.50	-	0.47 ± 0.24	-	-	7.96 ± 1.60	-
UR	3.96 ± 0.79	-	0.22 ± 0.09	-	-	18.73 ± 1.23	-

The trend of displacements and stiffnesses analysed, at each exposure (cycle) to high temperatures, is shown in Figs. 6.9-6.11 (a-b).

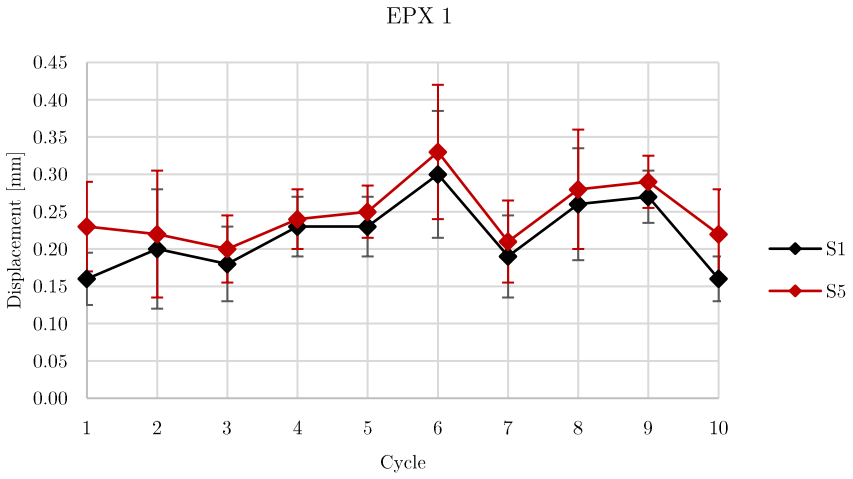

(a)

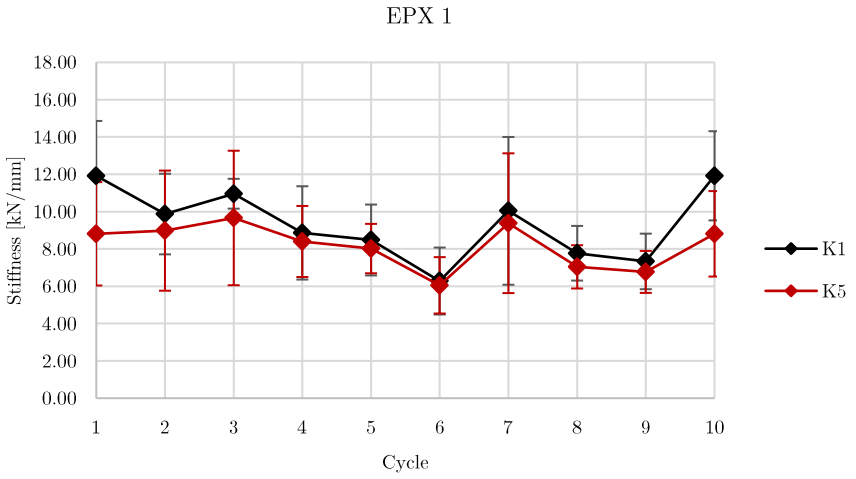

(b)

Figure 6.9. Development of displacements (a) and stiffness (b) of the adhesive joint assembled with EPX1 adhesive.

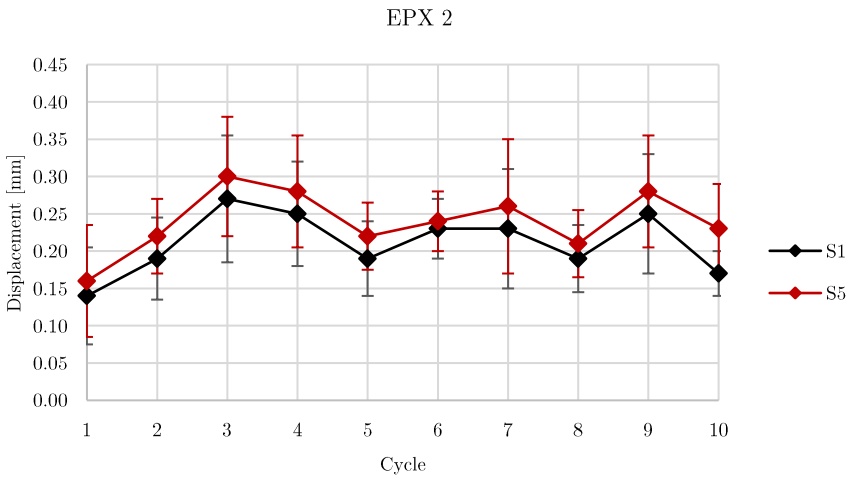

(a)

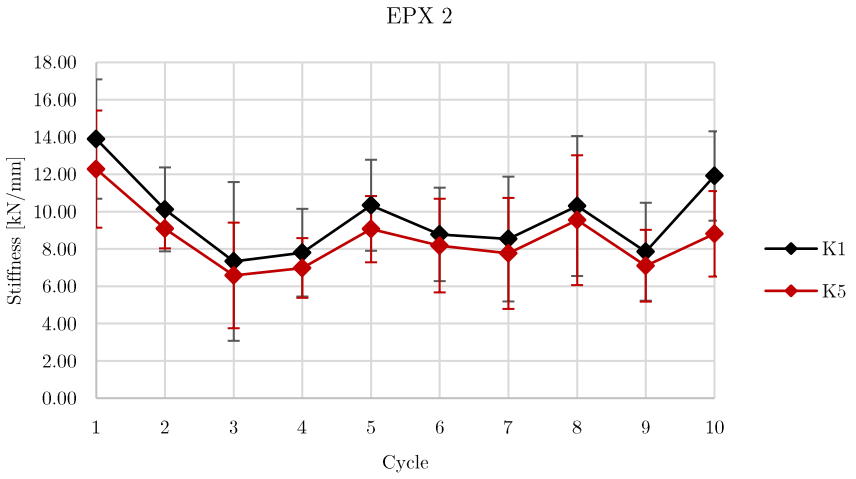

(b)

Figure 6.10. Development of displacements (a) and stiffness (b) of the adhesive joint assembled with EPX2 adhesive.

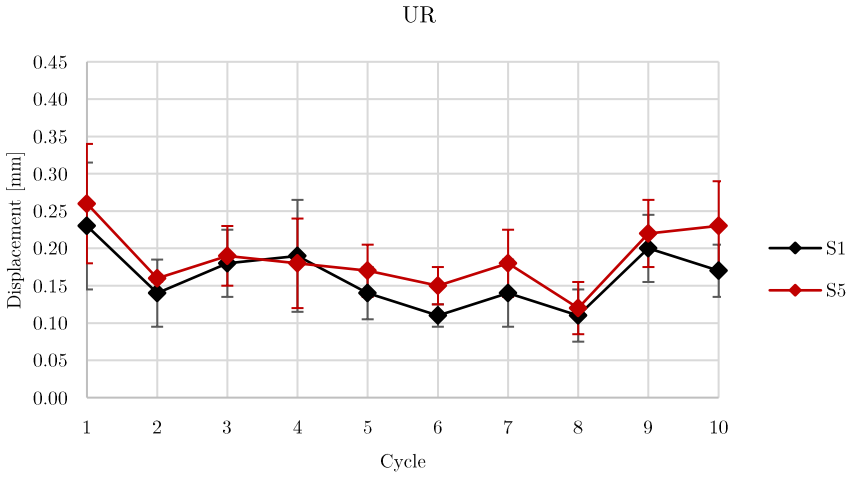

(a)

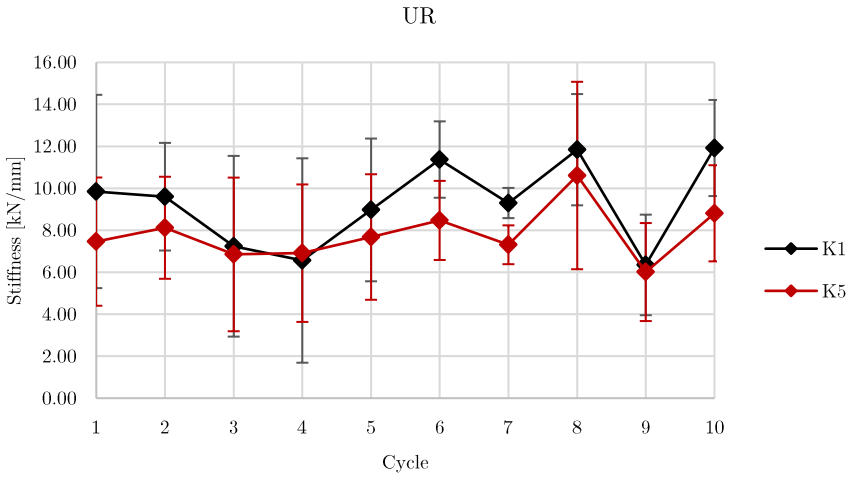

(b)

Figure 6.11. Development of displacements (a) and stiffness (b) of the adhesive joint assembled with UR adhesive.

As shown in Fig. 6.9(a-b), the EPX1 adhesive shows an increase in the value of the displacements after each exposure to high temperatures (85 °C), with the mean value of the displacements increasing from 0.01 to 0.07 mm. This leads to a reduction of the stiffness, with reduction peaks up to -3.11 kN/mm. The same mechanical behaviour could be observed for the joints assembled with EPX2 adhesive, as shown in Fig. 6.10(a-b). An increase in displacements up to a maximum of +0.06 (cycle 10) and a consequent decrease in stiffness is observed. The joints bonded with UR adhesive - Fig. 6.11(a-b) - show a similar trend in both displacements and stiffness, with a trend reversal after the 3rd and 4th cycles, where an increase in average stiffness is observed with respect to the first loading cycle (+0.35 kN/mm). At the end of the loading/unloading cycles, each specimen was loaded to failure with a monotonically increasing quasi-static tensile load.

The bonded joints show an increase in performance in terms of both ultimate strength and ultimate displacement. The joints assembled with adhesive EPX1 show a +23% increase in ultimate strength and a significant reduction in stiffness (-80%) compared to the joints tested under T0 conditions. The joints assembled with EPX2 and UR adhesives show an increase of +91% and +50%, respectively, compared to the joints tested under T0 conditions. Compared to the single-cycle temperature exposure (T1-85), higher ultimate displacements are observed, with similar failure loads.

6.5.3 Failure modes

In this section, the failure modes found observed after the described experimental campaign are illustrated. The classification used is that provided by ASTM D5573-99 [24]. Fig. 6.12 shows some representative failures detected.

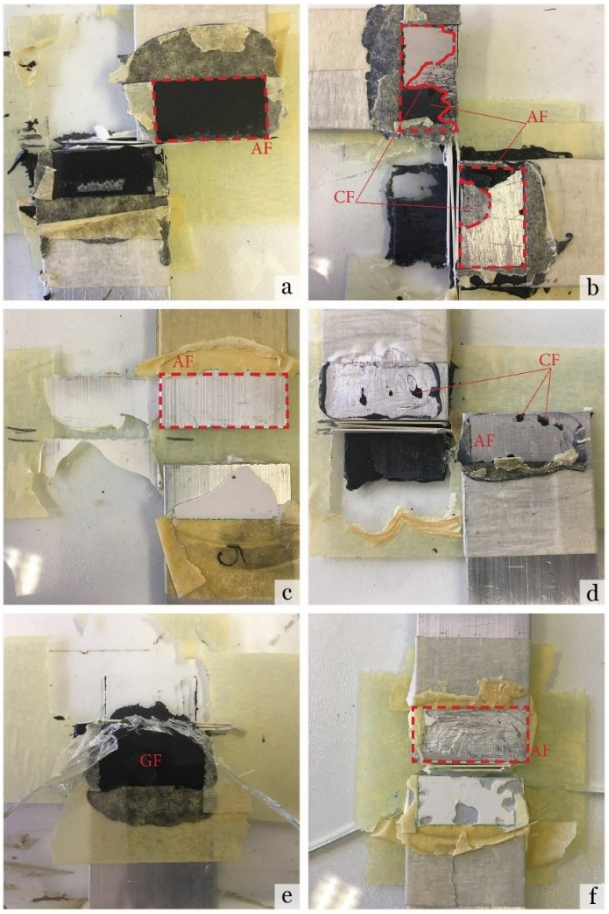

Figure 6.12. Failure modes of aluminium-glass double lap adhesive joints.

The observed failure modes are:

- ***Adhesive Failure*** (AF). Adhesive failure is occurring in the interface of the adhesive joint, with adhesive remaining attached to the surface of the glass or substrate; there is no adhesion on the opposite side;
- ***Cohesive Failure*** (CF). Separation occurs inside the adhesive layer, which remains on both surfaces of the adherends;
- ***Glass Failure*** (GF). Failure occurs in the glass adherends;

- ***Mixed Failure*** (MF). Combination of two or more of the mentioned modes (e.g., AF e CF).

Table 7 summarises the failure modes detected. The adhesive joints between glass and aluminium show high percentages of AF failures both as a single and combined with other modes (MF - mixed failure). Temporary exposure to high temperatures accelerates the adhesive polymerisation process, favouring failure modes with increasing percentages of cohesive failure (CF) and glass failure (GF). Prolonged thermal exposure shows a negative effect on the UR adhesive: a decay of adhesion, evidenced by purely adhesive failure modes in configuration T10-85, is observed. Fig. 6.13(a-d) summarises graphically the failure modes detected.

Table 6.7. Failure modes of aluminium-glass double lap adhesive joints.

Adhesive	*Configuration*	*Failure modes*
EPX 1	T_0	5 AF
	$T_{1\text{-}85}$	1 MF:(50% GF + 30% CF + 20% AF) 1 MF:(95% AF + 5% CF) 2 MF:(96% AF + 4% CF) 1 MF:(50% GF + 50% AF)
	$T_{10\text{-}85}$	1 MF:(95% AF + 5% CF) 1 AF 1 MF:(97% AF + 3% CF) 1 MF:(15% CF + 85% AF) 1 MF:(27% CF + 73% AF)
EPX 2	T_0	1 MF: (80% CF + 20% GF) 1 CF 3 MF: (CF 80% + 20% GF)
	$T_{1\text{-}85}$	1 MF:(50% GF + 50% AF) 1 MF:(76% AF + 24% CF) 1 MF:(50% GF + 46% AF + 4% CF) 1 MF:(2% CF + 98% AF) 1 MF:(50% CF + 50% AF)
	$T_{10\text{-}85}$	1 MF:(92% AF + 8% CF) 3 AF 1 MF:(50% GF + 50% AF)
EPX 3	T_0	5 AF
	$T_{1\text{-}85}$	3 AF 1 MF:(50% GF + 50% AF) 1 MF:(50% GF + 35% AF + 15% CF)
	$T_{10\text{-}85}$	-
UR	T_0	4 AF 1 MF:(50% AF + 5% CF)
	$T_{1\text{-}85}$	2 AF 1 MF:(98% AF + 2% CF) 1 MF:(1% CF + 99% AF) 1 MF:(96% AF + 4% CF)
	$T_{10\text{-}85}$	5 AF

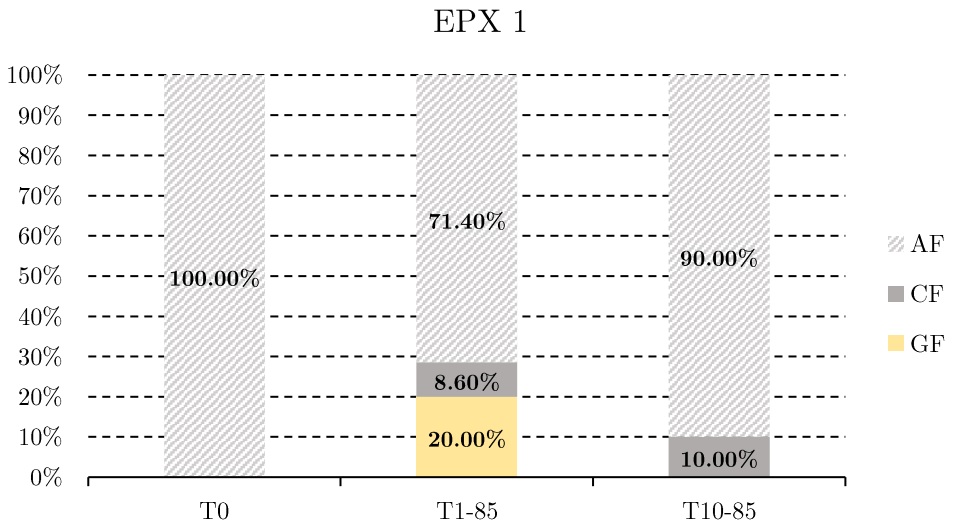
EPX 1
100%
90%
80%
70%
60%
50%
40%
30%
20%
10%
0%
100.00%
71.40%
8.60%
20.00%
90.00%
10.00%
T0
T1-85
T10-85
AF
CF
GF

(a)

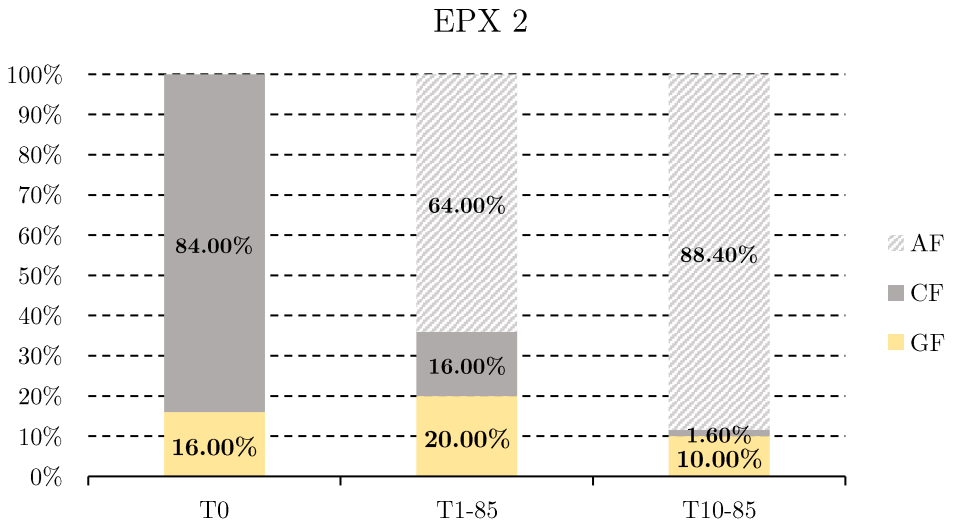
EPX 2
100%
90%
80%
70%
60%
50%
40%
30%
20%
10%
0%
84.00%
16.00%
64.00%
16.00%
20.00%
88.40%
1.60%
10.00%
T0
T1-85
T10-85
AF
CF
GF

(b)

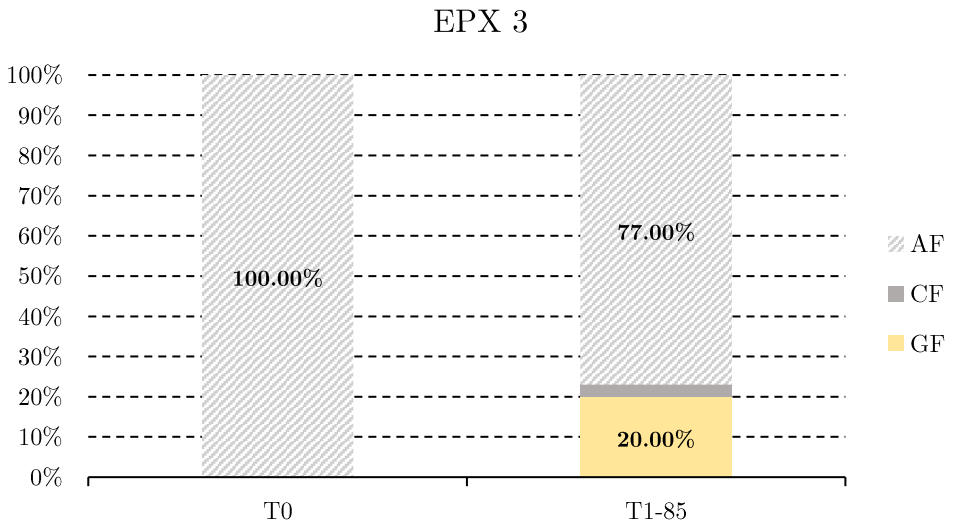

(c)

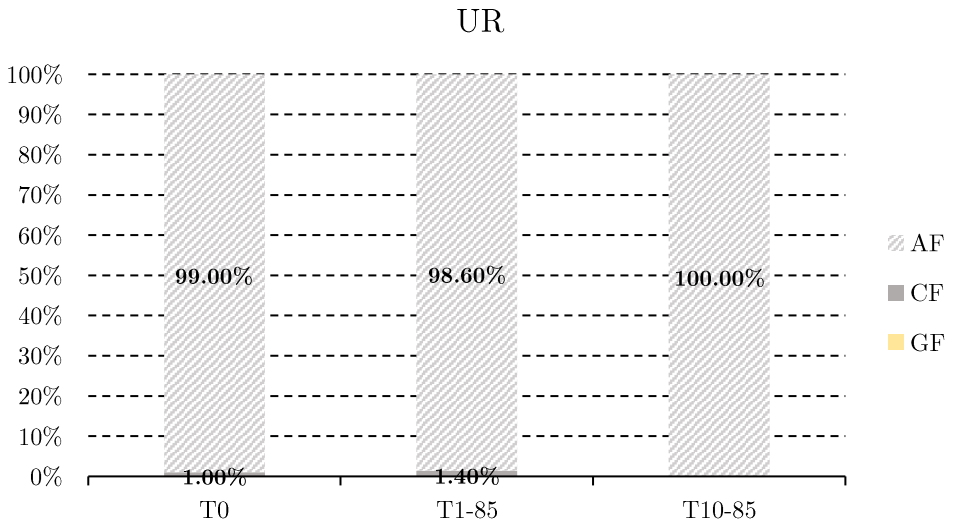

(d)

Figure 6.13. Graphical percentages of the failure modes observed.

6.6 Conclusions

The present study presents the results of an experimental campaign aimed at investigating the effect of exposure of adhesive joints between aluminium and glass adhesives at high temperatures (85 °C). The mechanical parameters studied concern the ultimate load and displacements, as well as the global stiffness of the joint under different exposure conditions, in order to verify their influence on the mechanical performance. These aspects are fundamental in the design phase of the adhesive joint for applications on building components (e.g., window frames, curtain walls). In particular, the main results obtained are the following:

- prolonged exposure (30 min) of the dogbones specimens at 85°C and subsequent cooling showed a decay of the mechanical performance of the adhesive in terms of both ultimate strength and stiffness;
- tensile tests performed after curing under laboratory conditions (T0) showed excellent adhesion between the tested materials, with ultimate load values suitable for civil engineering applications. The EPX1 adhesive showed the best performance in terms of both stiffness and ultimate load;
- tensile tests (T1-85) performed after a heating (85 °C) and cooling (20 °C) cycle showed a positive effect on the mechanical performance of the joints due to a better and complete catalysis of the epoxy adhesive components. A significant increase in stiffness and ultimate loads was observed for the adhesives EPX1, EPX2, UR. This phenomenon could be attributed to the acceleration of the polymerization process of the adhesives, caused by the exposure to high temperatures;
- the cyclic loading/unloading tests (T10-85) carried out after each heating (85 °C) and cooling (20 °C) process - up to ten repetitions - showed a strong nonlinear trend in the displacements and thus in the recorded stiffnesses. However, at the end of each loading/unloading cycle, an increase in the ductility of the joint is observed, i.e., a loss of stiffness due to the ageing of the adhesive under the heating and cooling cycles;
- a short exposure (T1-85) to high temperatures (85 °C) improves the failure modes: mixed failures (MF) are observed, with CF and GF failure modes coexist with adhesive failures (AF). Prolonged exposure to high temperatures negatively affects the joint failure modes and increases the percentage of AF failures.

In general, EPX1 and EPX2 adhesives showed the best mechanical performance. In building applications (e.g., windows and doors and curtain walls), the use of epoxy adhesives allows for stiff joints with low allowable displacements. Conversely, where larger allowable displacements and lower load-bearing capacity are required, UR adhesive has suitable mechanical properties. In addition, temperature exposure and durability should be carefully considered at the joint design phase.

6.7 References

[1] F. Marchione, P. Munafò, Influence of high temperature exposure on the mechanical performance of double-lap adhesive joints between glass and aluminium adherends, Constr. Build. Mater. 299 (2021) 124268. https://doi.org/10.1016/j.conbuildmat.2021.124268.

[2] J. R, G. Narayana Naik, R. Jairaja, G.N. Naik, Numerical studies on weak bond effects in single and dual adhesive bonded single lap joint between CFRP and aluminium, Mater. Today Proc. 21 (2020) 1064–1068. https://doi.org/https://doi.org/10.1016/j.matpr.2020.01.006.

[3] F. Marchione, Stress distribution in double-lap adhesive joints: Effect of adherend reinforcement layer, Int. J. Adhes. Adhes. 105 (2021). https://doi.org/10.1016/j.ijadhadh.2020.102780.

[4] J. R, G. Narayana Naik, Numerical studies on weak bond effects in single and dual adhesive bonded single lap joint between CFRP and aluminium, Mater. Today Proc. 21 (2020) 1064–1068. https://doi.org/https://doi.org/10.1016/j.matpr.2020.01.006.

[5] L. Adamos, P. Tsokanas, T. Loutas, An experimental study of the interfacial fracture behavior of Titanium/CFRP adhesive joints under mode I and mode II fatigue, Int. J. Fatigue. 136 (2020) 105586. https://doi.org/https://doi.org/10.1016/j.ijfatigue.2020.105586.

[6] J. Min, H. Wan, B.E. Carlson, J. Lin, C. Sun, Application of laser ablation in adhesive bonding of metallic materials: A review, Opt. Laser Technol. 128 (2020) 106188. https://doi.org/https://doi.org/10.1016/j.optlastec.2020.106188.

[7] M.D. Banea, M. Rosioara, R.J.C.C. Carbas, L.F.M.M. da Silva, Multi-material adhesive joints for automotive industry, Compos. Part B Eng. 151 (2018) 71–77. https://doi.org/https://doi.org/10.1016/j.compositesb.2018.06.009.

[8] A.L. Loureiro, L.F.M. da Silva, C. Sato, M.A. V. Figueiredo, Comparison of the Mechanical Behaviour Between Stiff and Flexible Adhesive Joints for the Automotive Industry, J. Adhes. 86 (2010) 765–787. https://doi.org/10.1080/00218464.2010.482440.

[9] J.M. Arenas, C. Alía, J.J. Narbón, R. Ocaña, C. González, Considerations for the industrial application of structural adhesive joints in the aluminium–composite material bonding, Compos. Part B Eng. 44 (2013) 417–423. https://doi.org/10.1016/j.compositesb.2012.04.026.

[10] K. Machalická, M. Eliášová, Adhesive joints in glass structures: effects of various materials in the connection, thickness of the adhesive layer, and ageing, Int. J. Adhes. Adhes. 72 (2017) 10–22. https://doi.org/10.1016/j.ijadhadh.2016.09.007.

[11] M. Overend, Q. Jin, J. Watson, The selection and performance of adhesives for a steelglass connection, Int. J. Adhes. Adhes. 31 (2011) 587–597. https://doi.org/10.1016/j.ijadhadh.2011.06.001.

[12] V.A. Silvestru, G. Kolany, B. Freytag, J. Schneider, O. Englhardt, Adhesively bonded glass-metal façade elements with composite structural behaviour under in-plane and out-of-plane loading, Eng. Struct. 200 (2019) 109692. https://doi.org/10.1016/j.engstruct.2019.109692.

[13] L.F.M. Da Silva, Improving bonding at high and low temperatures, in: Adv. Struct.

Adhes. Bond., Elsevier, 2010: pp. 516–546. https://doi.org/10.1533/9781845698058.4.516.
[14] M.K. Apalak, Z.G. Apalak, R. Gunes, E.S. Karakas, Steady-state thermal and geometrical non-linear stress analysis of an adhesively bonded tee joint with double support, Int. J. Adhes. Adhes. 23 (2003) 115–130. https://doi.org/10.1016/S0143-7496(03)00003-4.
[15] L.F.M. da Silva, R.D. Adams, M. Gibbs, Manufacture of adhesive joints and bulk specimens with high-temperature adhesives, Int. J. Adhes. Adhes. 24 (2004) 69–83. https://doi.org/https://doi.org/10.1016/S0143-7496(03)00101-5.
[16] M.D. Banea, L.F.M. da Silva, Adhesively bonded joints in composite materials: An overview, Proc. Inst. Mech. Eng. Part L J. Mater. Des. Appl. 223 (2009) 1–18. https://doi.org/10.1243/14644207JMDA219.
[17] K. Machalická, M. Vokáč, M. Eliášová, Influence of artificial aging on structural adhesive connections for façade applications, Int. J. Adhes. Adhes. 83 (2018) 168–177. https://doi.org/10.1016/j.ijadhadh.2018.02.022.
[18] B. Weller, C. Kothe, M. Kothe, J. Wunsch, Thermo Mechanical Behaviour of Polymeric Interlayer Materials, Glas. Perform. Days. (2009) 734–737.
[19] I. Katsivalis, O.T. Thomsen, S. Feih, M. Achintha, Development of cohesive zone models for the prediction of damage and failure of glass/steel adhesive joints, Int. J. Adhes. Adhes. 97 (2020) 102479. https://doi.org/10.1016/j.ijadhadh.2019.102479.
[20] V. Fiore, L. Calabrese, E. Proverbio, G. Galtieri, T. Scalici, V.M. Lo Presti, A. Valenza, Pull-off adhesion of hybrid glass-steel adhesive joints in salt fog environment, J. Adhes. Sci. Technol. 30 (2016) 2157–2174. https://doi.org/10.1080/01694243.2016.1178018.
[21] P. Munafò, Solaio Tensegrale, 00014426973, 2014.
[22] ASTM D3528-16, Standard Test Method for Strength Properties of Double Lap Shear Adhesive Joints by Tension Loading, (n.d.).
[23] EN ISO 527-1, Plastics — Determination of tensile properties — Part 1: General principles, 2012., (n.d.).
[24] ASTM D5573-99, Standard practice for classifying failure modes in fiber reinforced plastic (FRP) joints, (n.d.).

6.8 List of figures and tables

Figure 6.1. Scheme of the mobile frame (a) and window prototype (b). 96
Figure 6.2. Test specimen, according to UNI EN ISO 527-2 [21] (measures in mm). 99
Figure 6.3. Double-lap specimens geometry (mm), section view and plan view. 100
Figure 6.4. Manufactured specimen, curing phase at laboratory condition. 101
Figure 6.5. Comparison on stress-strain average curves. 102
Figure 6.6. Load-displacement curves of glass-aluminium double-lap specimens after maturation under laboratory conditions (T_0) 104
Figure 6.7. Load-displacement curves of glass-aluminium double-lap specimens after one high temperature cycle esposition ($T_{1\text{-}85}$) 105
Figure 6.8. Load-displacement curves of specimens after high-temperature exposure cycles ($T_{10\text{-}85}$). 108
Figure 6.9. Development of displacements (a) and stiffness (b) of the adhesive joint assembled with EPX1 adhesive. 111
Figure 6.10. Development of displacements (a) and stiffness (b) of the adhesive joint assembled with EPX2 adhesive. 112
Figure 6.11. Development of displacements (a) and stiffness (b) of the adhesive joint assembled with UR adhesive. 113
Figure 6.12. Failure modes of aluminium-glass double lap adhesive joints. 114
Figure 6.13. Graphical percentages of the failure modes observed. 117

Table 6.1. Technical and mechanical characteristics of the adhesives reported by manufacturers. 97
Table 6.2. Technical and mechanical characteristics of the adhesives reported by manufacturer. 98
Table 6.3. Dogbones mechanical parameters. 103
Table 6.4. Mechanical properties of the glass-aluminium double-lap specimens after maturation under laboratory conditions. 104
Table 6.5. Mechanical properties of the glass-aluminium double-lap specimens after one high temperature cycle esposition ($T_{1\text{-}85}$) 105
Table 6.6. Mechanical properties of double-lap joints after each exposure cycle at a temperature of 85°C. 108
Table 6.7. Failure modes of aluminium-glass double lap adhesive joints. 115

Chapter 7.

Preliminary experimental verification of glass decks applied on metal beams

The following section illustrates the experimental results obtained by the research team and reported in Ref. [1].

7.1 Abstract

In this section, the preliminary experimental results of testing the effectiveness of adhesive joint in steel-glass joints for glass deck applications are presented. The aim of the work is to verify the technical-constructive feasibility of the adhesive technology presented in the patent "Tensegrity Floor" (Patent No. 00014426973). The novelty of this patent consists in the structural cooperation between the glass deck and the metal substructure, achieved by using structural adhesives. In this experimental campaign, different adhesives (four epoxies, one acrylic and one silicone) are tested to verify their different mechanical contribution to the overall behaviour of the resulting structure. The experimental campaign is divided into two phases. In the first phase, compression and tensile tests are performed on the joints between aluminium adherends and on dogbones to determine the mechanical properties of the adhesives. In the second phase, cyclic loading tests were carried out on glass panels adhesively bonded to metal hollow beams, to simulate their mechanical behaviour under operating conditions. The results showed the effective structural cooperation between the deck and the substructure, which was underlined by the increase in the overall stiffness of the resulting element and the consequent reduction in the measured displacements. The joints made with epoxy adhesives showed the best mechanical behaviour in terms of stiffness in both compression and bending tests. On the other hand, the joints assembled with silicone or acrylic adhesives showed higher ductility. Finally, a FE simulation allowed the validation of the experimental results and the evaluation of the increase in stiffness obtained by using structural adhesives.

Nomenclature

ACR	Acrylic adhesive	T_g	Glass transition temperature
A_t	Application temperature	S_t	Service temperature
EPX1	First Epoxy Adhesive	W_t	Working temperature
EPX2	Second Epoxy Adhesive	ε_t	Tensile strain
EPX3	Third Epoxy Adhesive	σ_t	Tensile strength
EPX4	Fourth Epoxy Adhesive	σ_{yk}	Yield tensile stress
SIL	Silicone Adhesive	τ	Shear strength
E_t	Young Modulus in tension	ν	Poisson modulus

7.2 Introduction

In the field of civil engineering, glass finds today several applications, such as in curtain walls, floors [2], glass columns and beams [3–5]. The search for wall solutions with large glass surfaces is reflected in curtain walls, with panelling often arranged on several levels. Such glazing characterises the architectural aspect of the building, but at the same time influences comfort and the response of the wall to external actions (e.g., wind or earthquakes). The design and calculation of such structures must necessarily consider the interaction of the panels with the substructures on which they are applied. These joints are usually made with mechanical or adhesive joints.

Developments in the field of structural adhesives have made it possible to create hybrid joints between adherends made of glass and steel [6–8], timber [9–11] and other substrate materials, such as glass fibre reinforced composites (GFRP) [12] and carbon fibers (CFRP) [13]. Other advantages of this technology are the possibility of making joints without increasing weight of the substrate elements, as well as the possibility of a better distribution of stresses in the adhesive region, ensuring a greater contact area between the elements without significant deformation [14]. Therefore, the adhesive joint is a good alternative to traditional mechanical joining methods (e.g., bolting, riveting, welding).

The use of these type of joints allows the combination of brittle glass with a ductile material, which improves the load-bearing capacity, while ensuring a safer failure management for users.

Furthermore, adhesive bonding is a viable solution not only for hybrid structures, but also in the field of structural glass in general. When choosing the adhesive to be used, it could be opted towards a ductile (e.g., silicone), or relatively stiff (e.g., acrylic or epoxy adhesive) adhesive material depending on the required performance and applications.

Overend et al. [2] experimentally investigated adhesive joints between glass and steel considering five adhesives (i.e., one silicone, one polyurethane, two acrylics and one epoxy) on single-lap and T-peel joints. In other studies - such as those by Dias et al. [15], Richter et al. [6] and Caprili et al. [16] – the experimental results on glass-metal joints have been analytically validated considering both the tensile and compressive behaviour of the adhesives used. However, few data are available so far for the application areas investigated. This is due to both the use of structural adhesives, whose mechanical behaviour and durability are still under investigation [17], and the common use of glass as a pure substrate without any structural function.

The patent “Tensegrity Floor” (Patent No. 00014426973 [18]) is an example of a lightweight, modular and versatile solution for floors. The peculiarity of this system is the adhesive joints, that ensure the connection between the deck and the metal substrate.

The aim of this study is to verify the applicability of the adhesive joint in the technology shown in the “Tensegrity Floor” and to estimate the structural cooperation between glass and metal substructure, selecting the most suitable commercial structural adhesive for the intended application.

7.3 Materials and methods

The experimental campaign described below aims to verify the applicability of the adhesive joint in the tensegrity floor and to evaluate the structural cooperation between the glass and the metal substructure by estimating the possible increase in the overall stiffness.
The experimental tests include:

i. compression and tensile tests to characterise the different adhesives;
ii. bending tests on a hybrid structural system consisting of glass panels adhesively bonded on metal supports.

The tests reported do not include tests of shear mechanisms (e.g., single-lap or double-lap joints), as the stresses investigated relate to the flexural behaviour of the system.

7.3.1 Materials properties

This section describes the mechanical properties of the materials used in the experimental campaign described below.

7.3.1.1 Adherends

In the present work, two different substrates were used: AISI 304 steel and tempered glass laminated with a PVB safety layer. The mechanical properties of the materials - as given in the technical data sheets provided by the manufacturers - are listed in Table 7.1. No surface treatment was applied to the metal adherends before the bonding phase.

Table 7.1. Mechanical characteristics of the adherends reported by manufacturers.

TEMPERED GLASS*			**STEEL PROFILES****			
E_t (GPa)	σ_t (MPa)	$\boldsymbol{\nu}$ (-)	E_t (GPa)	σ_{vs} (MPa)	σ_t (MPa)	ε_t (%)
70	120	0.22	200	241	586	55

*according to CNR-DT 210/2013 standard [19]
**according to EN 10025-2:2004 standard [20]

7.3.1.2 Adhesives

In the experimental campaign described below, six commercial structural adhesives were selected, namely:

i. 3M™ Scotch-Weld™ 7260 B/A (***EPX1***),
ii. 3M™ Scotch-Weld™ 500 (***EPX2***),
iii. Gurit™ Spabond™ 345 (***EPX3***),
iv. Gurit™ Spabond™ 340 (***EPX4***).
v. Dow CorningTM 895 Structural Glazing Sealant (***SIL***).
vi. 3M™ VHB™ 4991 (***ACR***).

This choice was made taking into account their different mechanical characteristics in terms of elastic modulus, ultimate strength and glass transition temperature. Table 7.2 shows the mechanical characteristics provided by the manufacturer in the technical data sheets.

Table 7.2. Mechanical characteristics of the adhesives reported by manufacturers.

Adhesive	EPX1	EPX2	EPX3	EPX4	SIL	ACR
Chemical base	Two-part epoxy	Two-part epoxy	Two-part epoxy	Two-part epoxy	One-part silicone sealant	Acrylic
Viscosity	Thixotropic	Controlled flow	Pasty	Pasty	Pasty	Tape
W_t (min)	90÷300	20-30	16	17	15	15
A_t (°C)	15÷25	-	15-25	15-25	15÷30	-21÷38
T_g (°C)	61.07	23	55	54.60	-	-
S_t (°C)	-50÷120	-	-40÷80	-40÷84	-50÷150	-35÷90
τ*(MPa)	33.50	15.17	29.40	36.60	-	0.48
E_t (MPa)	3000	500	1800	2600	1	0.90
ε_t **(%)	3	120	-	-	600	-
Use	Structural	Structural	Structural	Semi-Structural	Structural	Structural

* On aluminium-steel adherends
**At failure.

The mechanical properties of the adhesives - except for the ACR tape - were measured by tensile tests on dogbones specimens according to EN ISO 527-1:2012 [21], EN ISO 527-2:2012 [22]. The dimensions of the dogbones are shown in Fig. 7.1. All the specimens were tested under laboratory conditions after curing for one month.
Table 3 shows the results in terms of mean and standard deviation and reflects the data provided by the manufacturers. The EPX1 adhesive and the SIL adhesive had the best and worst mechanical performance, respectively. The SIL adhesive had the highest deformability of all adhesives tested.

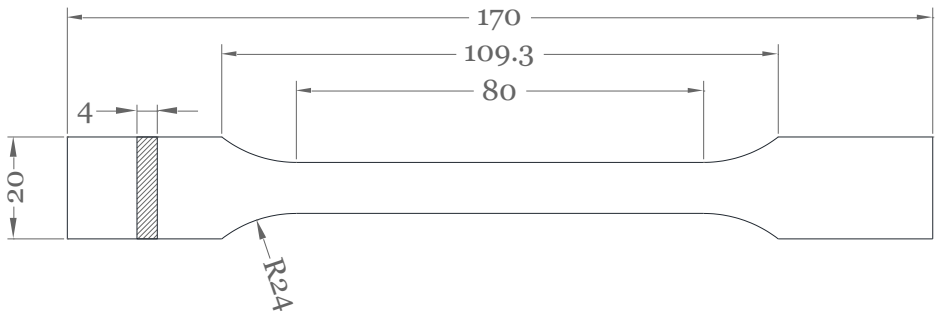

Figure 7.1. Dogbone specimen dimensions (measures in mm).

Table 7.3. Data of mechanical properties in tensile test of the adhesives.

Adhesive	E_t (MPa)	σ_t (MPa)	ε_t (%)
EPX1	2440.00 ± 53.30	32.20 ± 3.20	2.10 ± 0.69
EPX2	102.20 ± 4.64	12.20 ± 1.30	49.50 ± 9.60
EPX3	1774.00 ± 30.28	17.10 ± 0.70	3.80 ± 0.23
EPX4	1751.40 ± 69.27	38.00 ± 7.06	2.50 ± 0.71
SIL	0.50 ± 0.15	1.00 ± 0.03	151.20 ± 55.05

In addition, cyclic compression tests were performed to determine the mechanical behaviour of the adhesives under compressive loading. The setup of the compression tests reproduced the tensile condition in the adhesive joint subjected to the service loads for the intended application. The results were used to characterise the analytical model in the following numerical section. Fig. 7.2 shows the assembly steps of the described joint. The bonding area was delimited by a polychloroprene border (3 mm thick).

Figure 7.2. Bonding phase of the specimens: a) bonding region delimitation; b) adhesive bonding; c) assembled specimen.

The joint consists of two aluminium adhesives of size 40×40 mm^2 and an adhesive layer of 3 mm thickness for all the adhesives used, except for the acrylic adhesive (thickness 2.30 mm). The geometry of the specimens used is shown in Fig. 7.3.

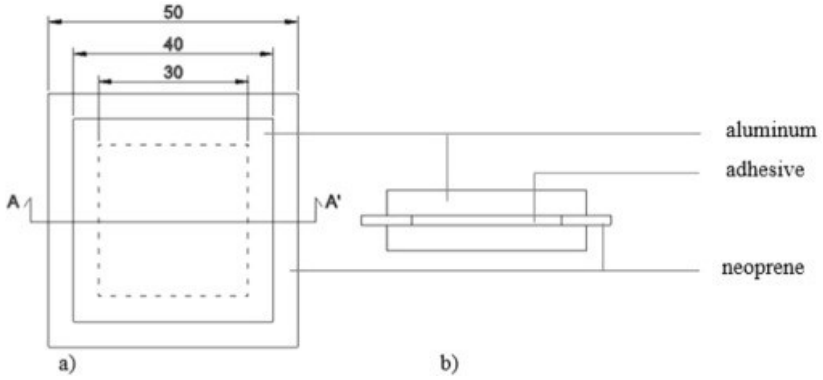

Figure 7.3. Specimens' geometry (mm): a) plane; b) section view.

The tests were carried out under laboratory conditions (19 ± 2 °C, RH 65 ± 10%), using a Zwick/Roell Z050 electromechanical machine, under stepwise cyclic loading (Fig. 7.4) at a loading speed rate of 1.25 mm/min.

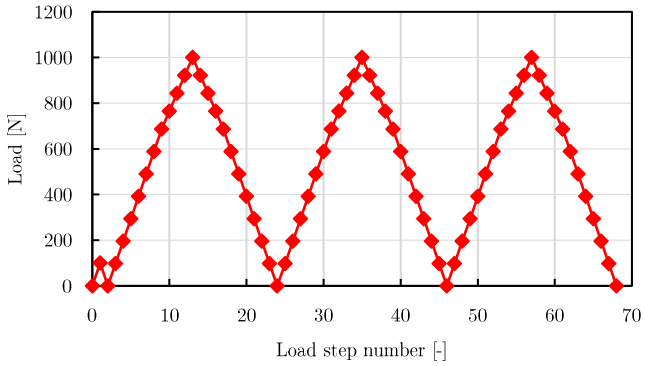

Figure 7.4. Load path.

Three specimens were tested for each adhesive and the results are shown in Table 7.4. The mechanical performance is evaluated in terms of displacement and stiffness in relation to the linearised force-displacement curves.

Table 7.4. Displacements and stiffnesses measured (compression tests).

Adhesive	***d* (mm)**	***k* (N/mm)**
EPX1	0.068 ±0.013	7603
EPX2	0.100 ±0.004	5065
EPX3	0.074 ±0.021	7260
EPX4	0.069 ±0.011	7396
SIL	0.239 ±0.105	2272
ACR	0.275 ±0.017	1736
S.SUPP.	2.352 ±0.064	22

The performance of the adhesive joints is compared with the simple support configuration (S.SUPP.), where the adhesive layer is not present and therefore the glass deck does not cooperate with the substructure. The polychloroprene layer was used as a separating layer between the glass and the metal to avoid the brittle failure of the glass.
As shown in Table 7.4, the EPX1 adhesive had the highest stiffness values (7603 N/mm), while the acrylic adhesive recorded the worst values (1735 N/mm). Since the stiffness is related to the recorded displacement values – at the same load – the same conclusions apply to the recorded displacements. High average values for maximum displacement (2.35 mm) and stiffness (22 N/mm) were recorded for the simply supported specimen.
It can be observed that:

i. the use of adhesive layer leads to an increase in the overall stiffness of the structural system;

ii. the S.SUPP. configuration presents high displacements values, partly due to the presence of the polychloroprene tape, which is very deformable and negligible in the configurations with adhesive. In fact, the adhesive absorbs a greater part of the compressive stresses due to its greater stiffness, so the presence of the tape in this configuration does not make a significant mechanical contribution.

Fig. 7.5 shows the trends of the tests for the EPX1 adhesive. The linearised curves are also shown, neglecting the non-linear trend recorded for load values below 100 N. These non-linearities are due to the settlement phase of the specimen. The linearisation performed approximates well the trend of the curves; this aspect indicates a linear elastic behaviour of the structural system in the stress range studied. Fig. 7.6 shows the force-displacement curves for the simply supported specimen. A non-linear behaviour can be observed, which is related to the influence of the residual deformations due to the polychloroprene layer. In this case, the linear approximation is carried out by interpolating the values contained in the same range of displacements in the case of the adhesive joint; beyond this limit the polychloroprene exhibits stiff behaviour.

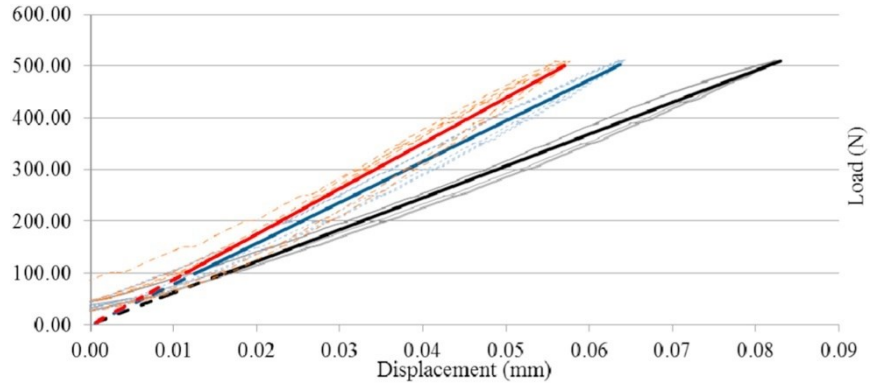

Figure 7.5. Compression test (EPX1): experimental curve (thin line) and linearized curve (thick line): 1st specimen (gray solid line), 2nd specimen (cyan dashed line), 3rd specimen sample (red dash-dotted line).

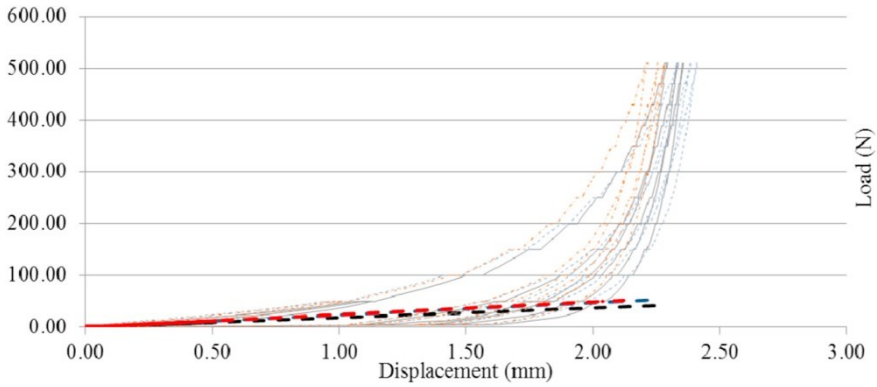

Figure 7.6. Compression test (S. SUPP.): experimental curve (thin line) and linearized curve (thick line): 1st specimen (gray solid line), 2nd specimen (cyan dashed line), 3rd specimen (red dash-dotted line).

7.4 Experiments

The purpose of the bending tests is to reproduce the stress of the "Tensegrity Floor" under the service load. This loading condition occurs in the design of structures of category C2/C3 according to the Italian building code NTC2018 [23]. The geometry of the assembled specimens is shown in Fig. 7.7.

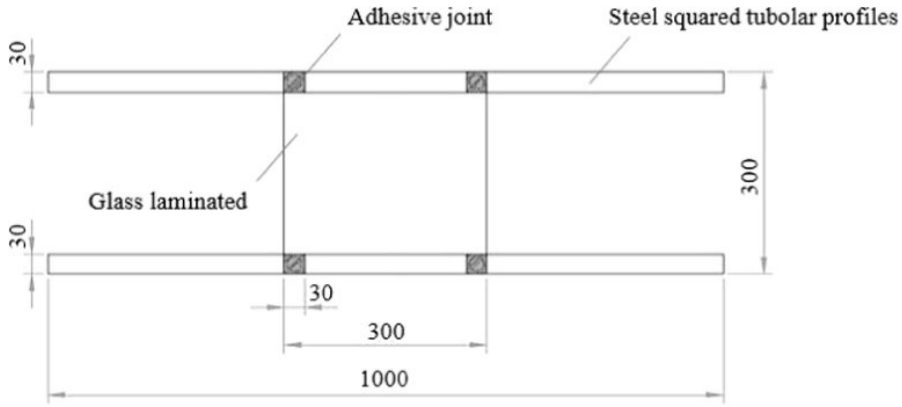

Figure 7.7. Geometry of the structural system (measures in mm).

Three specimens were tested for each adhesive and three for the simply supported system were tested, for a total of 21 specimens. Each specimen consists of two AISI 304 tubular steel profiles (2 mm thick) and a laminated glass panel (4/4 mm thick with a PVB layer in between, 0.76 mm thick), adhesively bonded together. An adhesive layer of 3 mm thickness was used for all specimens; for the acrylic tape, the thickness was 2.30 mm. To prevent the brittle failure of the glass due to contact between the glass panel and the metal profiles, a polychloroprene tape (3 mm thick) was placed between the panel and the steel profiles (Fig. 7.8).

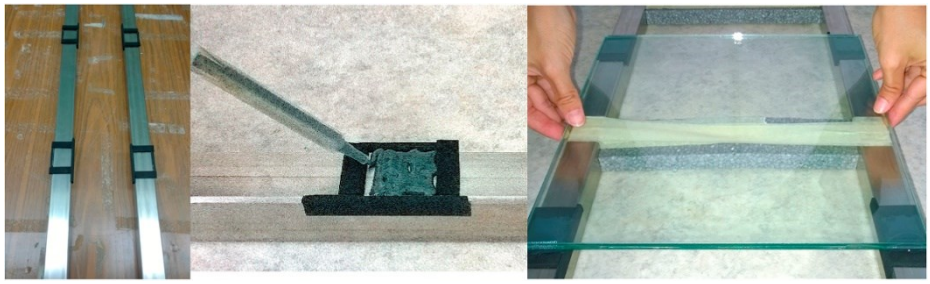

Figure 7.8. Specimens' assembly phases.

All the bonded regions were cleaned with isopropyl alcohol. The specimens were cured under laboratory conditions for 35 days. Subsequently, they were tested in a bending test with cyclic loading (Fig. 7.9).

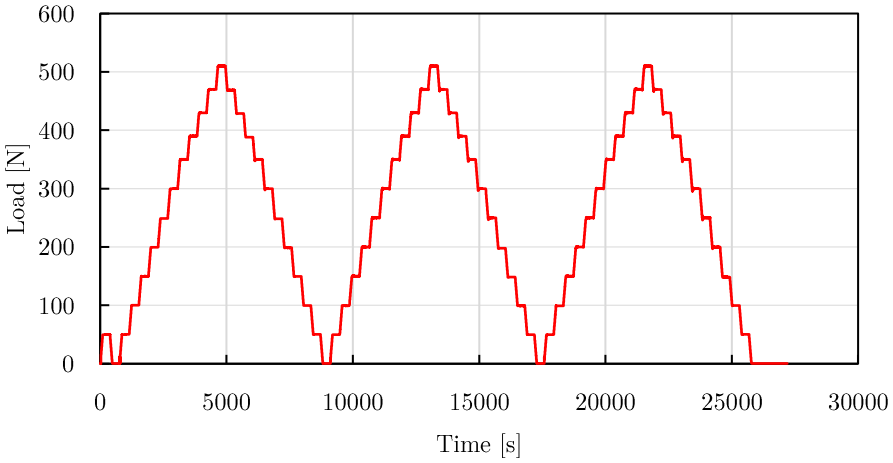

Figure 7.9. Cyclic load steps.

The test setup is shown in Fig. 7.10. The supports consisted of steel elements, spaced at 800 mm (Fig. 7.10a). Fig. 7.10b shows the corresponding static diagram. Clamps were used to measure only the deformations due to bending phenomena and to avoid unwanted torsional deformations.

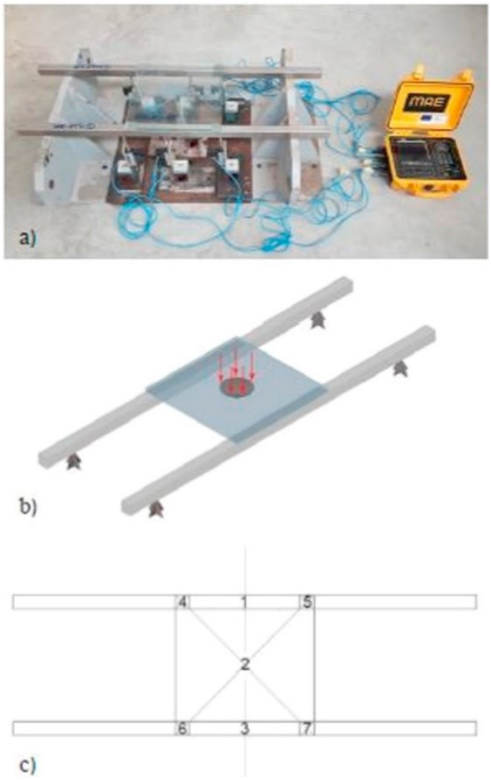

Figure 7.10. Flexural test: a) test set-up; b) static model; c) transducers location.

Displacements were measured at seven control points using analogue displacement transducers (24-bit MAE data system), shown in Fig. 7.11, placed on the inner sides of the metal profiles and in the centre of the glass panel.

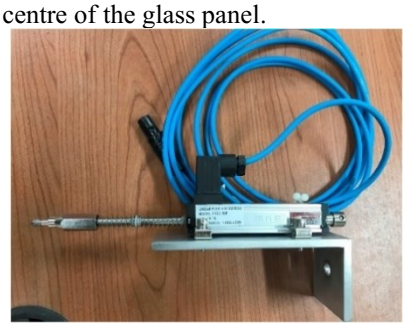

Figure 7.11. Displacement transducers.

The vertical transducers (model PY2C-50P) are supplied by MAE. Fig. 7.10c shows the planimetric arrangement of the control points.

A metal pin positioned at the centre of the glass panel was used to apply the load. The load path shown was preceded by an initial load of 98 N, to allow the specimen to settle. The load

was then applied by increasing the weight of the plates used (Fig. 7.12). The load path used consists of three loading and unloading phases, with a maximum load of 1000 N (Fig. 7.9). Fig. 7.13 illustrates the application of the load to the specimen.

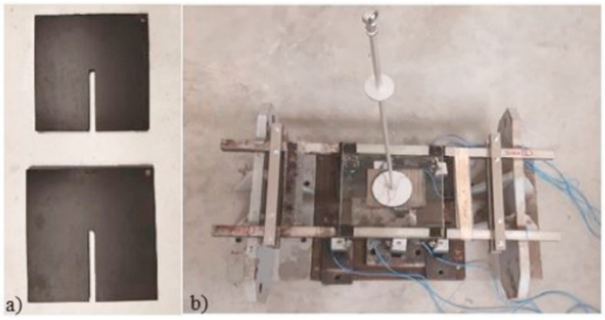

Figure 7.12. a) Load plates; b) Load application.

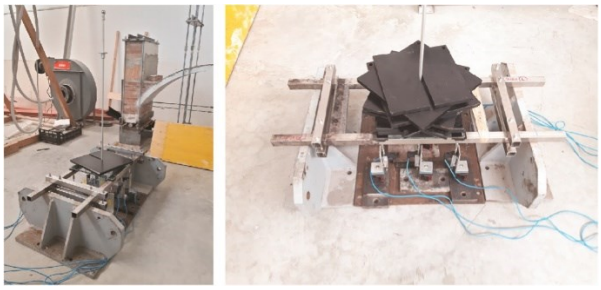

Figure 7.13. Load application on the assembled hybrid system.

7.5 Results and discussion

The following paragraph describes the mechanical performance of the tested structural system subjected to the bending tests. The measured stiffness values are listed in Table 7.5 and are compared to the stiffness measured for the simple support configuration, using the following equation:

$$\Delta = \frac{k_{adhesive} - k_{S.SUPP.}}{k_{S.SUPP.}} \cdot 100 \quad (1)$$

The results are referred to the control points at the midpoint of the glass panel (point 2), at the midpoint of the steel profiles (points 1-3), at the adhesive joints in the corners of the glass panel (points 4-5-6-7).

From the analysis of Table 7.5 the following considerations apply:

i. EPX1 is the best adhesive in terms of stiffness increase;

ii. EPX1, EPX2, EPX3 and EPX4 adhesives always provide an increase in stiffness;

iii. SIL adhesive achieves moderate stiffness increases; however, it has a stiffness reduction in point 2;

iv. ACR adhesive has up to 30% reduction in stiffness.

The results show that the metal sections experience bending deformation when the load is applied at the centre of the panel. When the glass panel is bonded to the substructure, the adhesive is fully compressed; this is due to the higher deformability of the glass panel compared to the steel beams (Table 7.5).

Table 7.5. Mechanical properties for the different configurations tested.

Adhesives	***Control point***	***k* (N/mm)***	***Δ (%)***
S. SUPP.	pt. 2	528.48	-
	pt. 1-3	1188.76	-
	pt. 4-5-6-7	1380.68	-
EPX1	pt. 2	607.57	+15
	pt. 1-3	1533.50	+29
	pt. 4-5-6-7	1739.66	+26
EPX2	pt. 2	533.76	+1
	pt. 1-3	1331.41	+12
	pt. 4-5-6-7	1532.55	+11
EPX3	pt. 2	533.76	+1
	pt. 1-3	1378.96	+16
	pt. 4-5-6-7	1422.10	+3
EPX4	pt. 2	554.90	+5
	pt. 1-3	1402.74	+18
	pt. 4-5-6-7	1532.55	+11
SIL	pt. 2	401.64	-24
	pt. 1-3	1283.86	+8
	pt. 4-5-6-7	1477.33	+7
ACR	pt. 2	369.94	-30
	pt. 1-3	1176.87	-1
	pt. 4-5-6-7	1353.07	-2

*at 1000.20 N load (maximum load value)

In this way, the glass plate contributes to the overall stiffness of the system due to its higher stiffness. On the other handt, a decrease in stiffness is observed in the presence of more ductile adhesives.

The load-displacement curves for each configuration tested are shown in Fig. 7.14. The curves refer to the control points at the centre of the glass plate (Fig. 7.14a), at the centre of the steel profiles (Fig. 7.14b), and at the adhesive joints in the corners of the glass plate (Fig. 7.14c).

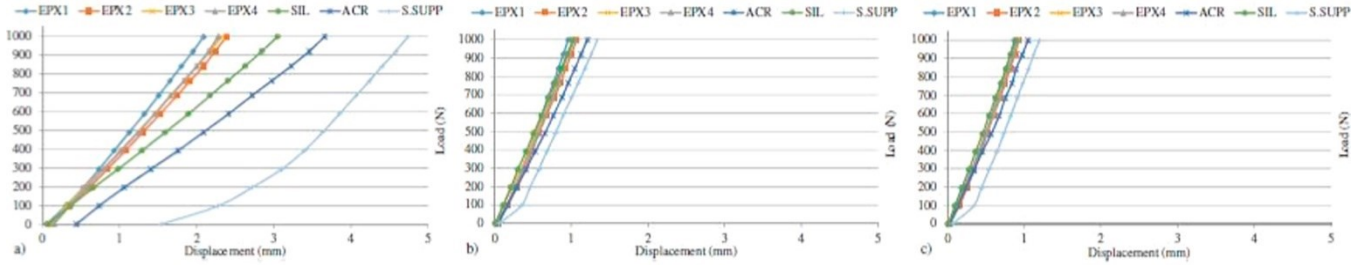

Figure 7.14. Comparison for all adhesives in "Tensegrity" specimens with the S.SUPP. configuration: stiffness increase; a) point 2; b) points 1–3; c) points 4-5-6-7.

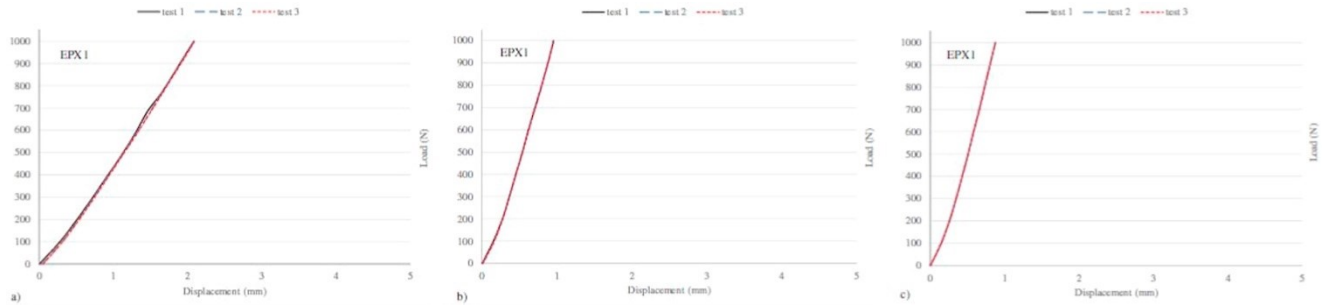

Figure 7.15. Representative load-displacement trend of "Tensegrity" specimen with EPX1 adhesive: cyclic load test: a) point 2; b) points 1–3; c) points 4-5-6-7.

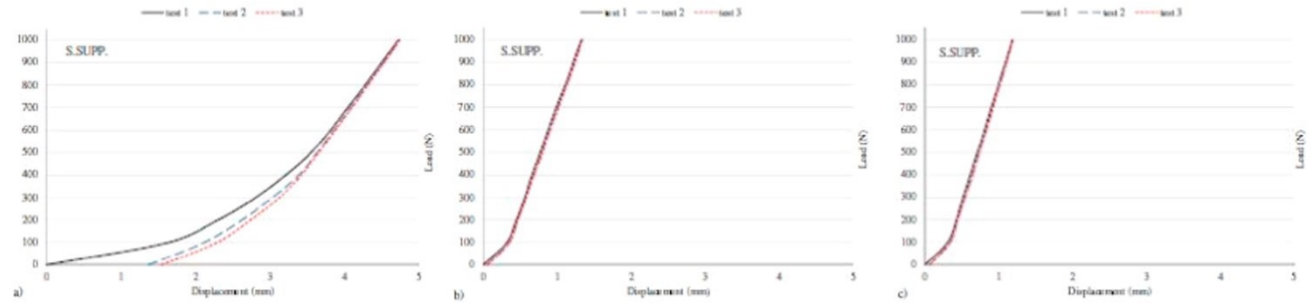

Figure 7.16. Representative load-displacement curves of the "Tensegrity" specimens simply-supported: cyclic load test: a) point 2; b) points 1–3; c) points 4-5-6-7.

From the experimental results, the stiffness of the structural system increases significantly in the presence of the adhesive joint; consequently, the simple support configuration exhibits higher deformations than those with adhesive joints. EPX1 adhesive again shows the best mechanical performance in terms of stiffness, while SIL and ACR adhesives show higher deformability.

Fig. 7.15 shows the detailed load-displacement curves for the specimens joined with the EPX1 adhesive. In contrast to the simply supported configuration (Fig. 7.16), an overlap between the load and unload curves can be observed. The presence of residual deformation in the simply supported specimens is due to the presence of the polychloroprene tape between the panel and the metal profiles. This phenomenon is avoided by the adhesive joint.
The expected deflections have been estimated analytically, and are contained in the provision of the Italian building code NTC2018 [23]:

$$d_{max} = \frac{L}{250} \tag{2}$$

Considering a maximum span area equal to 10.80 m × 10.80 m and a distributed load of 5.00 kN/m^2, representative of the live pedestrian load, the maximum deflection is about 30 mm, against the 43.20 mm expected by Eq. (2).

7.6 Numerical analysis

This section reports the results of the FE simulation carried out using the commercial software ABAQUS®. Fig. 7.17 illustrates the model used.

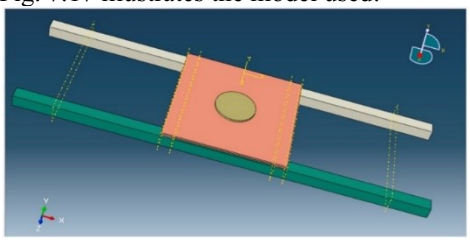

Figure 7.17. FE model.

To reproduce the load impression (Fig. 7.12b), a cylindrical solid was modelled on the glass surface.
The mechanical parameters of the materials are listed in Table 7.1. In particular, the steel was modelled according to an elastoplastic constitutive model, while the glass was modelled elastically. The glass deck was modelled as two panels connected by a PVB laminate layer. This layering allows the transfer of shear stresses between the glass panels.
The mesh was modelled by applying the element “3D STRESS”. The mesh illustration used is shown in Fig. 7.18.

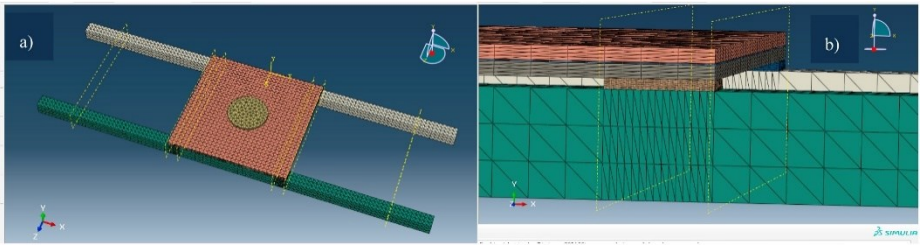

Figure 7.18. Mesh geometry: a) overall view; b) adhesive joint.

The adhesive used for the numerical simulation was the EPX1 adhesive, since the best experimental results were obtained with this adhesive. The adhesive layer is modelled as an elastic material, according to the mechanical properties in Tab. 7.3.

Table 7.6. Displacements of hybrid sample, experimental and FE results.

Control point	d_{EXP}* (mm)	d_{FEM}* (mm)	Δ (%)
pt. 2	1.990	1.936	2.71
pt. 1-3	0.795	0.802	-0.88
pt. 4-5-6-7	0.728	0.696	4.39

*at 1000.20 N load (maximum load value)

The numerical model was subjected to the same loading scheme as in the experimental phase, as shown in Fig. 7.16. The displacements obtained are summarised in Table 7.6, together with the percentage error, which is evaluated as follows:

$$\Delta = \frac{d_{experimental} - d_{FEM.}}{d_{experimental}} \cdot 100 \quad (3)$$

The percentage error is contained within 5%. Thus, the proposed FE modelling agrees well with the experimental results.
Fig. 7.19 shows the displacement maps.

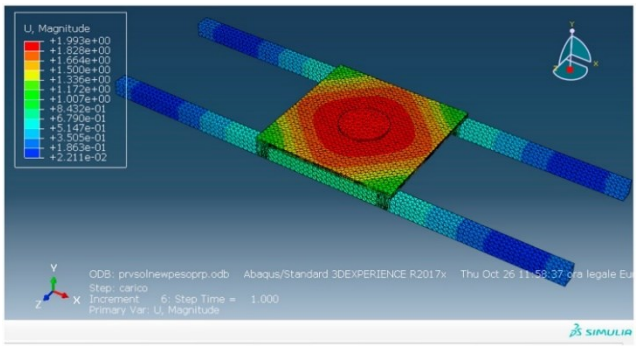

Figure 7.19. Displacement map.

Fig. 7.20 shows the stress map where the partialisation of the adhesive joint, as proposed in the analysis of the experimental results, is evident.

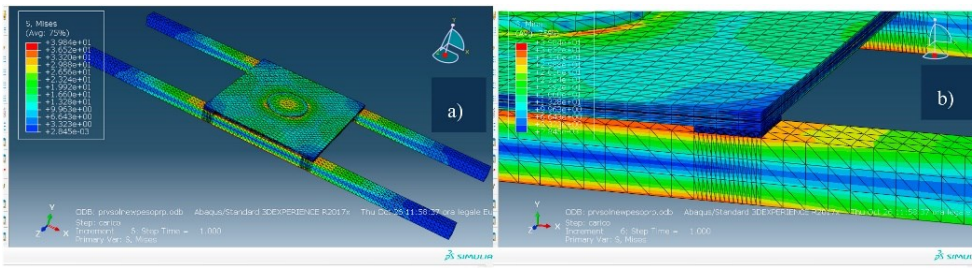

Figure 7.20. Stress map a) overall structural system; b) adhesive joint.

Due to the bending nature of the test performed, shear stresses may occur. However, the increase in stiffness is mainly due to the compressive properties of the adhesive layer.
Finally, the results from FE show the effectiveness of 3D modelling, which is the only way to correctly study the tensegrity system.

7.7 Conclusions

In this chapter, the results of an experimental campaign to study the mechanical behaviour of the adhesive joint between glass and steel, realised with different types of adhesives, are presented. In particular, the proposed study aims to verify the applicability of the adhesive joint in the "Tensegrity Floor".
The experimental results in terms of stiffness and consequently structural cooperation between the deck and the substructure were compared with the results obtained in the structural configuration with simple support. The experimental campaign was divided into a first phase of material characterization (i.e., tensile and compression tests of the adhesive) and a second phase of verification of the mechanical behaviour of the resulting structure.
In particular, load tests were performed on the hybrid structure to simulate the loads expected in service. The most important result is the increase in stiffness (+29%) obtained by using structural adhesives compared to the simply supported configuration. The best result in terms of stiffness is obtained by using EPX1 epoxy adhesive.
These results show that it is possible to obtain a structural cooperation between the glass deck and the metal substructure using the adhesive technology, the main innovation of the construction system proposed in the patent "Tensegrity Floor".
The 3D elastic linear FEA validation showed a good agreement with the experimental results, with errors within 5%.
In order to verify the feasibility of production, the durability of the proposed system needs to be investigated. Future developments will address the characterization of the hybrid structure under severe environmental conditions.

7.8 References

[1] T. Alderucci, V. Terlizzi, S. Urso, C. Borsellino, P. Munafò, Experimental study of the adhesive glass-steel joint behavior in a tensegrity floor, Int. J. Adhes. Adhes. 85 (2018) 293–302. https://doi.org/10.1016/j.ijadhadh.2018.04.017.

[2] M. Overend, Q. Jin, J. Watson, The selection and performance of adhesives for a steelglass connection, Int. J. Adhes. Adhes. 31 (2011) 587–597. https://doi.org/10.1016/j.ijadhadh.2011.06.001.

[3] F. Paolo, Behavior and Failure Strength of Laminated Glass Beams, J. Eng. Mech. 133 (2007) 1290–1301. https://doi.org/10.1061/(ASCE)0733-9399(2007)133:12(1290).

[4] S. Briccoli Bati, M. Fagone, G. Ranocchiai, Analysis of the post-crack behaviour of a laminated glass beam, in: 2009: pp. 349–352.

[5] L. Biolzi, S. Cattaneo, G. Rosati, Progressive damage and fracture of laminated glass beams, Constr. Build. Mater. 24 (2010) 577–584. https://doi.org/10.1016/j.conbuildmat.2009.09.007.

[6] C. Richter, B. Abeln, A. Geßler, M. Feldmann, Structural steel–glass facade panels with multi-side bonding – Nonlinear stress–strain behaviour under complex loading situations, Int. J. Adhes. Adhes. 55 (2014) 18–28. https://doi.org/10.1016/j.ijadhadh.2014.07.004.

[7] B. Abeln, E. Preckwinkel, Entwicklung hybrider Stahl-Glas-Träger, Stahlbau. 80 (2011) 218–225. https://doi.org/10.1002/stab.201101410.

[8] K. Machalická, M. Eliášová, Adhesive joints in glass structures: effects of various materials in the connection, thickness of the adhesive layer, and ageing, Int. J. Adhes. Adhes. 72 (2017) 10–22. https://doi.org/10.1016/j.ijadhadh.2016.09.007.

[9] L. Blyberg, E. Serrano, B. Enquist, M. Sterley, Adhesive joints for structural timber/glass applications: Experimental testing and evaluation methods, Int. J. Adhes. Adhes. 35 (2012) 76–87. https://doi.org/10.1016/j.ijadhadh.2012.02.008.

[10] P.J.S. Cruz, J. Pequeno, Timber-Glass Composite Beams: Mechanical Behaviour & Architectural Solutions, Challenging Glas. (2008) 439–448.

[11] J.M. Pequeno, P.J.S. Cruz, Structural Timber-Glass Linear System : Characterization & Architectural Potentialities, Glas. Perform. Days 2009 - Proc. 11th Int. Conf. (2009) 344–348.

[12] C. Pascual, J. Montali, M. Overend, Adhesively-bonded GFRP-glass sandwich components for structurally efficient glazing applications, Compos. Struct. 160 (2017) 560–573. https://doi.org/10.1016/j.compstruct.2016.10.059.

[13] C. Bedon, C. Louter, Structural glass beams with embedded GFRP , CFRP or steel reinforcement rods : Comparative experimental , analytical and numerical investigations, J. Build. Eng. 22 (2019) 227–241. https://doi.org/10.1016/j.jobe.2018.12.008.

[14] F. Marchione, Stress distribution in double-lap adhesive joints: Effect of adherend reinforcement layer, Int. J. Adhes. Adhes. 105 (2021). https://doi.org/10.1016/j.ijadhadh.2020.102780.

[15] V. Dias, C. Odenbreit, O. Hechler, F. Scholzen, T. Ben Zineb, International Journal of Adhesion & Adhesives Development of a constitutive hyperelastic material law

for numerical simulations of adhesive steel – glass connections using structural silicone, Int. J. Adhes. Adhes. 48 (2014) 194–209. https://doi.org/10.1016/j.ijadhadh.2013.09.043.
[16] S. Caprili, N. Mussini, W. Salvatore, An innovative solution for hybrid steel-glass self-bearing modular systems, J. Constr. Steel Res. 130 (2017) 159–176. https://doi.org/10.1016/j.jcsr.2016.12.014.
[17] R.D. Adams, J. Comyn, W.C. Wake, Structural adhesive joints in engineering, Chapman and Hall, 1997.
[18] P. Munafò, Solaio Tensegrale, 00014426973, 2014.
[19] CNR DT 210/2013, Istruzioni per la progettazione, l'Esecuzione ed il Controllo di Costruzioni con Elementi Strutturali di Vetro, (n.d.).
[20] EN 10025-2:2004, "Hot rolled products of structural steels - Part 2: Technical delivery conditions for non-alloy structural steels," (2004).
[21] EN ISO 527-1, Plastics — Determination of tensile properties — Part 1: General principles, 2012., (n.d.).
[22] EN ISO 527-2, Plastics - Determination of Tensile Properties - Part 2: Test Conditions for Moduling and Extrusion Plastics, 2012., (n.d.).
[23] NTC. Norme Tecniche Per Le Costruzioni. Rome, Italy; 2018, (n.d.).

7.9 List of figures and tables

Figure 7.1. Dogbone specimen dimensions (measures in mm)..... 126
Figure 7.2. Bonding phase of the specimens: a) bonding region delimitation; b) adhesive bonding; c) assembled specimen. 127
Figure 7.3. Specimens' geometry (mm): a) plane; b) section view. 128
Figure 7.4. Load path..... 128
Figure 7.5. Compression test (EPX1): experimental curve (thin line) and linearized curve (thick line): 1st specimen (gray solid line), 2nd specimen (cyan dashed line), 3rd specimen sample (red dash-dotted line)..... 130
Figure 7.6. Compression test (S. SUPP.): experimental curve (thin line) and linearized curve (thick line): 1st specimen (gray solid line), 2nd specimen (cyan dashed line), 3rd specimen (red dash-dotted line). 130
Figure 7.7. Geometry of the structural system (measures in mm). 131
Figure 7.8. Specimens' assembly phases..... 131
Figure 7.9. Cyclic load steps..... 132
Figure 7.10. Flexural test: a) test set-up; b) static model; c) transducers location. 133
Figure 7.11. Displacement transducers..... 133
Figure 7.12. a) Load plates; b) Load application. 134
Figure 7.13. Load application on the assembled hybrid system. 134
Figure 7.14. Comparison for all adhesives in "Tensegrity" specimens with the S.SUPP. configuration: stiffness increase; a) point 2; b) points 1–3; c) points 4-5-6-7. 136
Figure 7.15. Representative load-displacement trend of "Tensegrity" specimen with EPX1 adhesive: cyclic load test: a) point 2; b) points 1–3; c) points 4-5-6-7. 136
Figure 7.16. Representative load-displacement curves of the "Tensegrity" specimens simply-supported: cyclic load test: a) point 2; b) points 1–3; c) points 4-5-6-7. 136
Figure 7.17. FE model. 137
Figure 7.18. Mesh geometry: a) overall view; b) adhesive joint..... 138
Figure 7.19. Displacement map. 138
Figure 7.20. Stress map a) overall structural system; b) adhesive joint..... 139

Table 7.1. Mechanical characteristics of the adherends reported by manufacturers. 125
Table 7.2. Mechanical characteristics of the adhesives reported by manufacturers..... 126
Table 7.3. Data of mechanical properties in tensile test of the adhesives. 127
Table 7.4. Displacements and stiffnesses measured (compression tests)..... 128
Table 7.5. Mechanical properties for the different configurations tested..... 135
Table 7.6. Displacements of hybrid sample, experimental and FE results..... 138

Chapter 8.

Experimental assessment of the mechanical behaviour of the steel-glass adhesive joint on a 1:2 scale Tensegrity Floor prototype

The experimental campaign reported here evaluates the mechanical performance of the adhesive joint applied to a 1:2 scale prototype of a Tensegrity Floor, according to different load cases. The content of this chapter will be published in an international journal.

8.1 Abstract

The present work deals with the construction and verification of a 1:2 scale prototype of a modular system of a lightweight floor made of steel and glass with a tensegrity type load-bearing frame. In particular, the proposed study tests the applicability of the adhesive joint on the "Tensegrity Floor" (Patent No. 00014426973).
The Tensegrity Floor is a hybrid structural system characterised by an adhesive joint between steel and glass, which allows structural cooperation between the glass deck and the metal substructure, improving the structural system.
Initially, an experimental campaign was conducted to characterise the materials. The design of the nodes and joints is the result of a joint analysis aimed at studying the distribution of stresses on the nodes and on the adhesive layer, in order to optimise the profiles used. The experimental results confirm the applicability of the adhesive joint in the tensegrity system for horizontal closures, estimating the maximum deformations compatible with the limitations imposed by the building codes.
In the final phase of the research, a 1:2 scale prototype was realised and subjected to static load tests, allowing to verify the real behaviour of the structural model.

Nomenclature

A_t	Application temperature	S_t	Service temperature
EPX1	First Epoxy Adhesive	W_t	Working time
EPX2	Second Epoxy Adhesive	ε_y	Yielding strain
SIL	Silicone Adhesive	α	Thermal coefficient of expansion
OSM	Optical Stereoscopic Measurement	ε_{MAX}	Tensile strain at failure
LVDT	Linear Variable Displacement Transducer	σ_{MAX}	Tensile strength
E_t	Young Modulus in tension	σ_y	Yielding stress
k	Stiffness	γ	Shear strain at failure
τ	Shear strength		

8.2 Introduction

The term ‘tensegrity’, which is derived from the contraction of the terms ‘tensional’ and ‘integrity’, was coined by Richard Buckminster Fuller in the 1940s [1].
This terminology implies the integrity of a structure in equilibrium with continuous structural elements (ropes or cables) in tension and discontinuous, compressed structural elements (struts) [2]. In particular, the elements in tension are considered as flexible and global components, while the compressed elements are stiff and local.
Tensegrity structures are conceptually simple and efficient from an engineering point of view [2], since they maintain their functionality with only the smallest possible number of structural components [3]. Moreover, this type of structure allows large areas to be covered without the need for intermediate supports, thanks to the many advantages it offers. In fact, the possibility of using prestressed cables with high strength materials improves the overall mechanical performance and reduces the size of the compressed structural components.
Since the 1950s, this design principle has been applied in both art and architecture [4–6].
A famous example from civil engineering is the Georgia Dome [7], built in 1992 for sporting events with a maximum height of 82.50 m and a width of 185 m. Its success gave rise to other studies and realisations of tensegrity domes, as in Refs. [8,9].
A more recent example of a similar technology is the roof of the National Museum of Reggio Calabria by ABDR Group (Italy). The roof, which is a no-step area, consists partly of a flat structure with closed square meshes. This floor is stiffened by an underlying tensegrity structure, where a strut with cylindrical section is connected to a spherical node. The struts are compressed by cables acting as tie rods joined at pairs of knots and passing through holes drilled in the other end of each strut. The glass panels do not cooperate with the substructure since the tensegrity structure of the floor is only connected with the steel profiles of the flat mesh structure.
Today, the search for slim, transparent structures with high load bearing capacity is a widespread trend. In this context, glass is increasingly used - also as a structural element - for the construction of facades [10,11], floors and beams [12]. The search for lightweight and efficient structures characterised by technological simplification [13] – i.e., a reduced number of components – finds an example in the patent “Tensegrity Floor” [14], which is the subject of the present work.
The “Tensegrity Floor” (Fig. 8.1) is a hybrid structural system consisting of a glass deck that structurally cooperates with the tensegrity metal substructure through the use of structural adhesives. The Tensegrity structure allows the construction of a modular, transparent and versatile building element. The cooperation between the deck and the substructure is the main feature of the studied structural system.
In this paper, the results of the technical-design verification process with the construction of a 1:2 scale prototype of a tensegrity floor and the results of the load tests performed with different combinations of structural adhesives are presented.

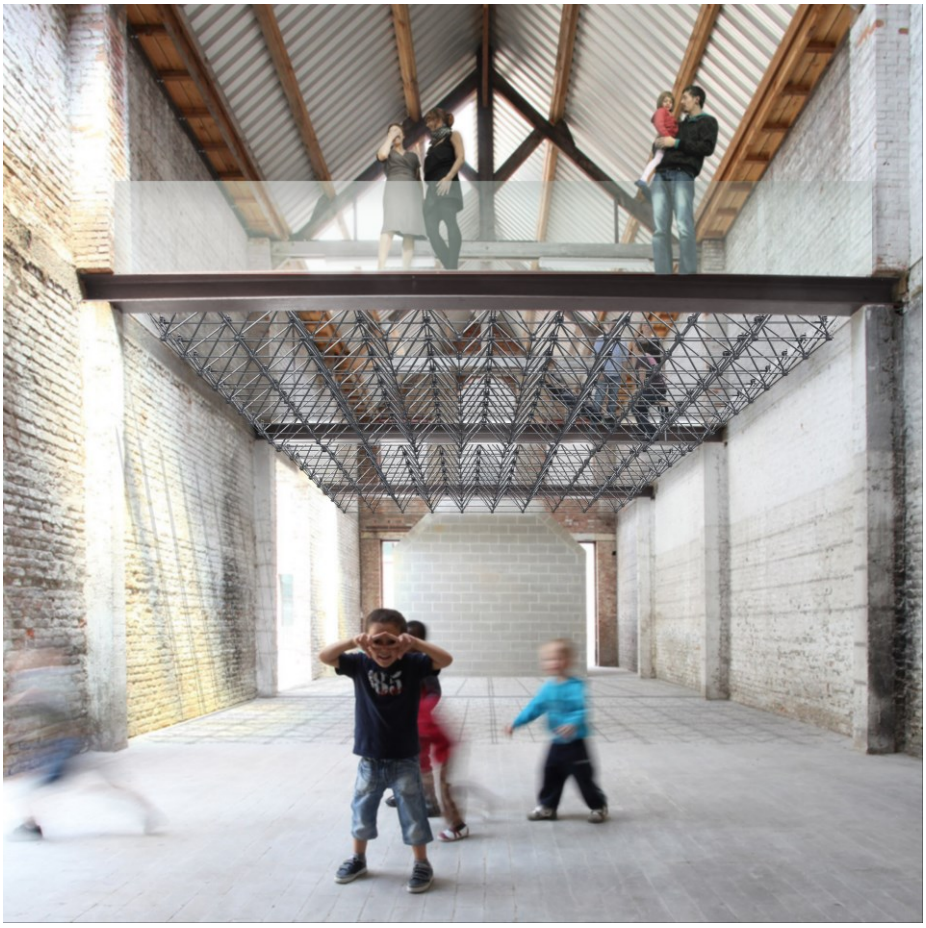

Figure 8.1. Tensegrity floor, rendering.

8.3 Tensegrity Floor

The main features of the patented tensegrity floor system (Patent No. 00014426973) are described below [14]).
Fig. 8.2 shows an axonometric view of the floor, in which the main components can be observed.

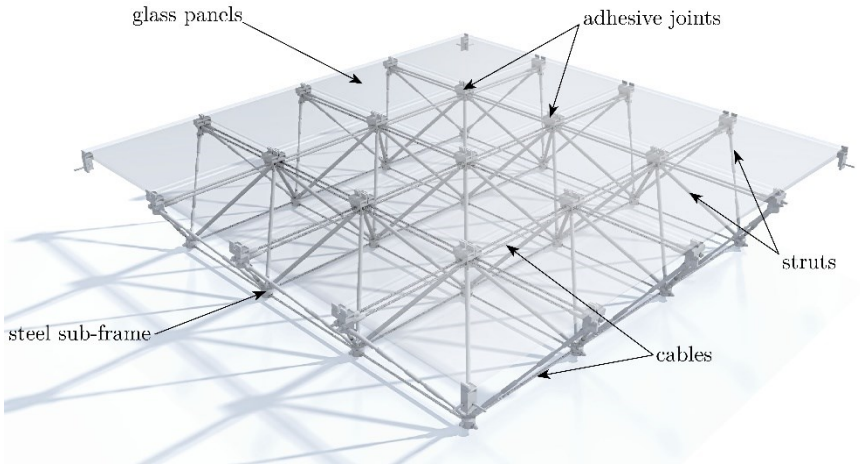

Figure 8.2. Tensegrity floor, axonometric view.

The cable and strut structural system determines a modular metal deck and substructure. The latter consists of struts arranged according to the lateral edges of a square pyramid (construction module). In the top of each module there is a node (4 for each module), and in the base corners there are nodes that allow connection with adjacent modules. At the extrados, cables support the upper nodes. As on the intrados, all lower nodes are also supported by cables. However, the most important innovation is the structural cooperation between the steel substructure and the glass deck, which is achieved through adhesive joints. The use of this technology makes it possible to reduce the size of the substructure compared to a solution with a non-cooperating (simply supported) deck. In addition, the modularity of the system enables mass production of the components.

8.3.1 Prototype

The construction phases on a 1:2 scale prototype are illustrated in this section. Fig. 8.3 shows the “Tensegrity Floor” prototype in plan and section view.

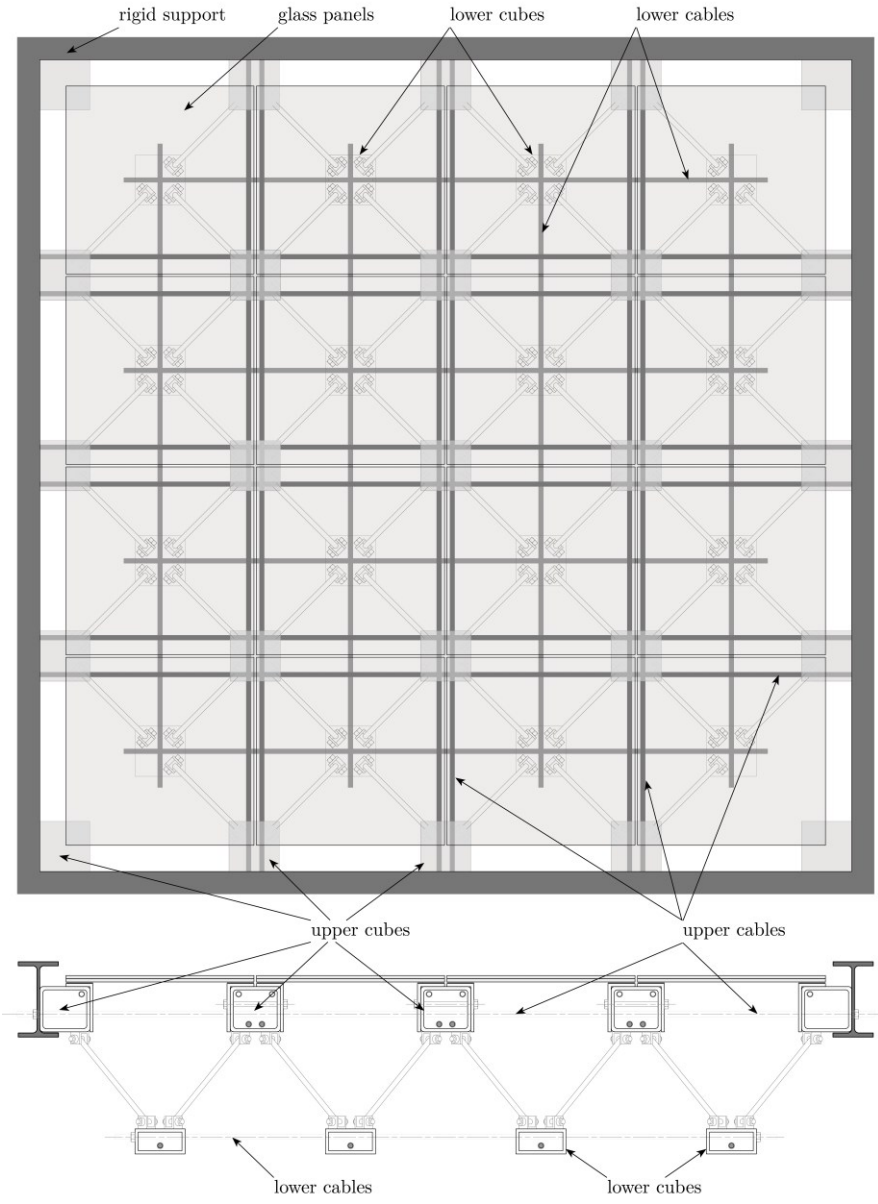

Figure 8.3. “Tensegrity Floor” prototype, plan and section view.

The “Tensegrity Floor” prototype consists of the following elements:

- glass deck consisting of 16 toughened glass panels (300 mm × 300 mm × 4+4 mm) with a layer of safety PVB (0.76 mm thick) in between;
- glass deck support elements (upper nodes), 25 steel cubes supported by the upper level of tensioned cables and connected to the deck by adhesive joints;
- a lower level (lower nodes), 16 steel cubes held by the lower level of tensioned cables and connected to the upper cubes by steel struts (turnbuckles);
- an intermediate level consisting of 36 steel turnbuckles whose function is to transfer tensile (perimeter) and compressive (intermediate) stresses to the two nodal levels (upper and lower);
- an upper and lower order of prestressed metal cables;
- a perimeter steel edge (IPE 160) to which the floor is constrained.

Fig. 8.4 shows the prototype.

Figure 8.4. “Tensegrity Floor" 1:2 scale prototype.

The height difference between the upper and lower nodes was set at 25 cm. During the assembly of the prototype, some structural problems arose. In particular, given the impossibility of prestressing all the cables at the same time, it was necessary to insert a perimeter UPN50 steel profile to connect the lower nodes in order to contain the differential displacements of the lower cubes. Another design problem is the use of stranded wires, which cause difficulties in controlling deformations during installation. For this reason, at least during the assembly phase, the cables were replaced by threaded rods made of high-strength steel rods, which, due to their greater stiffness compared to cables, are able to control deformations during assembly. For the assembly of the prototype and for the subsequent load tests it was decided to keep the threaded rods. Fig. 8.5 shows the final prototype in its modified configuration on which the load tests were performed.

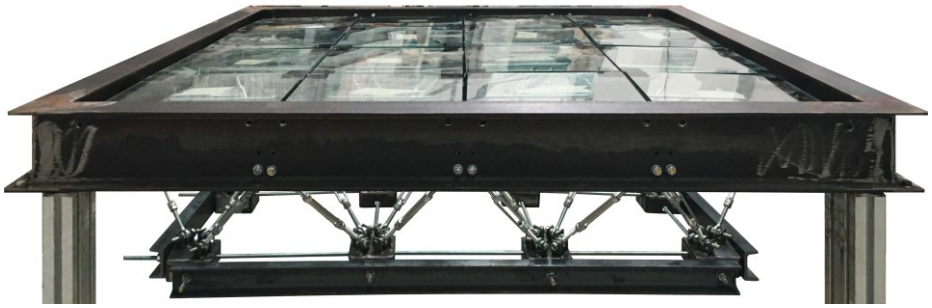

Figure 8.5. "Tensegrity Floor" 1:2 scale prototype, final configuration.

8.4 Materials and methods

The experimental campaign described in the following consists of static load tests performed - in different combinations - on the 1:2 scale prototype of the Tensegrity Floor. The mechanical properties of the materials used for the experiments are described in the following sections.

8.4.1 Materials properties

8.4.1.1 Adherends

The materials used in this experimental campaign are: S355JR steel and tempered glass panels laminated with PVB film, according to CNR-DT 210/2013 [15]. The mechanical properties of the materials are shown in Tab. 8.1.

Table 8.1. Mechanical characteristics of the adherends reported by manufacturers.

GLASS*			**STEEL (S355JR) ****			
α ($°C^{-1}$)	E_t (GPa)	σ_t (MPa)	α ($°C^{-1}$)	E_t (GPa)	σ_{vk} (MPa)	σ_t (MPa)
9×10^{-6}	70	120	2.30×10^{-5}	210	355	510

*according to CNR-DT 210/2013 standard, tempered glass [15]
**according to EN 10025-2:2004 standard [16]

The mechanical properties of the steel and threaded rods were also tested experimentally using tensile tests according to UNI EN 10002-1 [17]. The tensile tests were performed with a Zwick-Roell ZMART.PRO universal tensile machine with a loading speed rate of 1.27 mm/min. Specifically, for the S360JR steel, flat sections with dimensions 50 mm × 5 mm were tested with an initial length of 500 mm; for the threaded rods (M8, CL 8.8 according to NTC 2018 [18]) the initial length is 400 mm. Five repetitions were performed for each element type. The average σ-ε obtained from the tensile tests is shown in Fig. 8.6.

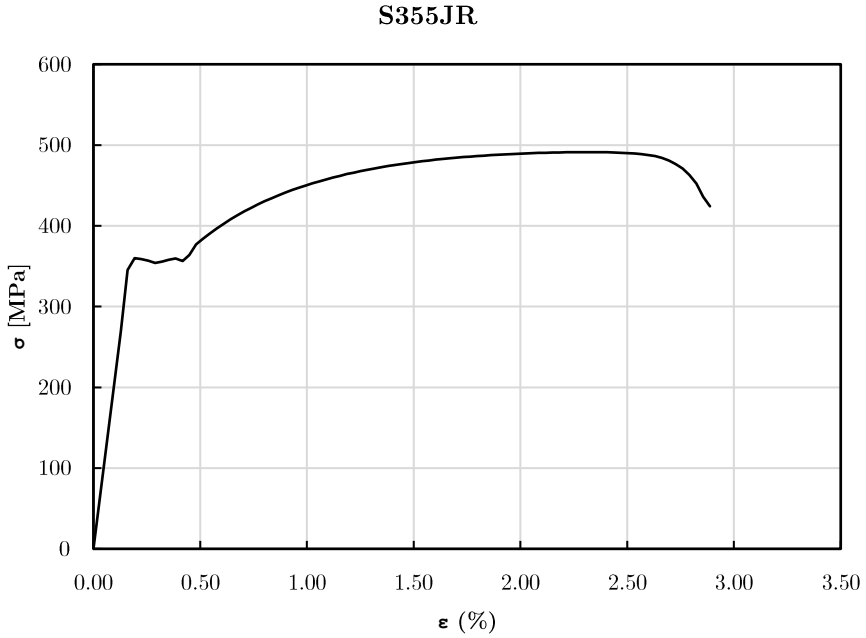

Figure 8.6. Stress-strain average curve for S355JR steel plates.

Tab. 8.2 shows the mechanical parameters measured by the experiment.

Table 8.2. Mechanical characteristics for S355JR plates (experimental).

Material	σ_{MAX} (MPa)	ε_{MAX} (%)	σ_y (MPa)	ε_y (MPa)	E_t (GPa)
S355JR	491.23 ±1.94	1.60 ±0.03	357.76 ±1.98	0.17 ±0.00	207 ±11.60

Fig. 8.7 shows the average σ-ε curve obtained from the tensile tests on the threaded rods used in the construction of the prototype.

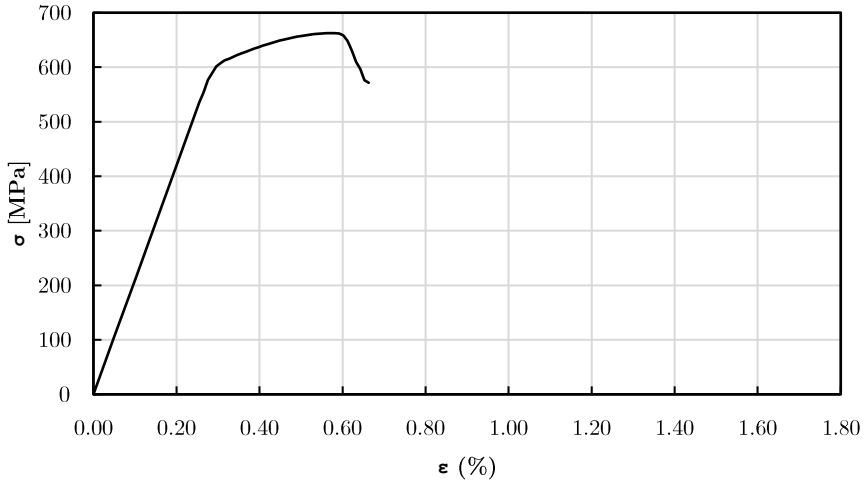

Figure 8.7. Stress-strain average curve for M8 threaded rods.

La Tab. 8.3 shows the mechanical parameters measured by the tensile tests.

Table 8.3. Mechanical characteristics for M8 rods (experimental).

Material	σ_{MAX} (MPa)	ε_{MAX} (%)	σ_y (MPa)	ε_y (MPa)	E_t (GPa)
M8 rods	663.17 ±7.45	0.65 ±0.00	600 ±9.01	0.28 ±0.02	212 ±14.24

8.4.1.2 Adhesives

In the experimental campaign described below, two commercial structural epoxy adhesives and one silicone were selected, namely: 3M™ Scotch-Weld™ 7260 B/A (EPX1), 3M™ Scotch-Weld™ 7240 B/A (EPX2), Dow Corning TM 895 Structural Glazing Sealant (SIL). The choice of these adhesives is due to their different elastic modulus values. Table 4 shows the mechanical and mechanical properties provided by the manufacturer in their data sheets.

Table 8.4. Mechanical characteristics of the adhesives reported by manufacturers.

Adhesive	**EPX 1**	**EPX 2**	**SIL**
Chemical base	Two-part epoxy	Two-part epoxy	One part silicone sealant
Viscosity	Thixotropic	Thixotropic	Pasty
W_t (min)	90÷300	16	15
A_t (°C)	15÷25	15÷25	15÷30
T_g (°C)	61.07	66.87	-
S_t (°C)	-50÷120	-40÷80	-50÷150
τ*(MPa)	33.50	29.40*	-
E_t (MPa)	3000	1500	1
ε_t **(%)	3	-	600
Use	Structural	Semi-Structural	Structural

* On aluminium-steel adherends
**At failure.

The mechanical properties were also evaluated experimentally by performing tensile tests on dogbones of the adhesives, which were carried out according to EN ISO 527-1:2012 [19]. Fig. 8.8 shows the geometry of the test specimens. The characterization of the adhesives was done by comparing the properties of the adhesives after maturation under laboratory conditions.

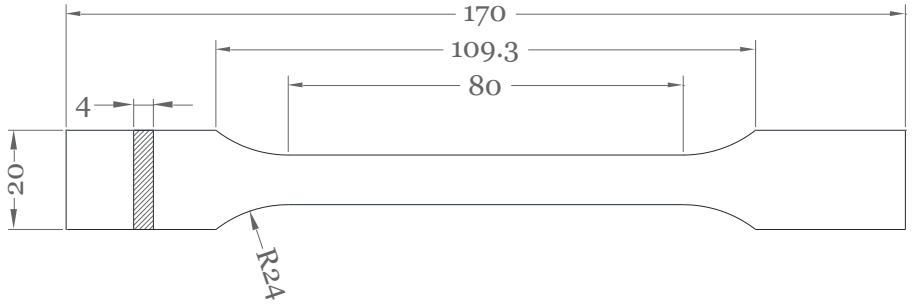

Figure 8.8. Test specimen, according to EN ISO 527-1:2012 [19], measures in mm.

The experimentally measured mechanical parameters for the tested adhesives are summarised - in terms of mean value and standard deviations - in Table 8.5.

Table 8.5. Dogbones mechanical parameters.

Adhesive	σ_{max} (MPa)	ε_{max} (%)	E_t (MPa)
EPX 1	32.10 ±5.66	3.01 ±2.24	2981 ±560
EPX 2	21.88 ±2.87	2.11 ±0.42	1373 ±289
SIL	1.00 ±0.03	151.20 ±55.05	0.50 ±0.15

The results shown in Table 5 confirm the higher stiffness of EPX1 adhesive and the lower tensile strength of EPX2 adhesive after curing under laboratory conditions (20 ± 1 °C/50 ± 5% RH).

8.5 Experiments

The load tests on the Tensegrity Floor prototype were performed by reproducing the pedestrian load conditions expected for environments subject to crowding.
The applied load was determined according to the values foreseen in the Italian technical standard (NTC 2018, [18]); in particular, a live load of 4.00 kN/m^2 was used in different geometric combinations during the experimental phase. All load tests were performed under laboratory conditions (22±3 °C, 50±5 % RH).
Before the assembly phase of the prototype, the stress to be applied to the steel bars was determined using a static analysis and the equivalent moment to be applied using a torque wrench: 6 Nm.
Fig. 8.9 shows the three loading conditions considered during the experiments. In particular, the following are distinguished:

i) Symmetrical load, distributed on the central span;
ii) Asymmetrical load distributed on the lateral span;
iii) Uniformly distributed load.;

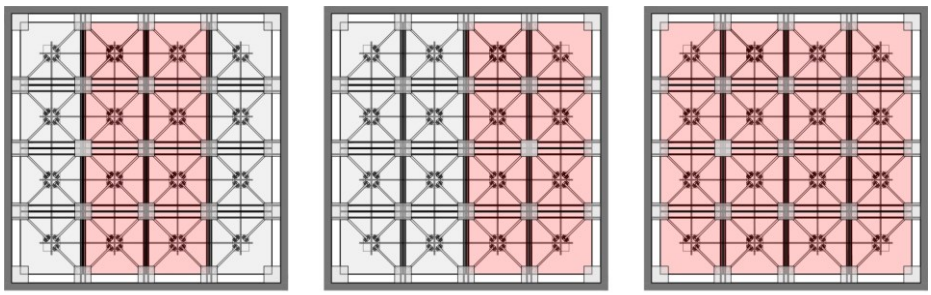

Figure 8.9. Load cases: a) symmetrical load distributed on the central span; b) asymmetrical load distributed on the lateral span; c) uniformly distributed load.

Each load configuration was applied both in the case of glass panels simply supported on the metal substructure (S. SUPP.) and in the case of panels bonded to the substructure by

adhesive joints, in order to highlight the contribution to the stiffness of the floor due to the cooperation between the metal substructure and the glass deck.
In the measurement of deformations, each load combination was applied three times.
Two different measurement systems were used and compared to measure the displacements: optical measurement and inductive displacement transducer measurement.
For the optical stereoscopic measurement (OSM), two CMOS cameras with a resolution of 1280×1024 pixels (Pixelink®B371F) were used, arranged at different angles, and allowing the simultaneous acquisition of stereoscopic images at regular intervals of 2 frames/second, which made it possible to associate each point of the studied surface with a specific pixel. The cameras are calibrated in three dimensions using the Heikkila algorithm with a common reference system. The principle on which the measurement of the displacement, and thus the calculation of the deformations is based is the determination of the spatial positions of circular markers attached to the glass structure. A code developed in Matlab® was used to determine the intrinsic parameters (focal lengths, optical centre coordinates, skewness), the extrinsic parameters (rotation angles, position vector) and the radial distortion coefficients for the two cameras. These parameters were then used to calculate the stereoscopic triangulation required to determine the position of the markers attached to the glass deck. In order to allow the correct acquisition of the stereoscopic images, the distribution of the loads was divided between the individual glass panel. In particular, the weights were arranged using cylindrical containers with a weight of 27 kgf each.
The measurements with digital transducers were made using PT50T sensors, with a range of 0-50 mm, supplied by MAE Instruments®. For both measurement techniques, the measurement error is ±0.01 mm.
Fig. 8.10 shows the test setup.

Figure 8.10. Experimental setup.

8.6 Results and discussion

In this section, the results obtained with the different load combinations are reported. In particular, the measured displacements for the different constraint configurations (i.e., simple support or bonding) and load distributions are analysed and compared. Fig. 8.11 shows the numbering of the nodes considered for the LVDTs measurements in the plane view. The optical measurement, on the other hand, allowed the displacements to be measured for all the upper nodes, except for the edge nodes.

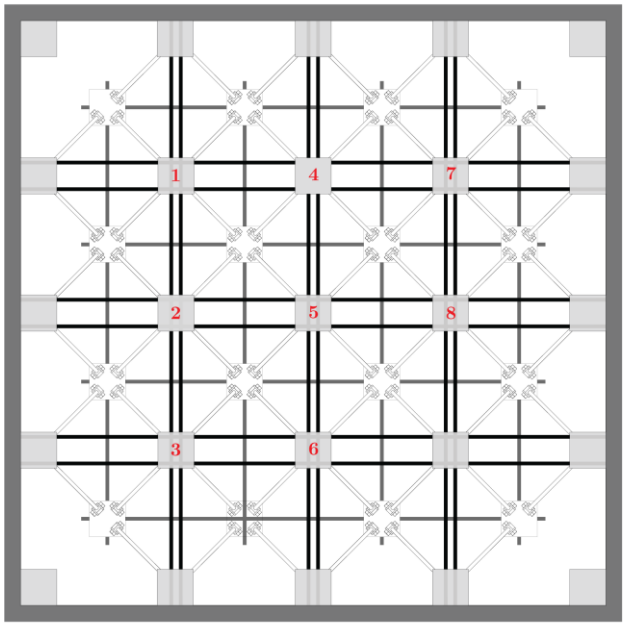

Figure 8.11. Layout of nodes considered for LVDTs measurements.

In the following graphical representations - in order to obtain a complete mapping of the displacements - the LVDTs values of the ninth point are obtained by linear interpolation of the displacements from the optical measurements.

8.6.1 Simply supported glass deck configuration – S. SUPP.

Figs. 8.12-8.14 show the graphic mapping of the vertical displacement values recorded by the digital measurement (LVDT) for the structural configuration with simply supported glass deck.

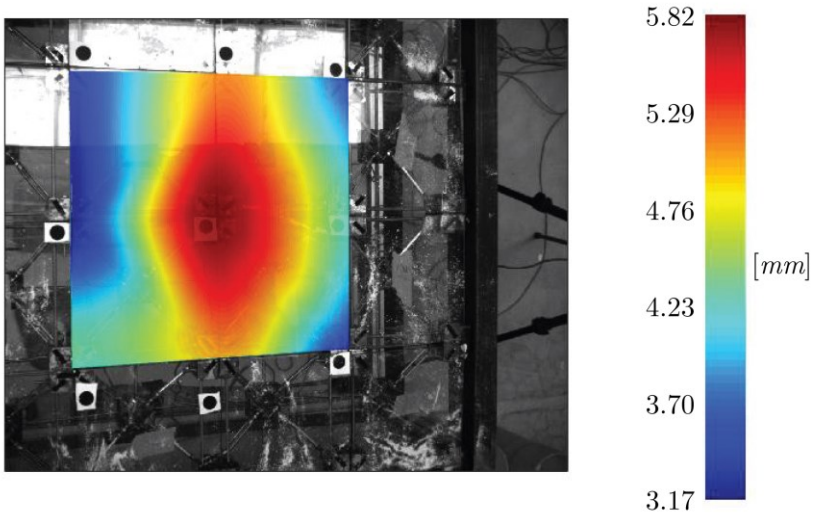

Figure 8.12. LVDTs - Mapping of average displacements for distributed load on central span (S. SUPP.).

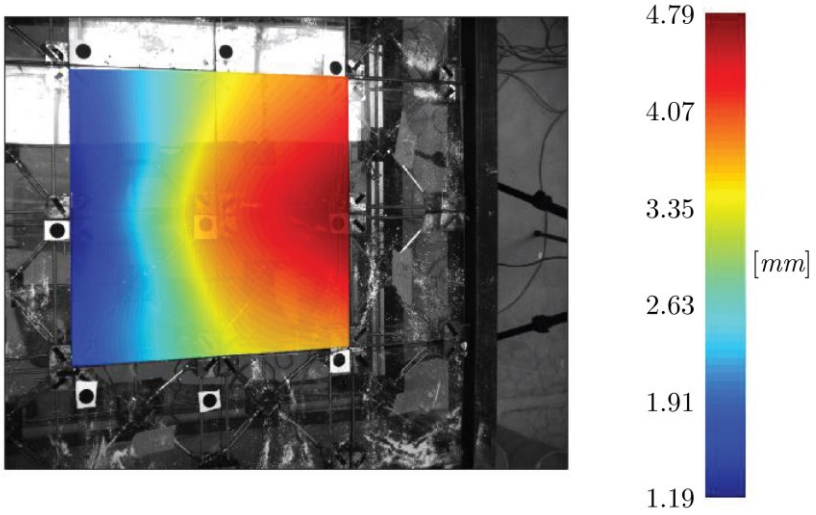

Figure 8.13. LVDTs - Mapping of average displacements for distributed load on lateral span (S. SUPP.).

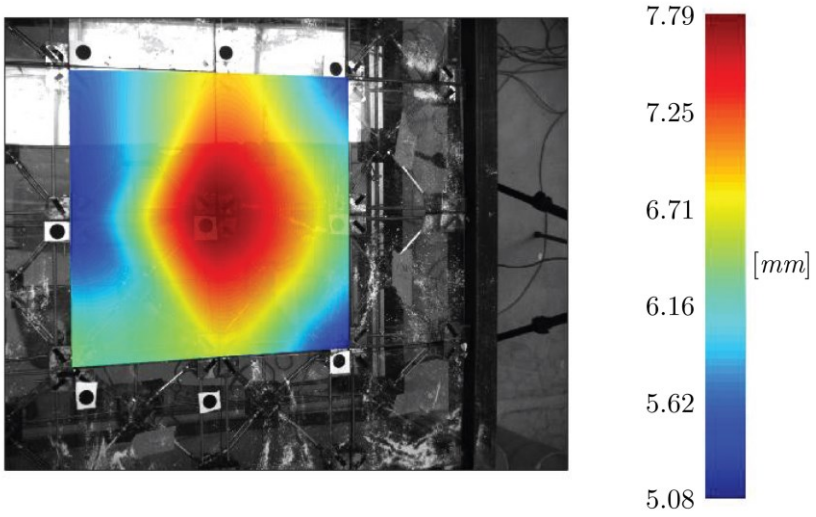

Figure 8.14. LVDTs - Mapping of average displacements for uniformly distributed load (S.SUPP.).

The results of the optical stereoscopic measurement are shown in Figs. 8.15-8.17. The displacements are mapped by a cubic interpolation between the values obtained from the markers positioned in correspondence with the upper structural nodes.

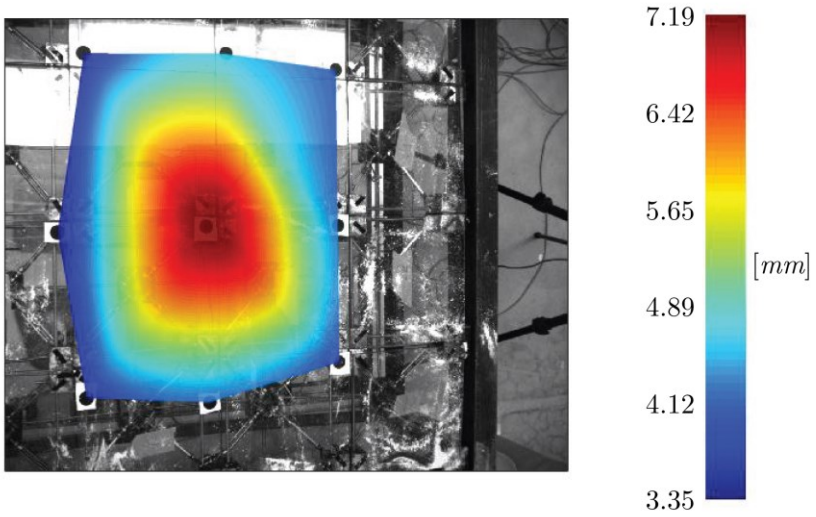

Figure 8.15. OSM - Mapping of displacements (cubic interpolation) for distributed load on central span (S. SUPP.).

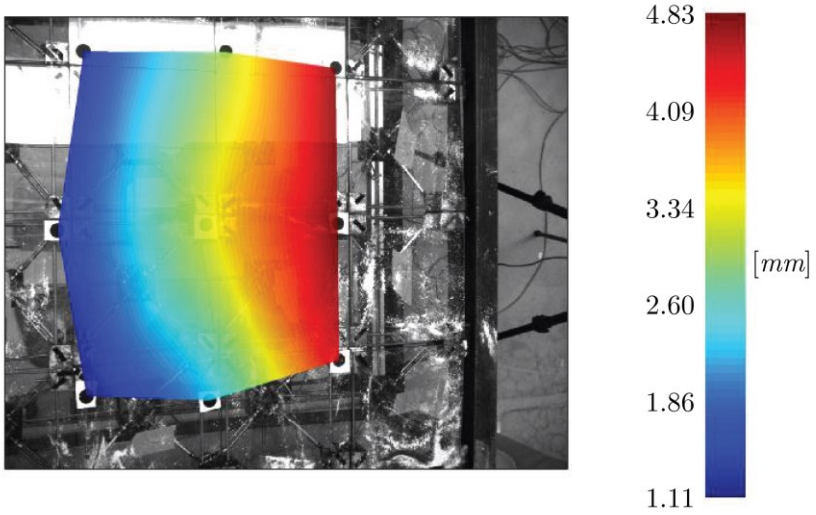

Figure 8.16. OSM - Mapping of displacements (cubic interpolation) for distributed load on lateral span (S. SUPP.).

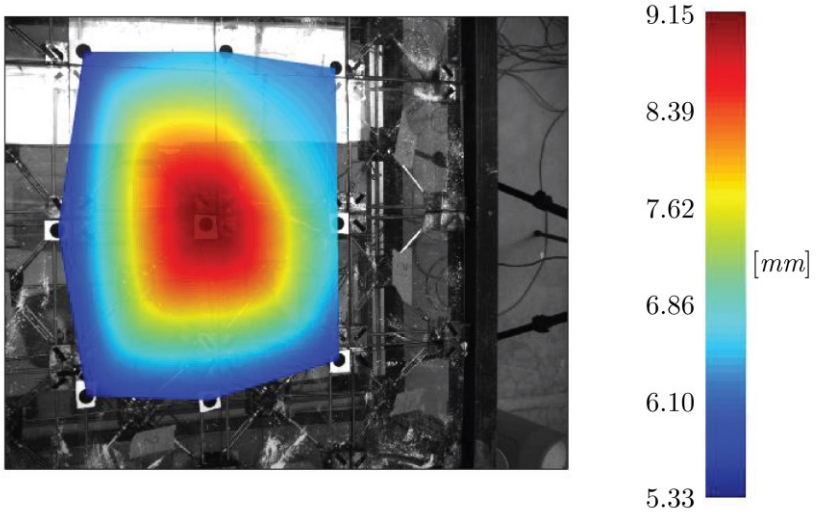

Figure 8.17. OSM - Mapping of displacements (cubic interpolation) for uniformly distributed load (S. SUPP.).

Fig. 8.18(a-c) summarises the average values for the different load cases and for the two different displacement measurement methods.

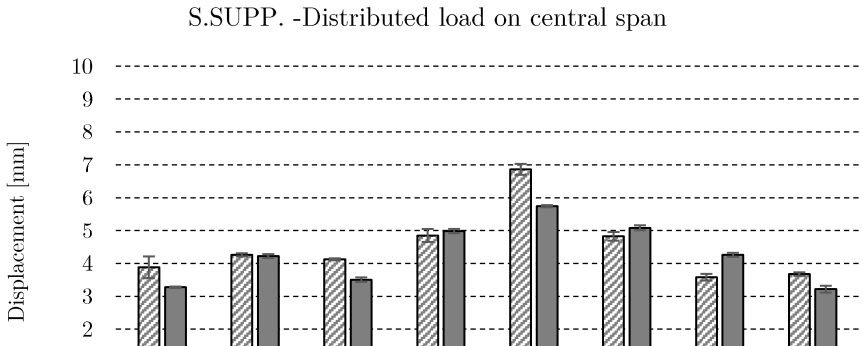

	1	2	3	4	5	6	7	8
OSM	3.88	4.26	4.13	4.85	6.86	4.82	3.58	3.68
LVDTs	3.28	4.23	3.51	4.99	5.74	5.09	4.26	3.22

(a)

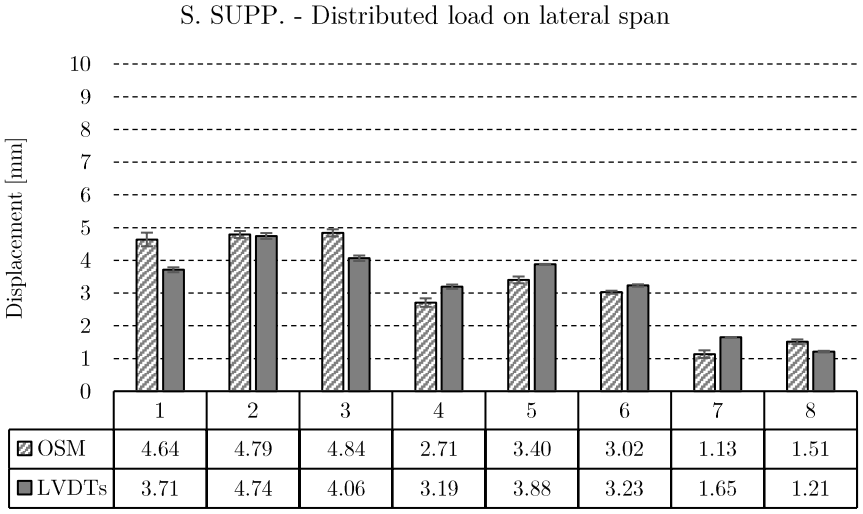

(b)

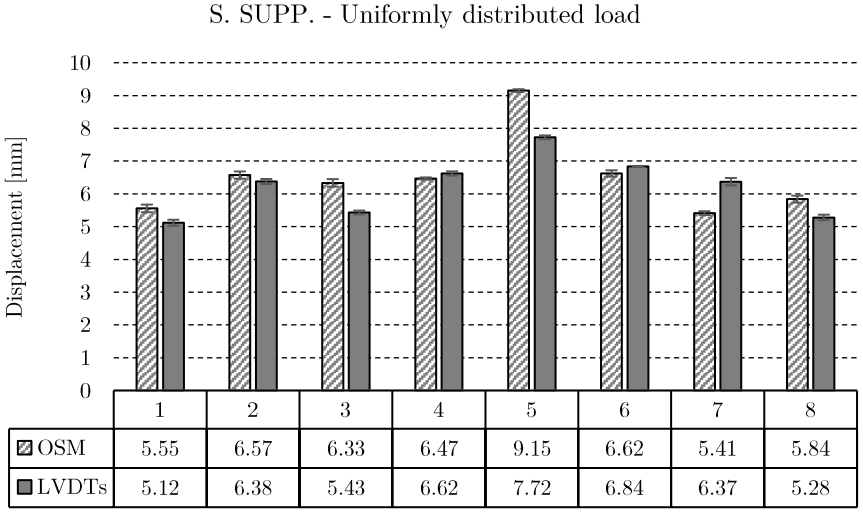

(c)

Figure 8.18. S. SUPP. – average displacements for each node: (a) for symmetric load distribution; (b) for asymmetric load distribution; (c) for uniformly distributed load.

The results obtained from the optical measurements slightly overestimate the magnitude of the displacements, especially at the most stressed nodes. In general, a good agreement between photogrammetric and digital measurements can be observed. This aspect highlights the applicability of optical measurement in the field of civil engineering, as it provides a valid solution for the measurements of the studied displacements when it is not possible to perform

conventional digital measurements. It is observed that, in the case of simply supported deck, the deflection exceeds the maximum allowable value indicated in the Italian building code (NTC 2018 [18], equal to 4.80 mm), as described in the following paragraphs.

8.6.2 Adhesively bonded glass deck – EPX1 adhesive

The measurements recorded for the deck bonded to the substructure with EPX1 epoxy adhesive are shown below. Figs. 8.19-8.21 show the graphical representation of the vertical displacement values recorded using digital measurements (LVDTs).

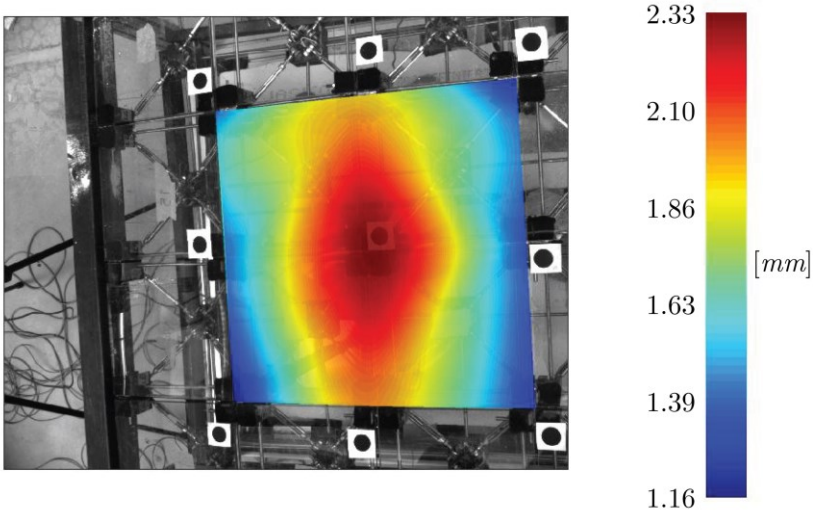

Figure 8.19. LVDTs – Mapping of average displacements for distributed load on central span (EPX1).

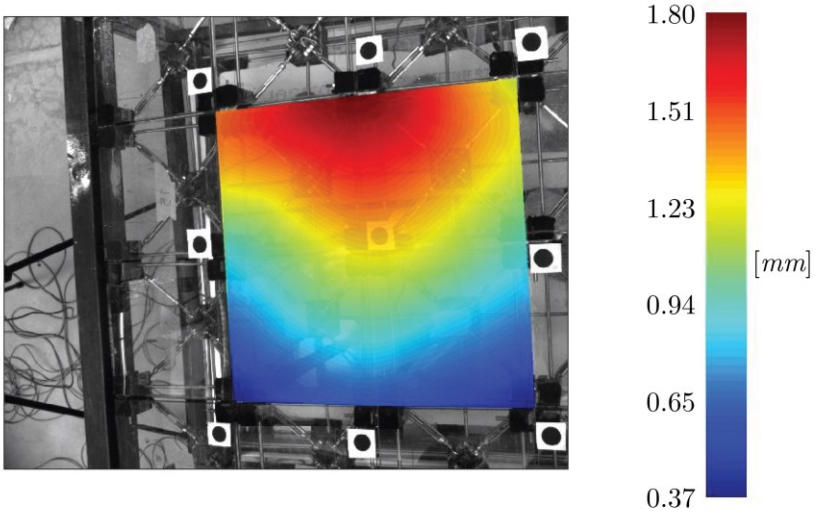

Figure 8.20. LVDTs - Mapping of average displacements for distributed load on lateral span (EPX1).

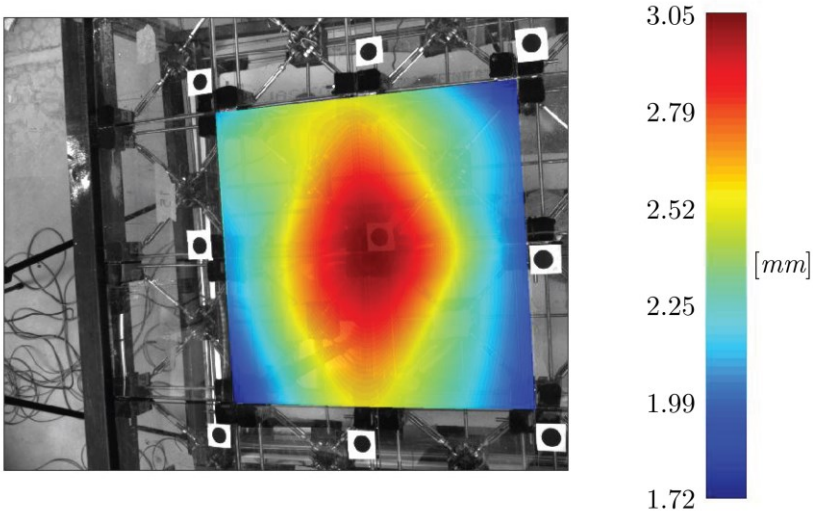

Figure 8.21. LVDTs - Mapping of average displacements for uniformly distributed load (EPX1).

The results of the optical measurement are shown in Figs. 8.22-8.24.

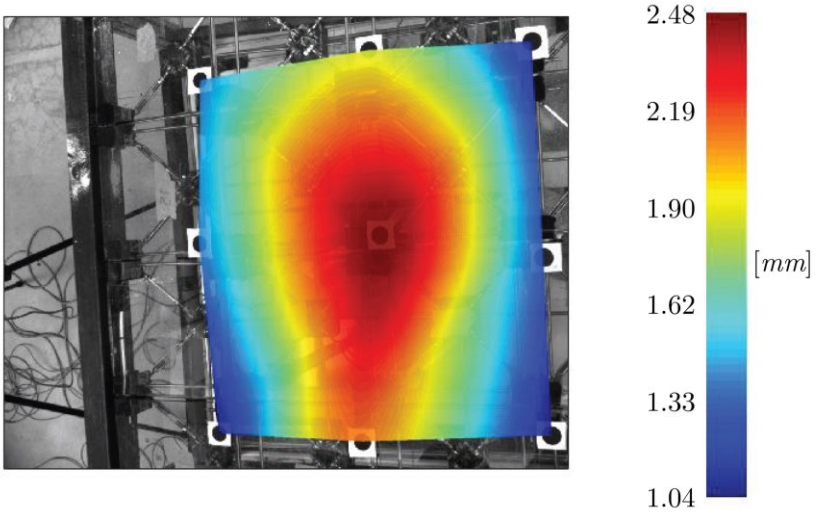

Figure 8.22. OSM - Mapping of displacements (cubic interpolation) for distributed load on central span (EPX1).

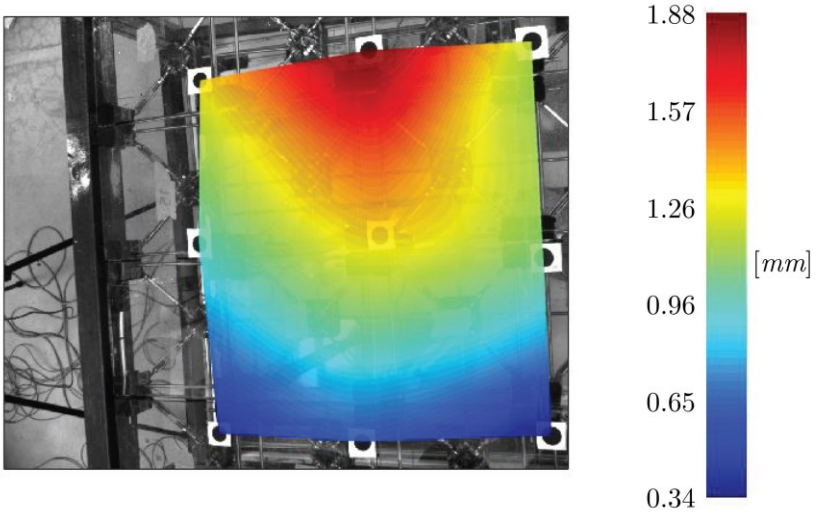

Figure 8.23. OSM - Mapping of displacements (cubic interpolation) for distributed load on lateral span (EPX1).

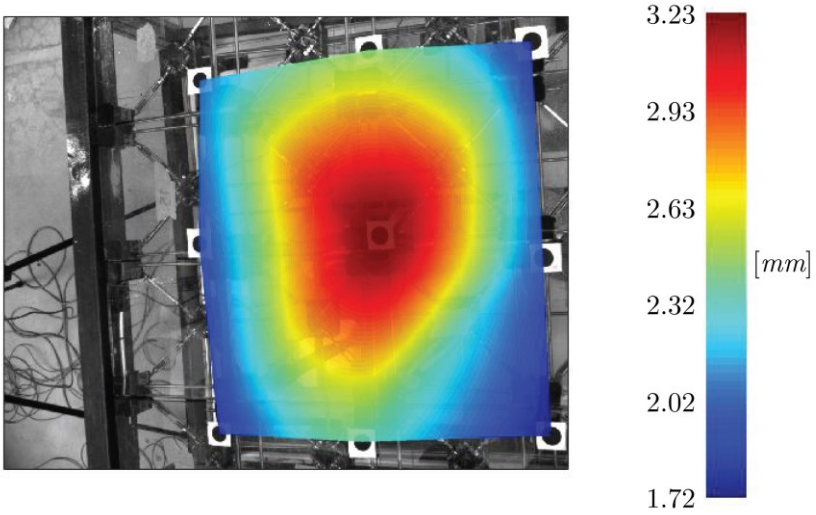

Figure 8.24. OSM - Mapping of displacements (cubic interpolation) for uniformly distributed load (EPX1).

Fig. 8.25(a-c) summarises for each node the values measured by optical (OSM) and digital (LVDTs) measurements.

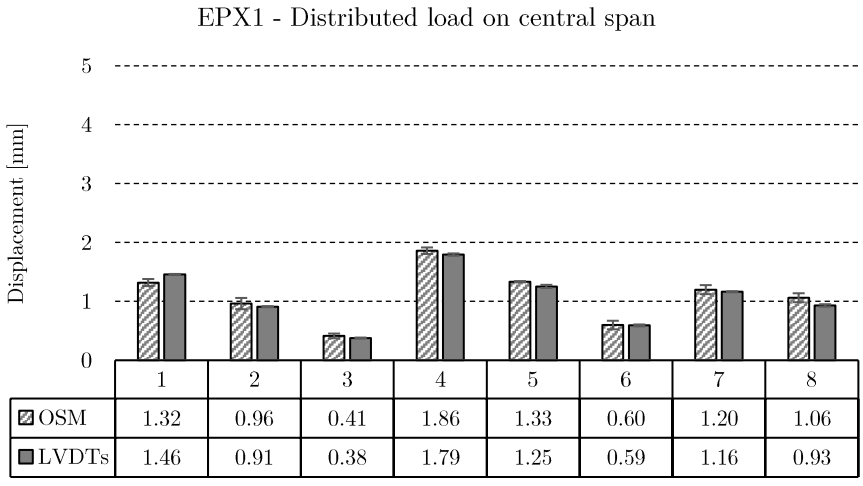

	1	2	3	4	5	6	7	8
OSM	1.32	0.96	0.41	1.86	1.33	0.60	1.20	1.06
LVDTs	1.46	0.91	0.38	1.79	1.25	0.59	1.16	0.93

(a)

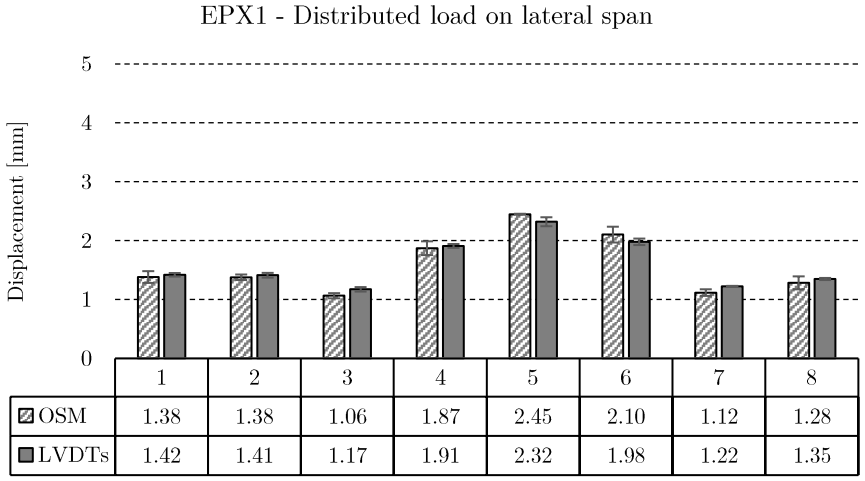

	1	2	3	4	5	6	7	8
OSM	1.38	1.38	1.06	1.87	2.45	2.10	1.12	1.28
LVDTs	1.42	1.41	1.17	1.91	2.32	1.98	1.22	1.35

(b)

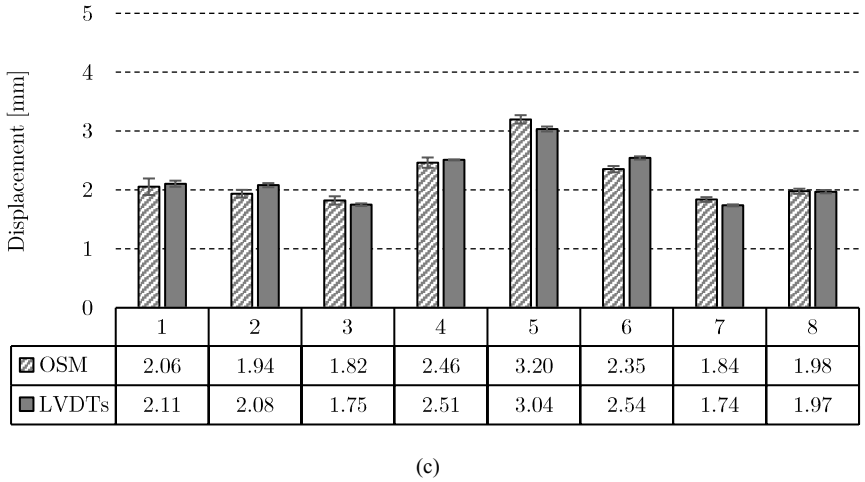

	1	2	3	4	5	6	7	8
OSM	2.06	1.94	1.82	2.46	3.20	2.35	1.84	1.98
LVDTs	2.11	2.08	1.75	2.51	3.04	2.54	1.74	1.97

(c)

Figure 8.25. EPX1 – average displacements for each node: (a) for symmetric load distribution; (b) for asymmetric load distribution; (c) for uniformly distributed load.

Considering the case of distributed load on the central span, a reduction in deflection of -69% and -68% was observed for the most stressed node (upper central node) according to the measurements obtained by optical and digital measurement, respectively. For the most stressed nodes under asymmetric loading, a reduction in deflection of -48% and -51% was observed by optical and digital measurement, respectively. Finally, it could be observed how

the worst configuration – i.e., the one characterised by a load uniformly distributed over the entire area of the floor – recorded a reduction in the maximum displacements (node No. 5) of -61% in the optical measurements and -59% in the digital measurements.
It may also be noted that the values of maximum deflection measured for the structural configuration with the deck constrained to the substructure respect the limit value established by the Italian building code (NTC 2018 [18]) on the allowable deformations of the floors in service conditions, given in Equation 1.

$$\frac{d_{max}}{L} = \frac{1}{250} \quad (1)$$

where d_{max} and L are the maximum deflection and the span of the floor, respectively. In the present case, the span is 1200 mm; therefore, the maximum allowable deflection is 4.80 mm. In contrast, in the case of simple support, there is no load case where the limitation expressed by Equation (1) can be met.
The results obtained illustrate the structural cooperation between the glass deck and the metal substructure, stiffening the structure at the same working load compared to an analogous solution with a deck not constrained to the substructure.

8.6.3 Adhesively bonded glass deck – EPX2 adhesive

The following is a report of the measurements recorded in the case of the deck cooperating with the substructure by adhesive joints. Figs. 8.26-8.28 show the graphical representation of the vertical displacement values recorded using digital measurements (LVDTs).

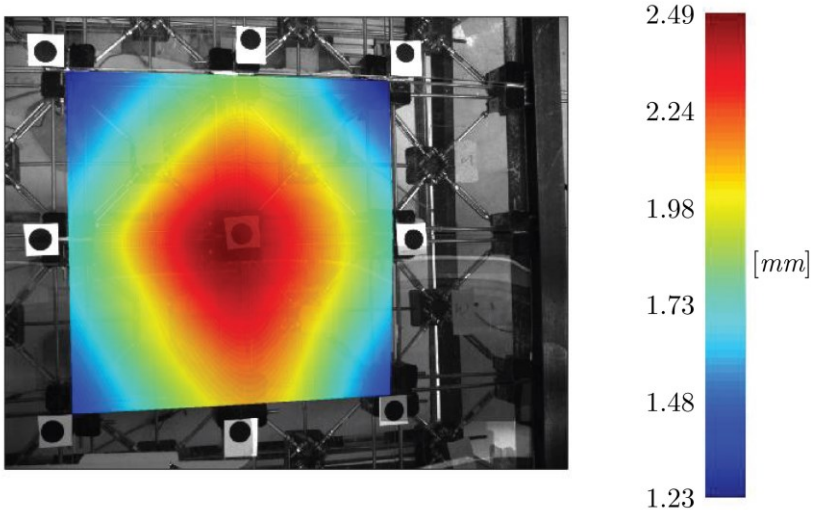

Figure 8.26. LVDTs - Mapping of average displacements for distributed load on central span (EPX2).

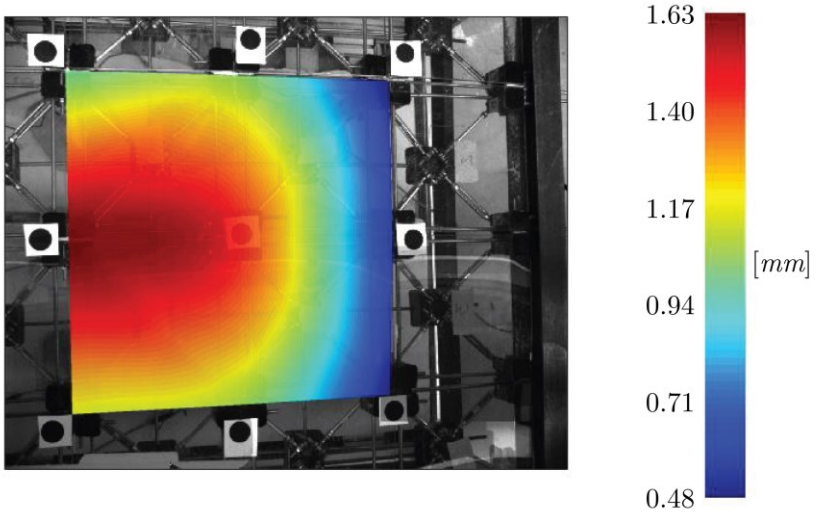

Figure 8.27. LVDTs - Mapping of average displacements for distributed load on lateral span (EPX2).

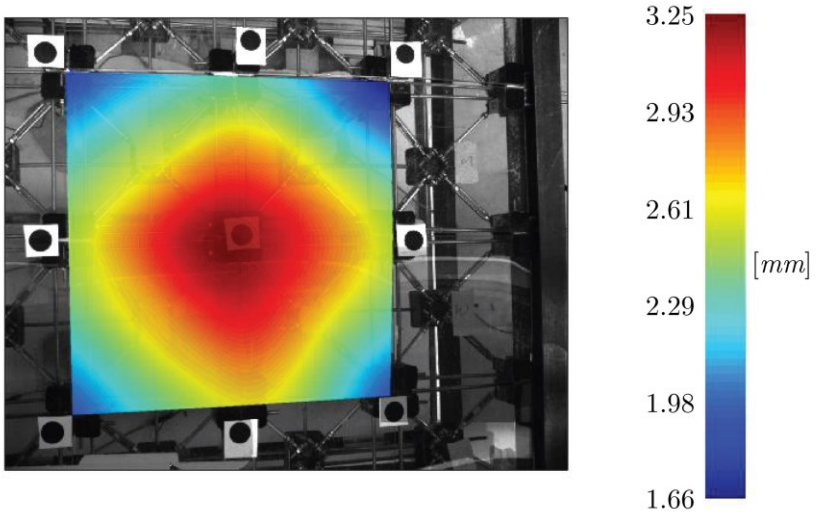

Figure 8.28. LVDTs - Mapping of average displacements for uniformly distributed load (EPX2).

The results obtained by optical measurement (OSM) are shown in Figs. 8.29-8.31.

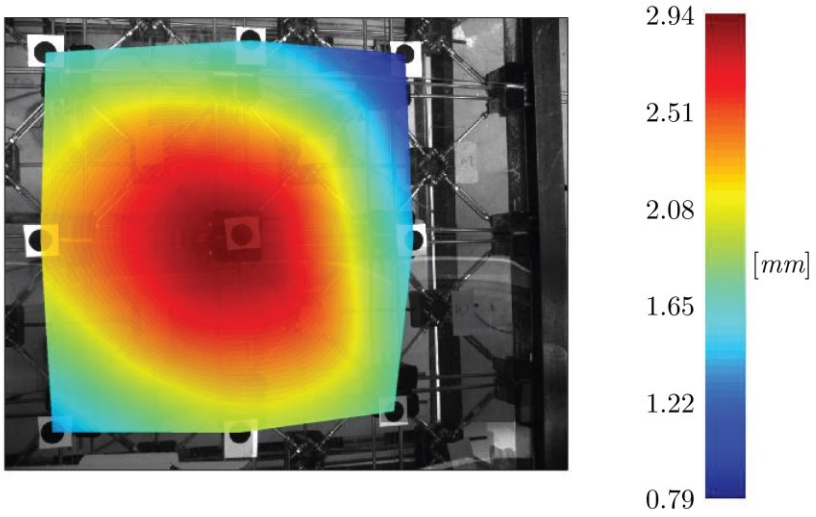

Figure 8.29. OSM - Mapping of displacements (cubic interpolation) for distributed load on central span (EPX2).

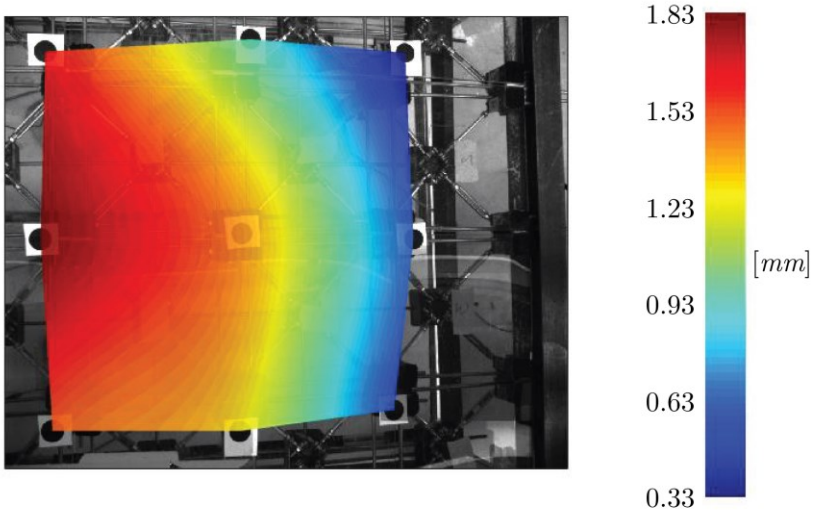

Figure 8.30. OSM - Mapping of displacements (cubic interpolation) for distributed load on lateral span (EPX2).

.

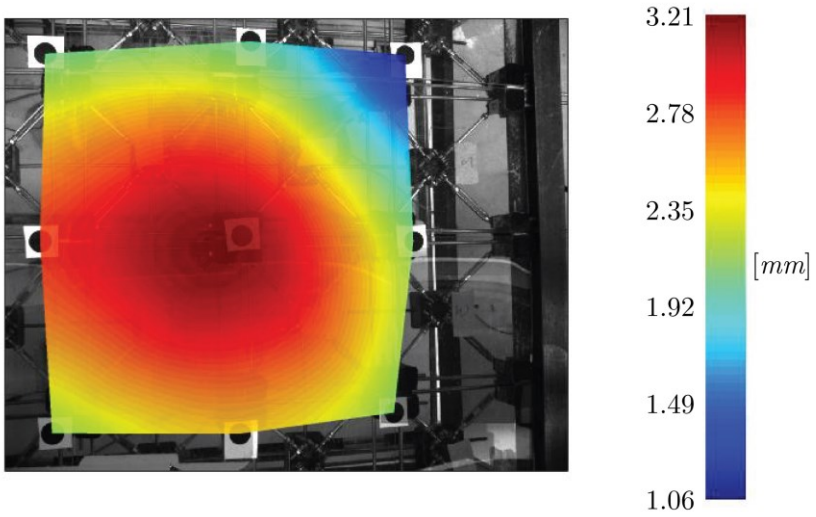

Figure 8.31. OSM - Mapping of displacements (cubic interpolation) for uniformly distributed load (EPX2).

Fig. 8.32(a-c) summarises the optical and digital measurement values (LVDTs) for each node.

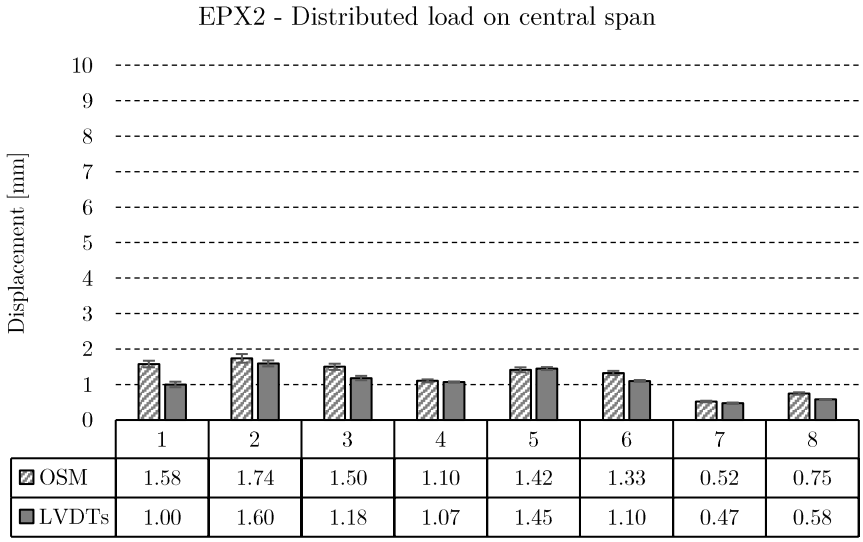

	1	2	3	4	5	6	7	8
OSM	1.58	1.74	1.50	1.10	1.42	1.33	0.52	0.75
LVDTs	1.00	1.60	1.18	1.07	1.45	1.10	0.47	0.58

(a)

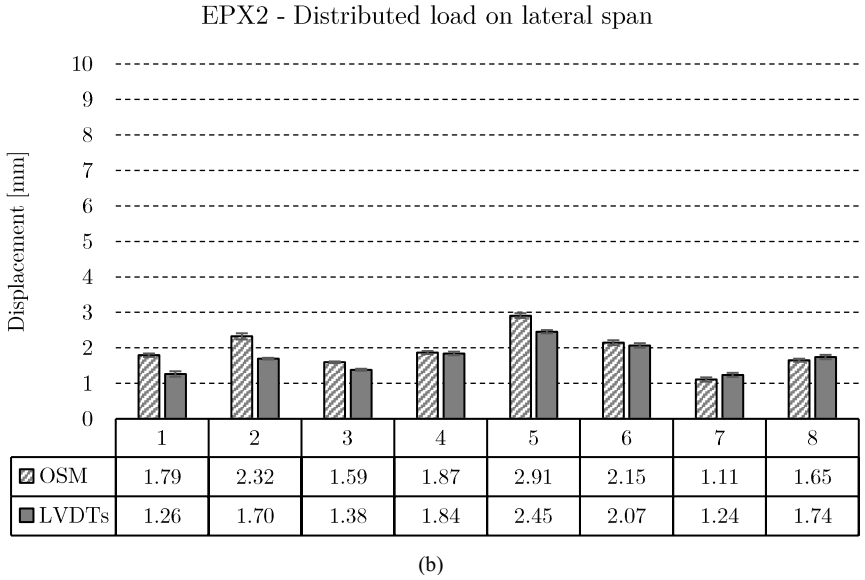

	1	2	3	4	5	6	7	8
OSM	1.79	2.32	1.59	1.87	2.91	2.15	1.11	1.65
LVDTs	1.26	1.70	1.38	1.84	2.45	2.07	1.24	1.74

(b)

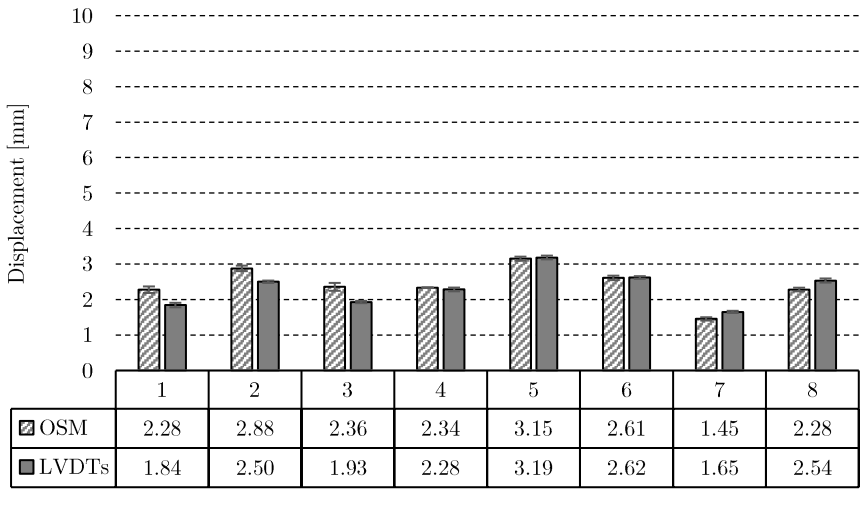

	1	2	3	4	5	6	7	8
OSM	2.28	2.88	2.36	2.34	3.15	2.61	1.45	2.28
LVDTs	1.84	2.50	1.93	2.28	3.19	2.62	1.65	2.54

(c)

Figure 8.32. EPX2 – average displacements for each node: (a) for symmetric load distribution; (b) for asymmetric load distribution; (c) for uniformly distributed load.

Considering the case of distributed load on the central span, a reduction in deflection of -70% and -75% was observed for the most stressed node (upper central node) according to the

measurements obtained by optical and digital technology, respectively. For the most stressed nodes in the case of asymmetric loading, a reduction in deflection of -39% and -48% was observed with optical (OSM) and LVDT technology, respectively. Finally, the worst load configuration shows a -59% reduction in the maximum deflection (node No. 5) with both optical and digital measurements.
Also in this case, the measured values of maximum deflection correspond to the limit prescribed by the Italian building code (NTC 2018 [18]) s on the allowable deformations of floors under service conditions.

8.6.4 Adhesively bonded glass deck – SIL adhesive

In the following, the measurements are performed for the case where the glass deck is bonded to the substructure by the SIL adhesive. Figs. 8.33-8.35 show the graphic mapping of the vertical displacement values recorded by means of digital measurements (LVDTs).

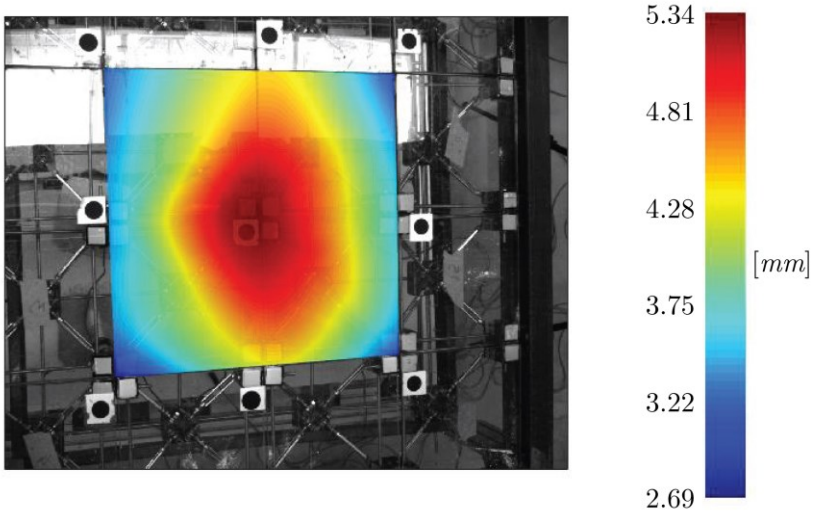

Figure 8.33. LVDTs – Mapping of average displacements for distributed load on central span (SIL).

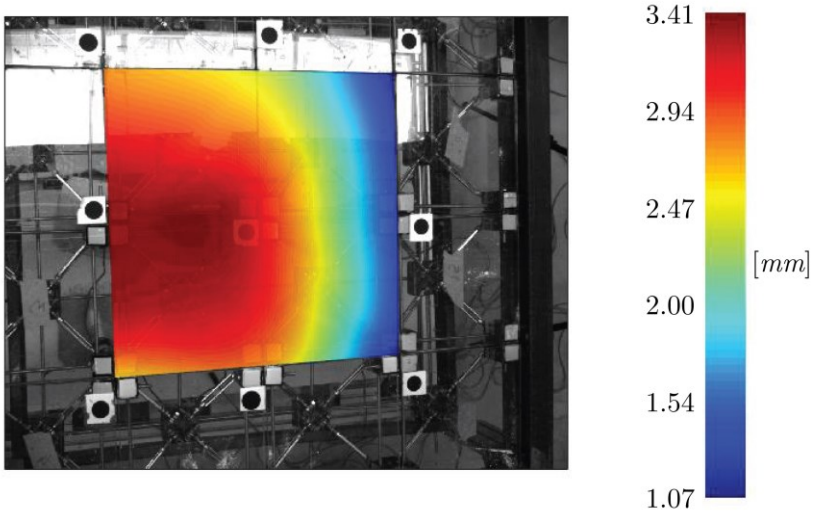

Figure 8.34. LVDTs - Mapping of average displacements for distributed load on lateral span (SIL).

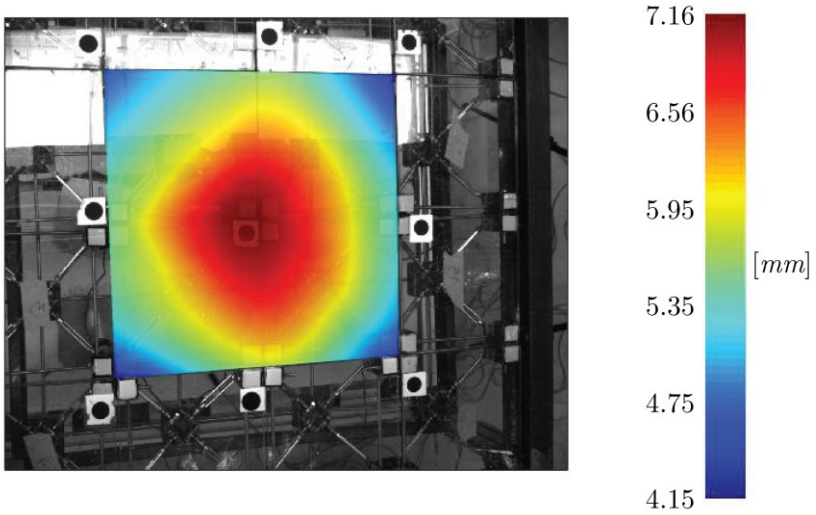

Figure 8.35. LVDTs - Mapping of average displacements for uniformly distributed load (SIL).

The results obtained by optical measurement (OSM) are shown in Figs. 8.36-8.38.

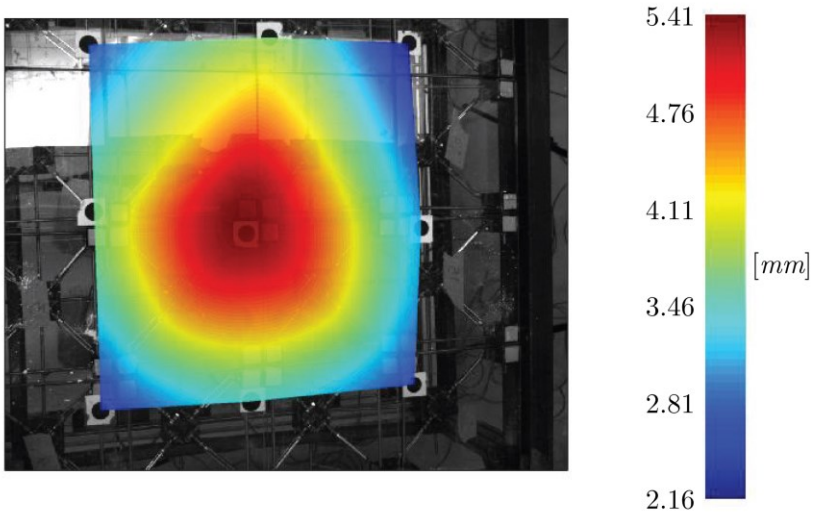

Figure 8.36. OSM - Mapping of displacements (cubic interpolation) for distributed load on central span (SIL).

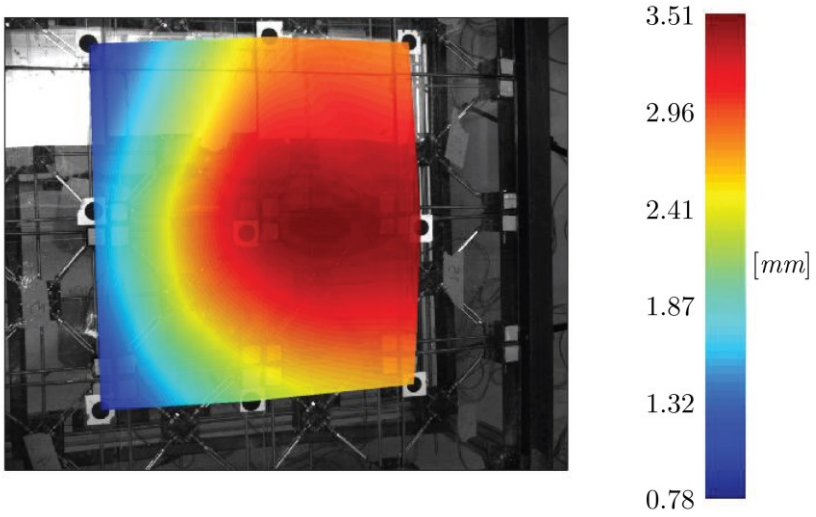

Figure 8.37. OSM - Mapping of displacements (cubic interpolation) for distributed load on lateral span (SIL).

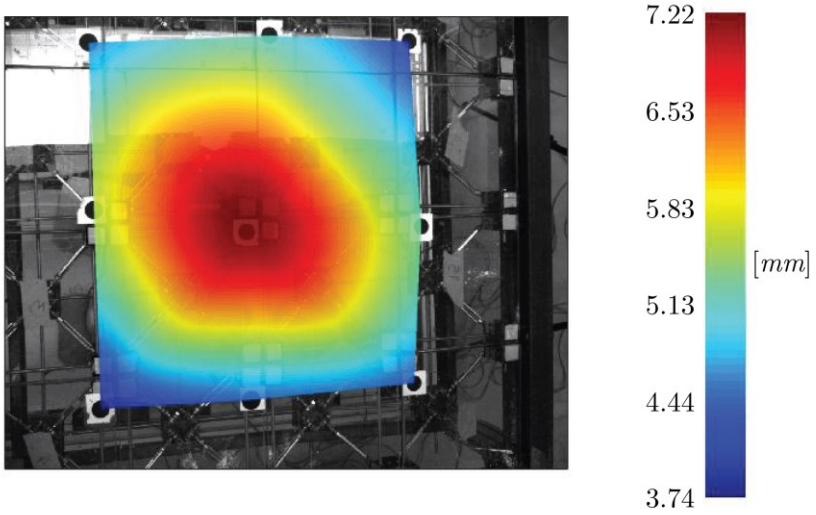

Figure 8.38. OSM - Mapping of displacements (cubic interpolation) for uniformly distributed load (SIL).

Fig. 8.39(a-c) summarises for each node the values measured by optical and digital measurement (LVDTs).

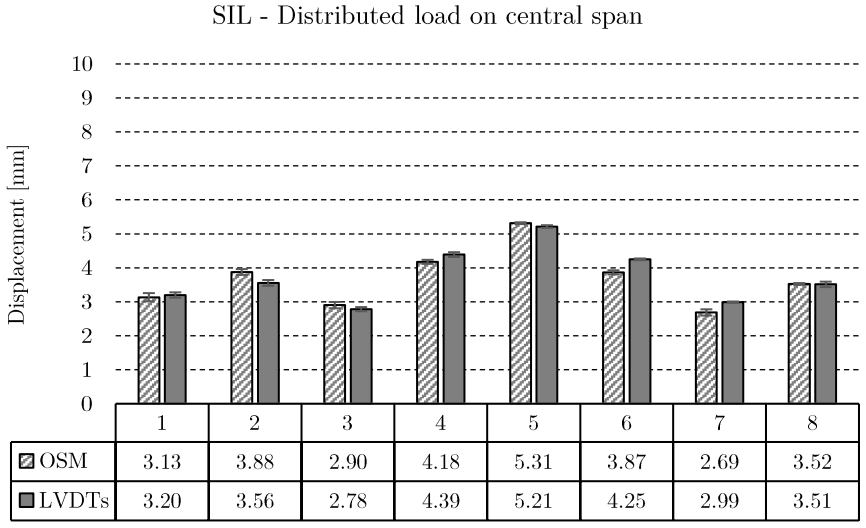

	1	2	3	4	5	6	7	8
OSM	3.13	3.88	2.90	4.18	5.31	3.87	2.69	3.52
LVDTs	3.20	3.56	2.78	4.39	5.21	4.25	2.99	3.51

(a)

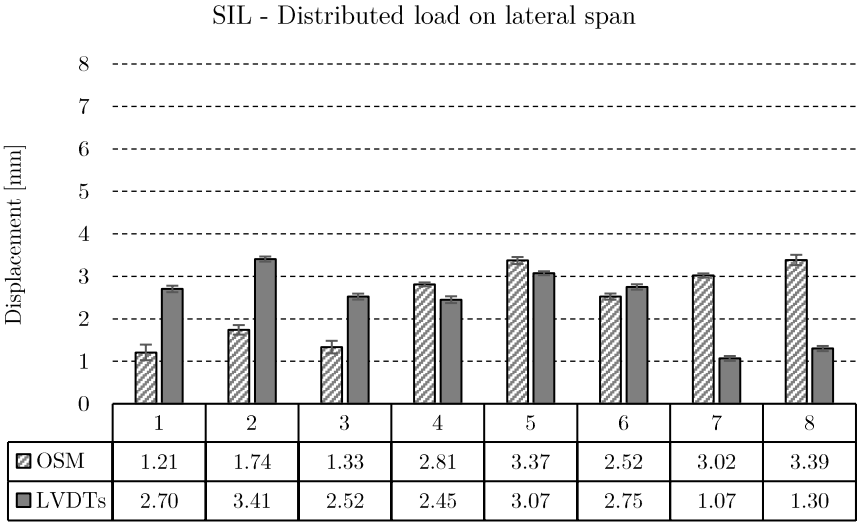

	1	2	3	4	5	6	7	8
OSM	1.21	1.74	1.33	2.81	3.37	2.52	3.02	3.39
LVDTs	2.70	3.41	2.52	2.45	3.07	2.75	1.07	1.30

(b)

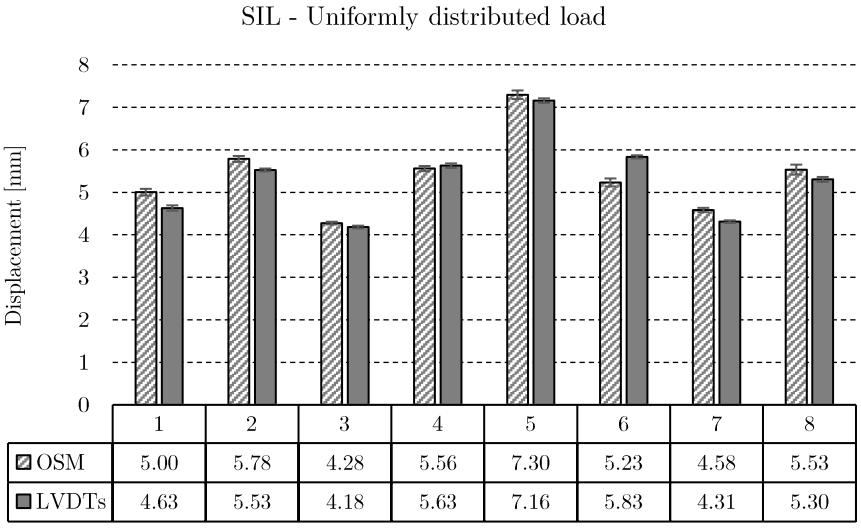

	1	2	3	4	5	6	7	8
OSM	5.00	5.78	4.28	5.56	7.30	5.23	4.58	5.53
LVDTs	4.63	5.53	4.18	5.63	7.16	5.83	4.31	5.30

(c)

Figure 8.39. SIL – average displacements for each node: (a) for symmetric load distribution; (b) for asymmetric load distribution; (c) for uniformly distributed load.

In the case of the glass deck bonded to the metal substructure with silicone adhesive (SIL), displacements were observed to be intermediate between those of the simply supported configuration (S. SUPP.) and those of the deck bonded with epoxy adhesives (EPX1 and EPX2). This aspect reflects the characteristic stiffness of the adhesive used, which in the

present case determines a modest increase in stiffness compared to the simply supported configuration.
It can be observed that the worst load case (i.e., uniformly distributed load) resulted in -33% reduction in the maximum displacements (node No. 5) in the digital measurements.
Fig. 8.40(a-c) summarises the displacements measured with digital technique for nodes 1-8 according to the type of adhesive used.

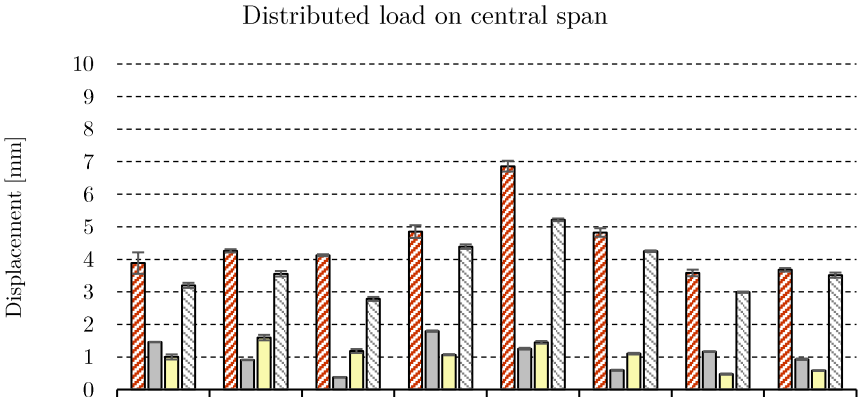

	1	2	3	4	5	6	7	8
S. SUPP.	3.88	4.26	4.13	4.85	6.86	4.82	3.58	3.68
EPX1	1.46	0.91	0.38	1.79	1.25	0.59	1.16	0.93
EPX2	1.00	1.60	1.18	1.07	1.45	1.10	0.47	0.58
SIL	3.20	3.56	2.78	4.39	5.21	4.25	2.99	3.51

(a)

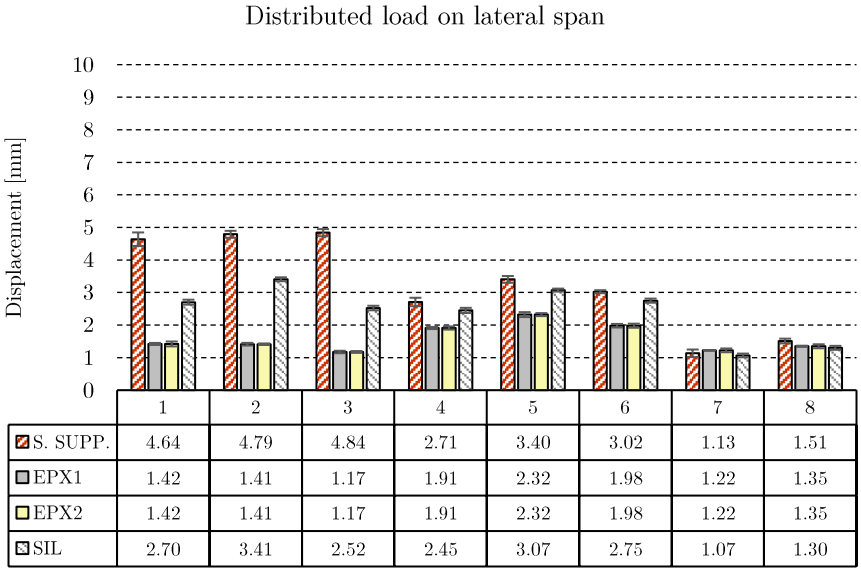

	1	2	3	4	5	6	7	8
S. SUPP.	4.64	4.79	4.84	2.71	3.40	3.02	1.13	1.51
EPX1	1.42	1.41	1.17	1.91	2.32	1.98	1.22	1.35
EPX2	1.42	1.41	1.17	1.91	2.32	1.98	1.22	1.35
SIL	2.70	3.41	2.52	2.45	3.07	2.75	1.07	1.30

(b)

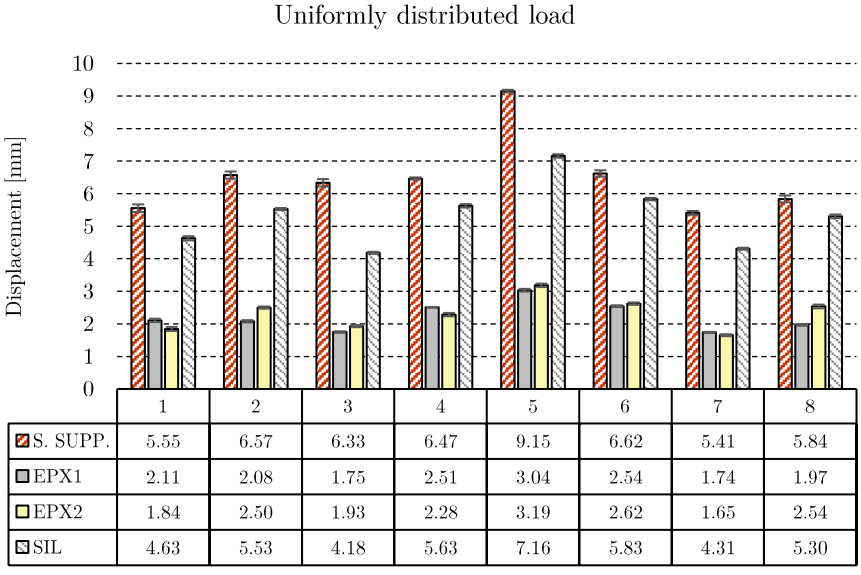

	1	2	3	4	5	6	7	8
S. SUPP.	5.55	6.57	6.33	6.47	9.15	6.62	5.41	5.84
EPX1	2.11	2.08	1.75	2.51	3.04	2.54	1.74	1.97
EPX2	1.84	2.50	1.93	2.28	3.19	2.62	1.65	2.54
SIL	4.63	5.53	4.18	5.63	7.16	5.83	4.31	5.30

(c)

Figure. 8.40. Summary of mean displacements (LVDTs) for each node, adhesive and load case tested: (a) for load distributed on central span; (b) for load distributed on lateral span; (c) for uniformly distributed load.

It is possible to observe how the use of the adhesive bonding affects the mechanical behaviour of the resulting hybrid structural system in terms of the deformations measured during its service condition.
The results show the effectiveness of the adhesive technology in increasing the overall stiffness of the structural element compared to a simply supported configuration. This aspect allows to obtain better mechanical performances for the same load, thus reducing the resistant sections of the materials used.
Moreover, the choice of adhesive in the design phase is determined not only by the cost and mechanical properties, but also by the specific application. Although EPX1 offers better performance, it is more expensive and has a lower glass transition temperature (Tg) than EPX2. Therefore, for applications that are exposed to high temperatures for a long period of time, it leads to the choice of the EPX2 adhesive as the most suitable.

8.7 Conclusions

This work presents the results of an experimental campaign to investigate the mechanical performance of a tensegrity floor with different constraint configurations between the glass deck and the metal substructure and under different loading conditions.
The main purpose of the presented study is to verify the influence of the adhesive joint on the mechanical performance of the "Tensegrity Floor" presented in the patent (Patent No. 000014426973). This verification was carried out through load tests on a 1:2 scale prototype, simulating the pedestrian live load and measuring the displacements using two different technologies (optical and digital measurements) in order to quantify the increase in stiffness obtained by changing the constraint conditions of the deck compared to the simple support configuration.
The main results are the following:

- from the point of view of mechanical performance, the configuration with the deck bonded to the substructure allows a significant increase in the global stiffness of the resulting structure (up to +75% - EPX2) compared to the simple support configuration;
- the overall mechanical performance reflects the mechanical characteristics of the adhesives used. Indeed, adhesives with higher intrinsic stiffness correspond to an increase in stiffness of the whole hybrid structural system;
- from the technical-design point of view, the use of structural adhesives allows a significant increase in the stiffness under load, thus reducing the resistant section of the structural elements used, respecting the limits imposed by the building code. This aspect simplifies the technology of the resulting industrial product, which is characterised by a reduced number of machining operations, elements and resulting environmental emissions.

Future research developments will focus on the behaviour of bonded joints after being exposed to severe environmental conditions (e.g., in a controlled environment with 100% RH at a temperature of 40°C, UV irradiation) and on the design and performance verification of new steel-glass adhesive joints to further improve the mechanical performance of the system and facilitate the production process.

8.8 References

[1] K. Snelson, Tensegrity masts, Shelter. Bolinas, CA. (1973).

[2] R. Motro, Tensegrity, Elsevier, 2003. https://doi.org/10.1016/B978-1-903996-37-9.X5028-8.

[3] M.C. Oliveira, R.E. Skelton, Tensegrity Systems, Springer US, Boston, MA, 2009. https://doi.org/10.1007/978-0-387-74242-7.

[4] D.G. Emmerich, D.G. Emmerich, D.G. Emmerich, H. Architect, D.G. Emmerich, H. Architecte, Structures tendues et autotendantes, Ecole d'Architecture La Villette, 1988.

[5] R. Motro, Tensegrity: from art to structural engineering, in: 2012 IASS-APCS Symp., 2012: pp. 14-p.

[6] H. Murakami, Static and dynamic analyses of tensegrity structures. Part 1. Nonlinear equations of motion, Int. J. Solids Struct. 38 (2001) 3599–3613. https://doi.org/10.1016/S0020-7683(00)00232-8.

[7] M.P. Levy, The Georgia Dome and beyond: achieving lightweight-longspan structures, in: Spat. Lattice Tens. Struct., ASCE, 1994: pp. 560–562.

[8] F. Fu, Structural behavior and design methods of Tensegrity domes, J. Constr. Steel Res. 61 (2005) 23–35. https://doi.org/10.1016/j.jcsr.2004.06.004.

[9] P.G. von Krüger, F.C. Rodrigues, L.E. Moreira, E.V. Mantilla Carrasco, M. Greco, Mechanical behavior of a tensegrity dome, Mech. Res. Commun. 35 (2008) 460–465. https://doi.org/10.1016/j.mechrescom.2008.05.007.

[10] B. Van Lancker, J. Dispersyn, W. De Corte, J. Belis, Durability of adhesive glass-metal connections for structural applications, Eng. Struct. 126 (2016) 237–251. https://doi.org/10.1016/j.engstruct.2016.07.024.

[11] K. V Machalická, M. Vokáč, P. Pokorný, M. Pavlíková, Effect of various artificial ageing procedures on adhesive joints for civil engineering applications, Int. J. Adhes. Adhes. 97 (2020) 102476. https://doi.org/https://doi.org/10.1016/j.ijadhadh.2019.102476.

[12] J. Cupać, C. Louter, A. Nussbaumer, Flexural behaviour of post-tensioned glass beams: Experimental and analytical study of three beam typologies, Compos. Struct. 255 (2021) 112971. https://doi.org/10.1016/j.compstruct.2020.112971.

[13] P. Munafò, Considerazioni sulle tematiche di ricerca del Settore Scientifico Disciplinare di Architettura Tecnica, in: Colloqui.AT.E, Artec, Bologna, 2015: pp. 21–24.

[14] P. Munafò, Solaio Tensegrale, 00014426973, 2014.

[15] CNR DT 210/2013, Istruzioni per la progettazione, l'Esecuzione ed il Controllo di Costruzioni con Elementi Strutturali di Vetro, (n.d.).

[16] EN 10025-2:2004, "Hot rolled products of structural steels - Part 2: Technical delivery conditions for non-alloy structural steels," (2004).

[17] UNI EN 10002-1:2004, "Materiali metallici - Prova di trazione - Parte 1: Metodo di prova a temperatura ambiente," (n.d.).

[18] NTC. Norme Tecniche Per Le Costruzioni. Rome, Italy; 2018, (n.d.).

[19] EN ISO 527-2, Plastics - Determination of Tensile Properties - Part 2: Test Conditions for Moduling and Extrusion Plastics, 2012., (n.d.).

8.9 List of figures and tables

Figure 8.1. Tensegrity floor, rendering. 146
Figure 8.2. Tensegrity floor, axonometric view..... 147
Figure 8.3. "Tensegrity Floor" prototype, plan and section view. 148
Figure 8.4. "Tensegrity Floor" 1:2 scale prototype..... 149
Figure 8.5. "Tensegrity Floor" 1:2 scale prototype, final configuration. 150
Figure 8.6. Stress-strain average curve for S355JR steel plates..... 151
Figure 8.7. Stress-strain average curve for M8 threaded rods. 152
Figure 8.8. Test specimen, according to EN ISO 527-1:2012 [19], measures in mm..... 153
Figure 8.9. Load cases: a) symmetrical load distributed on the central span; b) asymmetrical load distributed on the lateral span; c) uniformly distributed load. 154
Figure 8.10. Experimental setup. 156
Figure 8.11. Layout of nodes considered for LVDTs measurements. 157
Figure 8.12. LVDTs - Mapping of average displacements for distributed load on central span (S. SUPP.)..... 158
Figure 8.13. LVDTs - Mapping of average displacements for distributed load on lateral span (S. SUPP.)..... 159
Figure 8.14. LVDTs - Mapping of average displacements for uniformly distributed load (S.SUPP.)..... 159
Figure 8.15. OSM - Mapping of displacements (cubic interpolation) for distributed load on central span (S. SUPP.)..... 160
Figure 8.16. OSM - Mapping of displacements (cubic interpolation) for distributed load on lateral span (S. SUPP.). 160
Figure 8.17. OSM - Mapping of displacements (cubic interpolation) for uniformly distributed load (S. SUPP.)..... 161
Figure 8.18. S. SUPP. – average displacements for each node: (a) for symmetric load distribution; (b) for asymmetric load distribution; (c) for uniformly distributed load. 162
Figure 8.19. LVDTs – Mapping of average displacements for distributed load on central span (EPX1)..... 163
Figure 8.20. LVDTs - Mapping of average displacements for distributed load on lateral span (EPX1)..... 164
Figure 8.21. LVDTs - Mapping of average displacements for uniformly distributed load (EPX1)..... 164
Figure 8.22. OSM - Mapping of displacements (cubic interpolation) for distributed load on central span (EPX1)..... 165
Figure 8.23. OSM - Mapping of displacements (cubic interpolation) for distributed load on lateral span (EPX1)..... 165
Figure 8.24. OSM - Mapping of displacements (cubic interpolation) for uniformly distributed load (EPX1)..... 166
Figure 8.25. EPX1 – average displacements for each node: (a) for symmetric load distribution; (b) for asymmetric load distribution; (c) for uniformly distributed load. 167
Figure 8.26. LVDTs - Mapping of average displacements for distributed load on central span (EPX2)..... 169

Figure 8.27. LVDTs - Mapping of average displacements for distributed load on lateral span (EPX2). 170
Figure 8.28. LVDTs - Mapping of average displacements for uniformly distributed load (EPX2). 170
Figure 8.29. OSM - Mapping of displacements (cubic interpolation) for distributed load on central span (EPX2). 171
Figure 8.30. OSM - Mapping of displacements (cubic interpolation) for distributed load on lateral span (EPX2). 171
Figure 8.31. OSM - Mapping of displacements (cubic interpolation) for uniformly distributed load (EPX2). 172
Figure 8.32. EPX2 – average displacements for each node: (a) for symmetric load distribution; (b) for asymmetric load distribution; (c) for uniformly distributed load. 173
Figure 8.33. LVDTs – Mapping of average displacements for distributed load on central span (SIL). 174
Figure 8.34. LVDTs - Mapping of average displacements for distributed load on lateral span (SIL). 175
Figure 8.35. LVDTs - Mapping of average displacements for uniformly distributed load (SIL). 175
Figure 8.36. OSM - Mapping of displacements (cubic interpolation) for distributed load on central span (SIL). 176
Figure 8.37. OSM - Mapping of displacements (cubic interpolation) for distributed load on lateral span (SIL). 176
Figure 8.38. OSM - Mapping of displacements (cubic interpolation) for uniformly distributed load (SIL). 177
Figure 8.39. SIL – average displacements for each node: (a) for symmetric load distribution; (b) for asymmetric load distribution; (c) for uniformly distributed load. 178
Figure. 8.40. Summary of mean displacements (LVDTs) for each node, adhesive and load case tested: (a) for load distributed on central span; (b) for load distributed on lateral span; (c) for uniformly distributed load. 180

Table 8.1. Mechanical characteristics of the adherends reported by manufacturers. 150
Table 8.2. Mechanical characteristics for S355JR plates (experimental). 151
Table 8.3. Mechanical characteristics for M8 rods (experimental). 152
Table 8.4. Mechanical characteristics of the adhesives reported by manufacturers. 153
Table 8.5. Dogbones mechanical parameters. 154

Chapter 9.

Conclusions and future developments

9.1 Objectives reached

Recent advances in research on structural adhesives have made it possible to extend their fields of application to civil engineering [1,2], to joints between structural elements [3–5], and to the assembly of building elements (e.g., curtain walls [6–8]).
Adhesive bonding technology makes it possible to join materials with different mechanical properties, distribute stresses over a larger area and obtain ductile, high-performance joints [9–11]. This reduces both the number of assembly operations required and the number of elements used. These advantages lead to "technological simplification" [12], i.e., fast and economical production and installation processes with lower environmental impact in terms of CO_2 emissions.
The present work illustrates the applicability of the adhesive joint in the assembly of a scale prototype of a tensegrity floor, based on the idea presented in the patent "Tensegrity Floor" by P. Munafò (Patent No. 00014426973) [13].
The research activity was divided into two main phases.
The first phase was concerned with testing the mechanical compatibility between glass and metal substrates in adhesive joints and selecting the most suitable commercial structural adhesives for the intended purposes.
The second phase consisted in the analytical verification of the resulting tensegrity structure and FE modelling of the adhesive joints applied on the floor prototype. The second phase of the study consisted in the analytical verification of the resulting tensegrity structure and FE modelling of the adhesive joints applied on the prototype. The construction of the model made it possible to verify the technical-constructive feasibility of the tensegrity floor, with a view to mass production:

i) the experimental tests showed the mechanical compatibility between the glass and metal adherends (i.e., aluminium and steel) and the commercial adhesives investigated. In particular, the thixotropic two-component epoxy adhesives showed high mechanical performances even when exposed to severe environmental conditions (i.e., artificial ageing);
ii) The assembly of the prototype of a tensegrity floor at a scale of 1:2 allowed to verify and optimise the patent idea both from a mechanical and technical-construction point of view;
iii) The use of bonded joints between the deck and the tensegrity substructure allows to increase the overall stiffness of the resulting structure compared to the simple supported configuration;

iv) The use of the adhesive joints allows – for the same load – the realisation of a stiff resultant structure with reduced maximum displacements. Compared to the configuration with a simply supported deck, this aspect makes it possible to significantly reduce the resistant cross-sections of the structural elements used, while respecting the prescribed limits. Moreover, this aspect allows simplifying the technology of the industrial product, characterised by a reduced number of processes, elements and related environmental emissions;

v) The modularity of the construction system makes it possible to standardise the construction process, composing the whole on the basis of elementary units (pyramidal modules) aggregated and repeated to achieve the desired configuration;

vi) The FE analysis of the bonded joint has verified the distribution of normal and shear stresses in the adhesive layer, allowing to characterise the mechanical behaviour of the joint and to observe the magnitude of the normal stresses present (i.e., bending stresses).

9.2 Application values and limits

The presented study made it possible to verify the technical-constructive feasibility of the Tensegrity Floor. The proposed solution made it possible to create a versatile and transparent structural element, with a lower modular height compared to equivalent traditional structures, and consequently easier to transport and more economical.

The use of the glass deck, thanks to the structural cooperation between steel and glass, makes it possible to obtain structures characterised by high mechanical performance and visual permeability. It is also possible to create opaque decks made of other materials (e.g., wood, plastic), which are bonded to the substructure.

The small size of the modules and thus of the entire structural system is one of the consequences of the structural cooperation between deck and substructure.

The low weight of the various components facilitates their transportation and assembly, as well as their disassembly and recovery at the end of the service life of the building element.

The assembly phase on site is also simplified by the fact that only bolted connections are used, and that the system is modular. This feature makes it possible to standardise the construction process by assembling the whole based on the elementary units described.

The versatility is related to the possibility of using the Tensegrity Floor system in different application contexts, as shown in Fig. 9.1(a-c).

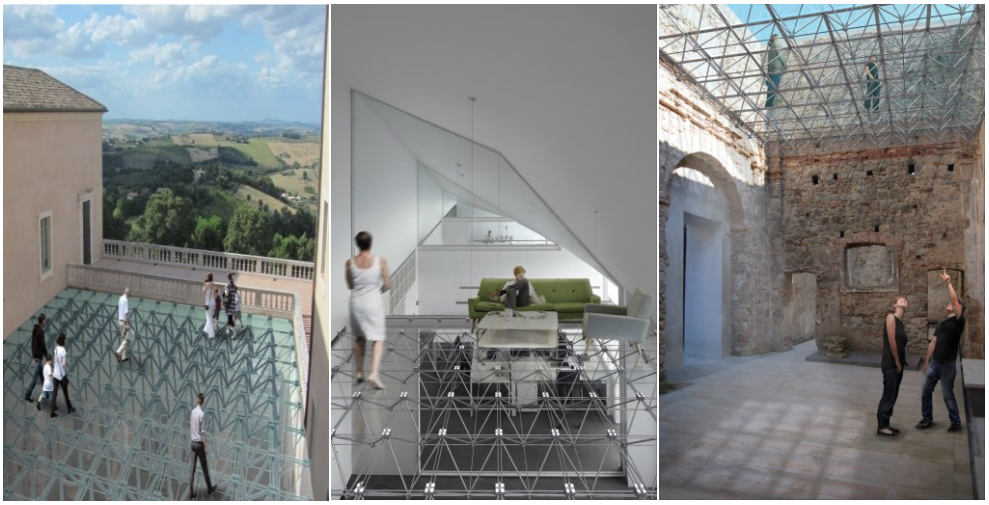

(a) (b) (c)

Figure 9.1. Application possibilities of the Tensegrity Floor: museum applications (a); new buildings (b); renovation of existing heritage (c).

Some applications are related to the conservation and musealization of archaeological finds, realising lightweight, accessible roofs that offer the possibility of creating ecologically controlled spaces with a microclimate suitable for the conservation of the building heritage. Other possible applications are new buildings and the restoration of existing buildings. The structural system used makes it possible to fill structural gaps in historic buildings from above, avoiding the use of temporary site supports.

However, the use of adhesive joints imposes certain limitations on the resulting building system. Although recent advances in research have enabled the development of high-strength adhesives, there are still some issues primarily related to the durability of the bonded joints.
Adhesives are extremely susceptible to environmental influences. Most structural adhesives absorb moisture and have significantly reduced ultimate strength.
When assembling the structural element, it is necessary – for economic and production reasons – to take into account the correct curing of the adhesive before the joined elements are put in place.
Compared to conventional mechanical joints, adhesive bonding technology is also very sensitive in terms of substrate surface preparation. This aspect is crucial for creating a permanent bond with sufficient strength. In addition, surface preparation of adhesives is difficult for in-situ repairs.
Adhesive joints are difficult to disassemble and often alter the surfaces of the adherends to which they are applied.

9.3 Installation and maintenance procedures

The assembly of the prototype in scale has allowed to highlight some critical aspects of the building system and to optimise the geometric-constructive configuration of the studied element.
The proposed assembly method is divided into a first prefabrication phase, in which all the planned welded and bonded joints are made, and a second phase, in which the parts are assembled on site with bolted joints. The phases of assembly of the parts and subsequent on-site assembly also allow for rapid disassembly of the structure at the end of its service life and retrievability of the parts.
The proposed assembly phases can be summarised as follows:

i) Insertion of the metal brackets into the perimeter support structure;
ii) Bolting of the top level of the nodes and threaded rods to the perimeter metal brackets;
iii) Bolting of the struts to the upper nodes;
iv) Bolting the lower nodes to the struts;
v) Laying of the lower bar assembly;
vi) Application of laminated glass panels, which are bolted to the metal substructure;
vii) Tensioning of the bars according to the expected torque;
viii) Sealing the joints between the panels with silicone adhesive.

The first two phases are shown in Fig. 9.2(a-b).

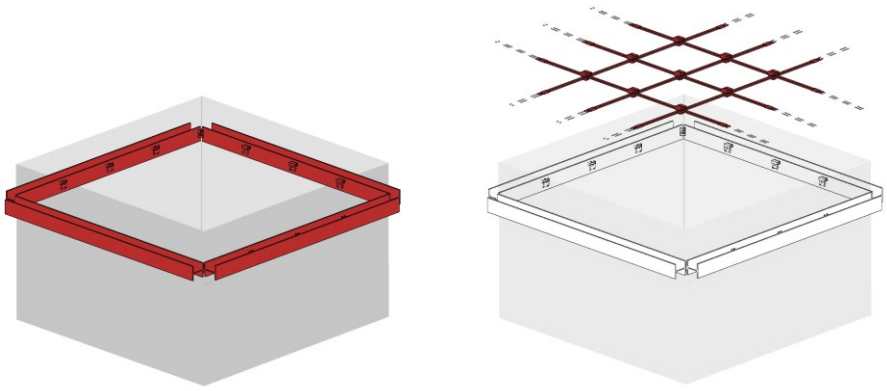

(a) (b)

Figure 9.2. Assembly phases: installation of the metal brackets in the perimeter structure (a); installation of the top order of rods and nodes (b).

The grid, consisting of the top-level nodes and bars, is pre-assembled on site and then raised to the required height for anchoring to the perimeter metal brackets.
Fig. 9.3(a-c) illustrates the successive assembly steps of the metal substructure.

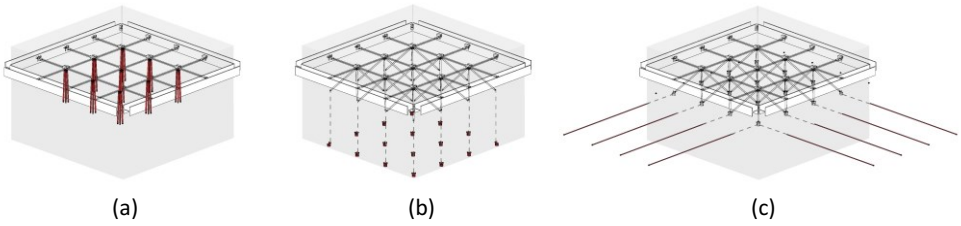

Figure 9.3. Assembly phases: installation of the struts to the top nodes (a); installation of the bottom nodes (b); insertion of the lower rods (c).

By anchoring the struts to the nodes of the lower level, the structure of the base module of the pyramid can be assembled. The lower struts are assembled in the same way as the upper struts.
Fig. 9.4 illustrates the installation phase of the glass deck.

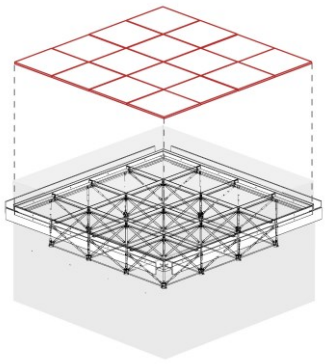

Figure 9.4. Installation of the glass deck.

The laminated and toughened glass panels are adhesively bonded – in controlled conditions – to the metal caps that allow the deck to be assembled by bolting it to the metal nodes underneath. Finally, the deck is sealed with a silicone adhesive in the gaps between the glass panels.

By using adhesive joints, high mechanical performance is achieved, stiffening the structure compared to a simply supported deck configuration. However, due to the polymeric nature of the adhesives, temperature and relative humidity can negatively affect performance of the adhesive bonding, especially when they interact. Therefore, scheduled maintenance activities must be established for both the metal substructure and the bonded joints, especially for outdoor applications or those exposed to special environmental conditions.

During maintenance activities to maintain the mechanical performance of the structural element, the integrity of all adhesive joints is verified by non-destructive testing. In case of damage, it is necessary to intervene by a complete restoration of the adhesive and a possible replacement of the bonded component (e.g., in case of propagation of defects inside the glass substrate).
The maintenance operations related to the metal substructure consist both in checking the tightness of the elements forming the joints and in checking the integrity and the presence of excessive deformations in the structural elements (i.e., checking of the global geometry of the floor).
Both maintenance procedures presented require inspection by specialised personnel, at regular intervals that vary depending on the application.

9.4 Optimisation of the construction system

As shown in the previous sections, the proposed joint in the scaled prototype is subjected to high peel peaks due to bending stresses caused by external loads. In this section, a new hypothesis is presented for the adhesive joint between the deck and the metal substructure, where a vertical adhesive layer is introduced at the interface between the metal substrate and the glass panels, as shown in Fig. 9.5.

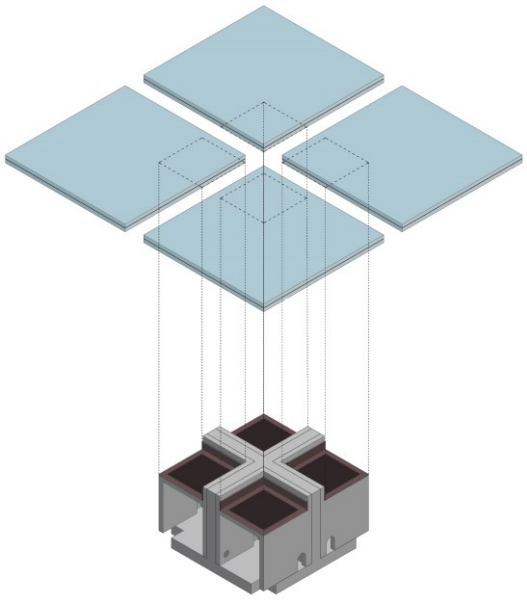

Figure 9.5. Adhesive joint: new configuration.

The introduction of the new adhesive layer is expected to reduce the normal stresses during service life.

9.4.1 FE modelling

In this section, the FE simulations carried out to determine the distribution of normal and shear stresses in the new adhesive joint are presented. As with the node typology already discussed, two different configurations were investigated, involving the central node (most heavily loaded) and the edge node, respectively (Fig. 9.6(a-b)). All numerical simulations were performed using the commercial software ANSYS 19.

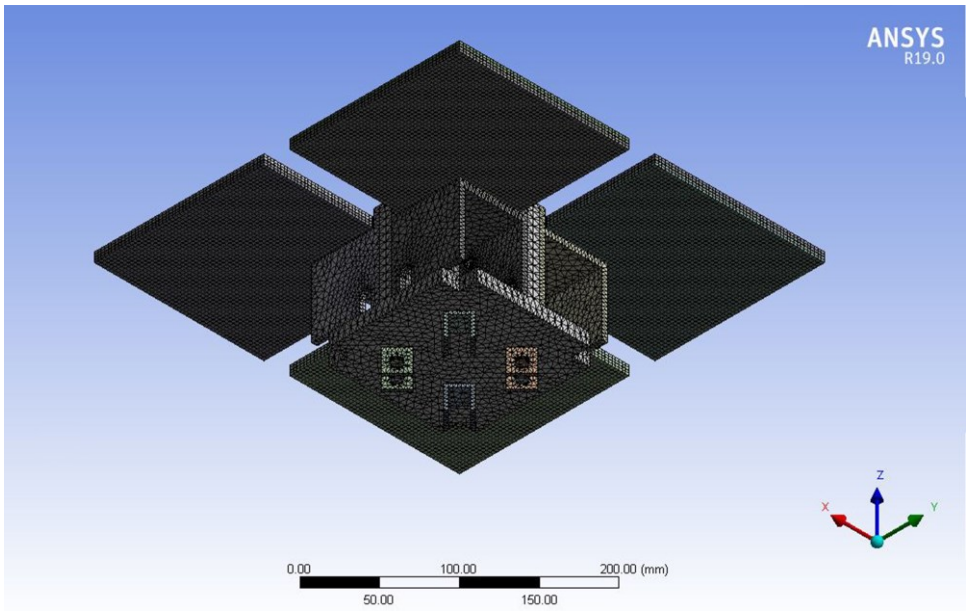

(a)

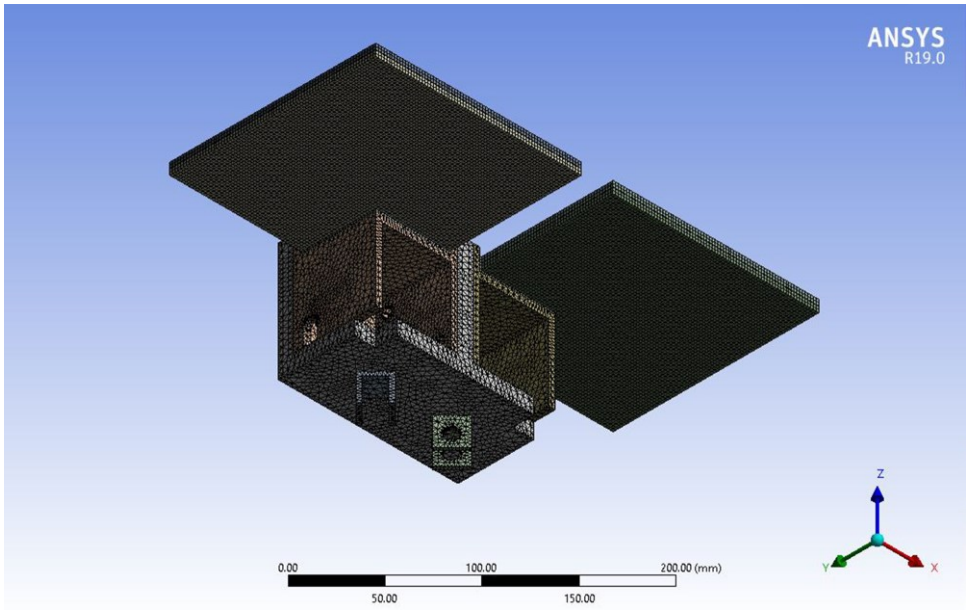

(b)

Figure 9.6. Axonometric view of the meshed nodes: (a) middle joint; (b) lateral joint.

As the single glass panel has double symmetry, only a quarter of the glazed area was modelled. As with the modelling presented previously, the bolted connection between the steel headers and the node was modelled using a bonded contact so that a linear analysis could be performed.
The cubes were constrained in the holes with the constraint "Cylindrical Support" (Radial=Axial= FIXED; Tangential= FREE).
A three-dimensional structural element with eight nodes (SOLID185 element) and a maximum mesh size of 0.50 mm was used to model the adhesive layer.
Each modelled glazed surface was loaded with its share of the working load specified in the Italian building code (NTC 2018 [14]). The distributed load was set at 4.00 kN/m^2, which corresponds to a load acting on the entire surface of the glass area. In this case, the portion of the load supported by each modelled panel part was estimated to be 67.50 N.
Finally, all modelled elements were subjected to the inertia force "Standard Earth Gravity".

9.4.2 FE results

The results of the FE simulations for the normal and shear stress distributions in the mid-plane of the adhesive support layer are shown below. Figures 9.7a, 9.7b and 9.7c show the normal stresses for the central joint in the mid-plane of adhesives EPX1, EPX2 and SIL respectively.

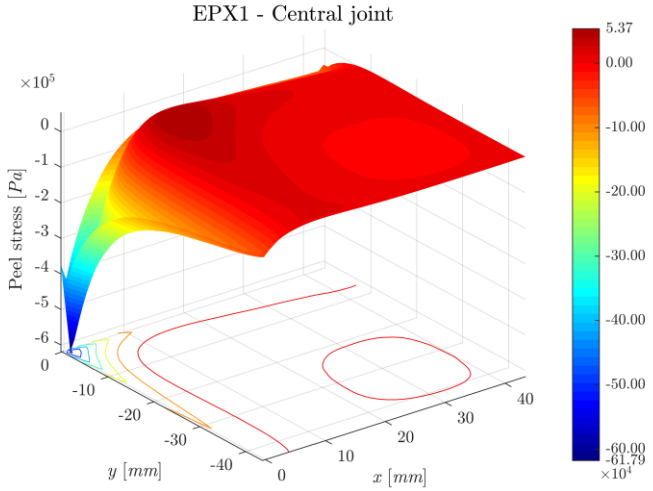

(a)

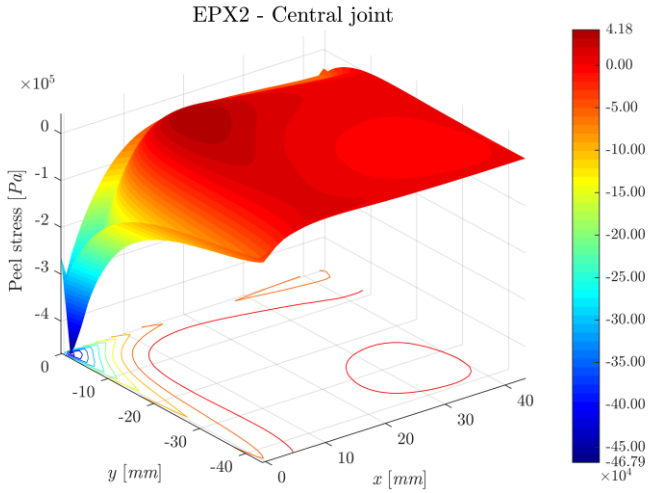

(b)

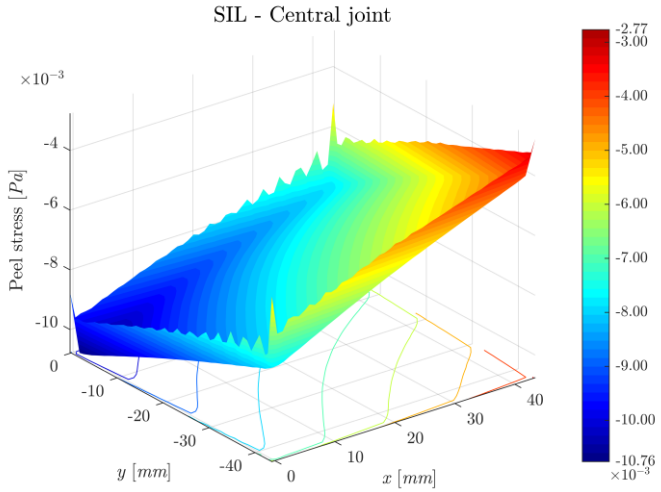

(c)

Figure 9.7. Peel stress for central joint: (a) EPX1 adhesive, (b) EPX2 adhesive; (c) SIL adhesive.

Figures 9.8a, 9.8b and 9.8c show the shear stresses for the central joint in the mid-plane of adhesives EPX1, EPX2 and SIL respectively.

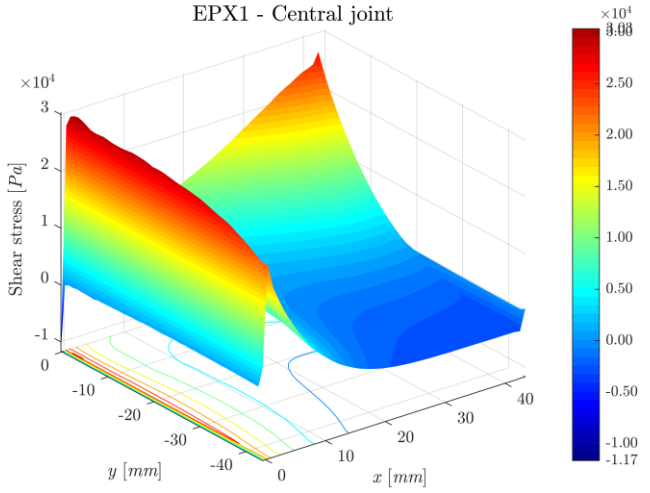

(a)

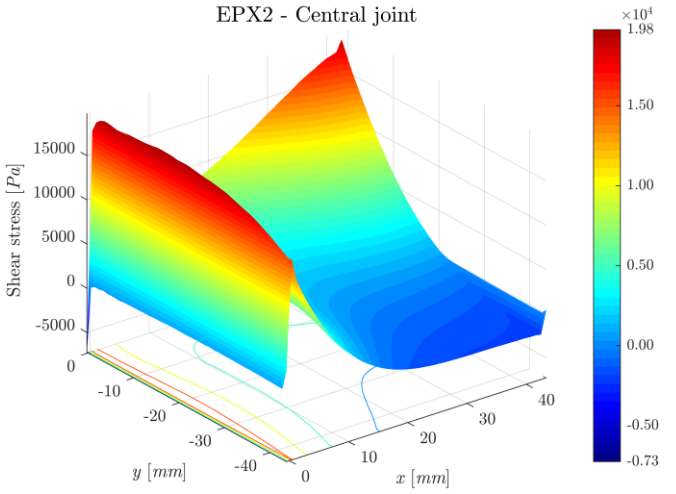

(b)

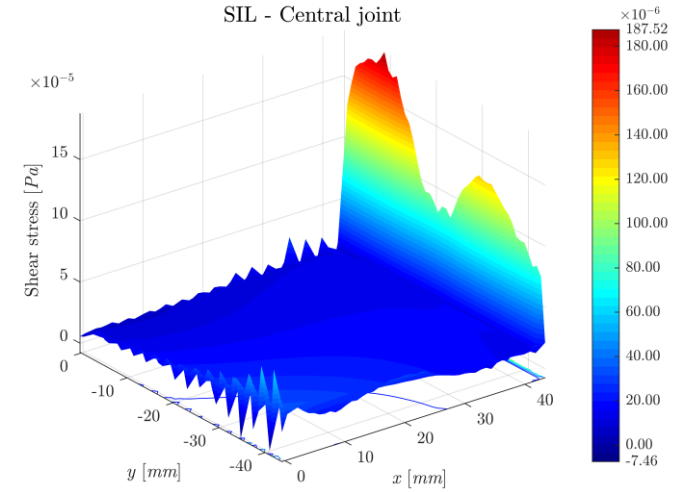

(c)

Figure 9.8. Shear stress for central joint: (a) EPX1 adhesive, (b) EPX2 adhesive, (c) SIL adhesive.

Figures 9.9a, 9.9b and 9.9c show the normal stresses for the lateral joint, in the mid-plane of the adhesives EPX1, EPX2 and SIL respectively.

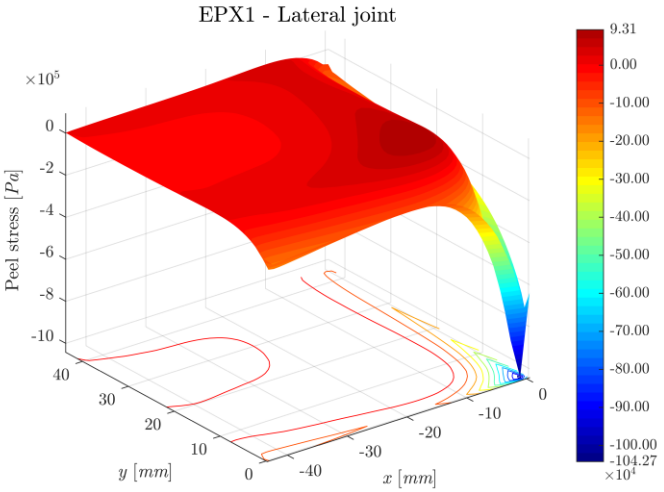
EPX1 - Lateral joint
×10^5
Peel stress [Pa]
0
-2
-4
-6
-8
-10
40
30
20
10
0
y [mm]
0
-10
-20
-30
-40
x [mm]
9.31
0.00
-10.00
-20.00
-30.00
-40.00
-50.00
-60.00
-70.00
-80.00
-90.00
-100.00
-104.27
×10^4

(a)

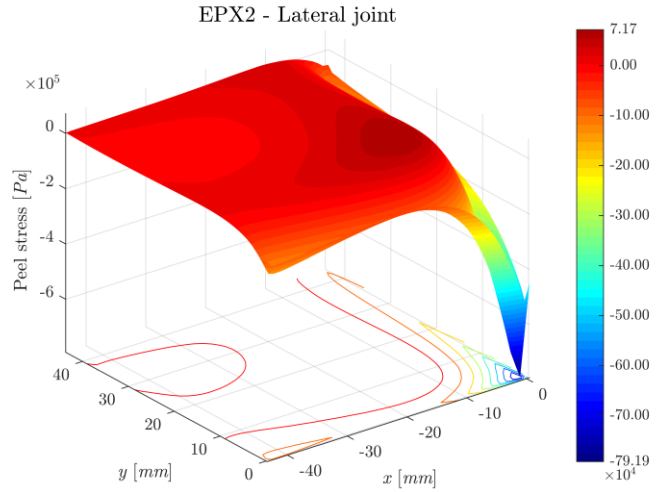
EPX2 - Lateral joint
×10^5
Peel stress [Pa]
0
-2
-4
-6
40
30
20
10
0
y [mm]
0
-10
-20
-30
-40
x [mm]
7.17
0.00
-10.00
-20.00
-30.00
-40.00
-50.00
-60.00
-70.00
-79.19
×10^4

(b)

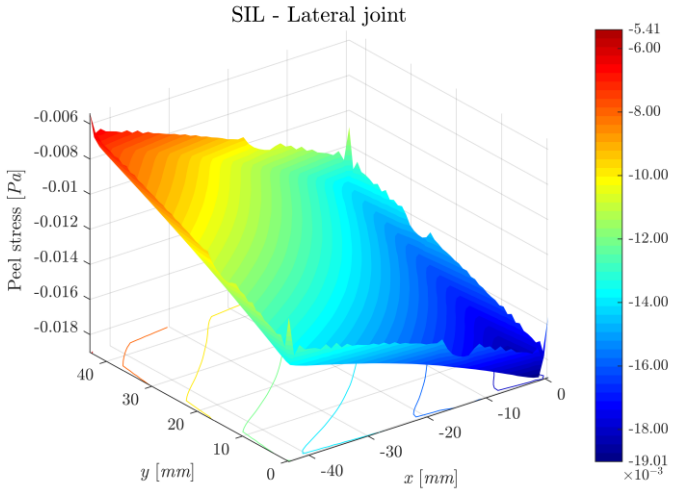

(c)

Figure 9.9. Peel stress for lateral joint: (a) EPX1 adhesive, (b) EPX2 adhesive, (c) SIL adhesive.

Figures 9.10a, 9.10b and 9.10c show the shear stresses for the lateral joint, in the mid-plane of the adhesives EPX1, EPX2 and SIL, respectively.

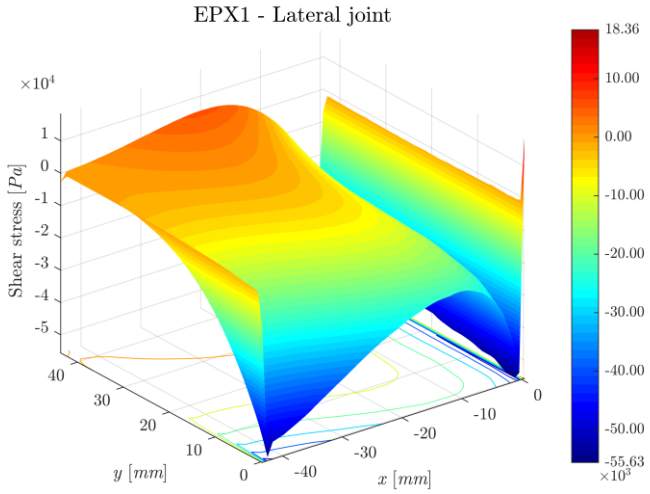

(a)

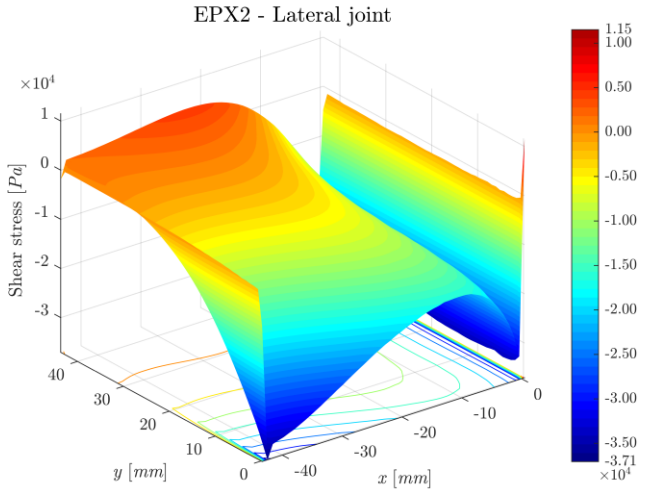

(b)

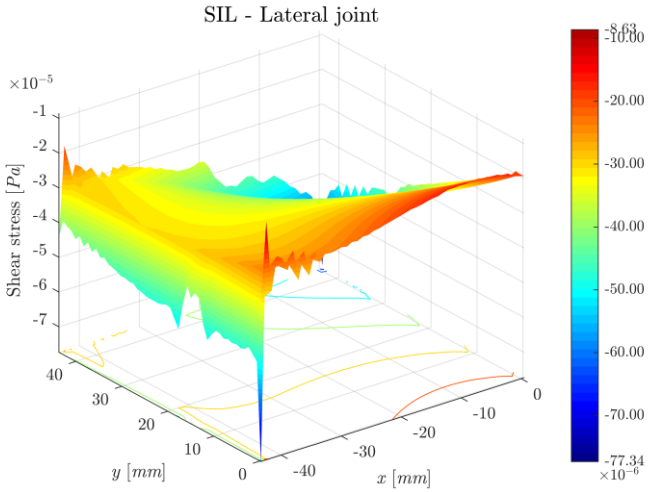

(c)

Figure 9.10. Shear stress for lateral joint: (a) EPX1 adhesive, (b) EPX2 adhesive, (c) SIL adhesive.

For both normal and shear stresses, a non-uniform distribution is again observed, characterised by the presence of stress peaks at the edge of the adhesive region near the load application. The magnitude of the stress peaks observed in the EPX1 and EPX2 adhesives are shown graphically in Fig. 9.11 and tabulated in Tab. 9.1.

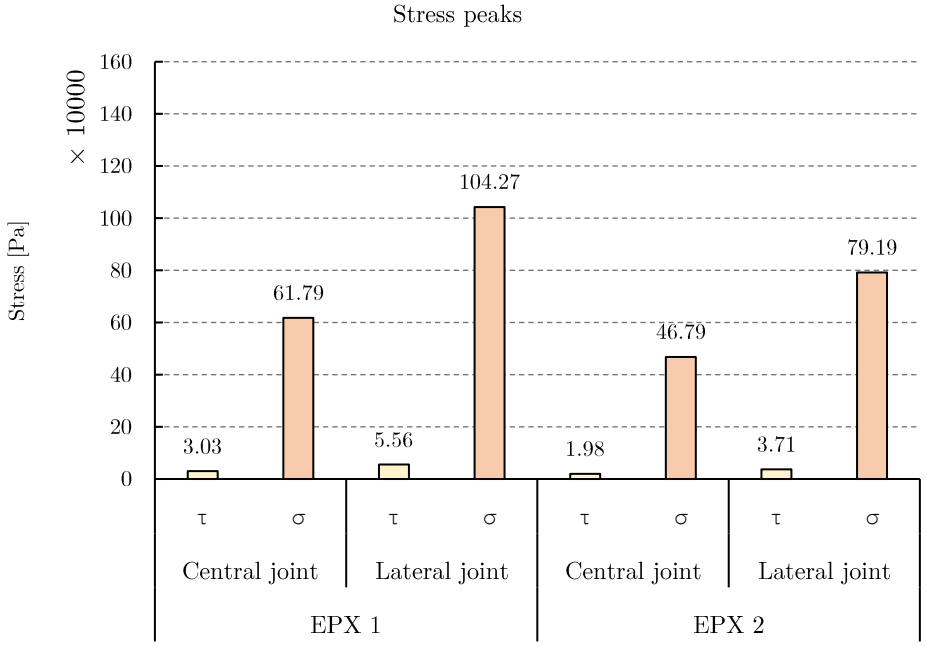

Figure 9.11. Stress peaks in the EPX1 and EPX2 adhesives middle planes.

Table 9.1. Stress peaks for the joints assembled with EPX1, EPX2 and SIL adhesives.

Adhesive	Central joint		Lateral joint	
	Shear [Pa]	Peel [Pa]	Shear [Pa]	Peel [Pa]
EPX 1	$3.03 \cdot 10^{4}$	$61.79 \cdot 10^{4}$	$5.56 \cdot 10^{4}$	$104.27 \cdot 10^{4}$
EPX 2	$1.98 \cdot 10^{4}$	$46.79 \cdot 10^{4}$	$3.71 \cdot 10^{4}$	$79.19 \cdot 10^{4}$
SIL	$0.19 \cdot 10^{-5}$	$1.08 \cdot 10^{-2}$	$7.73 \cdot 10^{-5}$	$1.90 \cdot 10^{-2}$

The results show that the new geometric configuration of the joint allows a -59% and -57% reduction in shear stress peaks for the central joints assembled with EPX1 and EPX2 adhesives, respectively. The reduction in normal stresses for both adhesives is about -19% for both adhesives in the case of the joint in the central position.
For the joints in lateral position, the new configuration leads to a reduction in shear stresses of -58% and -54% for the joints bonded with EPX1 and EPX2 adhesives, respectively. In this case, the decrease in normal stresses is about -22% for both adhesives.
The reduction in the stress peaks thus obtained allows – for the same load – the development of lower normal, which improves the mechanical behaviour of the joint with respect to bending stresses.
Fig. 9.12 shows in graphical form the stress peaks measured for the SIL adhesive.

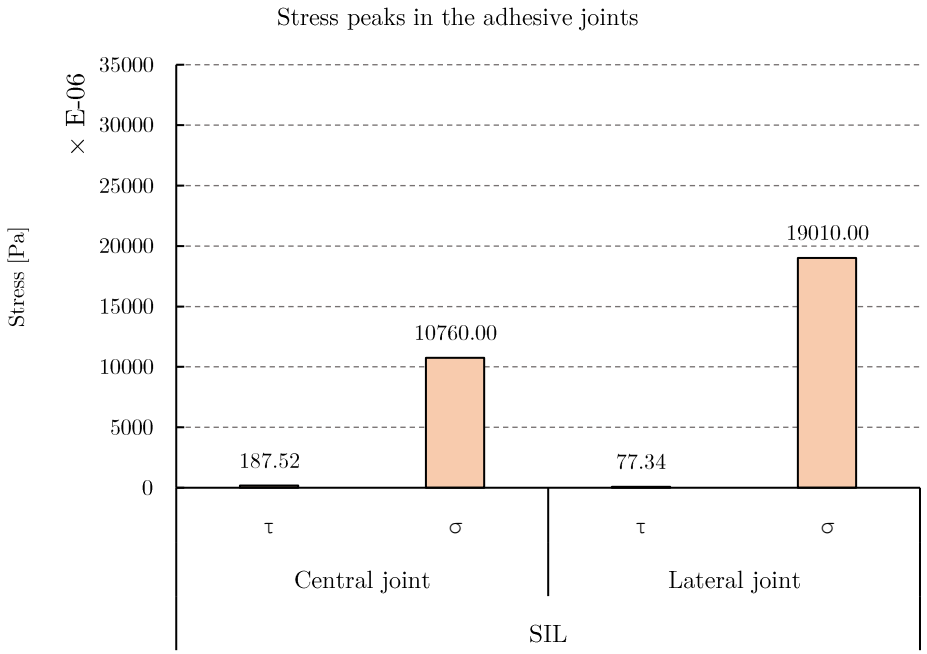

Figure 9.12. Stress peaks in the SIL adhesive middle plane.

The results show that the SIL adhesive – which has a significantly lower elastic modulus than epoxies – develops lower stress values (up to nine orders of magnitude), corresponding to higher strain values. The new geometric configuration of the node makes it possible to reduce the normal stress peaks, favouring shear mechanisms in the SIL adhesive, which improves the overall behaviour of the joint.

9.5 Future developments

In order to validate the constructive feasibility of the Tensegrity Floor in series, further developments of the presented research will concern the study of the mechanical performances related to the exposure to severe environmental conditions (e.g., high temperature and relative humidity, UV radiation, etc.). Moreover, the study of a symmetric shape can be adapted for further investigation of planar tensegrity systems with free spatial geometries. The serial repetition of the elementary unit is suitable for variations in the shape and extension of the mesh according to application requirements. The versatility is indeed related to the possibility of applying this floor system in different contexts and with different boundary conditions.

9.6 References

[1] G.C. Mays, A.R. Hutchinson, Adhesives in Civil Engineering, Adhes. Civ. Eng. (1992). https://doi.org/10.1017/cbo9780511529597.

[2] R.D. Adams, J. Comyn, W.C. Wake, Structural adhesive joints in engineering, Chapman and Hall, 1997.

[3] A. Godat, F. Légeron, V. Gagné, B. Marmion, Use of FRP pultruded members for electricity transmission towers, Compos. Struct. 105 (2013) 408–421. https://doi.org/10.1016/J.COMPSTRUCT.2013.05.025.

[4] T. Vallee, C. Grunwald, L. Milchert, S. Fecht, Design and dimensioning of a complex timber-glass hybrid structure: the IFAM pedestrian bridge, Glas. Struct. Eng. 1 (2016) 3–18. https://doi.org/10.1007/s40940-016-0007-4.

[5] G. Davis, The performance of adhesive systems for structural timbers, Int. J. Adhes. Adhes. 17 (1997) 247–255. https://doi.org/10.1016/S0143-7496(97)00010-9.

[6] V.A. Silvestru, G. Kolany, B. Freytag, J. Schneider, O. Englhardt, Adhesively bonded glass-metal façade elements with composite structural behaviour under in-plane and out-of-plane loading, Eng. Struct. 200 (2019) 109692. https://doi.org/10.1016/j.engstruct.2019.109692.

[7] K. Machalická, M. Vokáč, M. Eliášová, Influence of artificial aging on structural adhesive connections for façade applications, Int. J. Adhes. Adhes. 83 (2018) 168–177. https://doi.org/10.1016/j.ijadhadh.2018.02.022.

[8] C. Amadio, C. Bedon, Effect of circumferential sealant joints and metal supporting frames on the buckling behavior of glass panels subjected to in-plane shear loads, Glas. Struct. Eng. 1 (2016) 353–373. https://doi.org/10.1007/s40940-015-0001-2.

[9] F. Marchione, P. Munafò, Experimental investigation on timber-glass double-lap adhesive joints, Int. J. Adhes. Adhes. 106 (2021) 102818. https://doi.org/10.1016/j.ijadhadh.2021.102818.

[10] F. Marchione, Stress distribution in double-lap adhesive joints: Effect of adherend reinforcement layer, Int. J. Adhes. Adhes. 105 (2021). https://doi.org/10.1016/j.ijadhadh.2020.102780.

[11] K. Machalická, M. Vokáč, M. Kostelecká, M. Eliášová, Structural behavior of double-lap shear adhesive joints with metal substrates under humid conditions, Int. J. Mech. Mater. Des. 15 (2019) 61–76. https://doi.org/10.1007/s10999-018-9404-y.

[12] P. Munafò, Considerazioni sulle tematiche di ricerca del Settore Scientifico Disciplinare di Architettura Tecnica, in: Colloqui.AT.E, Artec, Bologna, 2015: pp. 21–24.

[13] P. Munafò, Solaio Tensegrale, 00014426973, 2014.

[14] NTC. Norme Tecniche Per Le Costruzioni. Rome, Italy; 2018, (n.d.).

9.7 List of figures and tables

Figure 9.1. Application possibilities of the Tensegrity Floor: museum applications (a); new buildings (b); renovation of existing heritage (c). 187
Figure 9.2. Assembly phases: installation of the metal brackets in the perimeter structure (a); installation of the top order of rods and nodes (b). 188
Figure 9.3. Assembly phases: installation of the struts to the top nodes (a); installation of the bottom nodes (b); insertion of the lower rods (c). 189
Figure 9.4. Installation of the glass deck. 189
Figure 9.5. Adhesive joint: new configuration. 190
Figure 9.6. Axonometric view of the meshed nodes: (a) middle joint; (b) lateral joint. ... 192
Figure 9.7. Peel stress for central joint: (a) EPX1 adhesive, (b) EPX2 adhesive; (c) SIL adhesive. 194
Figure 9.8. Shear stress for central joint: (a) EPX1 adhesive, (b) EPX2 adhesive, (c) SIL adhesive. 195
Figure 9.9. Peel stress for lateral joint: (a) EPX1 adhesive, (b) EPX2 adhesive, (c) SIL adhesive. 197
Figure 9.10. Shear stress for lateral joint: (a) EPX1 adhesive, (b) EPX2 adhesive, (c) SIL adhesive. 198
Figure 9.11. Stress peaks in the EPX1 and EPX2 adhesives middle planes. 199
Figure 9.12. Stress peaks in the SIL adhesive middle plane. 200

Table 9.1. Stress peaks for the joints assembled with EPX1, EPX2 and SIL adhesives. .. 199

Appendix 1.

Adhesives

Some contents of this chapter are extracted from:
"Adhesives in Civil Engineering", *G. C. Mays, A. R. Hutchinson*, 1992 [1];
www.adhesives.org.

1.1 Adhesives

An adhesive may be defined as a material which can join the surfaces together and resist their separation, as stated by Kinloch [2] . Recent advances in adhesive technology have led to a rapid growth in the use of adhesives in load-bearing joints, achieving structural performances and being used in civil engineering applications. The use of adhesives, in fact, can prove more convenient, less expensive, stronger, and more durable than traditional methods of joining [3].

Figure 1.1. Application of adhesives in the building/construction field.

1.2 Benefits of adhesives

The development of new materials with diverse applications puts additional challenges on processing technology. This is particularly so when different materials have to be joined to make components which retain their individual beneficial properties in the composite product. Traditional joining techniques have well-known disadvantages. With thermal techniques such as welding, the specific properties of the material alter within the heat-affected zone. Mechanical techniques such as riveting or the use of screws in their turn only allow force transfer at points; in addition, it is necessary to drill holes in the workpieces that are being joined, and this "damages" and hence weakens the materials. In contrast, bonding

technology will assume an ever more important role in industry and the handicraft sector in the future. There are four key reasons for this:

i. Material: with the specialist application, bonding technology can be used to bond virtually any desired combination of materials with each other, creating long-lasting bonds.
ii. Processing: the use of bonding technology in production processes, in general, allows the material properties of the substrates to be retained. Compared to welding and soldering/brazing, the bonding process requires relatively little heat input. No damage occurs, unlike when rivets or screws are used.
iii. Joining: in product manufacture, the two considerations enable the specific material properties of substrates to be optimally utilized in components. This allows new construction methods to be employed.
iv. Design: it is also possible to use bonding technology to introduce customized additional properties into the component via the actual joining. In addition, the use of bonding technology in industrial production can lead to time savings, can accelerate the production process, and hence give rise to specific economic benefits. In shipbuilding, for example, the inside decks can nowadays be bonded into the primary structure, so eliminating time-consuming straightening work that would be required if the inside decks were attached by welding.

Bonding technology also has the following further advantages:

- Transfer of high lap shear stresses due to the large bonding areas.
- Removal of unevenness on material surfaces; greater tolerances possible using gap-filling adhesives.
- Prevention of contact corrosion for metal bonds, in contrast to when rivets or screws are used (the adhesive functions as an insulator).

1.3 Classification of adhesives

There are many adhesive types for various applications. They may be classified in a variety of ways depending on their chemistries, their form, their cure mechanism, or their load carrying capability.

1.3.1 Load carrying capacity

1.3.1.1 Structural

Structural adhesives refer to relatively strong adhesives that are normally used well below their glass transition temperature, an important property for polymeric materials, above which polymers are rubbery and below which they are glassy. Common examples of structural adhesives include epoxies, cyanoacrylates, and certain urethanes and acrylic adhesives. Such adhesives can carry significant stresses and lend themselves to structural applications.

1.3.1.2 Semi-structural and non-structural

For many engineering applications, semi-structural (applications where failure would be less critical) and non-structural (applications of facades, etc. for aesthetic purposes) are also of significant interest to the design engineer and provide cost-effective means required for assembly of finished products. These include contact adhesives where a solution or emulsion containing an elastomeric adhesive is coated onto both adherents, the solvent is allowed to evaporate, and then the two adherents are brought into contact. Examples include rubber cement and adhesives used to bond laminates to countertops.

1.3.1.3 Pressure sensitive

Pressure sensitive adhesives are very low modulus elastomers, which deform easily under small pressures, permitting them to wet surfaces. When the substrate and adhesive are brought into intimate contact, van der Waals forces are sufficient to maintain the contact and can provide relatively durable bonds for lightly loaded applications. Pressure sensitive adhesives are normally purchased as tapes or labels for non-structural applications, although can also come as double-sided foam tapes which can be used in semi-structural applications. As the name implies, hot melts become liquid when heated, wetting the surfaces and then cooling into a solid polymer. These materials are increasing used in a wide array of engineering applications using more sophisticated versions of the glue guns widely used by consumers. Anaerobic adhesives cure within narrow spaces deprived of oxygen; such materials has been widely used in mechanical engineering applications to lock bolts or bearings in place. Cure in other adhesives may be induced by exposure to ultraviolet light or electron beams or may be catalysed by certain materials such as water, which are ubiquitous on many surfaces.

1.3.2 Cure mechanisms

1.3.2.1 Physically hardening

Physically hardening adhesives are adhesives which, on the application, are already present in their final chemical state. Only polymers that can be liquefied can be used for this category of adhesive, namely thermoplastics that can be melted, soluble thermoplastics or elastomers, or polymer dispersions. Although poorly crosslinked elastomers with good swelling properties are strictly speaking insoluble, they can still be used in certain cases to produce adhesives if they swell enough for the substrates to be wetted. Physically hardening adhesives provide a wide range of adhesive properties, generally good bond flexibility, and are used in a variety of applications. Four physically hardening adhesives are:

- Hot melts;
- Organic solvent adhesives;
- Platisols;

- Water-based adhesives.

1.3.2.2 Chemically curing

Chemically curing adhesives are reactive materials that require a chemical reaction to convert them from the liquid (or thermoplastic) to solid. Once cured, these adhesives generally provide high strength, flexible to rigid bond lines that resist temperature, humidity, and many chemicals. They may be classified into two groups:

- Single component. With single component adhesives, the adhesive components are premixed in their final proportions. However, they are chemically blocked. As long as they are not subjected to the specific conditions, which activate the hardener, they will not bond. They require either high temperature or substances or media (light, humidity) from the surroundings to initiate the curing mechanism. The containers in which this type of adhesive are transported and stored must be carefully chosen to prevent any undesired reactions. These adhesives are usually 100% solid systems. The six major subclasses are Anaerobic, Cyanoacrylates, Heat Cure, Moisture Cure, Radiation Cure, Silicones.
- Two-component. Two-component adhesives are 100% solids systems that obtain their storage stability by separating the reactive components. They are supplied as "resin" and "hardener" in separate containers. It is important to maintain the prescribed ratio of the resin and hardener in order to obtain the desired cure and physical properties of the adhesive. The two components are only mixed together to form the adhesive a short time before application with cure occurring at room temperature. Since the reaction typically begins immediately upon mixing the two components, the viscosity of the mixed adhesive increases with time until the adhesive can no longer be applied to the substrate or bond strength is decreased due to diminished wetting of the substrate. Formulations are available with a variety of cure speeds providing various working times (work life) after mixing and rates of strength build-up after bonding. Final strength is reached in minutes to weeks after bonding depending on the formulation. Adhesive must be cleaned from mixing and application equipment before cure has progressed to the point where the adhesive is no longer soluble. Depending on work life, two component adhesives can be applied by trowel, bead or ribbon, spray, or roller. Assemblies are usually fixture until sufficient strength is obtained to allow further processing. If the faster rate of cure (strength build-up) is desired, heat can be used to accelerate the cure. This is particularly useful when parts need to be processed more quickly after bonding or additional work life is needed but a slower rate of strength build-up cannot be accommodated. When cured, two component adhesives are typically tough and rigid with good temperature and chemical resistance.

Two-component adhesives can be mixed and applied by hand for small applications.
However, this requires considerable care to ensure the proper ratio of the components and sufficient mixing to ensure proper cure and performance. There is usually considerable waste involved in hand mixing as well. As a result, adhesive suppliers have developed packaging that allows the components to remain separate for storage and provides a means for

dispensing a mixed adhesive, e.g., side-by-side syringes, concentric cartridges. The package is typically inserted into an applicator handle and the adhesive is dispensed through a disposable mixing nozzle. The proper ratio of components is maintained by virtue of the design of the package and proper mixing is ensured using the mixing nozzle. The adhesive can be dispensed from these packages multiple times provided the time between uses does not exceed the work life of the adhesive. If the work life is exceeded, a new mixing nozzle must be used. For larger applications, meter-mix equipment is available to meter, mix, and dispense adhesive packaged in containers ranging from quarts to drums. Four major types of two-component adhesives include: Epoxies, Methyl Methacrylates, Silicone Adhesives, Urethanes.

1.3.2.3 Pressure sensitive

The special feature of pressure sensitive adhesives is that they do not solidify to form a solid material but remain viscous. As a result, they remain permanently tacky and have the ability to wet surfaces on contact. Bonds are made by bringing the adhesive film in contact with the substrate and applying pressure. If the inadequate pressure is applied or the processing temperature is too low, bonding faults such as bubbles or detachment can occur. Since these adhesives are not true solids, the strength of pressure sensitive adhesives decreases when the temperature is increased. Pressure sensitive adhesives also exhibit a tendency to undergo creep when subjected to loads. They are typically formulated from natural rubber, certain synthetic rubbers, and polyacrylates.
Pressure sensitive adhesives can be supplied dissolved in organic solvents, as an aqueous dispersion, as a hot melt, or coated on a release liner as tape. Liquid applied (solvent or water based, hot melt) pressure sensitive adhesives can be applied in bead or ribbon, sprayed, or roll coated. After coating (and drying of solvent or water-based systems), parts can be bonded, or the adhesive covered with release liner for bonding later. The adhesive can be coated in a pattern to provide bonded and unbounded areas, e.g., assembly of membrane switches, filter frames. Pressure sensitive adhesives are often used to temporarily hold components like gaskets in position during assembly.

1.3.3 Forms

Adhesives of various chemistries are available in many different forms as well. For structural applications, adhesives are available as pastes, liquids, films, and supported films. The latter are supported on loose knit or mat-scrim cloth to improve the handling properties and also to offer some measure of thickness control. Many of these adhesives produce little or no outgassing when cured, significantly reducing the likelihood of voids within the adhesive. It is important that these adhesives be kept dry, as absorbed moisture can create significant void problems.
Thermosetting structural adhesives are normally available in two-part forms that are mixed through carefully controlled stoichiometry into a product that cures within the desired time window. One-part forms are also available in which the resin and hardener (crosslinking

agent) are already mixed together. These one-part forms must be kept at sufficiently low temperature that the reaction does not occur prematurely, sometimes utilizing latent crosslinking agents that are not active at low temperatures. One-part thermosetting adhesives often have limited shelf life, and often must be stored at low temperatures, but do offer very high-performance capabilities. Pot life refers to the time after a two-part adhesive is mixed during which it is workable and will still make a satisfactory bond. Materials with too short of a pot life will harden too fast, and do not give the workers sufficient time to assemble the product. An excessively long pot life may delay the cure time and slow the assembly process. Adhesives may be applied in a variety of ways depending on the form it comes in. Adhesives may be spread on a surface manually or may be dispensed using a variety of sophisticated nozzles and robotic equipment that is currently available. Maintaining adherent cleanliness, providing proper jigs and fixturing during cure, and providing adequate cure conditions may all be important considerations for certain types of adhesives.

1.4 Epoxy adhesives

Because of their ability to adhere to a wide variety of materials, their high strength, their resistance to chemicals and environments, and their ability to resist creep under sustained load, epoxies are the most widely used structural adhesive. They are available in one component, heat curing, and two-component, room temperature curing systems. Unmodified epoxies cure to hard, brittle solids. Most adhesive formulations include modifiers to increase flexibility or toughness of the cured adhesive. This results in bond lines that are able to resist more peel and cleavage stress as well as impact.

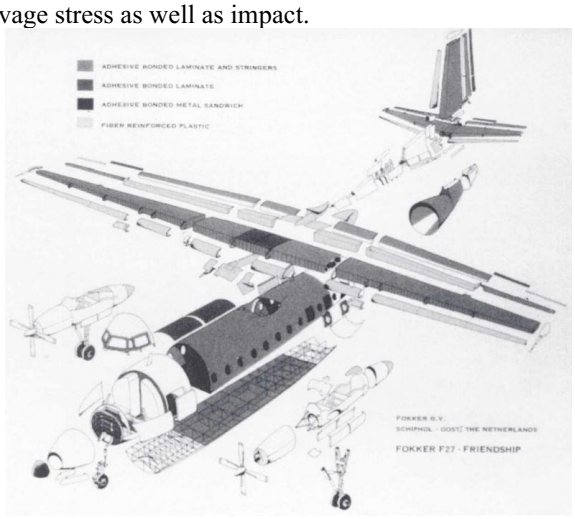

Figure 1.2. Adhesively bonded components in the Fokker Friendship F27 [4].

One component system typically cures at temperatures from 250 to 350°F (120 to 175°F). Cold storage is required to provide sufficient shelf life. They provide rigid but tough bond lines and have excellent adhesion to metals. Chemical and environmental resistance are

excellent. Most formulations have a paste consistency and can be applied by trowel or extruded as beads. They easily fill gaps and provide excellent sealing properties particularly against harsh chemicals. They are often used as alternatives to welding and rivets. Some formulations can tolerate processing oil on the substrate and still obtain satisfactory bond strength.

One component heat curing film adhesives are typically based on epoxy resin formulated with curative and modifiers. They are very high-performance adhesives providing high strength, high fatigue resistance, and high-temperature resistance. These curing film adhesives require cold storage and have limited shelf-life after warming to room temperature. They are especially suited for bonding and laminating large areas. Epoxy film adhesives find most of their applications in the aerospace industry for assemblies of components such as aircraft panels and helicopter rotor blades. To obtain optimal performance and durability, aluminum substrates are usually chemically treated.

Two component epoxy adhesives are found in all market segments. The work life (time adhesive can be processed and bonded after mixing) can vary from a few minutes to several hours. Assemblies must be fixtured until the adhesive has cured sufficiently to have enough strength for handling and additional processing. Final cure and ultimate strength are obtained over hours to weeks depending on the formulation. High ambient temperature accelerates the rate of cure and shortens the work life. Low ambient temperature slows the rate of cure and extends the time before assemblies can be further processed. In general, adhesives that cure faster have lower final strength than those that cure more slowly. The major advantage of two component epoxy adhesives is that they are suitable for bonding nearly all substrates - metal, plastic, glass and ceramic, wood and wood products, and many types of rubber. In general, they have high resistance to physical and chemical influences and in addition, they have high long-term stability because they only have a limited tendency to undergo creep. Depending on the type, they can withstand continuous temperatures from 200oF (95°C) up to 390 °F (200°C). Cured adhesives are typically hard and rigid and range from brittle to tough depending on the formulation.

1.5 Glass transition temperature

The glass transition temperature (T_g) is one of the most important properties of any polymer and refers to the temperature vicinity in which the amorphous portion of the polymer transitions from a hard, glassy material to soft, rubbery material. Although specific temperatures are often quoted for the glass transition temperature, it is important to remember that this transition temperature is a rate dependent process. For thermosetting structural adhesives, the glass transition temperature should normally be 50°C higher than the expected service temperature. Unless there are significant exotherms associated with the cure process, the glass transition temperature of an adhesive seldom exceeds the cure temperature. High performance structural bonds often require an elevated temperature cure to provide a sufficiently high T_g in a reasonable cure time. One concern with such conditions, however, are the residual stresses which may develop with an assembled joint is cooled from the cure temperature to the service conditions.

1.6 Reference

[1] G.C. Mays, A.R. Hutchinson, Adhesives in Civil Engineering, Adhes. Civ. Eng. (1992). https://doi.org/10.1017/cbo9780511529597.

[2] A.J. Kinloch, Adhesion and Adhesives, Springer Netherlands, Dordrecht, 1987. https://doi.org/10.1007/978-94-015-7764-9.

[3] R.D. Adams, J. Comyn, W.C. Wake, Structural adhesive joints in engineering, Chapman and Hall, 1997.

[4] G.C. Mays, A.R. Hutchinson, Adhesives in Civil Engineering, Cambridge University Press, 1992. https://doi.org/10.1017/CBO9780511529597.

1.7 List of figures

Figure 1.1. Application of adhesives in the building/construction field. 203

Figure 1.2. Adhesively bonded components in the Fokker Friendship F27 [4]. 208

Appendix 2.

Experimental data

This section shows the optical (OSM - cubic interpolation) and digital measurements for each load test carried out on the Tensegrity Floor prototype.

2.1 Simply supported glass deck

Figs. 2.1–2.3 show the graphic mapping of the vertical displacement values recorded by digital measurement (LVDT) for simple support joints between glass and metal substructure.

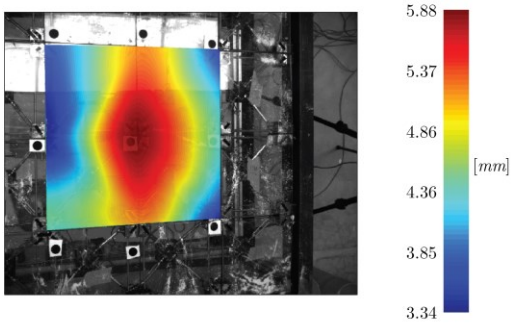

(a)

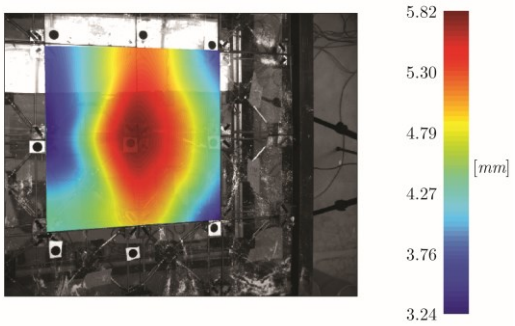

(b)

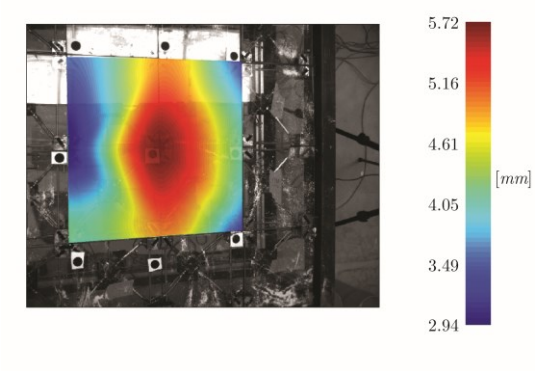

(c)

Figure 2.1. LVDTs – Displacement mapping for distributed load on central span: (a) 1st repetition, (b) 2nd repetition, (c) 3rd repetition (S. SUPP.).

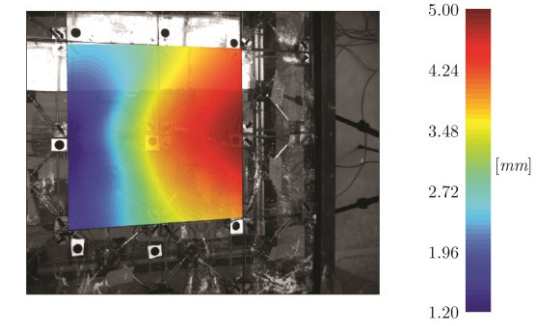

(a)

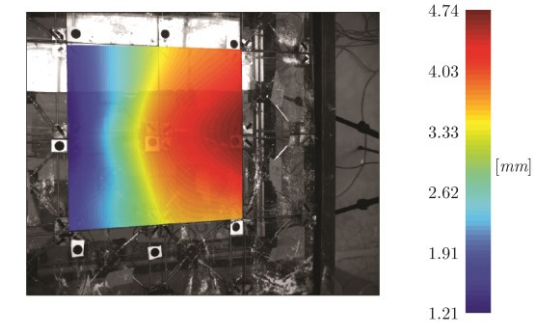

(b)

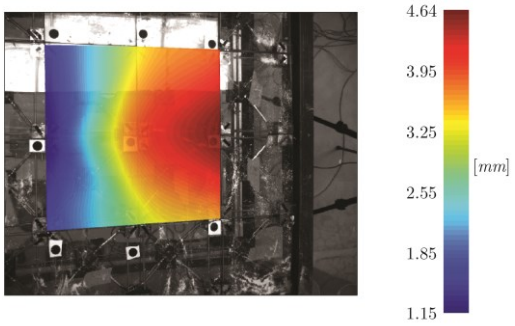

(c)

Figure 2.2. LVDTs – Displacement mapping for distributed load on lateral span: (a) 1st repetition, (b) 2nd repetition, (c) 3rd repetition (S. SUPP.).

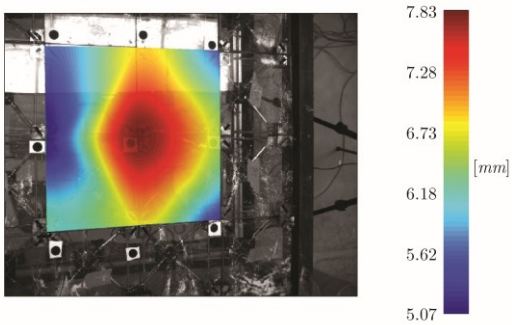

(a)

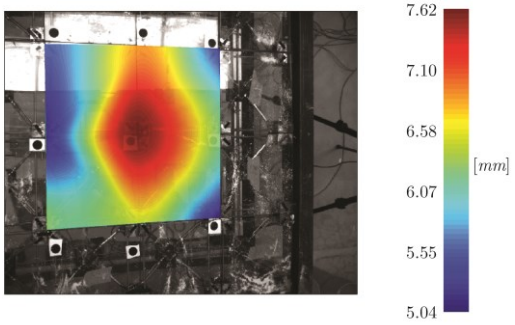

(b)

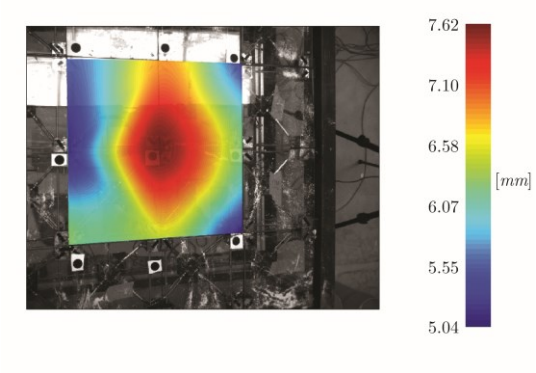

(c)

Figure 2.3. LVDTs – Displacement mapping for uniformly distributed load: (a) 1st repetition, (b) 2nd repetition, (c) 3rd repetition (S. SUPP.).

The results obtained from the optical measurement – using OSM technology – are shown in Figs. 2.4-2.6.

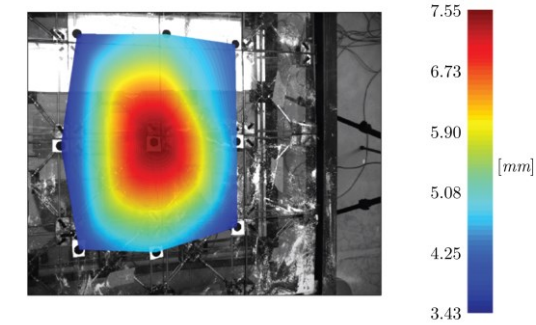

(a)

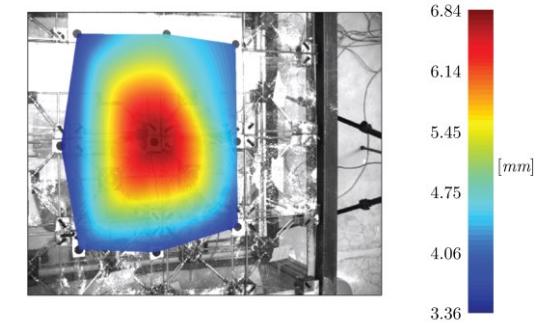

(b)

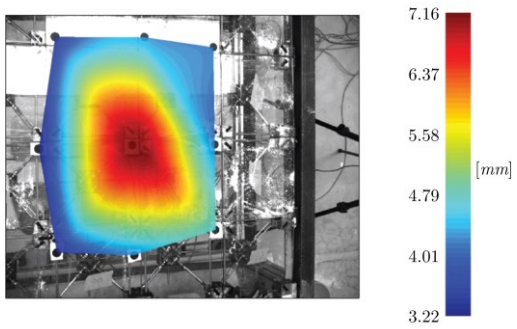

(c)

Figure 2.4. OSM – Displacement mapping for distributed load on central span: (a) 1st repetition, (b) 2nd repetition, (c) 3rd repetition (S. SUPP.).

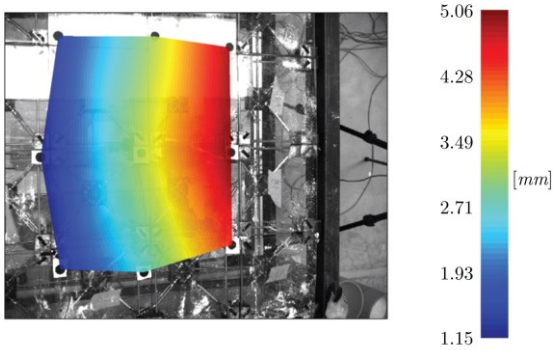

(a)

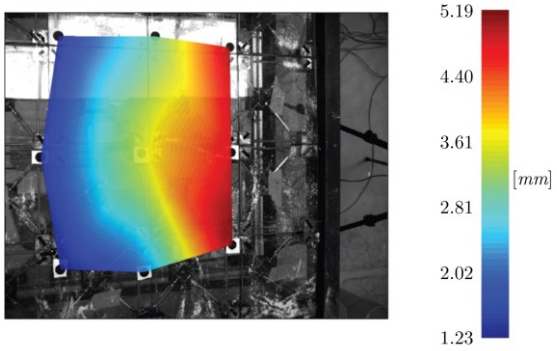

(b)

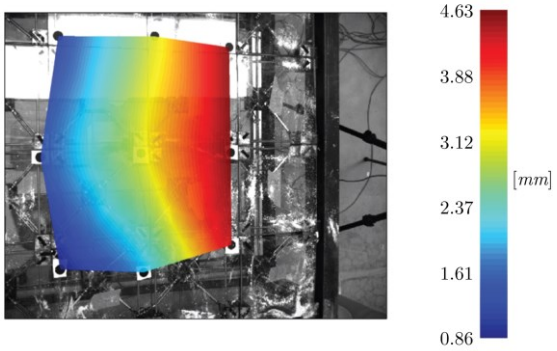

(c)

Figure 2.5. OSM – Mapping of displacements for distributed load on lateral span: (a) 1st repetition, (b) 2nd repetition, (c) 3rd repetition (S. SUPP.).

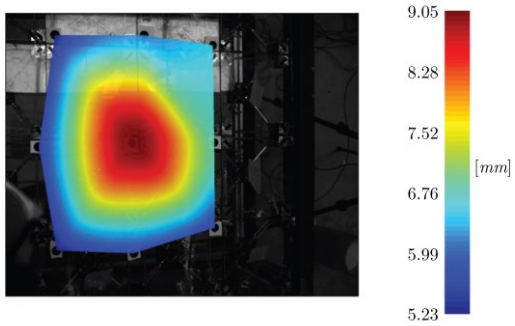

(a)

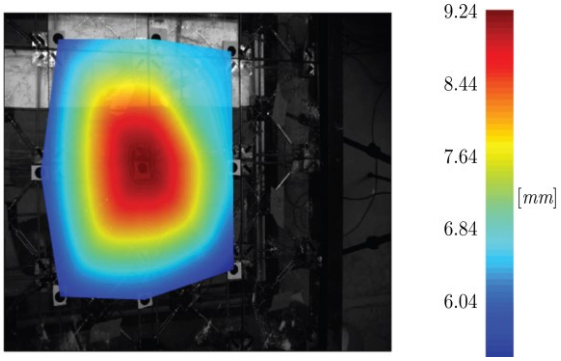

(b)

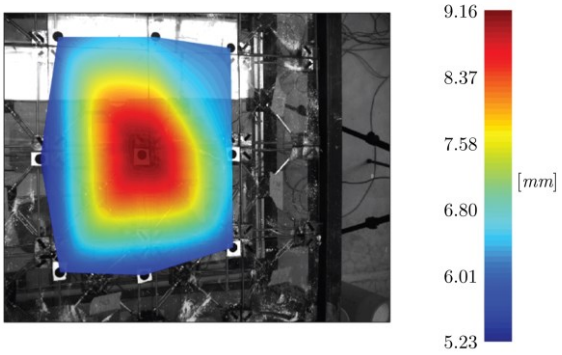

(c)

Figure 2.6. OSM – Displacement mapping for uniformly distributed load: (a) 1st repetition, (b) 2nd repetition, (c) 3rd repetition (S. SUPP.).

2.2 Glass deck adhesively bonded with EPX1 adhesive

Figs. 2.7-2.9 show the graphic mapping of the vertical displacement values recorded by digital measurement (LVDT) for the glass deck adhesively bonded with EPX1 adhesive.

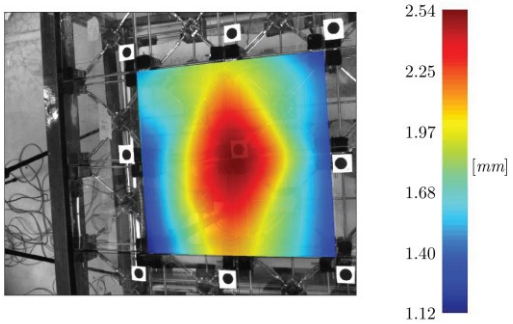

(a)

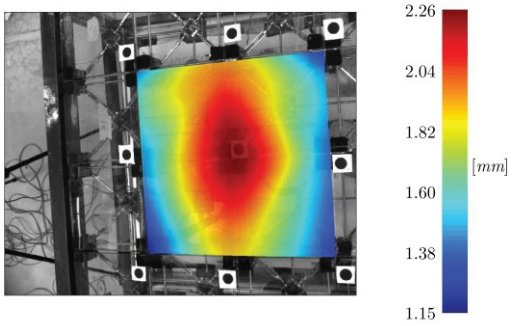

(b)

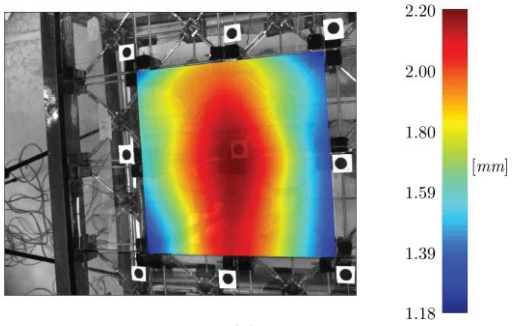

(c)

Figure 2.7. LVDTs – Displacement mapping for distributed load on central span: (a) 1st repetition, (b) 2nd repetition, (c) 3rd repetition (EPX1).

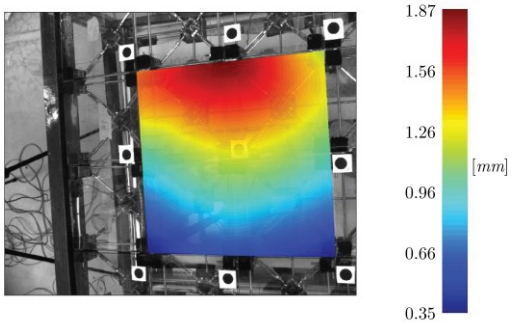

(a)

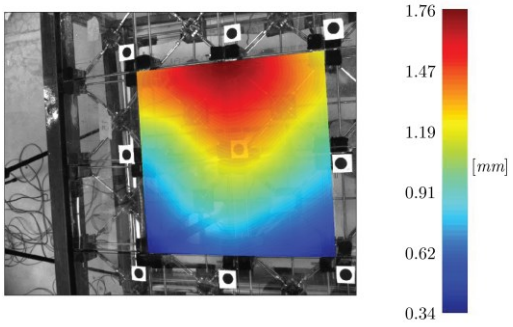

(b)

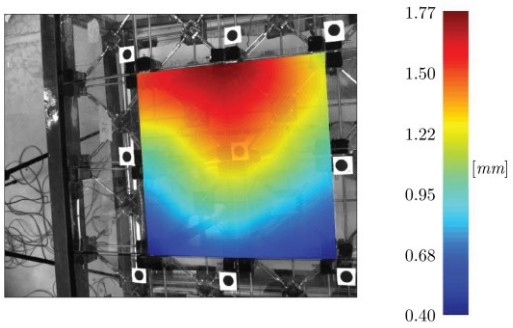

(c)

Figure 2.8. LVDTs – Displacement mapping for distributed load on lateral span: (a) 1st repetition, (b) 2nd repetition, (c) 3rd repetition (EPX1).

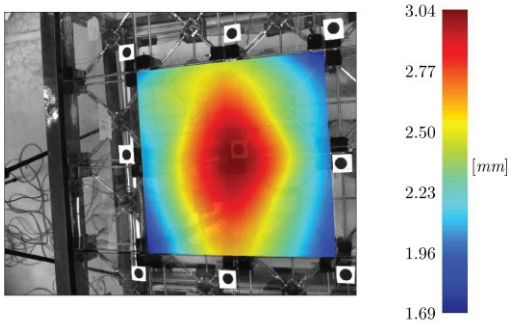

(a)

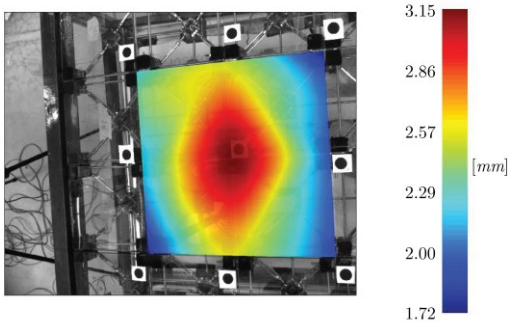

(b)

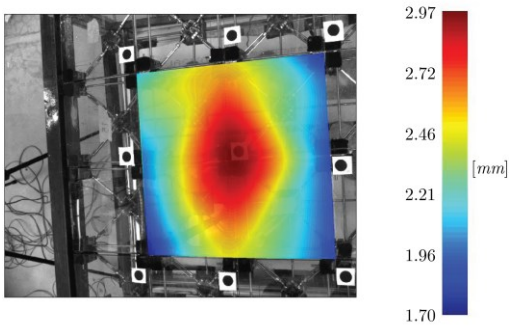

(c)

Figure 2.9. LVDTs – Displacement mapping for uniformlly distributed loadp: (a) 1st repetition, (b) 2nd repetition, (c) 3rd repetition (EPX1).

The results obtained from the optical measurement – using OSM technology – are shown in Figs. 2.10-2.12.

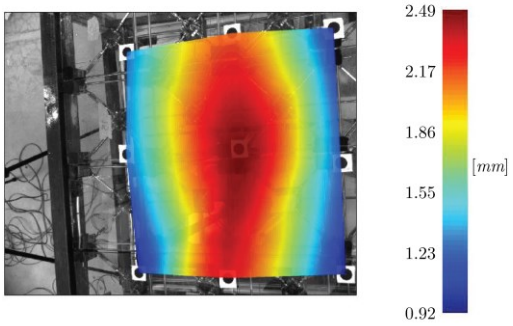

(a)

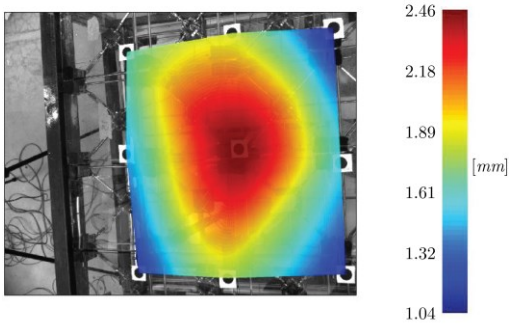

(b)

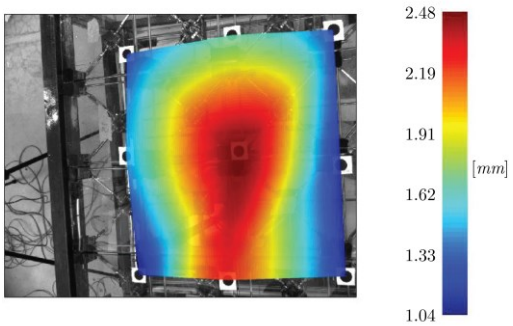

(c)

Figure 2.10. OSM – Displacement mapping for distributed load on central span: (a) 1st repetition, (b) 2nd repetition, (c) 3rd repetition (EPX1).

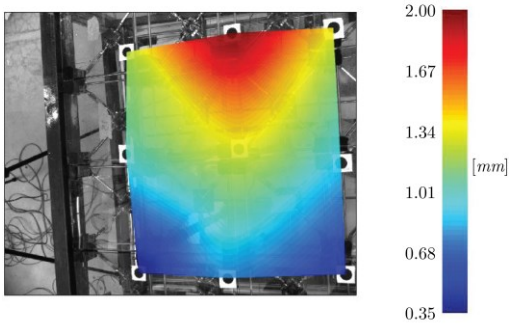

(a)

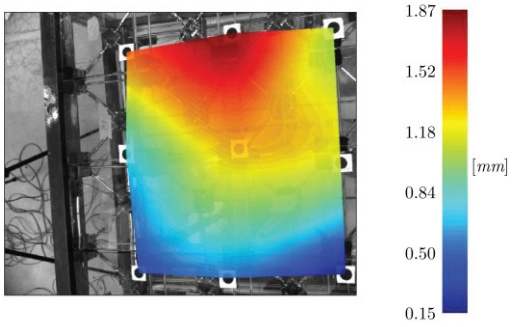

(b)

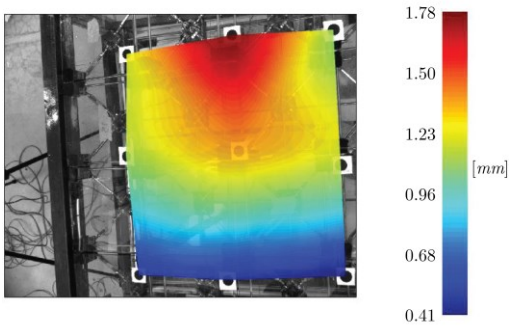

(c)

Figure 2.11. OSM – Displacement mapping for distributed load on lateral span: (a) 1st repetition, (b) 2nd repetition, (c) 3rd repetition (EPX1).

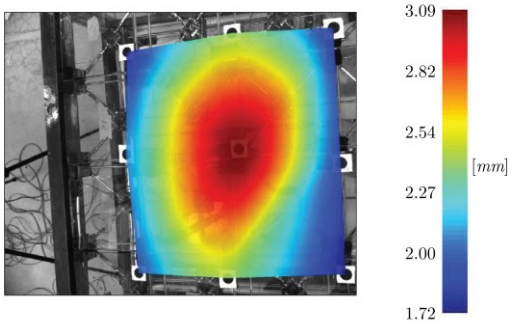

(a)

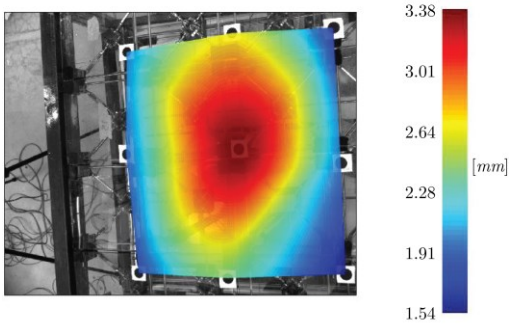

(b)

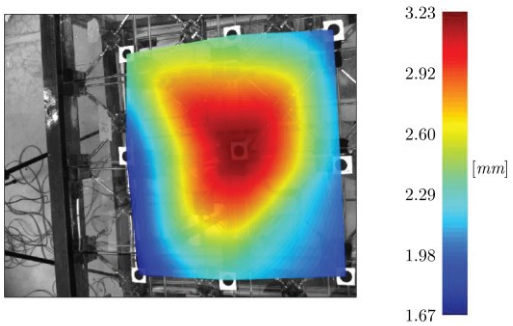

(c)

Figure 2.12. OSM – Displacement mapping for uniformly distributed load: (a) 1st repetition, (b) 2nd repetition, (c) 3rd repetition (EPX1).

2.3 Glass deck adhesively bonded with EPX2 adhesive

Figs. 2.13–2.15 show the graphic mapping of the vertical displacement values recorded by digital measurement (LVDT) for the glass deck adhesively bonded with EPX2 adhesive.

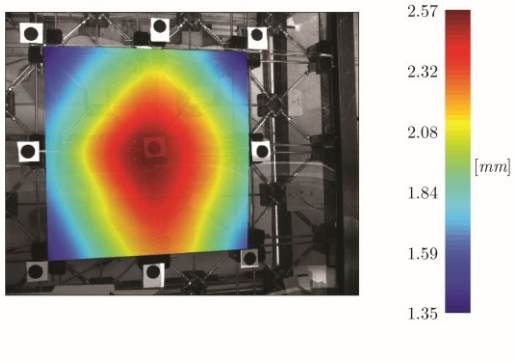

(a)

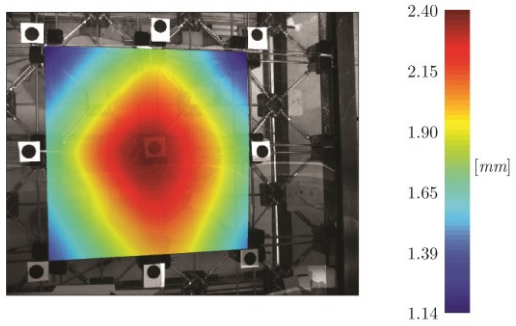

(b)

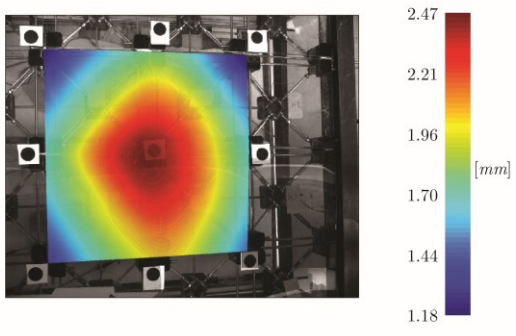

(c)

Figure 2.13. LVDTs – Displacement mapping for distributed load on central span: (a) 1st repetition, (b) 2nd repetition, (c) 3rd repetition (EPX2).

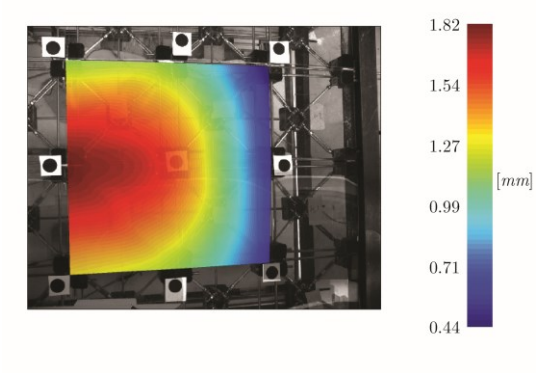

(a)

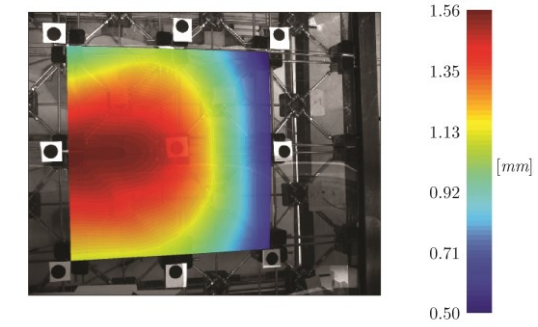

(b)

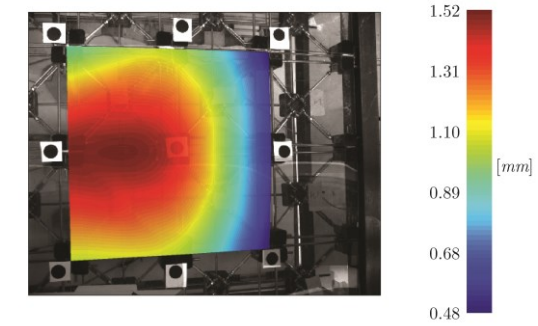

(c)

Figure 2.14. LVDTs – Displacement mapping for distributed load on lateral span: (a) 1st repetition, (b) 2nd repetition, (c) 3rd repetition (EPX2).

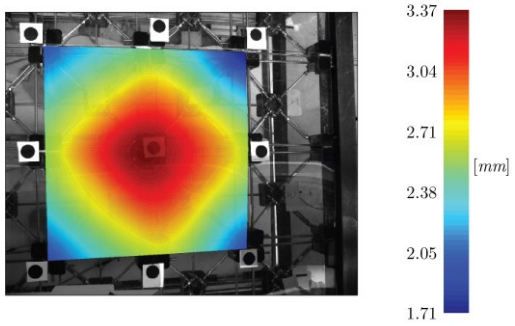

(a)

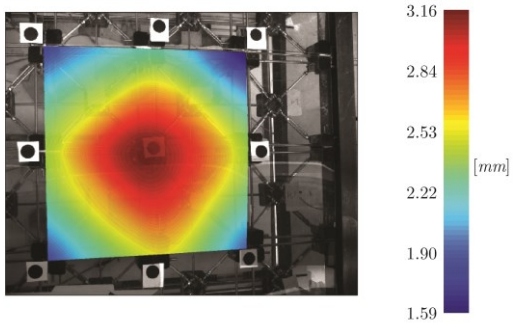

(b)

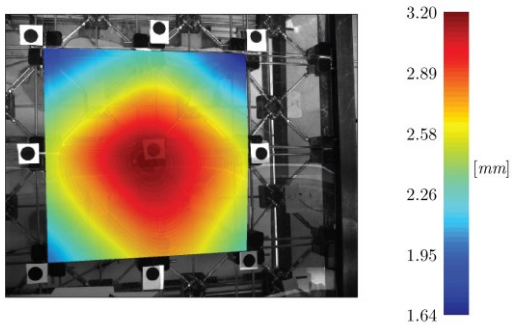

(c)

Figure 2.15. LVDTs – Displacement mapping for uniformly distributed load: (a) 1st repetition, (b) 2nd repetition, (c) 3rd repetition (EPX2).

The results obtained from the optical measurement – using OSM technology – are shown in Figs. 2.16–2.18.

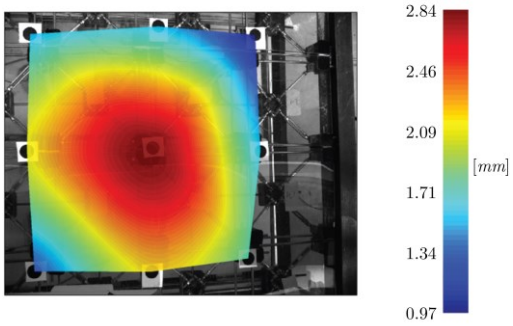

(a)

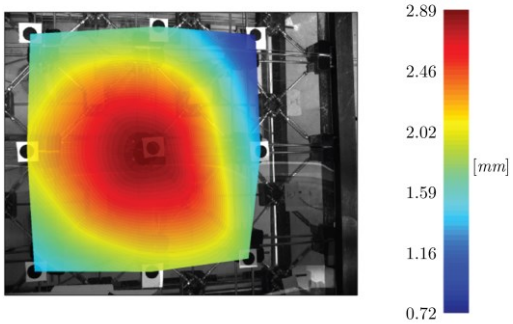

(b)

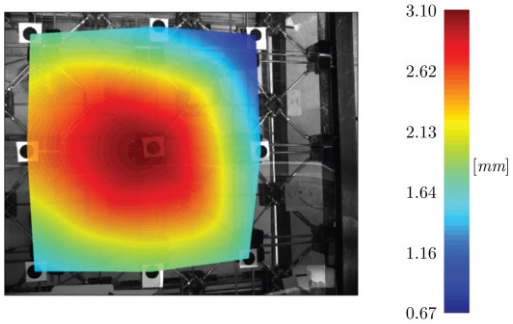

(c)

Figure 2.16. OSM – Displacement mapping for distributed load on central span: (a) 1st repetition, (b) 2nd repetition, (c) 3rd repetition (EPX2).

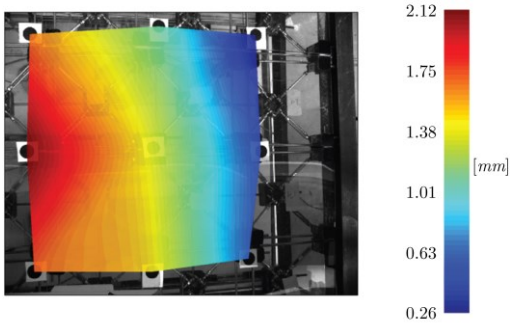

(a)

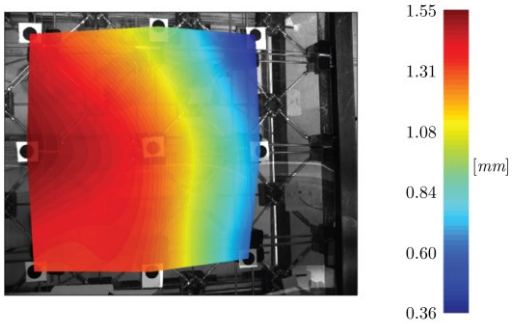

(b)

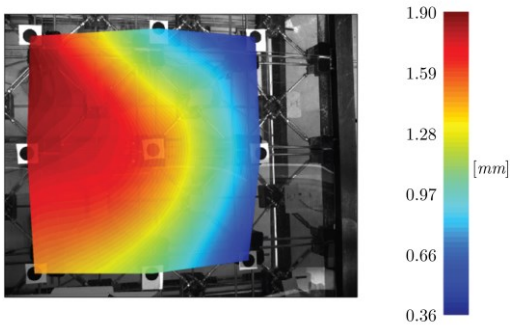

(c)

Figure 2.17. OSM – Displacement mapping for distributed load on lateral span: (a) 1st repetition, (b) 2nd repetition, (c) 3rd repetition (EPX2).

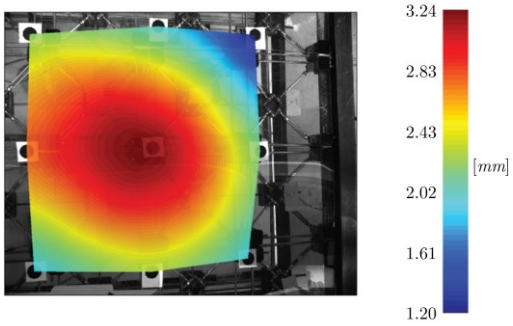

(a)

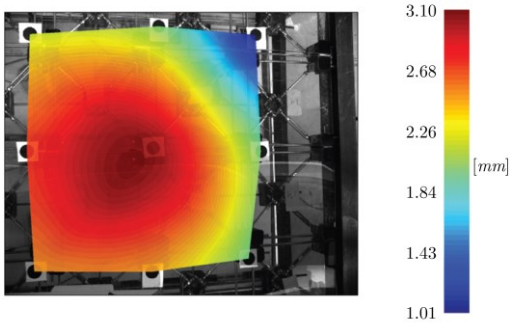

(b)

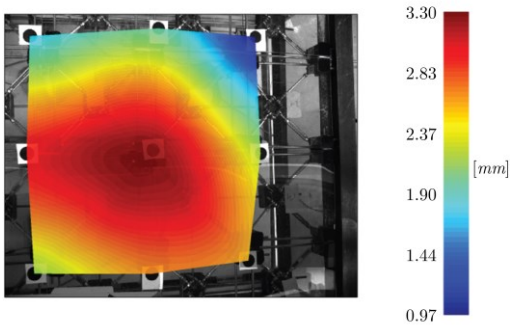

(c)

Figure 2.18. OSM – Displacement mapping for uniformly distributed load: (a) 1st repetition, (b) 2nd repetition, (c) 3rd repetition (EPX2).

2.4 Glass deck adhesively bonded with SIL adhesive

Figs. 2.19–2.21 show the graphic mapping of the vertical displacement values recorded by digital measurement (LVDT) for the glass deck adhesively bonded with SIL adhesive.

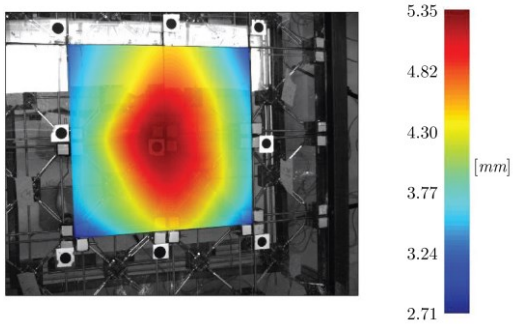

(a)

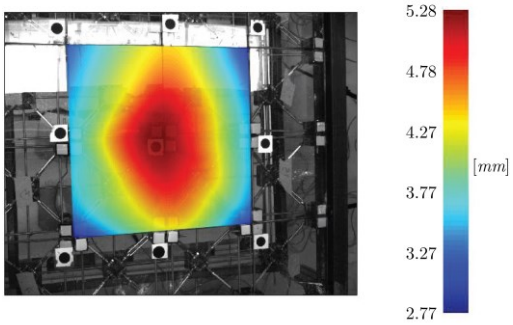

(b)

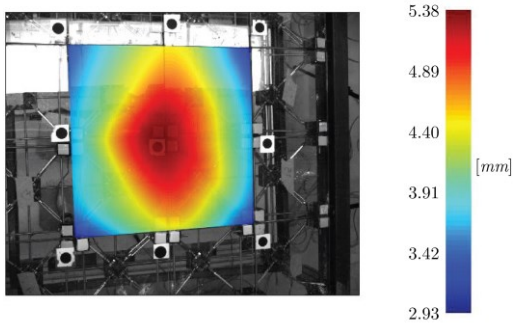

(c)

Figure 2.19. LVDTs – Displacement mapping for distributed load on central span: (a) 1st repetition, (b) 2nd repetition, (c) 3rd repetition (SIL).

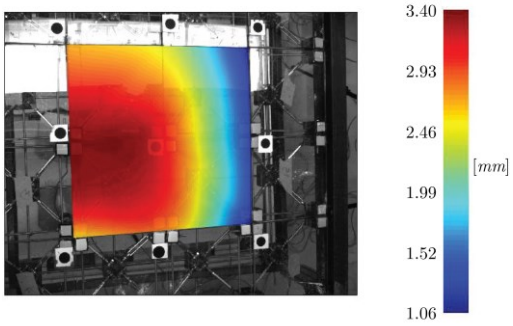

(a)

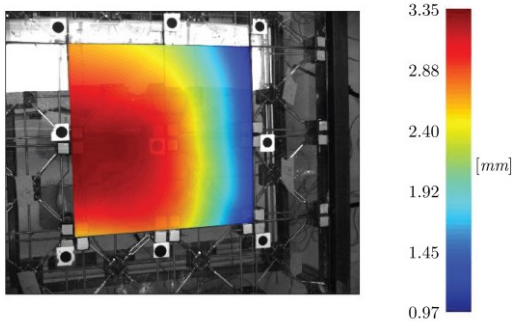

(b)

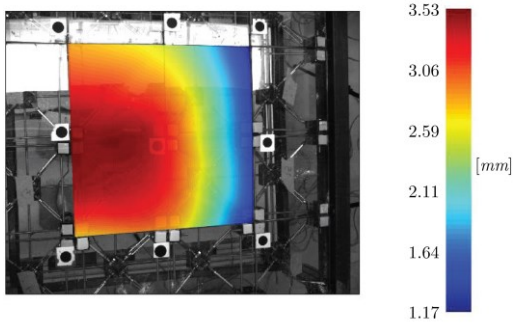

(c)

Figure 2.20. LVDTs – Displacement mapping for distributed load on lateral span: (a) 1st repetition, (b) 2nd repetition, (c) 3rd repetition (SIL).

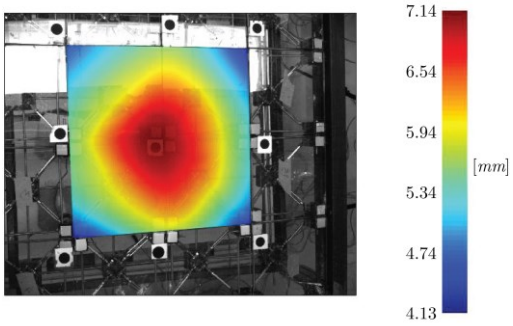

(a)

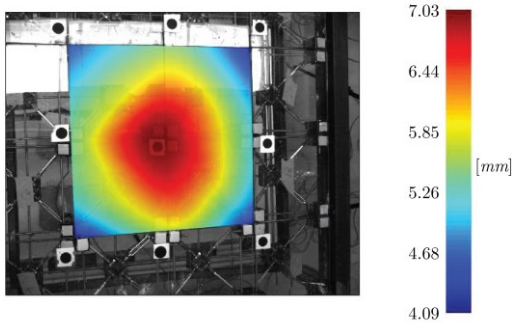

(b)

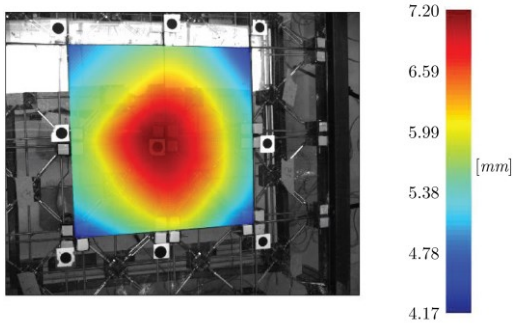

(c)

Figure 2.21. LVDTs – Displacement mapping for uniformly distributed load: (a) 1st repetition, (b) 2nd repetition, (c) 3rd repetition (SIL).

The results obtained from the optical measurement – using OSM technology – are shown in Figs. 2.22–2.24.

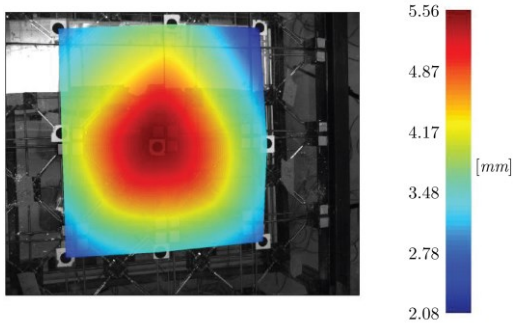

(a)

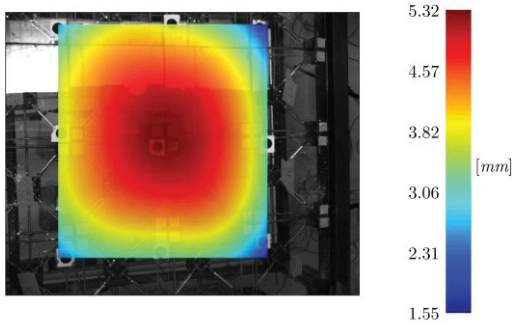

(b)

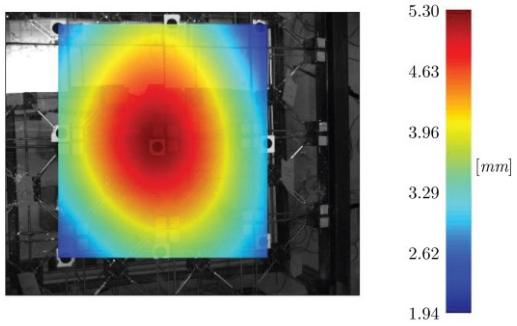

(c)

Figure 2.22. OSM – Displacement mapping for distributed load on central span: (a) 1st repetition, (b) 2nd repetition, (c) 3rd repetition (SIL).

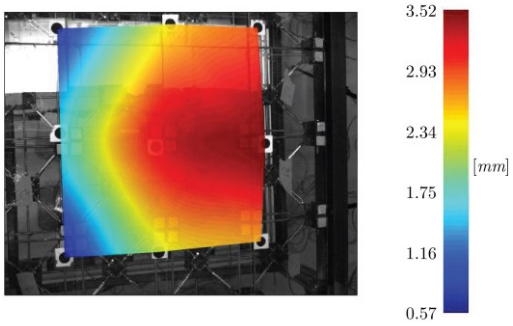

(a)

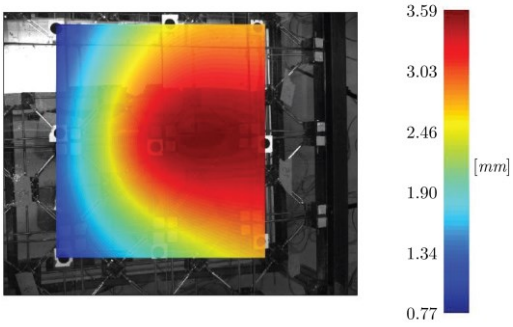

(b)

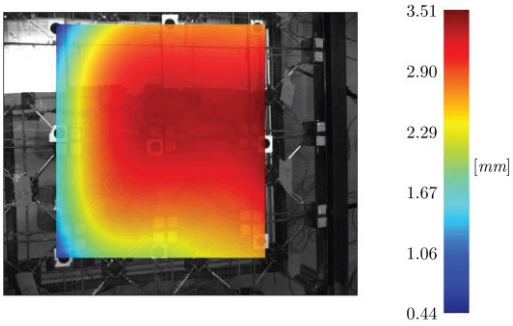

(c)

Figure 2.23. OSM – Displacement mapping for distributed load on lateral span: (a) 1st repetition, (b) 2nd repetition, (c) 3rd repetition (SIL).

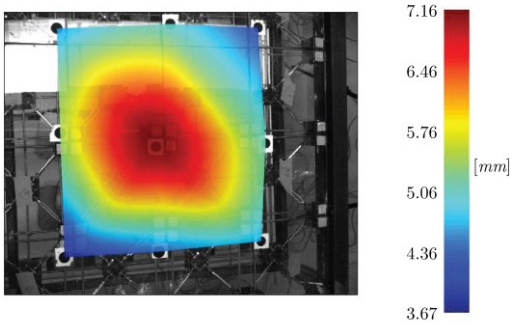

(a)

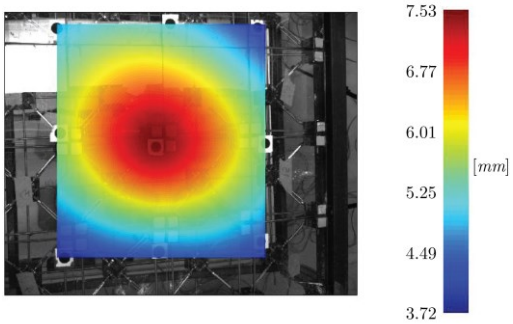

(b)

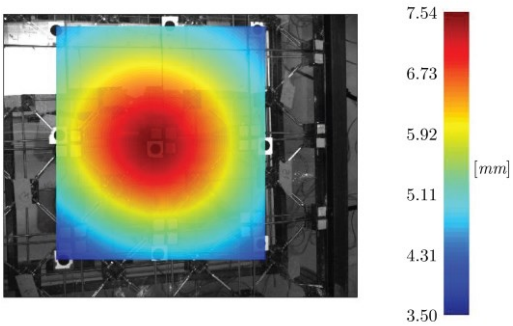

(c)

Figure 2.24. OSM – Displacement mapping for uniformly distributed load: (a) 1st repetition, (b) 2nd repetition, (c) 3rd repetition (SIL).

2.5 List of figures

Figure 2.1. LVDTs – Displacement mapping for distributed load on central span: (a) 1st repetition, (b) 2nd repetition, (c) 3rd repetition (S. SUPP.). 212
Figure 2.2. LVDTs – Displacement mapping for distributed load on lateral span: (a) 1st repetition, (b) 2nd repetition, (c) 3rd repetition (S. SUPP.). 213
Figure 2.3. LVDTs – Displacement mapping for uniformly distributed load: (a) 1st repetition, (b) 2nd repetition, (c) 3rd repetition (S. SUPP.). 214
Figure 2.4. OSM – Displacement mapping for distributed load on central span: (a) 1st repetition, (b) 2nd repetition, (c) 3rd repetition (S. SUPP.). 215
Figure 2.5. OSM – Mapping of displacements for distributed load on lateral span: (a) 1st repetition, (b) 2nd repetition, (c) 3rd repetition (S. SUPP.). 216
Figure 2.6. OSM – Displacement mapping for uniformly distributed load: (a) 1st repetition, (b) 2nd repetition, (c) 3rd repetition (S. SUPP.). 217
Figure 2.7. LVDTs – Displacement mapping for distributed load on central span: (a) 1st repetition, (b) 2nd repetition, (c) 3rd repetition (EPX1). 218
Figure 2.8. LVDTs – Displacement mapping for distributed load on lateral span: (a) 1st repetition, (b) 2nd repetition, (c) 3rd repetition (EPX1). 219
Figure 2.9. LVDTs – Displacement mapping for uniformlly distributed loadp: (a) 1st repetition, (b) 2nd repetition, (c) 3rd repetition (EPX1). 220
Figure 2.10. OSM – Displacement mapping for distributed load on central span: (a) 1st repetition, (b) 2nd repetition, (c) 3rd repetition (EPX1). 221
Figure 2.11. OSM – Displacement mapping for distributed load on lateral span: (a) 1st repetition, (b) 2nd repetition, (c) 3rd repetition (EPX1). 222
Figure 2.12. OSM – Displacement mapping for uniformly distributed load: (a) 1st repetition, (b) 2nd repetition, (c) 3rd repetition (EPX1). 223
Figure 2.13. LVDTs – Displacement mapping for distributed load on central span: (a) 1st repetition, (b) 2nd repetition, (c) 3rd repetition (EPX2). 224
Figure 2.14. LVDTs – Displacement mapping for distributed load on lateral span: (a) 1st repetition, (b) 2nd repetition, (c) 3rd repetition (EPX2). 225
Figure 2.15. LVDTs – Displacement mapping for uniformly distributed load: (a) 1st repetition, (b) 2nd repetition, (c) 3rd repetition (EPX2). 226
Figure 2.16. OSM – Displacement mapping for distributed load on central span: (a) 1st repetition, (b) 2nd repetition, (c) 3rd repetition (EPX2). 227
Figure 2.17. OSM – Displacement mapping for distributed load on lateral span: (a) 1st repetition, (b) 2nd repetition, (c) 3rd repetition (EPX2). 228
Figure 2.18. OSM – Displacement mapping for uniformly distributed load: (a) 1st repetition, (b) 2nd repetition, (c) 3rd repetition (EPX2). 229
Figure 2.19. LVDTs – Displacement mapping for distributed load on central span: (a) 1st repetition, (b) 2nd repetition, (c) 3rd repetition (SIL). 230
Figure 2.20. LVDTs – Displacement mapping for distributed load on lateral span: (a) 1st repetition, (b) 2nd repetition, (c) 3rd repetition (SIL). 231
Figure 2.21. LVDTs – Displacement mapping for uniformly distributed load: (a) 1st repetition, (b) 2nd repetition, (c) 3rd repetition (SIL). 232

Figure 2.22. OSM – Displacement mapping for distributed load on central span: (a) 1st repetition, (b) 2nd repetition, (c) 3rd repetition (SIL). 233
Figure 2.23. OSM – Displacement mapping for distributed load on lateral span: (a) 1st repetition, (b) 2nd repetition, (c) 3rd repetition (SIL). 234
Figure 2.24. OSM – Displacement mapping for uniformly distributed load: (a) 1st repetition, (b) 2nd repetition, (c) 3rd repetition (SIL). 235

ITALIAN PATENT OFFICE

Document No.

102014902301335A1

Publication Date

20160415

Applicant

UNIVERSITA' POLITECNICA DELLE MARCHE

Title

SOLAIO TENSEGRALE

DESCRIZIONE

Annessa a domanda di brevetto per INVENZIONE INDUSTRIALE avente per titolo

"Solaio tensegrale**"**

A nome: Università Politecnica delle Marche
con sede in: Piazza Roma 22, 60121 Ancona
Inventore designato: Placido Munafò
Mandatario: Basilio CICCARELLO iscritto all'Albo con il n. 512 BM,
domiciliato presso la INGENIIS s.a.s. di B. Ciccarello e C.,
Via Antonio De Berti, 24 - 00143 Roma.

****

La presente invenzione ha per oggetto un solaio tensegrale.

"Tensegrale" o "tensintegro" sono la traduzione italiana del termine "tensegrity" coniato da Richard Buckminster Fuller (1985-1983) con la contrazione dei due vocaboli inglesi "tensional" e "integrity".

Secondo la definizione di René Motro, tensegrale è un sistema in uno stato di auto-equilibrio stabile comprendente una serie discontinua di componenti compressi all'interno di un continuum di componenti tesi.

Sino ad oggi le strutture che utilizzano il principio della tensegrity hanno avuto applicazioni pratiche occasionali, spesso a scopo dimostrativo.

Il solaio tensegrale della tecnica anteriore più vicina alla presente invenzione è quello realizzato su progetto di Loris Manfroni per lo studio ABDR Architetti Associati di Roma (http://complexitys.com/english/about-tensegrity-abdr-architects/#.VCZ-TxabEvk) nel museo di Reggio Calabria, al cui interno il solaio sovrasta la sala denominata "La Piazza".

Il solaio del museo di Reggio Calabria, attualmente inagibile, è una copertura di ampie dimensioni che ha una parte di estradosso costituita da una struttura piana a maglie chiuse. Le maglie chiuse, di forma quadrata, sono formate da profilati speciali cavi d'acciaio a sezione triangolare saldati

nei nodi delle maglie. Le maglie più esterne sono chiuse su di un telaio periferico poggiato su travi perimetrali della sala. Sulle maglie, a loro volta, sono fissate lastre di vetro. Questa struttura piana a maglie chiuse è irrigidita, per limitarne la deformazione, da una sottostante struttura tensegrale di intradosso in cui un puntone a forma di asta cilindrica è unito, ad una sua estremità, ad un nodo sferico saldato ad ogni nodo di maglia della struttura piana a maglie chiuse. I puntoni sono compressi da cavi funzionanti da tiranti che sono uniti a coppie di nodi e passano attraverso fori ricavati nell'altra estremità di ogni puntone. I puntoni dei nodi più vicini al telaio periferico hanno una dimensione inferiore a quella degli altri puntoni.

Nel solaio del museo di Reggio Calabria le lastre di vetro che sono fissate sulle maglie della struttura piana di estradosso hanno soltanto una funzione di copertura e non collaborano alla limitazione della deformazione della struttura piana in quanto la struttura tensegrale di intradosso collabora a tale scopo soltanto con i profilati di acciaio della struttura piana a maglie chiuse. Quindi, i profilati di acciaio, che hanno la funzione di sorreggere il loro peso, quello della copertura a lastre di vetro, il peso della sottostante struttura tensegrale nonché il peso dei carichi fissi, quali l'arredamento, e dei carichi mobili, come le persone che calpestano la copertura, devono essere dimensionati adeguatamente. Tale dimensionamento comporta un conseguente notevole ingombro dell'insieme di struttura piana di estradosso e struttura tensegrale di intradosso. Inoltre, i puntoni sono posizionati con inclinazioni diverse rispetto al piano in cui giace la struttura piana di estradosso allo scopo di creare su di essi una forza antagonista al peso, forza che è diversa da nodo a nodo e, quindi, va calcolata in modo corretto.

In questo contesto, il compito tecnico alla base della presente invenzione è proporre un solario tensegrale che superi gli inconvenienti della tecnica nota sopra citati.

In particolare, è scopo della presente invenzione mettere a disposizione un solaio tensegrale in cui l'elemento di copertura di lastre di vetro collabori strutturalmente con gli altri componenti del solaio.

Ulteriore scopo della presente invenzione è quello di fornire un solaio tensegrale i cui componenti strutturali non richiedano una loro diversa disposizione a seconda delle luci da coprire.

Ancora uno scopo della presente invenzione è quello di proporre un telaio tensegrale che comporti un ridotto ingombro rispetto alla soluzione nota.

Uno scopo aggiuntivo della presente invenzione è quello di fornire un solaio tensegrale modulare che utilizza ripetutamente gli stessi componenti su tutta la luce del solaio.

Il compito tecnico precisato e gli scopi specificati sono sostanzialmente raggiunti da un solaio tensegrale, comprendente le caratteristiche tecniche esposte in una o più delle unite rivendicazioni.

Ulteriori caratteristiche e vantaggi della presente invenzione appariranno maggiormente chiari dalla descrizione indicativa, e pertanto non limitativa, di una forma di realizzazione preferita ma non esclusiva di un solaio tensegrale, come illustrato negli uniti disegni in cui:

- la figura 1 è una vista prospettica in esploso di una struttura portante e di un pavimento facente parte di un solaio tensegrale secondo l'invenzione;
- la figura 2 è una vista in pianta dall'alto della struttura portante e di pavimento della figura 1, unita ad un telaio periferico;
- la figura 3 è una sezione ricavata lungo un piano di traccia A-A della figura 2;
- la figura 4 è una vista prospettica schematica parziale di un nodo superiore laterale del solaio tensegrale della figura 2;
- la figura 5 è una vista prospettica schematica parziale di un nodo superiore di vertice del solaio tensegrale della figura 2;
- la figura 6 è una vista prospettica schematica parziale di un nodo superiore

interno del solaio tensegrale della figura 2;

- la figura 7 è una sezione ingrandita ricavata lungo un piano di traccia B-B della figura 3;

- la figura 8 è una sezione ingrandita ricavata lungo un piano di traccia C-C della figura 3;

- le figure 9a, b, c, d, e, sono rispettivamente una vista prospettica dall'alto e una vista in pianta dall'alto di un attacco del nodo superiore laterale della figura 4, e viste sezionata e laterali ricavate secondo le linee VL6-VL6, VL7-VL7, VL8-VL8, rispettivamente, della figura 9b;

- le figure 10a, b, c, d, sono rispettivamente una vista prospettica dall'alto e una vista in pianta dall'alto di un attacco del nodo superiore laterale consecutivo a quello della figura 4, e viste laterali ricavate secondo le linee VL9-VL9, e VL10-VL10 rispettivamente, della figura 10b;

- le figure 11a, b, c, d, sono rispettivamente una vista prospettica dall'alto e una vista in pianta dall'alto di un attacco del nodo superiore di vertice della figura 5, e viste sezionata e laterale ricavate secondo le linee VL4-VL4, e VL5-VL5 rispettivamente, della figura 11b;

- le figure 12a, b, c, d, e, sono rispettivamente una vista prospettica dall'alto e una vista in pianta dall'alto di un attacco del nodo superiore centrale della figura 6, e viste laterali ricavate secondo le linee VL1-VL1, VL2-VL2, VL3-VL3, rispettivamente, della figura 12b;

- la figura 13 è una vista prospettica schematica parziale di un nodo inferiore d'angolo del solaio tensegrale della figura 1;

- le figure 14a, b, sono una vista in pianta dall'alto e, rispettivamente, una vista laterale di un attacco del nodo inferiore d'angolo della figura 13;

- la figura 15 è una vista prospettica schematica parziale di un nodo inferiore centrale del solaio tensegrale della figura 1; e

- la figura 16 è una vista prospettica in esploso di un attacco del nodo inferiore centrale della figura 15.

Si faccia riferimento inizialmente alle figure 1 a 3 che sono, rispettivamente, una vista prospettica in esploso di una struttura portante e di un pavimento di estradossos facente parte di un solaio tensegrale secondo l'invenzione, una vista in pianta dall'alto della struttura portante e di pavimento della figura 1, unita ad un telaio o cordolo periferico, e una sezione ricavata lungo un piano di traccia A-A della figura 2.

La struttura portante è indicata complessivamente con 1, il pavimento con 2 e il telaio periferico o cordolo con 3.

Il pavimento 2 è formato da pannelli quadrilateri 4; nella forma di realizzazione illustrata i pannelli 4 sono quadrati e sono fatti di vetro strutturale, anche di tipo stratificato. Il pannello scelto è quello ad esempio prodotto dalla Saint Gobain e contraddistinto dal marchio SGG LITE-FLOOR®, ma ovviamente qualsiasi altro pannello o lastra di qualunque materiale adatto può essere impiegato nel solaio tensegrale secondo la presente invenzione. Inoltre, il pannello può essere di vetro opaco o trasparente. Il pavimento di estradosso 2 è sostenuto dalla struttura portante 1 tramite una molteplicità di nodi superiori di un sistema a tiranti e puntoni.

La struttura portante 1 è unita al telaio periferico 3, rappresentato nella forma di realizzazione illustrata nelle figure 2 e 3, con quattro lati 5 e quattro vertici 6. Ogni lato 5 del telaio periferico 3 è collegato all'ossatura di un edificio, rappresentata schematicamente e indicata come O. Anche se questa forma di realizzazione è presentata in modo da formare un solaio, essa non deve necessariamente essere pensata esclusivamente integrata in un'ossatura di edificio ma può essere integrata in qualunque telaio o cordolo per realizzare una piattaforma, una passerella o altra struttura piana.

In generale, il sistema a tiranti e puntoni adottato per la struttura portante 1 è di tipo modulare, formato da puntoni disposti secondo gli spigoli laterali di una piramide a base quadrata. Considerando inferiore l'intradosso, nel

vertice superiore di ogni piramide è previsto un nodo superiore, mentre nei suoi vertici di base sono previsti nodi inferiori mediante i quali ogni piramide è collegata con i puntoni di piramidi adiacenti. I nodi superiori sono sostenuti da tiranti fissati alle loro estremità opposte a lati opposti del telaio periferico; anche tutti i nodi inferiori sono collegati fra loro da tiranti; i nodi inferiori di estremità nelle file di nodi sono collegati anche con altri tiranti allo stesso telaio periferico.

Il particolare sistema a tiranti e puntoni scelto per la struttura portante è solamente esemplificativo. Si dovrebbe comprendere invece che la caratteristica distintiva principale della presente invenzione è rappresentata dal fatto che la struttura portante applica una forza vincolare concentrata su un punto del bordo di ogni pannello del pavimento tramite ogni nodo superiore che è situato fra un pannello e un altro pannello adiacente. In altre parole, ogni pannello è sottoposto generalmente a compressione, e il pavimento tutto collabora con la struttura portante al sostegno del solaio sull'ossatura dell'edificio. Di conseguenza, la struttura portante è alleggerita rispetto al caso di una pavimentazione non collaborante, il suo ingombro in altezza può essere ridotto, ed anche il costo.

Come si vedrà in seguito, ogni pannello presenta opportunamente nei suoi angoli elementi angolari di trattenuta solidali con il pannello, mentre i nodi superiori prevedono alla loro sommità un attacco comprendente un profilato speciale semicavo di aggancio provvisto di un'apertura superiore per l'inserimento di almeno un elemento angolare di trattenuta del pannello.

Tuttavia, prima di descrivere in maggiore dettaglio il collegamento di ogni pannello di pavimento con i nodi superiori della struttura portante, si descrive nei particolari quest'ultima.

La molteplicità di nodi superiori comprende nodi superiori laterali 7, 8, fissati a lati 5 rispettivamente consecutivi del telaio periferico 3, nodi superiori di vertice 9, ognuno fissato ad un vertice 6 del telaio periferico 3, e

nodi superiori interni 10 non a contatto col telaio periferico 3.

Come mostrato in particolare nelle figure 2 e 3, coppie di nodi superiori laterali 7, 7 sono fissati a lati opposti 5 del telaio periferico 3 mediante almeno una coppia di tiranti superiori 11, 11 passanti attraverso nodi superiori interni 10 che sono interposti fra i nodi superiori laterali opposti 7, 7 ed allineati con essi. Come mostrato nella figura 4, che è una vista prospettica schematica parziale di un nodo superiore laterale 7 del solaio tensegrale della figura 2, due tiranti superiori 11, 11 attraversano, con loro terminali 12, 12, fori passanti 13 ricavati in un primo attacco 19 che costituisce il cuore del nodo superiore laterale 7. Ogni terminale 12 è dotato di una filettatura esterna 14 per il fissaggio con dadi 15 in fori ricavati nell'ala 16 del profilato a doppio T del lato 5 del telaio periferico 3. Ogni terminale 12 ha una cava interna per il fissaggio del trefolo 17 del tirante 11. Oltre al nodo superiore laterale 7 e ai tiranti superiori 11, nella figura 4 sono mostrati due elementi angolari di trattenuta 18, 18 destinati ad essere solidali con rispettivi pannelli 4, 4, ed inseriti in un primo profilato speciale semicavo di aggancio 20 previsto nell'attacco 19 che costituisce la parte superiore del nodo superiore laterale 7. Gli elementi angolari di trattenuta 18, 18 sono destinati ad interporsi fra rispettivi pannelli 4, 4 e l'ala 16, ad essi prospiciente, della trave a doppio T del lato 5 del telaio periferico 3. Cuscinetti 21 di gomma sono previsti sul profilato speciale semicavo di aggancio 20 e sugli elementi angolari di trattenuta 18 per l'appoggio sicuro della base e, rispettivamente, del bordo dei pannelli 4, 4. La gomma dei cuscinetti può essere trasparente oppure no.

Il nodo superiore laterale 7 è rappresentato in dettaglio nelle figure 9a, b, c, d, e, che sono rispettivamente una vista prospettica dall'alto, una vista in pianta dall'alto e viste sezionata e laterali del primo attacco 19 del nodo superiore laterale 7 della figura 4. Si può osservare che il nodo superiore laterale 7 presenta il primo profilato speciale semicavo di aggancio 20,

dotato di una prima apertura passante superiore 22 per l'inserimento degli elementi angolari di trattenuta 18, 18 mostrati nella figura 4. Il primo attacco 19 del nodo superiore laterale 7 comprende inoltre prime piastre angolari 23, 23 dove sono ricavati i fori 13, 13 per il passaggio dei terminali 12 dei tiranti 11, 11 e fori 24, 24 per l'attacco di aste a lunghezza regolabile, funzionanti da tiranti laterali, come si vedrà in seguito.

Si faccia adesso riferimento alle figure 10a, b, c, d, che sono, rispettivamente, una vista prospettica dall'alto, una vista in pianta dall'alto e viste laterali di un primo attacco 25 del nodo superiore laterale di lato consecutivo a quello della figura 4. Questo nodo laterale consecutivo, indicato con 8, è mostrato inserito nella struttura portante 1 nella figura 1. Questo nodo superiore laterale consecutivo 8 ha un primo profilato speciale semicavo 26 provvisto di una prima apertura 27 che fornisce una battuta per gli elementi angolari 18 di trattenuta dei pannelli 4. Come per il nodo superiore laterale 7, anche il nodo superiore laterale consecutivo 8 comprende prime piastre angolari 23, 23 dove sono ricavati i fori 13, 13 per il passaggio dei terminali 12, 12 dei tiranti 11, 11 e fori 24, 24 per l'aggancio di aste a lunghezza regolabile, funzionanti da tiranti laterali, come si vedrà in seguito.

Facendo riferimento alla figura 5, in essa è mostrata una vista prospettica schematica parziale di un nodo superiore di vertice 9 del solaio tensegrale della figura 2. Esso comprende un secondo attacco 28 formato da un secondo profilato speciale cavo 29 dotato di una seconda apertura passante superiore 30. Il secondo profilato speciale cavo 29 si prolunga verso il basso con due piastre ortogonali 31, 31 dotate di un foro passante 32, 32 per due bulloni 33, 33. Oltre al nodo superiore di vertice 9 e ai bulloni 33, 33, nella figura 5 è mostrato un elemento angolare di trattenuta 18 destinato ad essere solidale con un rispettivo pannello 4, ed inserito nel profilato speciale semicavo di aggancio 29 previsto nell'attacco 28 che costituisce la parte

superiore del nodo superiore di vertice 9.

Il nodo superiore di vertice 9 è rappresentato in dettaglio nelle figure 11a, b, c, d, che sono rispettivamente una vista prospettica dall'alto, una vista in pianta dall'alto e viste laterali del secondo attacco 28 del nodo superiore laterale della figura 5. Si può osservare che il nodo superiore laterale 7 presenta il secondo profilato speciale semicavo di aggancio 29, dotato di un'apertura passante superiore 30 per l'inserimento degli elementi angolari di trattenuta 18, 18 mostrati nella figura 4. Il nodo superiore laterale 7 comprende inoltre piastre ortogonali 31, 31 dove sono ricavati i fori 32, 32 per il passaggio dei bulloni 33, 33 per l'attacco nel vertice 6 del telaio periferico 3.

Si faccia riferimento adesso alla figura 6, che una vista prospettica schematica parziale di un nodo superiore interno 10 del solaio tensegrale della figura 2. Due coppie di tiranti superiori 11, 11 attraversano ortogonalmente un terzo attacco 35 del nodo superiore interno 10 in fori passanti 13, 13 di piastre ortogonali 37 del nodo superiore interno 10.

Oltre al nodo superiore laterale 10 e ai tiranti superiori 11 disposti ortogonalmente, nella figura 6 sono mostrati quattro elementi angolari di trattenuta 18, 18 destinati ad essere solidali con rispettivi pannelli 4, 4, ed inseriti in un profilato speciale semicavo di aggancio 34 previsto nell'attacco 35 che costituisce la parte superiore del nodo superiore laterale. Gli elementi angolari di trattenuta 18, 18 sono destinati ad interporsi fra rispettivi pannelli 4, 4 e l'ala 16 ad essi prospiciente della trave a doppio T del lato 5 del telaio periferico 3. Cuscinetti 21 di gomma sono previsti sugli elementi angolari di trattenuta 18 per l'appoggio sicuro della base e, rispettivamente, del bordo dei pannelli 4, 4.

Il nodo superiore interno 10 è rappresentato in dettaglio nelle figure 12a, b, c, d, e, che sono rispettivamente una vista prospettica dall'alto, una vista in pianta dall'alto e viste laterali di un terzo attacco 35 del nodo superiore

interno della figura 6. Si può osservare che il nodo superiore laterale 7 presenta il terzo profilato speciale semicavo di aggancio 34, dotato di un'apertura passante superiore 36 per l'inserimento degli elementi angolari di trattenuta 18, 18 mostrati nella figura 6. Il nodo superiore laterale 10 comprende inoltre piastre ortogonali 37 dove sono ricavati i fori 13, 13 per il passaggio dei tiranti inferiori 11, 11 e fori 38, 38 per l'attacco di puntoni come si vedrà in seguito.

Tutti i nodi superiori interni 10 sono intorno al vertice geometrico di sommità di una molteplicità di piramidi a base quadrata, ognuna delle quali ha per spigoli laterali quattro puntoni 39. Ogni puntone 39, quindi, nella sua estremità superiore è fissato al vertice superiore della piramide. in prossimità dell'estradosso, e nella sua estremità inferiore confluisce in un nodo inferiore in ciascuno dei quattro vertici inferiori della piramide.

Il collegamento fra i nodi superiori interni 10 e i puntoni 39 è illustrato nella figura 7, che è una sezione ingrandita ricavata lungo un piano di traccia B-B della figura 3. Nella stessa figura si può osservare il passaggio dei tiranti 11, 11 attraverso il nodo superiore interno 10 e l'appoggio su quest'ultimo dei pannelli di vetro 4, 4 con l'interposizione dei cuscinetti di gomma 21. Fra un pannello 4 e l'altro è prevista una sigillatura 40. La sigillatura può essere fatta di silicone o altro materiale adatto.

Nella figura 8, che è una sezione ingrandita ricavata lungo un piano di traccia C-C della figura 3, è mostrato il passaggio dei tiranti 11, 11 attraverso il nodo superiore esterno 7 e l'appoggio su quest'ultimo dei pannelli di vetro 4, 4 con l'interposizione dei cuscinetti di gomma 21. Fra un pannello 4 e l'altro è prevista una sigillatura 40. La sigillatura 40 può essere di silicone o altro materiale adatto.

Inferiormente il nodo superiore esterno 7 è collegato con una coppia di aste a lunghezza variabile 41, 41 funzionanti da tiranti, collegate inferiormente a rispettivi nodi inferiori prossimali 42 vicini al telaio periferico 3, come

mostrato nella figura 3.

Oltre ai nodi inferiori prossimali 42, vi è una pluralità di nodi inferiori distali 43, distanti dal telaio periferico 3 e disposti sostanzialmente al centro del reticolo di nodi inferiori come mostrato nella figura 2.

Le figure 1 e 3 mostrano che nodi inferiori prossimali opposti 42, 42 sono collegati tra loro mediante tiranti 44 paralleli ai lati del telaio periferico e passanti per nodi inferiori prossimali 42 o distali 43 interposti fra i nodi inferiori prossimali opposti 42, 42 ed allineati con essi.

Un nodo inferiore prossimale 42, in particolare d'angolo, è rappresentato nella figura 13 che è una sua vista prospettica schematica parziale.

Nel nodo inferiore prossimale 42 è visibile un primo morsetto 45 meglio mostrato nelle figure 14a, 14b che sono una vista in pianta dall'alto e, rispettivamente, una vista laterale del primo morsetto 45. Il primo morsetto 45 ha pareti a T 47 dotate di fori 48 per il fissaggio di un puntone 39 e di due aste a lunghezza variabile 41.

Inferiormente, il primo morsetto 45 ha un corpo 46 e una base rimovibile 49, entrambi dotati di asole 51 per il passaggio di due tiranti inferiori 44, 44 disposti ortogonalmente e bloccati sul morsetto 45 mediante rispettivi dadi 50, 50. Dovrebbe essere evidente che in questo modo i tiranti inferiori 44, 44 si trovano su piani paralleli diversi in maniera da non intersecarsi all'interno del primo morsetto 45.

Si faccia adesso riferimento alle figure 15 e 16 che sono, rispettivamente, una vista prospettica schematica parziale di un nodo inferiore distale 43 del solaio tensegrale della figura 1 e una vista prospettica in esploso di un secondo morsetto 52 del nodo inferiore distale 43 della figura 15.

Il secondo morsetto 52 ha un corpo 53 con pareti ortogonali 54 dotate di fori 55 per il fissaggio di quattro puntoni 39. Inferiormente il secondo morsetto 52 ha una base rimovibile 56 dotata di asole 57 per il passaggio di due tiranti inferiori 44, 44 disposti ortogonalmente su due piani paralleli

diversi in maniera da non intersecarsi all'interno dell'attacco 52. Il corpo 53 e la base rimovibile 56 sono uniti mediante bulloni 58.

Si comprende come siano stati raggiunti gli scopi della presente invenzione per la realizzazione di un solaio tensegrale, fungente anche come semplice copertura, utilizzando acciaio o altro materiale in grado di avere analoghe caratteristiche di capacità di resistenza agli sforzi di trazione e di compressione, come ad esempio i profili in pultruso. E' evidente che anche altri materiali adatti possano essere impiegati, quali legno, nylon, ceramica (ossido di zirconio).

La scelta dei pannelli di vetro conferisce trasparenza al solaio. La scelta dei componenti modulari dà rapidità di assemblaggio, leggerezza, economicità grazie alla loro riproducibilità in serie, alla loro versatilità, ovvero alla possibilità di applicazioni in differenti ambiti costruttivi.

Ing. Basilio CICCARELLO
(Albo iscr. n. 512 BM)

RIVENDICAZIONI

1. Solaio tensegrale, comprendente una struttura portante (1) unita ad un telaio periferico (3), avente quattro lati (5) e quattro vertici (6), ed un pavimento di estradosso (2) formato da pannelli quadrilateri (4), aventi bordi e angoli, e sostenuto da detta struttura portante (1) tramite una molteplicità di nodi superiori (7, 8, 9, 10) di un sistema a tiranti e puntoni, caratterizzato dal fatto che detta struttura portante (1) applica una forza vincolare concentrata su un punto del bordo di ogni pannello tramite ogni nodo superiore (7, 8, 9, 10) che è situato fra un pannello (4) e un altro pannello (4) adiacente del pavimento di estradosso (2).

2. Solaio tensegrale secondo la rivendicazione 1, in cui ogni nodo superiore (7, 8, 9, 10) è collocato in prossimità di un angolo di pannello quadrilatero (4) dotato di un elemento angolare di trattenuta (18) che è inserito in detto nodo superiore (7, 8, 9, 10).

3. Solaio tensegrale secondo la rivendicazione 1, in cui detta molteplicità di nodi superiori (7, 8, 9, 10) comprende nodi superiori laterali (7, 8) fissati a detti lati (5) di telaio periferico (3), nodi superiori di vertice (9), ognuno fissato ad un vertice (6) di detto telaio periferico (3), e nodi superiori interni (10) non a contatto con detto telaio periferico (3).

4. Solaio tensegrale secondo la rivendicazione 3, in cui coppie di nodi superiori laterali opposti (7, 8) sono fissati a lati opposti (5) del telaio periferico (3) mediante almeno una coppia di tiranti superiori (11, 11) passanti attraverso nodi superiori interni (10) che sono interposti fra detti nodi superiori laterali (7, 8) opposti, ed allineati con essi.

5. Solaio tensegrale secondo la rivendicazione 3, in cui ad ognuno di detti nodi superiori interni (10) sono fissati quattro puntoni (39) diretti lungo gli spigoli laterali di una piramide a base quadrata, ogni puntone avendo un'estremità superiore nel vertice superiore di detta piramide corrispondente a detto nodo superiore interno (10), e un'estremità inferiore in uno dei

quattro vertici inferiori di detta piramide formante un nodo inferiore (42, 43).

6. Solaio tensegrale secondo la rivendicazione 5, in cui detti nodi inferiori (42, 43) comprendono una pluralità di nodi inferiori prossimali (42), vicini a detto telaio periferico (3), e una pluralità di nodi inferiori distali (43), distanti da detto telaio periferico (3).

7. Solaio tensegrale secondo la rivendicazione 6, in cui nodi inferiori prossimali (42) opposti sono collegati mediante tiranti inferiori (44) paralleli ai lati (5) del telaio periferico (3) e passanti per nodi inferiori prossimali (42) o distali (43) che sono interposti fra detti nodi inferiori prossimali (42) opposti ed allineati con essi.

8. Solaio tensegrale secondo la rivendicazione 6, in cui ognuno di detti nodi inferiori prossimali (42) è collegato mediante due aste (41) a lunghezza regolabile a due nodi superiori laterali (7, 8).

9. Solaio tensegrale secondo la rivendicazione 1, in cui detti pannelli quadrilateri (4) sono fatti di vetro strutturale.

10. Solaio tensegrale secondo la rivendicazione 2, in cui detti pannelli quadrilateri (4) poggiano su detti nodi superiori (7, 8, 9, 10) con l'interposizione di un cuscino (21) di gomma, e ogni pannello quadrilatero (4) è unito al pannello quadrilatero (4) adiacente mediante una sigillatura (40).

11. Solaio tensegrale secondo la rivendicazione 4, in cui detti nodi superiori laterali (7, 8) sono sotto forma di un primo attacco (19, 25) comprendente un primo profilato speciale semicavo di aggancio (20, 26) provvisto di una prima apertura superiore (22, 27) per l'inserimento di un elemento angolare di trattenuta (18) del pannello (4), e prime piastre (23), mutuamente ortogonali e ortogonali a detto profilato speciale semicavo (20, 26), che sono forate per il passaggio di detta almeno una coppia di tiranti superiori (11, 11) fissati al telaio periferico (3).

12. Solaio tensegrale secondo la rivendicazione 4, in cui detti nodi superiori di vertice (9) sono sotto forma di un secondo attacco (28) comprendente un secondo profilato speciale semicavo di aggancio (29) provvisto di una seconda apertura superiore (30) per l'inserimento di un elemento angolare di trattenuta (18) del pannello (4), e seconde piastre (31), mutuamente ortogonali e ortogonali a detto profilato speciale semicavo (29), che sono forate per il passaggio di due bulloni (33, 33) fissati a un vertice (6) del telaio periferico (3).

13. Solaio tensegrale secondo la rivendicazione 4, in cui detti nodi superiori interni (10) sono sotto forma di un terzo attacco (35) comprendente un terzo profilato speciale semicavo di aggancio (34) provvisto di una terza apertura superiore (36) per l'inserimento di coppie contrapposte di elementi angolari di trattenuta (18) del pannello (4), e terze piastre (37), mutuamente ortogonali e ortogonali a detto terzo profilato speciale semicavo di aggancio (34), che sono forate per il passaggio di due coppie di tiranti superiori (11).

14. Solaio tensegrale secondo la rivendicazione 6, in cui un nodo inferiore prossimale (42) comprende un primo morsetto (45) avente pareti a T (47) dotate di fori (48) per il fissaggio di un puntone (39) e di due aste a lunghezza variabile (41), il primo morsetto 45 avendo un corpo (46) e una base rimovibile (49), entrambi dotati di asole (51) per il passaggio di due tiranti inferiori (44, 44) disposti ortogonalmente e bloccati sul primo morsetto (45) mediante rispettivi dadi (50, 50).

15. Solaio tensegrale secondo la rivendicazione 6, in cui un nodo inferiore distale (43) comprende un secondo morsetto (52) avente un corpo (53) con pareti ortogonali (54) dotate di fori (55) per il fissaggio di quattro puntoni (39), ed una base rimovibile (56) dotata di asole (57) per il passaggio di due tiranti inferiori (44, 44) disposti ortogonalmente, il corpo (53) e la base rimovibile (56) essendo uniti mediante bulloni (58).

p.i. di Università Politecnica delle Marche

IL MANDATARIO
Ing. Basilio CICCARELLO
(Albo iscr. n. 512 BM)

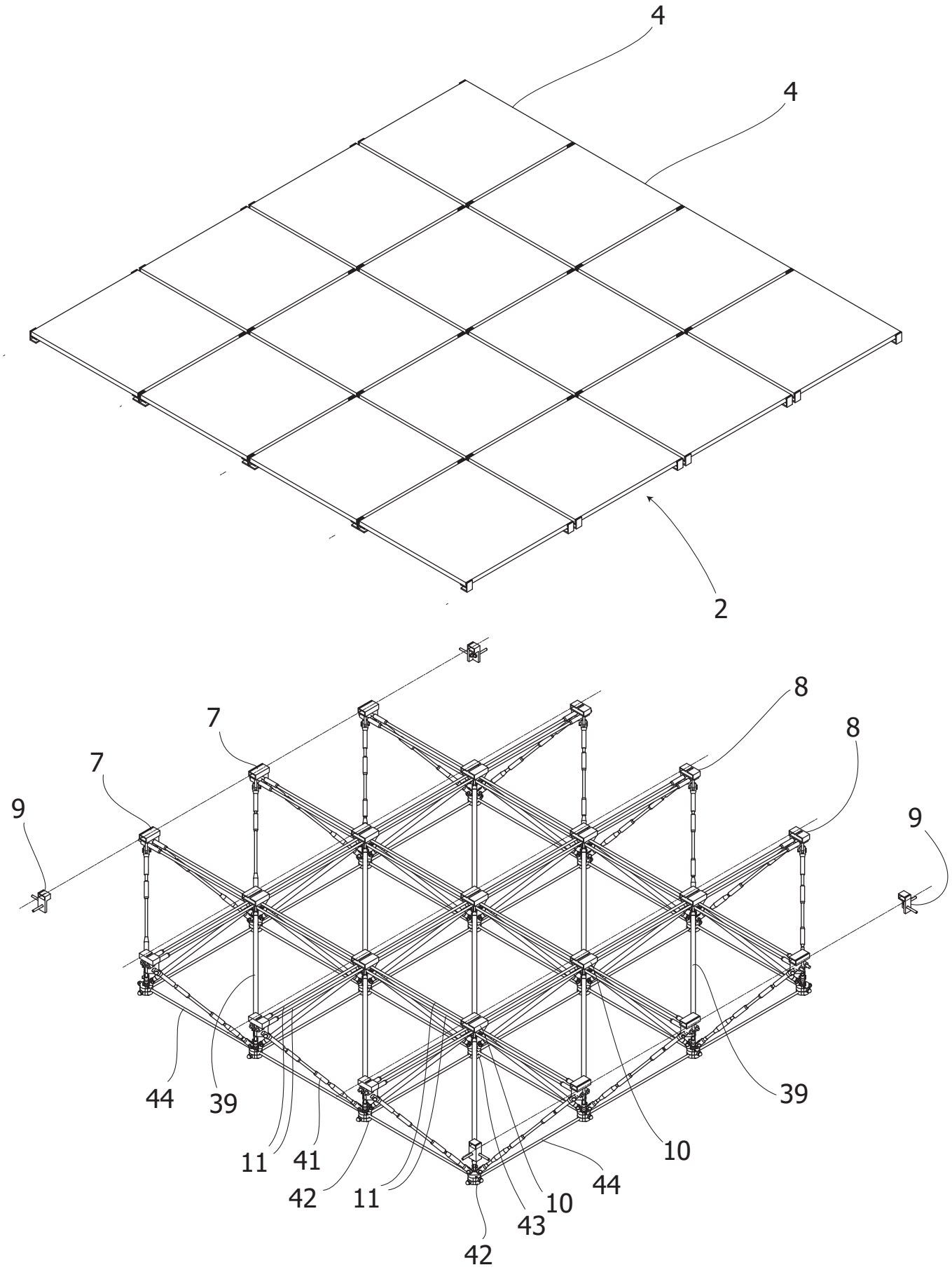

Fig.1

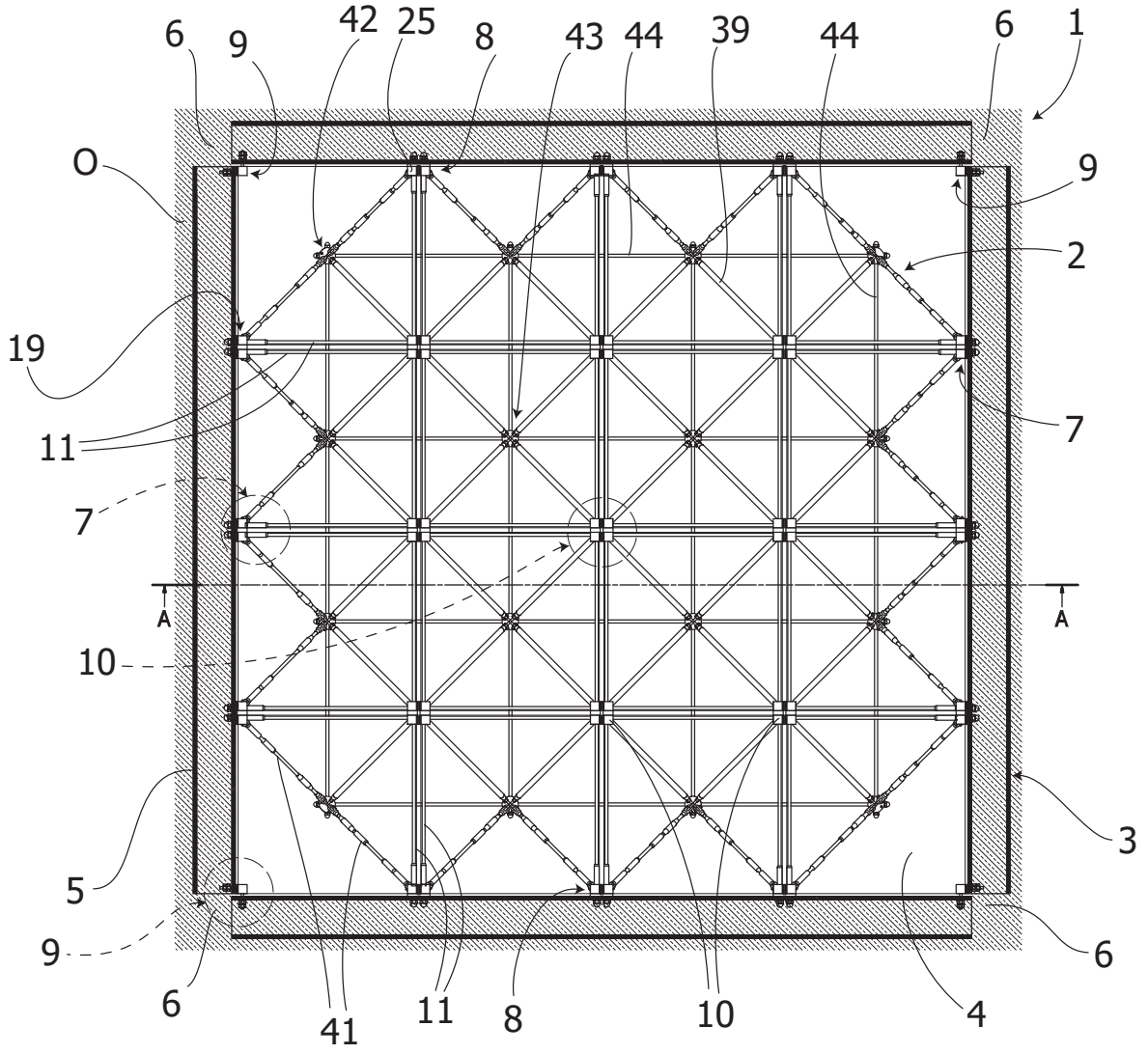
6
9
42
25
8
43
44
39
44
6
1
O
9
2
19
11
7
7
A
A
10
3
5
9
6
6
41
11
8
10
4

Fig.2

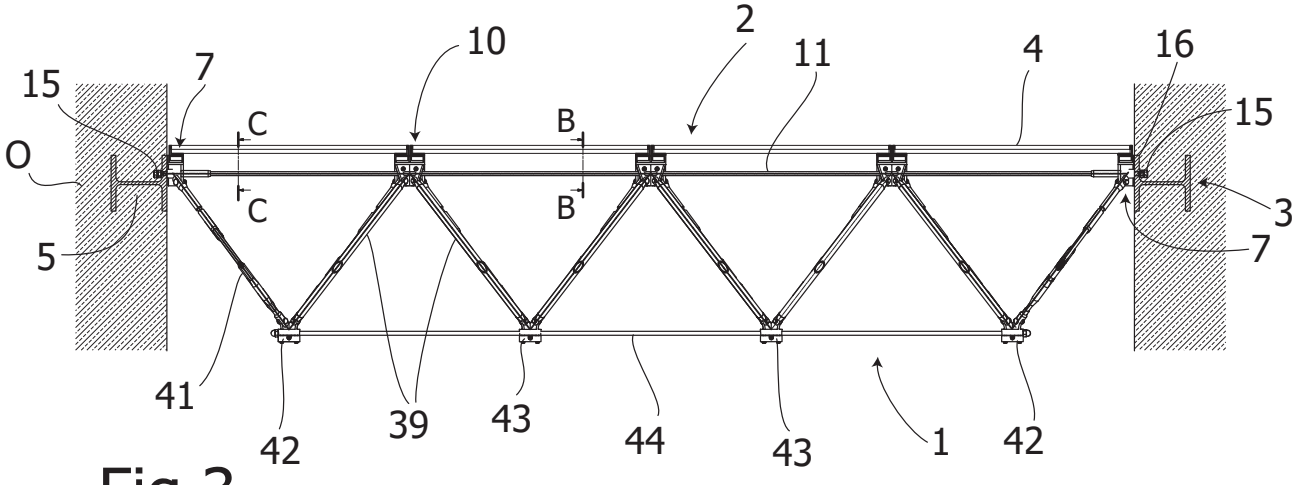
15
7
10
2
11
4
16
15
O
C
C
B
B
3
5
7
41
42
39
43
44
43
1
42

Fig.3

Fig. 4

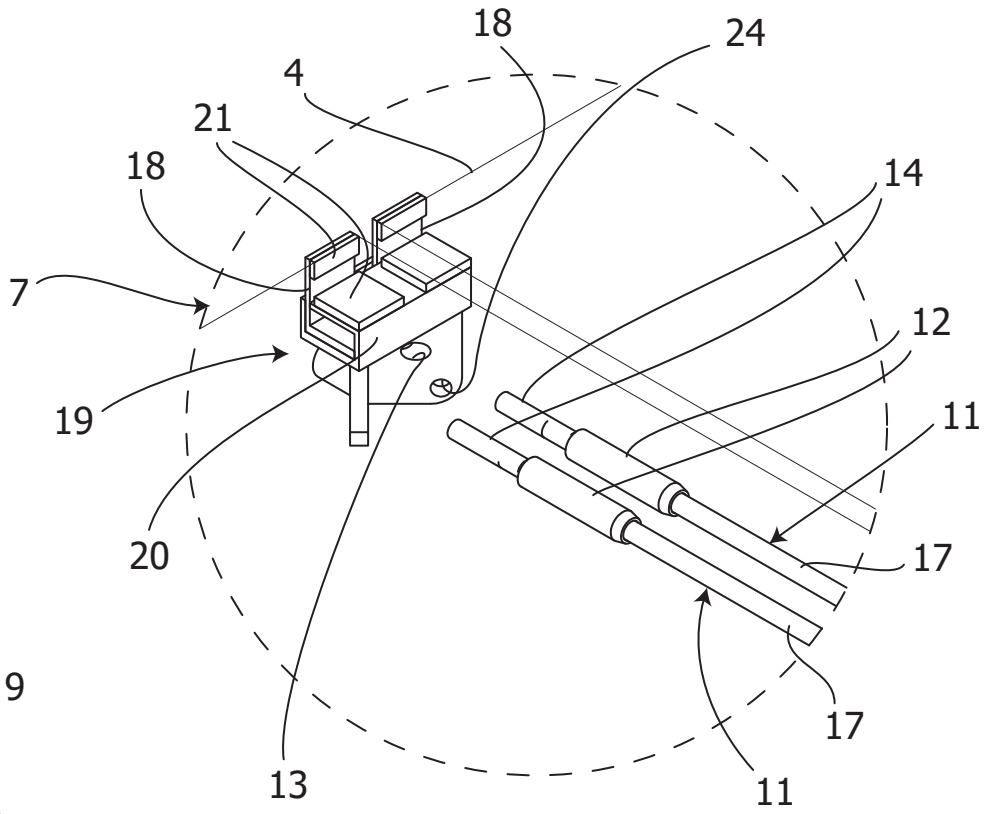

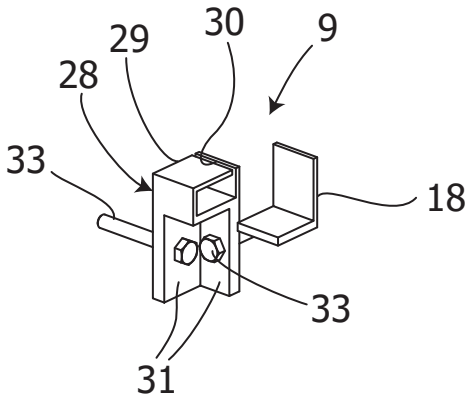

Fig. 5

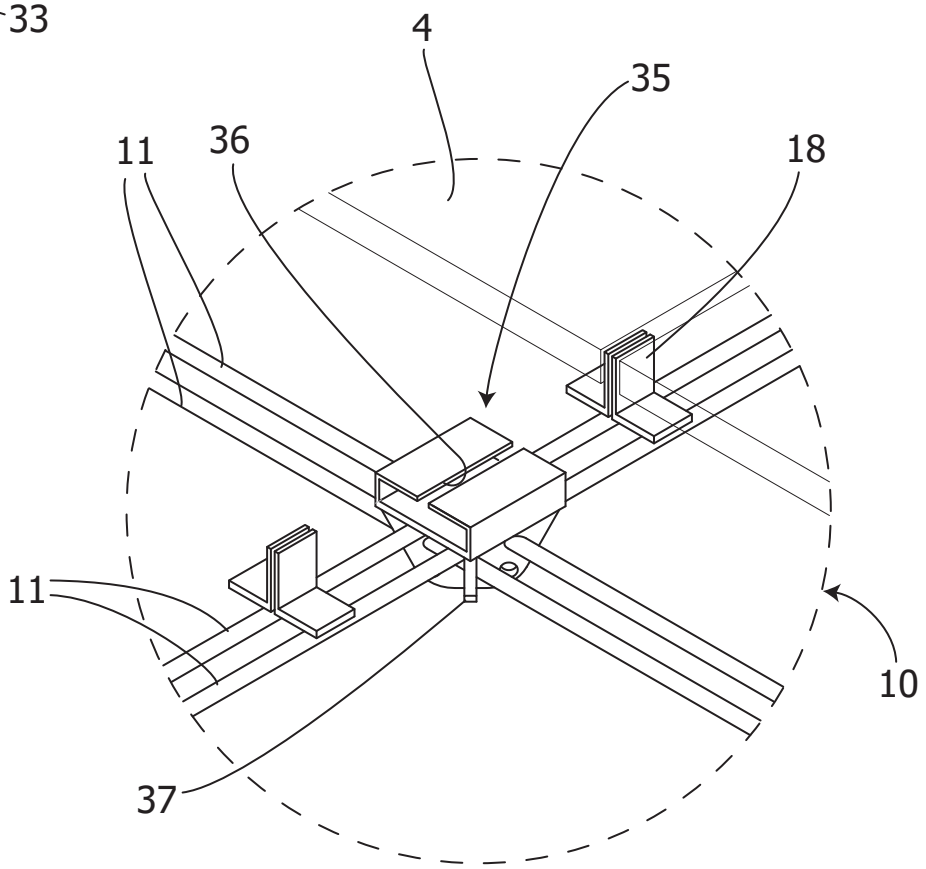

Fig. 6

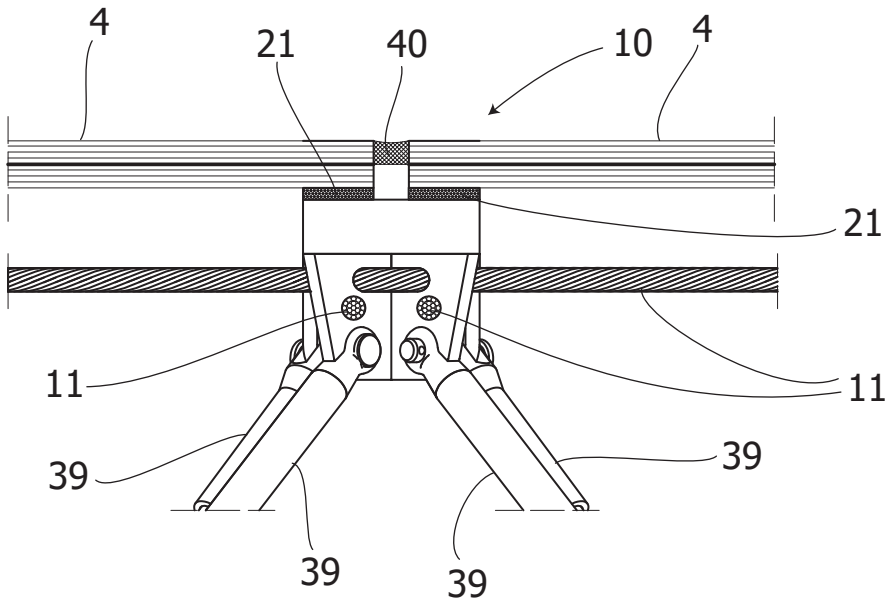

Fig. 7

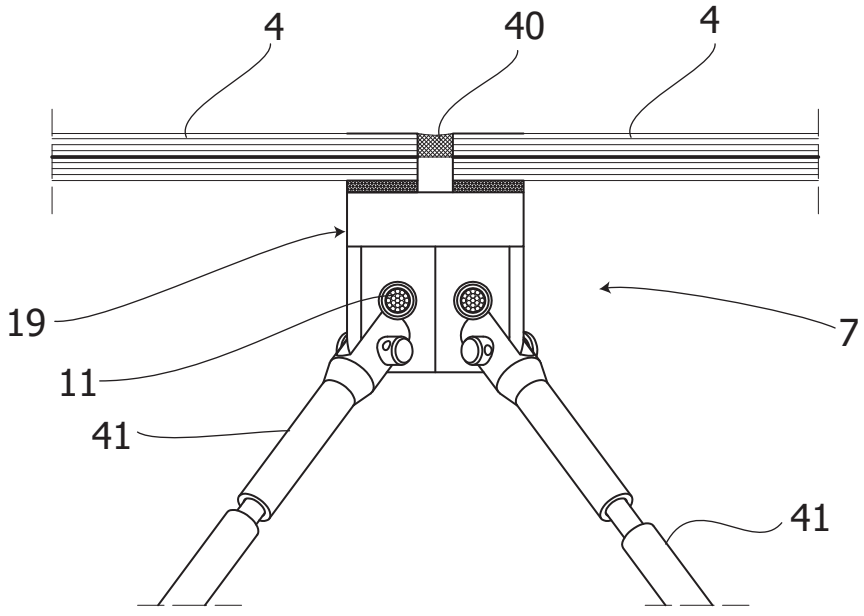

Fig. 8

Fig. 9a

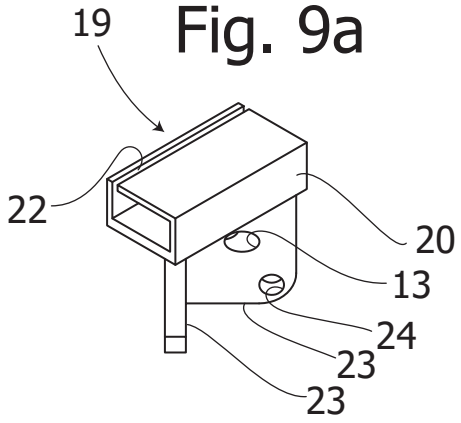

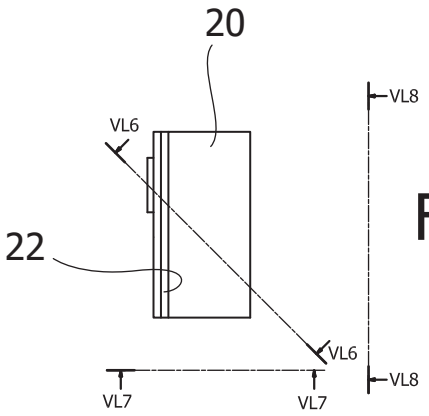

Fig. 9b

Fig. 9c

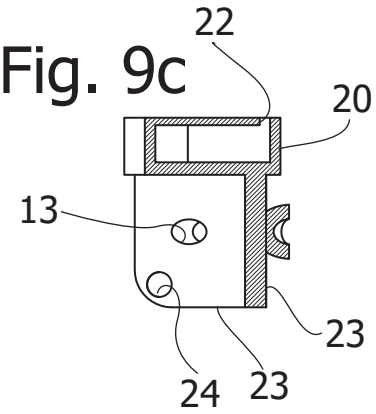

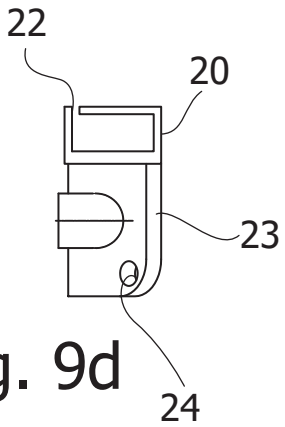

Fig. 9d

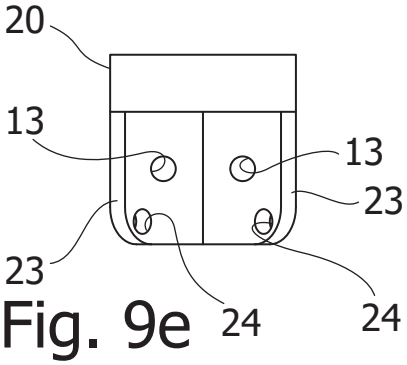

Fig. 9e

Fig. 10a

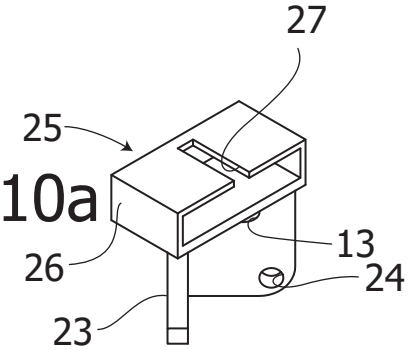

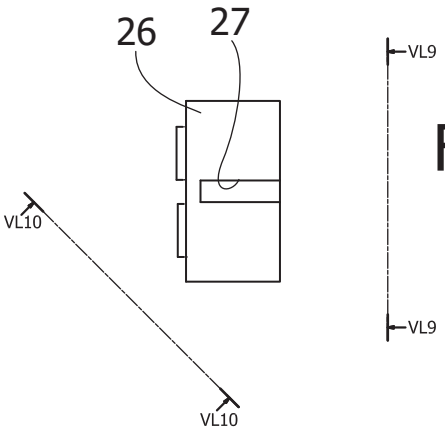

Fig. 10b

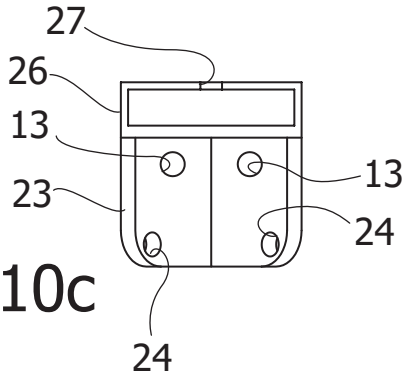

Fig. 10c

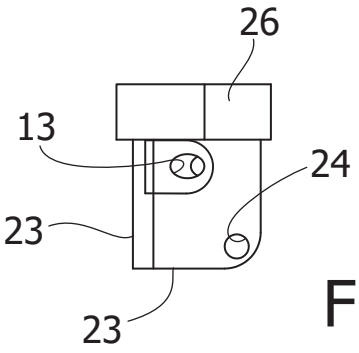

Fig. 10d

Fig. 11a

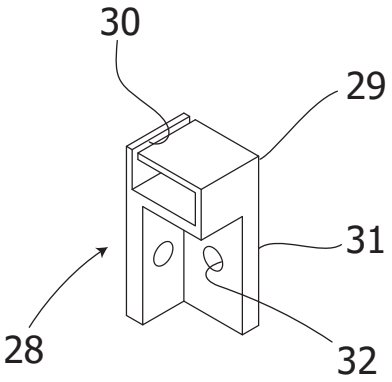

Fig. 11b

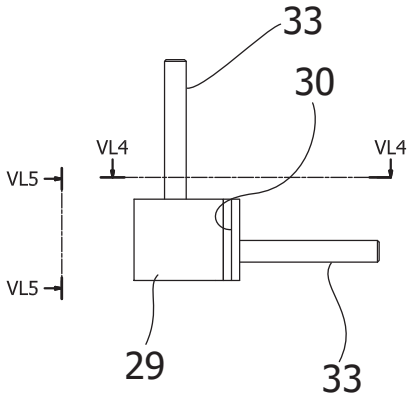

Fig. 11c

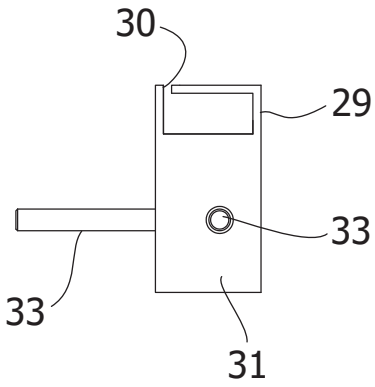

Fig. 11d

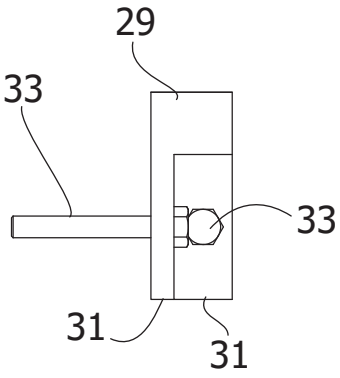

Fig. 12a

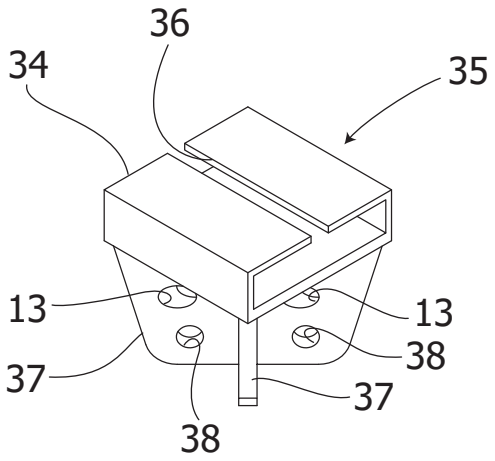

Fig. 12b

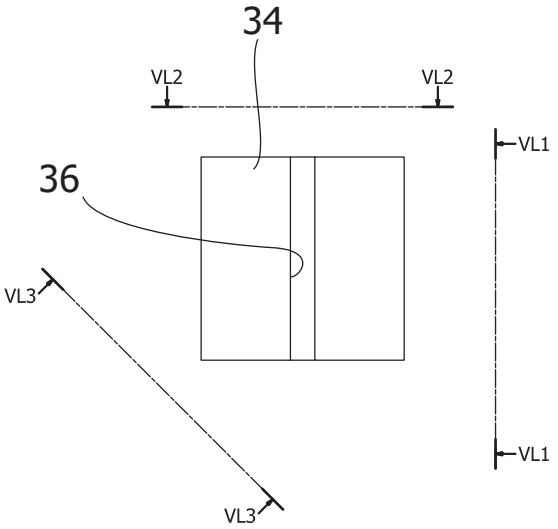

Fig. 12c

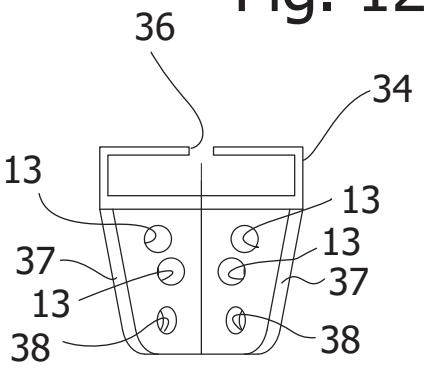

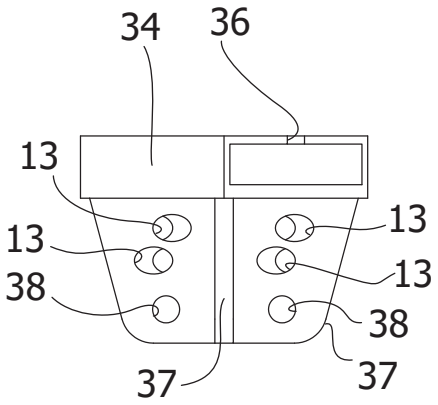

Fig. 12d

Fig. 12e

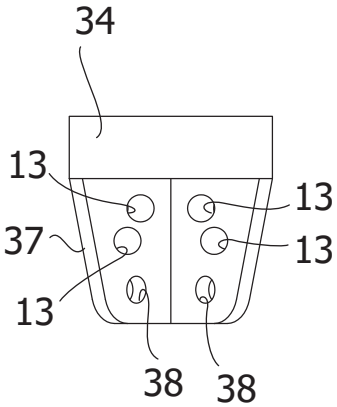

Fig. 13

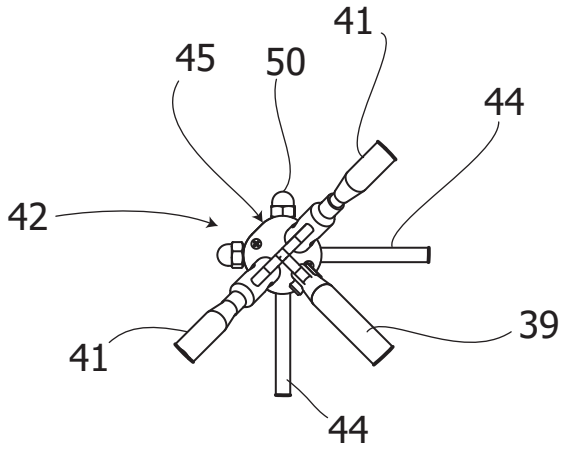

Fig. 14b

Fig. 14a

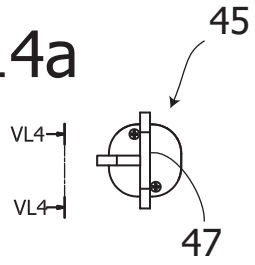

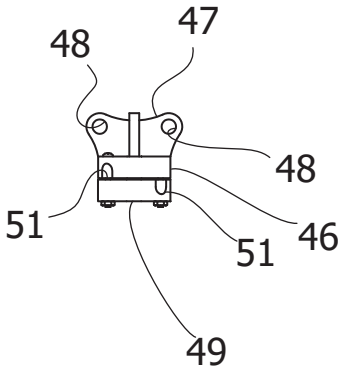

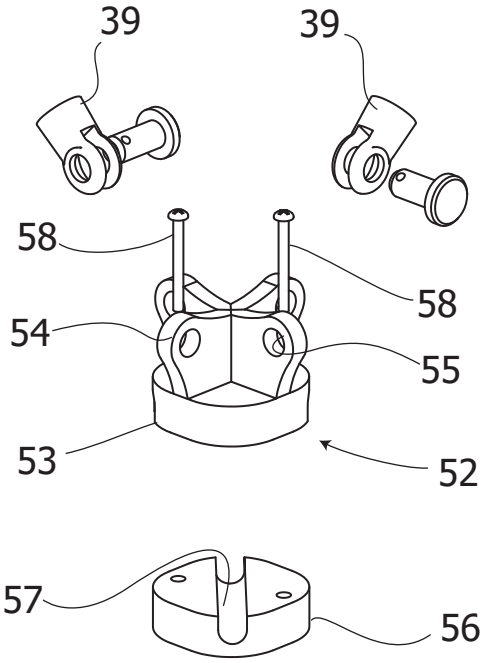

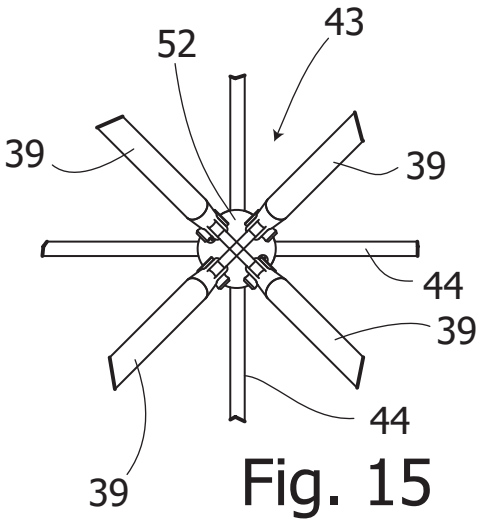

Fig. 15

Fig. 16